Hidden structures within structured light

Observing geometric phases and topologies for vector beams and their tomography

Amy McWilliam

A thesis submitted in fulfilment of the requirements for the degree of
Doctor of Philosophy

School of Physics and Astronomy
College of Science and Engineering
University of Glasgow
June 2024

Abstract

Structured light, recognised for its intricate spatial patterns in amplitude, phase and polarisation, has captivated researchers not only within the field of optics, but across various other disciplines. In this thesis, I cover topics centred around vector beams, known for their spatially varying polarisation distributions, highlighting some of the not so obvious (hidden) properties and structures within shaped light.

Many key aspects of structured light will be explored, ranging from technical considerations, more fundamental concepts (for example, geometric phases and optical skyrmions), and applications. The technical aspects of this thesis surround the generation of arbitrary vector beams using digital devices and their tomography. Applications that will be presented include single-shot Mueller matrix determination and a quantum key distribution protocol.

In optics, additional phase shifts arise due to the geometry of the system in which a beam propagates. Here, we present an experimental investigation into the non-planar propagation of scalar and vector light fields, demonstrating the rotation of both polarisation and intensity profiles and linking the rotations seen to geometric phases. The geometric phase acquired upon non-planar propagation is proportional to the total angular momentum number of the beam, allowing the concept of the angular momentum redirection phase to be introduced.

Optical skyrmions are topological structures embedded within the polarisation structures of vector light beams. We will present a new topological method for identifying and characterising skyrmion beams, using polarisation singularities and associated winding numbers. This approach provides an intuitive geometric insight and can be more robust when analysing noisy experimental data. Additionally, we present the propagation of optical skyrmions and a new method of generating tunable optical multi-skyrmions.

The tomography of vector beams is normally carried out using multiple sequential measurements in order to determine spatially varying polarisation profiles as well as spatial mode decomposition. Here, we present a system for the single-shot characterisation of vector beams by performing positive operator valued measurements, building on previous work. The measurements are performed using a Sagnac interferometric setup with proven stability over hours. The single-shot nature allows for superior acquisition speeds in comparison to other techniques, allowing for

time-resolved measurements. This will be demonstrated through dynamic Muller matrix polarimetry to measure changing optical activity, with a temporal resolution limited only by the camera frame rate.

Towards the end of this thesis, I also explore how vector beams can be used to implement a rotational reference frame invariant quantum key distribution protocol, their invariance to unitary perturbations, and also introduce and characterise a new family of orthonormal beams, the complex Zernike modes.

This thesis covers a diverse range of concepts, united by the theme of structured light, specifically, the topological structures within vector beams, their fundamental properties and applications. Here, we aim to show that by fully understanding and engaging with the additional degrees of freedom offered by vector light beams, we can unlock new possibilities, applications and theoretical insights that will further the field of optics.

Contents

List of Figures

Acknowledgements

First and foremost, I would like to thank my supervisor, Sonja Franke-Arnold, for her support, guidance and encouragement throughout not only my PhD, but also my masters project. Thank you for giving me the opportunity to undertake a PhD in the Optics group, I have learnt a lot over the last few years, and I couldn't have asked for a better supervisor.

Secondly, I would like to thank Claire Cisowski, for mentoring me when I first joined the Optics group. I enjoyed working with you in the lab near the beginning of my PhD and all of our interesting discussions. But, mostly, I'd like to thank you for always being willing to help and answering my many questions.

Thank you to my second supervisor, Rob Bennett, I enjoyed working with you on my first ever paper, and also to the "skyrmion team". It has been great to be able to work so closely with the Quantum Theory group throughout my time at Glasgow.

Finally, I would like to thank everyone in the Optics group, for making such a friendly and welcoming working environment. In particular, I would like to thank those who I have shared a lab and office with over the years, and those who provided me with regular puzzles and riddles to solve (which were, only sometimes, successful in distracting me from my work).

To my family, who do not understand what I do, thank you for always feigning interest when I talk about physics.

Author's Declaration

The thesis presented here for the examination for a PhD degree of the University of Glasgow is solely my own work, except where explicit reference is made to the work of others. I declare that this thesis does not include work forming part of a thesis submitted for any other degree.

Amy McWilliam
June 2024

Publications

Below is a list of the papers I contributed to during my PhD which have either been published, been submitted for publication, or are currently in preparation.

1. A. McWilliam, C. M. Cisowski, R. Bennett, and S. Franke-Arnold, "Angular momentum redirection phase of vector beams in a non-planar geometry," *Nanophotonics*, **11**(4), 727–736 (2022). https://doi.org/10.1515/nanoph-2021-0528

2. I. Nape, K. Singh, A. Klug, W. Buono, C. Rosales-Guzman, A. McWilliam, S. Franke-Arnold, A. Kritzinger, P. Forbes, A. Dudley, and A. Forbes, "Revealing the invariance of vectorial structured light in perturbing media," *Nature Photonics*, **16**, 538–546 (2022). https://doi.org/10.1038/s41566-022-01023-w

3. A. McWilliam, C. M. Cisowski, Z. Ye, F. C. Speirits, J. B. Götte, S. M. Barnett and S. Franke-Arnold, "Topological approach of characterizing optical skyrmions and multi-skyrmions," *Laser and Photonics Reviews*, **17**(9), 2300155 (2023). https://doi.org/10.1002/lpor.202300155

4. S. M. Barnett, C. M. Cisowski, A. McWilliam, F. C. Speirits, Z. Ye, J. B. Götte, and S. Franke-Arnold,"Optical Skyrmions," Proc. SPIE 12647, *Active Photonic Platforms (APP) 2023*, 126470A (4 October 2023). https://doi.org/10.1117/12.2676688

5. A. McWilliam, C. M. Cisowski, Z. Ye, F. C. Speirits, J. B. Götte, S. M. Barnett and S. Franke-Arnold, "A topological approach to characterising optical skyrmions," Proc. SPIE 12901, *Complex Light and Optical Forces XVIII*, 1290105 (12 March 2024). https://doi.org/10.1117/12.3002420

6. A. McWilliam, M. A. Al Khafaji, S. J. Svensson, S. Pádua, and S. Franke-Arnold, "Dynamic Mueller matrix polarimetry using generalised measurements", *Optics Express* **32**(12), 21909-21924 (2024). https://doi.org/10.1364/OE.521069

7. Z. Ye, S. M. Barnett, S. Franke-Arnold, J. B. Götte, A. McWilliam, F. C. Speirits, and C. M. Cisowski, "Theory of paraxial optical skyrmions," *Proceedings of the Royal Society A* **480** (2024). https://doi.org/10.1098/rspa.2024.0109

8. A. McWilliam, K. Maxwell, D. Sugic, S. Franke-Arnold, and M. R. Dennis, "Spinning Zernike beams in free space" (In progress).

9. A. McWilliam, S. J. Svensson, S. Croke, and S. Franke-Arnold, "A BB84 protocol using rotationally symmetric states and a Fresnel cone" (In progress).

10. P. L. Lalaguna, P. Souchu, N. Mackinnon, F. Crimin, R. Kumar, S. K. Chaubey, A Sarguroh, A. McWilliam, A. Y. Ganin, D. A. MacLaren, S. Franke-Arnold, J. B. Götte, S. M. Barnett, N. Gadegaard, and M. Kadodwala, "Spatial Control of 2D Nanomaterial Electronic Properties using Chiral Light Beams," *ACS Nano*, **18**(31), 20401-20411 (2024). https://doi.org/10.1021/acsnano.4c04506

The contents of my first publication (1) are detailed in chapter 3, papers 3, 4, 5 and 7 are covered in chapter 4, 6 in chapter 5, and 9 in chapter 6. For the second (2) and eighth (8) papers, I had a slightly smaller contribution to the projects, with the experiments performed as an aside to my core PhD work. However, the work is still related to this thesis, therefore, I will briefly discuss my contribution to both projects and the relevant results in chapter 7.

Introduction

Optics is perhaps the oldest discipline of physics, with its roots lying within ancient astronomy. The field began with the development of lenses made from polished crystal, by the ancient Egyptians and Mesopotamians, or by filling glass spheres with water, as done by the ancient Romans and Greeks. Shortly after, geometric optics was born, describing light as propagating rays with the use of simple geometry. A concise history of the field of light and optics up until the start of the 21st century is given by Hecht in the first chapter of Ref. [1].

The diffraction of light was first recorded by Professor Francesco Maria Grimaldi (1618–1663), which later led to the first hypothesis of the wave-like nature of light in the late 17th century by Robert Hooke (1635–1703), after also observing the diffraction phenomenon. At about the same time, Christiaan Huygens (1629–1695) introduced the first mathematical description of light, derived the Laws of Reflection and Refraction and even discovered polarisation, all of which have become fundamental concepts in optics.

In the mid-1900s, there were two significant inventions that are related to the work that will be presented in this thesis and are therefore worth highlighting. The first is that of holography, introduced by Gabor in 1948 [2], and is a technique allowing the recording and reconstruction of wavefronts. The second is the development of the laser in 1960 [3], which brought about significant advancements, in not just optics but within science and technology more generally. Lasers produce highly coherent light beams, and are available in a wide variety of specifications, such as wavelength, power, and the option between continuous wave and pulsed outputs. Laser technology has found many applications, from gas sensing [4, 5], measuring object distances (LIDAR) [6, 7], spectroscopy [8], microscopy [9, 10] and communication [11, 12].

The invention of the laser also made an impact in the area of structured light [13]. Structured light refers to the *tailoring* of the properties of a light beam, for example, its intensity, phase, wavelength or polarisation [14]. In fact, it was the advent of the laser along with holographic techniques that really propelled this subfield of optics, along with the emergence of small devices which allow the dynamic spatial control of light beams, which in turn, allow the implementation of computer generated holograms. Two such devices which have become popular in the optics

and structured light communities are spatial light modulators (SLMs) and digital micromirror devices (DMDs) [15–18].

Classical optics has a long history, nevertheless, despite how developed the field has become, modern optics continues to surprise and intrigue researchers. Whilst some concepts, such as the wave nature of light, is rarely questioned, other optical effects still intrigue us, and, it is perhaps surprising how much there is still to be explored with classical light.

In contrast to the extensive history of optics overall, the field of structured light as we recognise it today remains relatively young, accelerating in the early to mid-2000s when photonic devices in the form of re-writable SLMs and DMDs became commercially available, along with advances in readily accessible computing power [13]. Structured light has many applications, arising from the flexibility in the control of light fields. Examples include microscopy, where particular shaped light beams have been shown to provide smaller focal spots [19, 20], optical trapping and tweezing of small particles [21], microstructure fabrication [22, 23], and for optical communications, where structured beams can enable efficient data transmission by offering additional degrees of freedom [24–27].

In this thesis, the focus will be less on the applications of structured light fields but instead, more on the properties of the beams themselves. Specifically, this work will concentrate mainly on a particular class of shaped light, known as vector beams, which contain spatially varying polarisation. The experimental generation of these beams will be discussed as well as ways of generating and controlling other arbitrary structured light fields.

In Chapter 3, I will present the first project undertaken as part of my PhD, looking at geometric phases of vector beams. Geometric phases are an important and central concept in physics, particularly in optics, where optics played a vital role in its discovery and in developing the theoretical framework. And it is in the field of optics where the first experimental demonstrations were carried out [28]. For this experiment, we look at the combined effects of two geometric phases, specifically the spin- and orbital-redirection phases, by propagating vector beams along a non-planar trajectory.

In recent years, topological structures that can be found in optics and structured light fields have become of interest. In chapter 4, I focus on the experimental generation and identification of vector beams containing skyrmionic structures. I will provide a theoretical overview of the topological properties of such beams, with a comparison to skyrmions found in other areas of physics, introduce a new way of characterising them, and new ways of generating multi-skyrmions.

Chapter 5 concerns the tomography of vector beams using generalised measurements. The experimental scheme I will introduce is based on a Sagnac interferometer configuration and allows the spatially varying polarisation profiles of vector beams to be obtained with a single camera frame. In this chapter, I will also demonstrate an application of this experimental measurement system in the form of dynamic

Mueller matrix polarimetry. This is useful for determining optical activity changes over time and could be applied to the investigation of biological samples or chemical reaction processes.

Optics is widely used for communication applications and, due to the ability to generate and control single photons and send them long distances using optical fibres, optics provides a favourable platform for the implementation of quantum key distribution (QKD) protocols, allowing for theoretically secure communication channels [29–33]. In chapter 6, I present a QKD protocol using rotationally symmetric vector beams as basis states, and a measurement system that makes the entire protocol rotational reference frame invariant. The measurement system incorporates a solid glass optical component known as a Fresnel cone, which relies solely on total internal reflection [34]. The Fresnel cone can also be used as a static device for generating vector beams, and the mechanism behind this will be explained, and examples shown.

Finally, in chapter 7, I will describe two additional short projects undertaken as part of my PhD work. These projects were completed in collaboration with other universities and as an aside to my main PhD work. Nonetheless, the experiments are related to this thesis and my contribution will be discussed. The first project concerned the experimental generation and characterisation of a new family of spatial light beams - complex Zernike modes. The second project looked at the invariance of the "vectorness" of vector beams to unitary perturbations. For my contribution, I investigated the invariance of vector beams after propagating through chiral media.

All of these projects are linked in that they are concerned with structured light beams and either their properties or applications. However, the theoretical aspects of each are quite distinct. Therefore, I have chosen to structure this thesis such that all the required theory for each project is contained within the relevant chapter. In Chapter 1, I will give a broad overview of structured light and the basic background theory common to all of the individual projects completed throughout my PhD. In Chapter 2, I will give the details pertaining to the experimental generation and analysis of vector beams with spatially varying polarisation, as well as some other experimental details and considerations required for all of the different experiments that will be discussed. The remaining chapters will then focus on the specific theory and experimental details belonging to one individual project, presenting the relevant results therein.

Chapter 1

Background theory and conventions

1.1 Chapter 1 introduction

In this chapter, I will provide the background theory that is relevant to all of the individual projects completed throughout my PhD. The theory presented here forms the foundation on which the work shown in this thesis is derived. I will start by giving an overview of the wave nature of light as well as introducing the concept of polarisation and the different ways in which it can be represented.

In § 1.4, I present the mathematical description of the Gaussian beam and its higher order modes, before moving on to discuss structured light more generally and the differences between scalar and vectorial light fields. Descriptions of general vector beams will be given, along with how we can theoretically construct light beams with spatially varying polarisation. With this, I will give a brief introduction to some of the structures and topologies that can be found in beams with spatially varying polarisation.

Finally, I will discuss the angular momentum of light, comparing both the spin and orbital components.

1.2 The wave theory of light and the wave equation

The nature of light is central to the complete treatment and understanding of the field of optics. Furthermore, understanding light as a wave is paramount to the structuring of light fields in both the scalar and vectorial regimes.

Isaac Newton (1642-1727) proposed that light consists of particles (photons), whereas Christian Huygens (1629–1695) took opposing views, believing that light behaved as a wave, propagating perpendicular to its direction of motion [1]. This brought about the much contested question: "Is light a particle or a wave?" The concept of wave particle duality from quantum mechanics embraces the different

properties of light, acknowledging that particles can exhibit wave-like qualities, and waves particle-like qualities, depending on the experimental circumstances [35].

James Clerk Maxwell's 1865 paper [36], and subsequent developments, made evident the electromagnetic nature of light. The field of quantum electrodynamics describes electromagnetic interactions and energy transport in terms of the massless photons [37]. However, in optics, the quantum nature of light is not always apparent, and it is more often than not, not a practical concern (as is the case for the work presented in this thesis). Despite this, both the classical and quantum mechanical approaches to the treatment of light use the mathematical description of waves, as such, I will begin with a description of how the vectorial wave nature of light emerges from Maxwell's equations.

Normally, and for the work that will be presented here, we are concerned with light travelling in free space, therefore, assuming a vacuum and in the absence of free charges, Maxwell's Equations can be written as [1],

$$\nabla \cdot \mathbf{E} = 0 \qquad (1.1a) \qquad \nabla \times \mathbf{E} = -\frac{\partial \mathbf{B}}{\partial t} \qquad (1.1b)$$

$$\nabla \cdot \mathbf{B} = 0 \qquad (1.1c) \qquad \nabla \times \mathbf{B} = \mu_0 \varepsilon_0 \frac{\partial \mathbf{E}}{\partial t} \qquad (1.1d)$$

where $\mathbf{E}$ is the electric field, $\mathbf{B}$ the magnetic field, μ_0 and ε_0 are the permeability and permittivity of free space, respectively, and ∇ is the nabla operator. Individually, there four equations are the differential form of Gauss's Law for electric fields and magnetic fields (Eqs. 1.1a and 1.1c), the differential form of Faraday's law (Eq. 1.1b) and Ampere's law (Eq. 1.1d), but together they form Maxwell's equations, describing electromagnetic waves in free space. These equations can now be used to derive the free space wave equation, as outlined in Ref. [1].

By taking the curl of Eq. 1.1b and using Eq. 1.1d to eliminate $\mathbf{B}$ gives,

$$\nabla \times (\nabla \times \mathbf{E}) = -\mu_0 \varepsilon_0 \frac{\partial^2 \mathbf{E}}{\partial^2 t}. \qquad (1.2)$$

Applying Lagrange's formula for the vector triple product[1], and recalling that $\nabla \cdot \mathbf{E} = 0$ when no charges are present, leaves us with,

$$\nabla^2 \mathbf{E} - \mu_0 \varepsilon_0 \frac{\partial^2 \mathbf{E}}{\partial^2 t} = 0. \qquad (1.3)$$

Together, the term $\mu_0 \varepsilon_0$ has dimensions of (time/length)^2 allowing us to define $c = \frac{1}{\sqrt{\mu_0 \varepsilon_0}} = 2.998 \times 10^8 \mathrm{ms}^{-1}$, which is of course the speed of light in a vacuum.

[1] $\nabla \times (\nabla \times \mathbf{V}) = \nabla(\nabla \cdot \mathbf{V}) - \nabla^2 \mathbf{V}$ for any vector $\mathbf{V}$ [1,38].

From this and the fact that the above expression is a linear second-order partial differential equation, we can recognise that Eq. 1.3 has the standard form of a wave equation for the electric field,

$$\nabla^2\mathbf{E} - \frac{1}{c^2}\frac{\partial^2\mathbf{E}}{\partial^2 t} = 0. \tag{1.4}$$

Following a similar procedure, we can also arrive at an expression for the wave equation for the magnetic field component,

$$\nabla^2\mathbf{B} - \frac{1}{c^2}\frac{\partial^2\mathbf{B}}{\partial^2 t} = 0. \tag{1.5}$$

The **E** and **B**-fields are always perpendicular to each other and are perpendicular to the direction of propagation of the wave. Maxwell's equations can be used to describe how these waves propagate in space - a changing electric field induces a changing magnetic field (Ampere's law Eq. 1.1d) and a changing magnetic field creates a changing electric field (Faraday's law Eq. 1.1b). It is this continual cycle that allows light waves (and indeed all electromagnetic radiation) to propagate through space.

One simple, but important solution to the wave equation Eq. 1.4, is that of a sinusoidal plane wave. For such a wave travelling in the $\hat{r}$ direction, and for spatial and temporal coordinates $\mathbf{r} = [x, y, x]$ and t, the plane wave solution can be written as,

$$\mathbf{E}(\mathbf{r}, t) = E_0(\mathbf{r})\mathrm{e}^{i(\mathbf{k}\cdot r - \omega t + \phi_0)}\mathbf{e}_r, \tag{1.6}$$

where $E_0(\mathbf{r})$ is the amplitude, ϕ_0 is the phase offset at time $t = 0$, and $\mathbf{e}_r$ is a unit vector in the direction of the waves oscillation, defining the polarisation (see § 1.3). The wave vector, $\mathbf{k}$, indicates the direction of propagation and is perpendicular to surfaces of constant phase ($\phi = \mathbf{k}\cdot\mathbf{r} - \omega t + \phi_0 = constant$). Its magnitude $|\mathbf{k}|$ is given by the wave number $k = \omega/c = 2\pi/\lambda$ for monochromatic wavelength λ. Again, we can write a similar expression for a plane wave in terms of the magnetic field. From the requirements of Eqs. 1.1a and 1.1c, we can obtain the relation,

$$\mathbf{k}\cdot\mathbf{E}_0 = \mathbf{k}\cdot\mathbf{B}_0 = 0, \tag{1.7}$$

confirming that **E** and **B** are both perpendicular to each other and also to the direction of propagation given by **k**. Waves that satisfy this condition are known as *transverse waves* [39].

Substituting the plane wave solution into the wave equation (Eq. 1.4), results in the Helmholtz equation [39],

$$\nabla^2\mathbf{E}(\mathbf{r}) + k^2\mathbf{E}(\mathbf{r}) = 0. \tag{1.8}$$

This is just a time-independent version of the wave equation, valid for the case of single frequencies. However, if we choose a fixed constant direction for the electric

field, then we become only interested in its magnitude, denoted $E(\mathbf{r})$. This allows us to write a *scalar* form of the Helmholtz equation [40, 41],

$$(\nabla^2 + k^2)E(\mathbf{r}) = 0. \tag{1.9}$$

The significance of the difference between the scalar and vectorial forms of the Helmholtz equation will become evident in § 1.5.

One feature of the plane wave solution is that knowing the values of $E(\mathbf{r})$ and ϕ in a single transverse plane at any arbitrary position along the propagation axis z, fully determines their values in any other plane. Therefore, controlling these two (spatial) parameters plays a crucial role in the structuring of light beams. Additionally, it is important to note that linear combinations of solutions of the form of Eq. 1.6, are also solutions to the wave equation, which, as we will see, produces interesting effects in terms of the spatial polarisation control. Without loss of generality, we can consider propagation in the z direction, allowing a general solution to be written as,

$$\mathbf{E}(z,t) = \sum_j E_{0j}(z)\mathrm{e}^{i(kz-\omega t+\phi_j)}\mathbf{e}_j, \tag{1.10}$$

where, we have assumed the same wavelength (therefore the same angular frequency ω) between the superimposed waves, as this is the relevant case for the work presented here.

1.2.1 The paraxial approximation

For the work that will be presented in this thesis we will only be concerned with paraxial light. In ray optics, the paraxial approximation assumes that a light ray only ever makes small angles (θ) with the optical axis, allowing the small-angle approximation to be exploited. It is often applied in Gaussian optics when tracing rays of light through entire optical systems, assuming that θ remains small [1, 41, 42].

In the paraxial regime, the three spatial components of the light field (x, y and z in a Cartesian system), never mix together, allowing for them to be independently treated [41]. As the magnitude of the wave vector depends on the quadrature addition of its components, $|\mathbf{k}| = k = \sqrt{k_x^2 + k_y^2 + k_z^2} = 2\pi/\lambda$, and assuming propagation in the z-direction, the x and y components of the wave vector must be much smaller than k, i.e.,

$$\frac{\sqrt{k_x^2 + k_y^2}}{k} \ll 1. \tag{1.11}$$

In fact, it is this approximation that leads to the scalar form of the Helmholtz equation above (Eq. 1.9).

1.3 Polarisation

It was Fresnel (in 1818) who first proposed a wave theory of light,[2] postulating that an optical field consisted of two orthogonal components, oscillating in the transverse plane to the propagation direction [43]. This was later confirmed experimentally by both Fresnel and Arago [44]. The oscillation of these orthogonal field components will have a specific orientation, or direction, at any given time as the electromagnetic field propagates. In the plane wave solution (Eq. 1.6) to the wave equation, I included a unit vector $\mathbf{e}_r$ which describes this orientation of the oscillations. The magnitude and orientation of this oscillation, described by $\mathbf{e}_r$, is known as the *polarisation*.

To consider the direction of the electric field oscillation at any point in time, we can follow on from Fresnel's ideas by considering the orthogonal components of the electric field. In a Cartesian coordinate system, it is conventional to consider a beam propagating in the z direction, and the decomposition of the electric field into orthogonal x and y components [44],

$$\begin{aligned} E_x(z,t) &= E_{0x}\cos\left(kz-\omega t+\phi_x\right) \\ E_y(z,t) &= E_{0y}\cos\left(kz-\omega t+\phi_y\right) \\ E_z(z,t) &= 0, \end{aligned} \tag{1.12}$$

where the x, y and z subscripts indicate the components in the x, y and z directions, respectively. Additionally, Eq. 1.12 are all solutions to the wave equation, and a graphical representation of the waves described by E_x and E_y is shown in Figure 1.1.

From Figure 1.1 it can clearly be seen that E_x describes sinusoidal oscillations in the x-z plane and, similarly, E_y describes oscillations in the y-z plane. These waves do not provide much insight when considered individually. However, by considering them together, we can get an expression for the relation between E_x and E_y, representing the curve traced out by the tip of the electric field vector. To do this, we can start by rewriting Eq. 1.12 as,

$$\begin{aligned} \frac{E_x}{E_{0x}} &= \cos\tau\cos\phi_x-\sin\tau\sin\phi_x \\ \frac{E_y}{E_{0y}} &= \cos\tau\cos\phi_y-\sin\tau\sin\phi_y, \end{aligned} \tag{1.13}$$

where the substitution $\tau = kz - wt$ has been made. Hence,

$$\begin{aligned} \frac{E_x}{E_{0x}}\sin\phi_y-\frac{E_y}{E_{0y}}\sin\phi_x &= \cos\tau\sin\left(\phi_y-\phi_x\right) \\ \frac{E_x}{E_{0x}}\cos\phi_y-\frac{E_y}{E_{0y}}\cos\phi_x &= \sin\tau\cos\left(\phi_y-\phi_x\right). \end{aligned} \tag{1.14}$$

[2] Now known as Fresnel's wave theory or the Huygens-Fresnel principle due to the influence of Christiaan Huygens's mathematical principles on Fresnel's work.

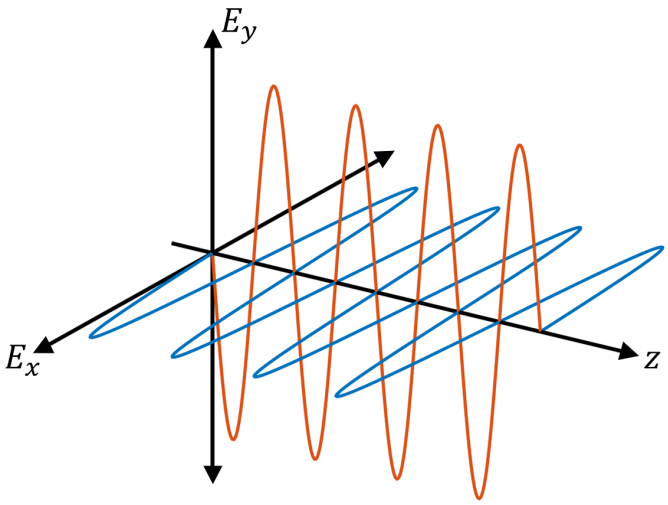

Figure 1.1: Representation of the oscillation of the orthogonal electric field components as described by Eq. 1.12.

Squaring and adding the previous expressions gives,

$$\left(\frac{E_x}{E_{0x}}\right)^2 + \left(\frac{E_y}{E_{0y}}\right)^2 - 2\frac{E_x}{E_{0x}}\frac{E_y}{E_{0y}}\cos\Delta\phi = \sin^2\Delta\phi \tag{1.15}$$

where $\Delta\phi = \phi_y - \phi_x$ [45]. Equation 1.15 is the equation of an ellipse (although, in its nonstandard form). Note that, we have eliminated the $\tau = kz - \omega t$ term, but the $E_x(z,t)$ and $E_y(z,t)$ are still both time and space dependent [44]. An example of an ellipse described by Eq. 1.15 is shown in Figure 1.2. As it is a representation of a polarisation state, it is referred to as the *polarisation ellipse*.

In Figure 1.2, I show the ellipse in reference to the Cartesian coordinate system with x and y axes and also the rotated coordinate system of the ellipse with a and b axes. The ellipse can be characterised using two angular parameters ψ and χ, representing the orientation and ellipticity respectively. These parameters are given by the expressions [44, 45],

$$\begin{aligned} \tan(2\psi) &= \frac{2E_{0x}E_{0y}}{E_{0x}^2 - E_{0y}^2}\cos\Delta\phi, \qquad 0 \le \psi \le \pi \\ \sin(2\chi) &= \frac{2E_{0x}E_{0y}}{E_{0x}^2 + E_{0y}^2}\sin\Delta\phi, \quad -\frac{\pi}{4} \le \chi \le \frac{\pi}{4}. \end{aligned} \tag{1.16}$$

For homogeneously polarised beams, the amplitudes E_{0x} and E_{0y} and the phase difference $\Delta\phi$ remains constant, meaning that the polarisation ellipse is unchanged as the beam propagates under the paraxial regime. However, as we will see, this is not always the case for beams with spatially varying polarisation, or when the propagation is no longer paraxial.

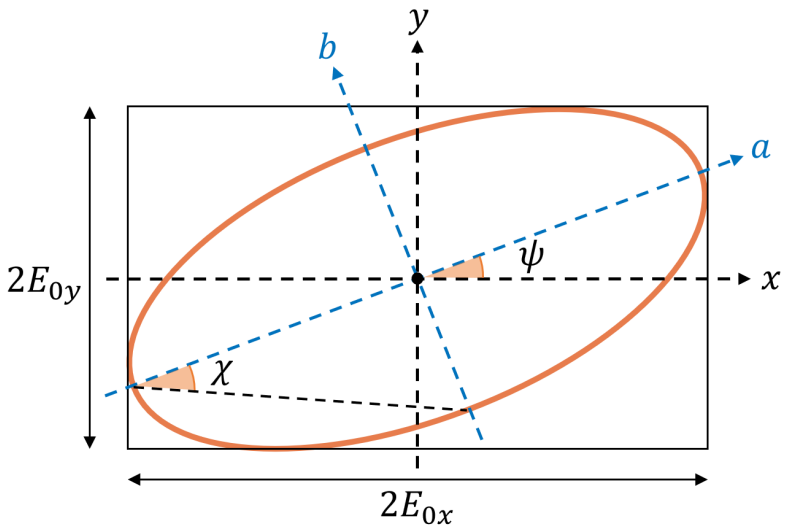

Figure 1.2: Representation of a polarisation ellipse with orientation ψ and ellipticity χ. The Cartesian coordinate system of the plane wave decomposition is indicated by the x-y axes. The a-b axes represent the rotated coordinate system of the ellipse.

In general, a polarisation state can have any ψ and χ, but there are some 'simple' polarisation states that are of particular interest, occurring for the two extreme values of ellipticity, $|\chi| = 0$ or $\pi/4$. This corresponds to the polarisation being either completely linear ($\chi = 0$) or circular ($|\chi| = \pi/4$), examples of which are shown in Figure 1.3.

When $E_{0y} = 0$ or $E_{0x} = 0$, we get linear horizontal or vertical polarisation, respectively. When $E_{0x} = E_{0y} = E_0$ and $\Delta\phi = 0$ or π, we get linear polarisation orientated at $\pm 45°$, which we refer to as diagonal or anti-diagonal polarisation. If we still have equal amplitudes, but instead $\Delta\phi = \pm\pi/2$ then we get either left-handed or right-handed circular polarisation. With this, we have defined three sets of orthogonal polarisations, each comprising a set of mutually unbiased bases (MUBs). For this reason, throughout this thesis I will often refer to these (normalised) polarisation states using bra-ket notation with $|\hat{h}\rangle$, $|\hat{v}\rangle$, $|\hat{d}\rangle$, $|\hat{a}\rangle$, $|\hat{r}\rangle$ and $|\hat{l}\rangle$ corresponding to the horizontal, vertical, diagonal, anti-diagonal, right-handed circular and left-handed circular polarisation states respectively, as indicated in Figure 1.3. In the following sections, we will see how these particular states become important for the measurement and characterisation of polarisation and also for the representation of polarisation in another way - by employing the Poincaré sphere (see § 1.3.3).

As mentioned, the tip of the electric field traces out a polarisation ellipse. The individual oscillations of the electric field components are too fast to be measured experimentally. Nonetheless, the polarisation state can still be measured, and this measurement is an average over many oscillations. How polarisation can be measured experimentally will be discussed in § 2.3, but first, it is useful to detail the

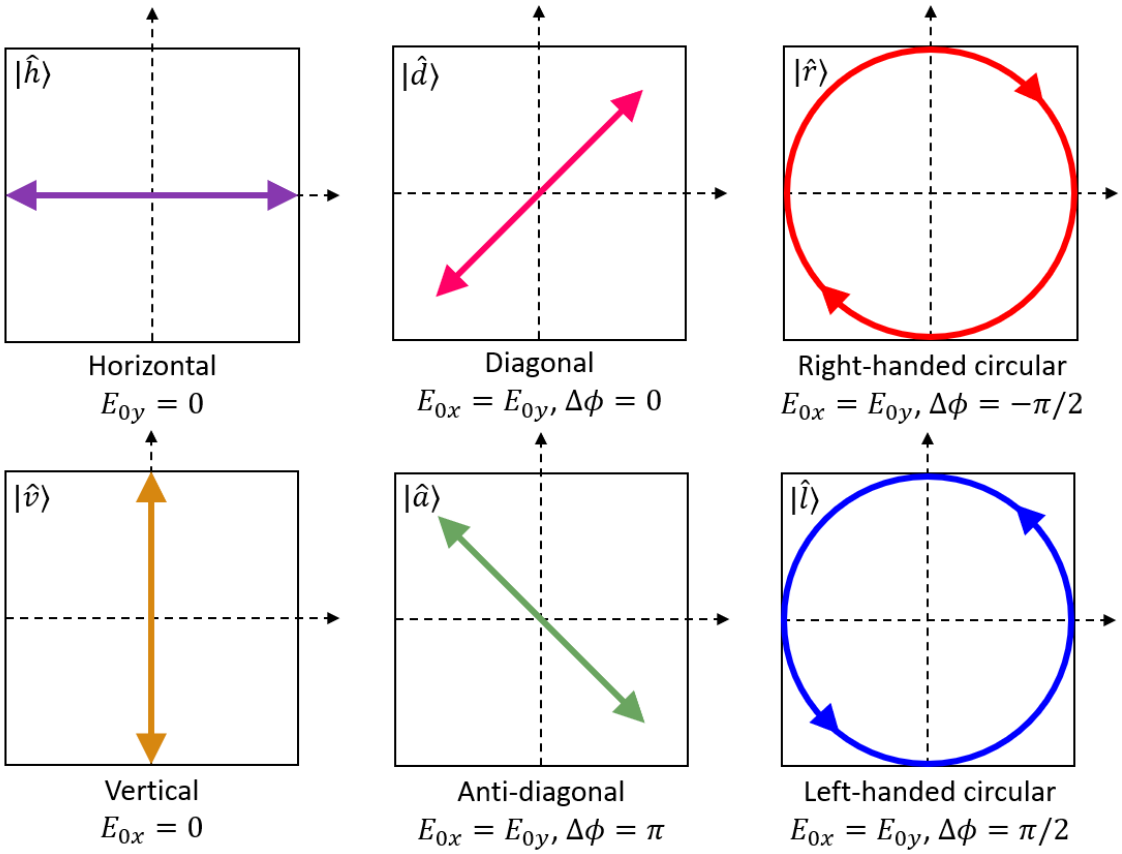

Figure 1.3: Polarisation ellipses for three sets of orthogonal polarisation states, described by the Jones vectors in Eq. 1.21.

most common formalism's used for describing a polarisation state, namely, Jones vectors and Stokes vectors.

1.3.1 Jones vector representation

R. Clark Jones, in 1941 [46], devised a two-dimensional matrix algebra for describing *fully* polarised light and the action of polarisation altering optical elements. Note that the limitation of this algebra only describing fully polarised light means that it does not apply to the cases of unpolarised or partially polarised light (e.g. sunlight). For this, the Stokes representation must be used, as outlined in the next section (§ 1.3.2). However, the Jones representation is often preferred as it is very concise, and is useful for situations in which field amplitudes (rather than intensities) must be known, e.g. when considering interference.

For his mathematical representation, R. C. Jones used the property of a light beam being entirely transverse in the paraxial regime. As such, the polarisation can be decomposed into two orthogonal components. As mentioned above, in a Cartesian coordinate system, it is conventional to consider a beam propagating in the z direction, and the decomposition of the electric field into orthogonal x and y components, allowing Eq. 1.10 to be written as,

$$\begin{aligned}\mathbf{E}(z,t) &= E_{0x}\mathrm{e}^{i(kz-\omega t+\phi_x)}\mathbf{e}_x + E_{0y}\mathrm{e}^{i(kz-\omega t+\phi_y)}\mathbf{e}_y, \\ &= \left(E_{0x}\mathrm{e}^{i\phi_x}\mathbf{e}_x + E_{0y}\mathrm{e}^{i\phi_y}\mathbf{e}_y\right)\mathrm{e}^{i(kz-\omega t)},\end{aligned} \tag{1.17}$$

where the x and y subscripts indicate the components in the x and y directions, respectively. The polarisation is not time-dependent, so the time-dependent $\mathrm{e}^{i(kz-\omega t)}$ term can be neglected, allowing the above expression to be written in a vector form,

$$\mathbf{E} = \begin{bmatrix} E_x \\ E_y \end{bmatrix} = \begin{bmatrix} E_{0x}\mathrm{e}^{i\phi_x} \\ E_{0y}\mathrm{e}^{i\phi_y} \end{bmatrix}. \tag{1.18}$$

This is the *Jones vector* describing the polarisation state of the light beam. As it is just the phase difference between the x and y components that is important to describe the polarisation, an equivalent vector can be written as,

$$\mathbf{E} = \begin{bmatrix} E_{0x} \\ E_{0y}\mathrm{e}^{i\Delta\phi} \end{bmatrix}. \tag{1.19}$$

If E_x and/or E_y are spatially varying, then $\mathbf{E}$ will also be spatially varying.

The E_x and E_y components are of course complex quantities, and can be used to obtain the intensity I of the beam,

$$I = \begin{bmatrix} E_x^* E_y^* \end{bmatrix} \begin{bmatrix} E_x \\ E_y \end{bmatrix} = E_x E_x^* + E_y E_y^* = |E_x|^2 + |E_y|^2. \tag{1.20}$$

The normalised Jones vectors for the six polarisation states shown in Figure 1.3 are,

$$|\hat{h}\rangle = \begin{bmatrix}1\\0\end{bmatrix}, \qquad |\hat{v}\rangle = \begin{bmatrix}0\\1\end{bmatrix},$$

$$|\hat{d}\rangle = \frac{1}{\sqrt{2}}(|\hat{h}\rangle + |\hat{v}\rangle) = \frac{1}{\sqrt{2}}\begin{bmatrix}1\\1\end{bmatrix}, \qquad |\hat{a}\rangle = \frac{1}{\sqrt{2}}(|\hat{h}\rangle - |\hat{v}\rangle) = \frac{1}{\sqrt{2}}\begin{bmatrix}1\\-1\end{bmatrix}, \tag{1.21}$$

$$|\hat{l}\rangle = \frac{1}{\sqrt{2}}(|\hat{h}\rangle + i\,|\hat{v}\rangle) = \frac{1}{\sqrt{2}}\begin{bmatrix}1\\i\end{bmatrix}, \qquad |\hat{r}\rangle = \frac{1}{\sqrt{2}}(|\hat{h}\rangle - i\,|\hat{v}\rangle) = \frac{1}{\sqrt{2}}\begin{bmatrix}1\\-i\end{bmatrix},$$

where the imaginary i results from a phase difference of $\Delta\phi = \pi/2$. From Eq. 1.21, it can be seen that the superposition of two Jones vectors results in an other Jones vector.

Jones Matrices

Suppose we have a beam with polarisation described by a Jones vector $\mathbf{E}_{\text{in}}$ incident on an optical element. If the action of the optical element changes the polarisation then we end up with an output beam given by $\mathbf{E}_{\text{out}}$. This process can be described mathematically using Jones calculus [46]. As a polarisation state can be described by 2×1 vector, then we can describe transformations using a 2×2 matrix [1],

$$\mathbf{E}_{\text{out}} = \mathbf{J}\mathbf{E}_{\text{in}} = \begin{bmatrix}J_{11} & J_{12}\\J_{21} & J_{22}\end{bmatrix}\begin{bmatrix}E_x^{\text{in}}\\E_y^{\text{in}}\end{bmatrix}, \tag{1.22}$$

where $\mathbf{J}$ is known as the *Jones matrix*. We can obtain Jones matrices to describe the action of any optical element, and some of the most common ones (e.g. for waveplates and polarisers) will be given in § 2.2.3 in Chapter 2, where I focus on experimental equipment and techniques. However, we can also obtain a Jones matrix to describe the action of an entire optical system by using the product of n matrices for the n individual elements that a beam interacts with in the system,

$$\mathbf{J}_{\text{system}} = \mathbf{J}_n\mathbf{J}_{n-1}\ldots\mathbf{J}_3\mathbf{J}_2\mathbf{J}_1. \tag{1.23}$$

The order of multiplication is important, as the matrices do no necessarily commute [1]. They must be applied in the order in which the beam passes through the elements, with $\mathbf{J}_1$ acting on the input Jones vector $\mathbf{E}_{\text{in}}$ first.

1.3.2 Stokes vector representation

Another mathematical representation of polarisation comes in the form of *Stokes vectors*, devised from the work by Sir George Gabriel Stokes in 1852 [47].

One limitation of representing polarisation using ellipses, is that the orientation (ψ) and ellipticity (χ) angles characterising the ellipse are not directly measurable [44]. G. G. Stokes introduced four quantities that depend only on measurable observables of the electromagnetic field, from which the parameters of the ellipse can be obtained. These four quantities are now known as the *Stokes parameters* [1].

A general Stokes vector, $\mathbf{S}$, can be written as,

$$\mathbf{S} = \begin{bmatrix} S_0 \\ S_1 \\ S_2 \\ S_3 \end{bmatrix}, \tag{1.24}$$

where S_0, S_1, S_2 and S_3 are the Stokes parameters,[3] which are related to intensities after the beam has been projected into three sets of orthogonal polarisation bases - i.e. six different polarisation states. Specifically, these polarisations correspond to the horizontal, vertical, diagonal, anti-diagonal, right-handed circular and left-handed circular polarisations as shown in Figure 1.3.

The Stokes parameters can be found from the following relations,

$$S_0 = I_{|\hat{h}\rangle} + I_{|\hat{v}\rangle} = I_{|\hat{d}\rangle} + I_{|\hat{a}\rangle} = I_{|\hat{r}\rangle} + I_{|\hat{r}\rangle} = I_0, \tag{1.25a}$$

$$S_1 = I_{|\hat{h}\rangle} - I_{|\hat{v}\rangle}, \tag{1.25b}$$

$$S_2 = I_{|\hat{d}\rangle} - I_{|\hat{a}\rangle}, \tag{1.25c}$$

$$S_3 = I_{|\hat{r}\rangle} - I_{|\hat{l}\rangle}. \tag{1.25d}$$

where $I_{|\hat{j}\rangle}$ correspond to intensities after projection into the $|\hat{j}\rangle$ polarisation state and I_0 is the total intensity. As the Stokes parameters are dependent only on intensity measurements, they are easy to obtain experimentally and methods for doing so are outlined in § 2.3. However, they do not contain the phase information of the polarised light (unlike Jones vectors).

The Stokes parameters can be related to the components of a Jones vector, allowing one to be easily rewritten in the form of the other. For a Jones vector described by $\mathbf{E} = [E_x, E_y]^T = [E_{0x}, E_{0y}\mathrm{e}^{i\Delta\phi}]^T$, the Stokes vector, in complex notation, becomes,

$$\mathbf{S} = \begin{bmatrix} S_0 \\ S_1 \\ S_2 \\ S_3 \end{bmatrix} = \begin{bmatrix} E_x E_x^* + E_y E_y^* \\ E_x E_x^* - E_y E_y^* \\ 2\mathrm{Re}(E_x E_y^*) \\ 2\mathrm{Im}(E_x E_y^*) \end{bmatrix} = \begin{bmatrix} E_{0x}^2 + E_{0y}^2 \\ E_{0x}^2 - E_{0y}^2 \\ 2E_{0x}E_{0y}\cos\Delta\phi \\ 2E_{0x}E_{0y}\sin\Delta\phi \end{bmatrix}, \tag{1.26}$$

where Re and Im correspond to the real and imaginary components, respectively [44].

[3] Note that the Stokes parameters are sometimes called I, Q, U and V rather than S_0, S_1, S_2 and S_3.

There is also an alternative way to obtain the Stokes parameters, by employing the Pauli spin matrices [48],

$$S_0 = \mathbf{E}^* \sigma_0 \mathbf{E}, \qquad S_1 = \mathbf{E}^* \sigma_3 \mathbf{E}, \qquad S_2 = \mathbf{E}^* \sigma_1 \mathbf{E}, \qquad S_3 = \mathbf{E}^* \sigma_2 \mathbf{E} \tag{1.27}$$

where,

$$\sigma_0 = \begin{bmatrix} 1 & 0 \\ 0 & 1 \end{bmatrix}, \qquad \sigma_1 = \begin{bmatrix} 0 & 1 \\ 1 & 0 \end{bmatrix}, \qquad \sigma_2 = \begin{bmatrix} 0 & -1 \\ i & 0 \end{bmatrix}, \qquad \sigma_0 = \begin{bmatrix} 1 & 0 \\ 0 & -1 \end{bmatrix}, \tag{1.28}$$

and it is easy to see that the normalised Stokes parameters (S_1/S_0, S_2/S_0, S_3/S_0) correspond to the coordinates of a Bloch vector. This fact will come in useful for yet another representation of polarisation (see § 1.3.3).

From Eq. 1.26 we can read off the relation,

$$S_0^2 = S_1^2 + S_2^2 + S_3^2, \tag{1.29}$$

demonstrating that the Stokes parameters are related to each other and only three of the four of them are independent. However, a Jones vector can only describe fully polarised light, whereas Stokes vectors can also describe partially polarised light. In this scenario, the relation in Eq. 1.29 no longer holds, and we can replace it with a more general inequality,

$$S_0^2 \geq S_1^2 + S_2^2 + S_3^2, \tag{1.30}$$

which holds for both fully and partially polarised light. In this more general case, the four Stokes parameters are independent from each other and therefore, each of them must be measured. The degree of polarisation (DoP) $\mathcal{P}$, is a quantity that defines how polarised a light beam is, and is given by the ratio of the polarised component of the intensity to the total intensity. Therefore, it can simply be calculated from the Stokes parameters as,

$$\mathcal{P} = \frac{I_{\text{pol}}}{I_{\text{tot}}} = \frac{\sqrt{S_1^2 + S_2^2 + S_3^2}}{S_0}, \qquad 0 \leq \mathcal{P} \leq 1. \tag{1.31}$$

For a completely polarised beam, $\mathcal{P} = 1$, for a completely unpolarised beam, $\mathcal{P} = 0$, and for a partially polarised beam, $\mathcal{P}$ lies somewhere in the interval between 0 and 1.

Using the relationship between the Jones and Stokes vectors given in Eq. 1.26, we can obtain Stokes vectors for the same six polarisations described by Eq. 1.21

and shown in Figure 1.3,

$$\mathbf{S}_{|\hat{h}\rangle} = I_0 \begin{bmatrix} 1 \\ 1 \\ 0 \\ 0 \end{bmatrix}, \qquad \mathbf{S}_{|\hat{v}\rangle} = I_0 \begin{bmatrix} 1 \\ -1 \\ 0 \\ 0 \end{bmatrix},$$

$$\mathbf{S}_{|\hat{d}\rangle} = I_0 \begin{bmatrix} 1 \\ 0 \\ 1 \\ 0 \end{bmatrix}, \qquad \mathbf{S}_{|\hat{a}\rangle} = I_0 \begin{bmatrix} 1 \\ 0 \\ -1 \\ 0 \end{bmatrix}, \tag{1.32}$$

$$\mathbf{S}_{|\hat{r}\rangle} = I_0 \begin{bmatrix} 1 \\ 0 \\ 0 \\ 1 \end{bmatrix}, \qquad \mathbf{S}_{|\hat{l}\rangle} = I_0 \begin{bmatrix} 1 \\ 0 \\ 0 \\ -1 \end{bmatrix}.$$

Here, I_0 is the intensity, as above, but this is often normalised to unity [44]. These Stokes vectors are all for fully polarised light. It may be interesting to note that the Stokes vector for unpolarised light is simply $I_0[1, 0, 0, 0]^T$, and partially polarised light can be written as a mixture of fully polarised and unpolarised light,

$$\mathbf{S} = \begin{bmatrix} S_0 \\ S_1 \\ S_2 \\ S_3 \end{bmatrix} = (1 - \mathcal{P}) \begin{bmatrix} S_0 \\ 0 \\ 0 \\ 0 \end{bmatrix} + \mathcal{P} \begin{bmatrix} S_0 \\ S_1 \\ S_2 \\ S_3 \end{bmatrix}, \tag{1.33}$$

where it is simple to see that this reduces to the Stokes vectors for unpolarised or fully polarised light in the limits of $\mathcal{P} = 1$ or 0 [44].

All that is left to do is relate the measurable Stokes parameters to the polarisation ellipse. The orientation (ψ) and ellipticity (χ) angles describing the ellipse are related to the Stokes parameters via,

$$S_1 = S_0 \cos(2\chi)\cos(2\psi), \quad S_2 = S_0 \cos(2\chi)\sin(2\psi), \quad S_3 = S_0 \sin(2\chi). \tag{1.34}$$

Combining these gives,

$$2\psi = \arctan\left(\frac{S_2}{S_1}\right), \quad 2\chi = \arctan\left(\frac{S_3}{\sqrt{S_1^2 + S_2^2}}\right) = \arcsin\left(\frac{S_3}{S_0}\right). \tag{1.35}$$

The factor of two in front of both of these angular variables represents that any polarisation ellipse is indistinguishable from one rotated by 180° and also from one with its semi-major and semi-minor axis lengths swapped followed by a 90° rotation.

1.3.3 The Poincaré sphere and polarisation colour scheme

From the form of Eq. 1.34, we can notice that there is a resemblance to a spherical coordinate system between the Stokes parameters and the ellipticity and orientation angles. This leads to another useful representation of polarisation that was introduced by Henri Poincaré in 1892 [49]. He provided an intuitively geometric way of representing polarisation by employing a unit sphere, known as the *Poincaré sphere*, in which every possible polarisation state exists. This sphere is created by mapping S_1, S_2 and S_3 onto a Cartesian coordinate system and associating the angles 2ψ and 2χ with the spherical angular coordinates, as shown in Figure 1.4(a).

Although the mapping to the Poincaré sphere is somewhat arbitrary, conventionally, the S_1 parameter is chosen to lie along the x-axis, S_2 along the y-axis and S_3 along the z-axis, resulting in the points of circular polarisation being located at the north and south poles, with the linear polarisation states located along the equator. Any polarisation state described by a Stokes vector $\mathbf{S}$ can be plotted at a unique point on, or within, the Poincaré sphere. All fully polarised states will lie on the sphere's surface, and partially polarised states will lie inside the sphere. The radial distance from the origin being given by the degree of polarisation $\mathcal{P}$, making $\mathcal{P}$ the third variable (along with 2ψ and 2χ) describing the spherical coordinate system.

Using the Poincaré sphere provides a geometric way of describing polarisation, and we will see that adopting this state space becomes useful tool in the characterisation of structured light beams.

Throughout this thesis, I will use two ways of visually representing polarisation. The first is simply using ellipses, this is useful for depicting the ellipticity of the polarisation and orientation for linear and elliptical states but does not distinguish between the handedness of circular polarisation. For the second, I have adopted a colour scheme as depicted in Figure 1.4(b). This colour scheme assigns a unique colour for every single point on the surface of the Poincaré sphere and therefore, every possible polarisation state. In Figure 1.4(b) I show the Poincaré sphere from two different view points, showing the colours as well as an unwrapped version of the colour map indicating the ellipticity and orientation angles as well as polarisation ellipses for clarity. These are indeed the same colours that were used for the polarisation ellipses shown in Figure 1.3. In this thesis, we will only be interested in fully polarised light, which is why we have only defined a colour map for the surface of the sphere, but throughout, I will use this colour scheme to visually represent the polarisation of both simulated and experimentally measured polarised beams. Additionally, I will represent the intensity distribution as opacity.

1.3.4 Mueller matrices

Above, I outlined how a Jones matrix can be used to describe the action of an optical element on the polarisation state of light. In a similar way, Mueller matrices are a

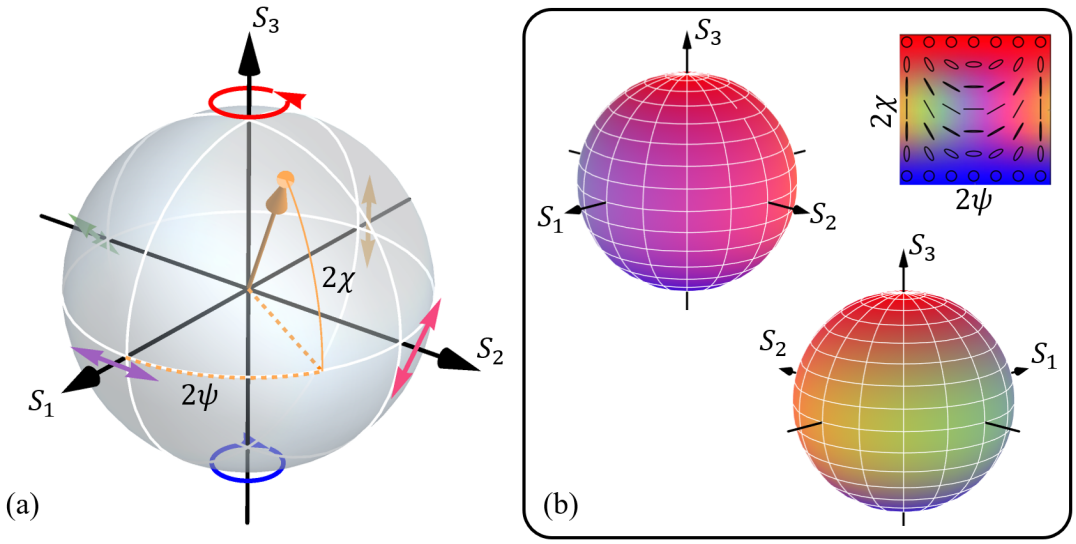

Figure 1.4: The Poincaré sphere and polarisation colour scheme. (a) The Poincaré sphere with axes corresponding to the Stokes parameters, and the location of the $|\hat{h}\rangle$, $|\hat{v}\rangle$, $|\hat{d}\rangle$, $|\hat{a}\rangle$, $|\hat{r}\rangle$ and $|\hat{l}\rangle$ polarisations shown as ellipses. The orange point depicts the location of an arbitrary elliptical polarisation state with orientation ψ and ellipticity χ. (b) The polarisation colour scheme used throughout this thesis, identifying every point on the surface of the Poincaré sphere with a unique colour. In the top right, an unwrapping of the colour map is shown along with polarisation ellipses. When this colour scheme is used to show polarisation, intensity is depicted as opacity.

mathematical representation of the action of optical elements. They were developed by Hans Mueller in 1943 [50] and are a matrix-based method for manipulating Stokes vectors [51]. The output polarisation $\mathbf{S}_{\text{out}}$ after a beam, described by $\mathbf{S}_{\text{in}}$ interacts with an optical element can be calculated from,

$$\mathbf{S}_{\text{out}} = \mathbf{M}\mathbf{S}_{\text{in}}, \tag{1.36}$$

where $\mathbf{M}$ is the 4×4 Mueller matrix, describing either a single optical element or an entire optical system. For an optical system containing n components, $\mathbf{M}$ is the product of the separate components,

$$\mathbf{M}_{\text{system}} = \mathbf{M}_n\mathbf{M}_{n-1}\ldots\mathbf{M}_3\mathbf{M}_2\mathbf{M}_1, \tag{1.37}$$

where the order of multiplication is important and depends on the order in which the beam interacts with each element.

It is possible to transform a 2×2 Jones matrix $\mathbf{J}$ into a Mueller matrix via,

$$\mathbf{M} = \mathbf{A}(\mathbf{J} \otimes \mathbf{J}^*)\mathbf{A}^{-1}, \tag{1.38}$$

where,

$$\mathbf{A} = \begin{bmatrix} 1 & 0 & 0 & 1 \\ 1 & 0 & 0 & -1 \\ 0 & 1 & 1 & 0 \\ 0 & i & -i & 0 \end{bmatrix}. \tag{1.39}$$

and $\otimes$ represents the Kronecker product [52].

During the transformation given by Eq. 1.38, an overall phase factor is lost, meaning that many Jones matrices can be mapped onto the same Mueller matrix. However, depolarisation cannot be described by Jones matrices and, as a Mueller matrix acts on a Stokes vector it has an advantage that the Stokes parameters are experimentally measurable quantities, through simple intensity measurements, in turn making the Mueller matrix experimentally measurable. In § 5.4, I will outline an experiment with the aim of obtaining Mueller matrix measurements.

1.4 The Gaussian beam and higher order light modes

So far I have mainly focused on the polarisation property of light, however, the amplitude and phase of a light beam are equally important properties. Above, in Eq. 1.6, I provided the plane wave solution to the wave equation. This solution has a single value for the amplitude and phase in any transverse plane. However, this transverse plane extends out to infinity, which is of course, not physically realisable in practice. For more realistic solutions, the intensity profile must tend towards zero at infinitely large distances from the beam axis. This is where *Gaussian optics* comes in.

The framework of Gaussian optics (sometimes also referred to as *first-order* or *paraxial optics*) was introduced by mathematician and physicist Carl Friedrich Gauss in 1841 [1]. It relies heavily on the paraxial approximation, building on geometrical optics, where light is treated as rays, and applies to systems where all the optical surfaces are either flat or portions of a sphere [53].

1.4.1 Gaussian beam

Perhaps the most prevalent solution to the paraxial wave equation, in which the amplitude tends to zero at infinity, is that of the simple Gaussian beam. The complex electric field amplitude for a Gaussian beam propagating in free-space and in the z-direction can be written as [53],

$$E(r,z) = E_0 \frac{w_o}{w(z)} \exp\left(-\frac{r^2}{w(z)^2}\right) \exp\left(-i\left(kz + k\frac{r^2}{2R(z)} - \psi(z)\right)\right), \tag{1.40}$$

where $r = \sqrt{x^2+y^2}$ is the radial distance from the centre of the beam, for Cartesian coordinates x and y, and k is the wave number. The complex electric field at the centre of the beam at time, $t = 0$, is described by E_0. The beam size at a distance z is denoted by $w(z)$ and $w_0 = w(0)$ is the beam waist. Here, the Gouy phase, $\psi(z) = \arctan(z/z_R)$, is given in terms of the Rayleigh range, $z_R = \pi w_0^2/\lambda$, which denotes the distance along the optical axis from the beam waist where the beam's cross-sectional area is double in size. The radius of curvature of the wavefronts at z is denoted by $R(z)$, which again depends on the Rayleigh range by, $R(z) = z[1+(\frac{z_R}{z})^2]$ [42].

Figure 1.5 shows a depiction of the cross-section of the Gaussian beam with propagation, indicating some of the important features as defined above. The orange line shows the "edge" of the beam, although, in reality, the tails of the Gaussian function never truly reach zero as $r \to \infty$. Instead, the beam edge is defined to be at $r = w(z)$, the radial distance at which the intensity has dropped to $1/e^2$ of the on-axis value. From Figure 1.5, it can be seen that the overall profile remains Gaussian as the beam propagates, only changing in size due to diffraction. The phase fronts of a Gaussian beam (shown as dashed blue lines) form parabolic surfaces, apart from at $z = 0$, where $w(z) = w_0$. At this plane the phase fronts are flat.

1.4.2 Higher order Gaussian modes

The Gaussian beam is not the only solution to the paraxial wave equation, higher order modes exist. Solutions that are of particular interest are those with the same spherical wavefronts of the Gaussian beam, but with different intensity distributions. Two common sets of transverse modes are the Hermite-Gaussian (HG) and Laguerre-Gaussian (LG) modes. The terms in the field equations which modify and

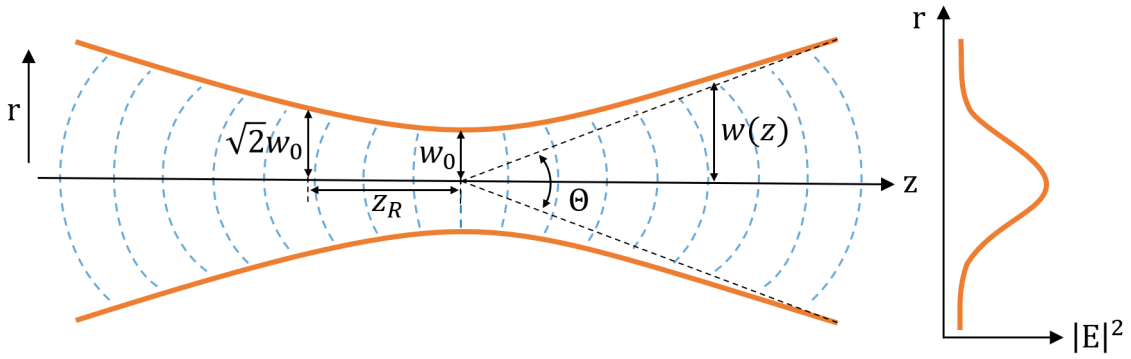

Figure 1.5: Features of a Gaussian beam. Left: $w(z)$ as a function of propagation distance z. The orange lines indicate the radial distance at which the intensity falls to $1/e^2$ of the on-axis value. The cone with apex angle Θ describes the angular spread of the beam. Blue dashed lines represent the phase fronts. Right: Cross-section of the intensity ($|E|^2$) profile.

define these modes are the Hermite and Laguerre polynomials. These in turn determine the order of the individual mode [53]. The HG and LG modes are perhaps the most commonly used spatial modes, and will be used throughout the work presented in this thesis, and as such their mathematical details will be given in the following sections. However, other interesting spatial modes exist, and complex beam shaping is often based on the superpositions of interesting spatial light modes. Some examples include: Ince-Gauss beams[4] [54], Bessel beams [55], Airy beams [56], as well as Mathieu [57] and Pearcey beams [58].

As will be discussed in more detail in chapter 2, it is in theory possible to generate a light beam with any profile you want in a single transverse plane, you do not need to use one of aforementioned spatial light modes. However, the generated beam will not necessarily be an eigenmode of propagation, with its intensity distribution not conserved, or easily defined, with propagation. Generally, only exact solutions to the wave equation will be well defined over all propagation distances.

Hermite-Gaussian modes

By deriving solutions to the paraxial wave equation using a rectangular coordinate system, we arrive at a complete set of solutions known as the Hermite-Gaussian

[4] As we will see, HG and LG modes are solutions of the wave equation in Cartesian and cylindrical coordinates using Hermite and Laguerre polynomials, respectively. Ince-Gauss beams are instead solutions in elliptical coordinates using Ince-polynomials. By changing the ellipticity parameter, Ince-Gauss beams offer a continuous transition between HG and LG modes, becoming HG and LG modes at the two ellipticity extremes.

(HG) modes. The complex amplitude of a Hermite-Gaussian beam is given by [53],

$$\begin{aligned}\mathrm{HG}_{nm}(x,y,z) = E_0\frac{w_0}{w(z)}H_n\left(\frac{\sqrt{2}x}{w(z)}\right)H_m\left(\frac{\sqrt{2}x}{w(z)}\right)\exp\left[-\frac{(x^2+y^2)}{w(z)^2}\right] \\ \times\exp\left(-ikz\right)\exp\left[-ik\frac{(x^2+y^2)}{2R(z)}\right]\exp\Big[i(n+m+1)\psi(z)\Big],\end{aligned} \tag{1.41}$$

where H_n and H_m are the n^{th} and m^{th} order Hermite polynomials, respectively, and all the other variables have the same definitions as given previously. A HG beam appears as a rectangular grid of intensity spots, with $n+1$ columns and $m+1$ rows of spots. The positive integers n and m also define the mode number, or the order of the mode, given by [42],

$$N = n + m, \qquad n,\, m \in \mathbb{N}. \tag{1.42}$$

By setting $n = m = 0$ in Eq. 1.41, we obtain the lowest order HG mode, which is the fundamental Gaussian mode. Examples of the intensity and phase distribution of different HG modes at $z = 0$ can be seen in Figure 1.6. From the phase profiles, it can be seen that neighbouring intensity lobes are π out of phase. This phase step is what causes the zero intensity regions between the lobes due to deconstructive interference.

Laguerre-Gaussian modes

Another complete set of solutions to the paraxial wave equation can be obtained by writing the wave equation in cylindrical coordinates (r, ϕ, z) and using separation of variables in r and ϕ, instead of in x and y, as was done for the HG modes [42]. In this case, we obtain beams with circular symmetry, known as the Laguerre-Gaussian (LG) modes. The complex amplitude of an LG beam is given by [53],

$$\begin{aligned}\mathrm{LG}_p^{\ell}(r,\phi,z) = \sqrt{\frac{2p!}{\pi(p+|\ell|)!}}\frac{w_0}{w(z)}\left(\frac{r\sqrt{2}}{w(z)}\right)^{|\ell|}\exp\left(-\frac{r^2}{w(z)^2}\right)L_p^{|\ell|}\left(\frac{2r^2}{w(z)^2}\right) \\ \times\exp\left(-ik\frac{r^2}{2R(z)}\right)\exp\left(i\ell\phi\right)\exp\Big[i(2p+|\ell|+1)\psi(z)\Big],\end{aligned} \tag{1.43}$$

where, $L_p^{|l|}$ are the generalised Laguerre polynomials. The LG_p^l modes are indexed using the radial integer p and the azimuthal integer l (also referred to as the topological charge or the orbital angular momentum (OAM) number), where $p \geq 0$ and l can be either positive, negative or zero. For an LG beam, the mode number is given by,

$$N = 2p + |\ell|, \qquad p \in \mathbb{N},\ \ell \in \mathbb{Z}, \tag{1.44}$$

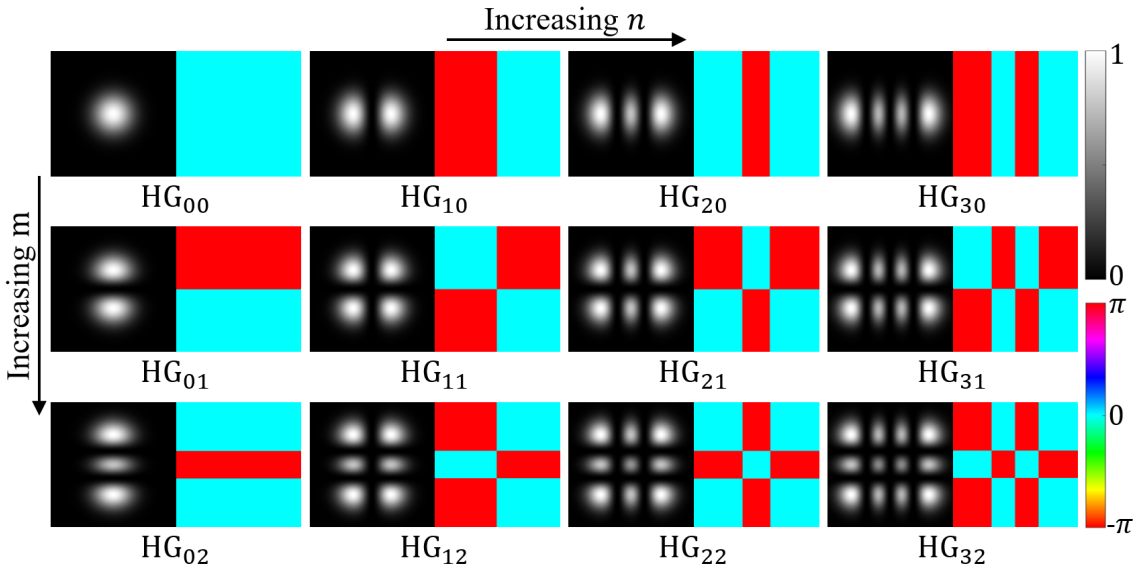

Figure 1.6: Intensity (left) and phase (right) distributions of Hermite-Gaussian modes HG_{nm}. The intensity has been peak normalised and the colour maps which denote intensity and phase values are shown on the far right. These same colour scales are used throughout this thesis.

where again, setting $\ell = p = 0$ results in the fundamental Gaussian mode.

The intensity profile of an LG beam mode will have $p + 1$ maxima in the radial direction, with the first maximum appearing at the centre of the beam when $l = 0$. Examples of the transverse intensity and phase profiles of various LG beams can be seen in Figure 1.7. From the phase profiles in Figure 1.7, it can be seen that adjacent intensity rings are π out of phase, resulting in intensity minima between the rings. Additionally, the intensity profiles of beams with equal p and magnitude of $|\ell|$ are the same.

The $\exp(i\ell\phi)$ phase factor in Eq. 1.43 determines if the phase is advanced ($\ell > 0$) or retarded ($\ell < 0$), with the magnitude of the topological charge number, ℓ, defining the number of complete 2π phase cycles, or helical phase surfaces present about the propagation axis. The LG beams are well known for carrying orbital angular momentum (OAM) when $\ell \neq 0$ [59]. When $\ell \neq 0$, the phase rotates about the centre of the beam, creating a phase singularity, and therefore an area of zero intensity at the centre. This is known as an optical vortex.

From Figure 1.7, it is apparent that the LG beams are larger for larger N but for the same beam waist w_0. An expression for the "effective radius" of all orders of LG beams was derived by Phillips and Andrews [60], which depends on the waist of the Gaussian (LG_0^0 mode) and the mode number,

$$r_{\mathrm{eff}}(z) = w(z)\sqrt{2p + |\ell| + 1}. \tag{1.45}$$

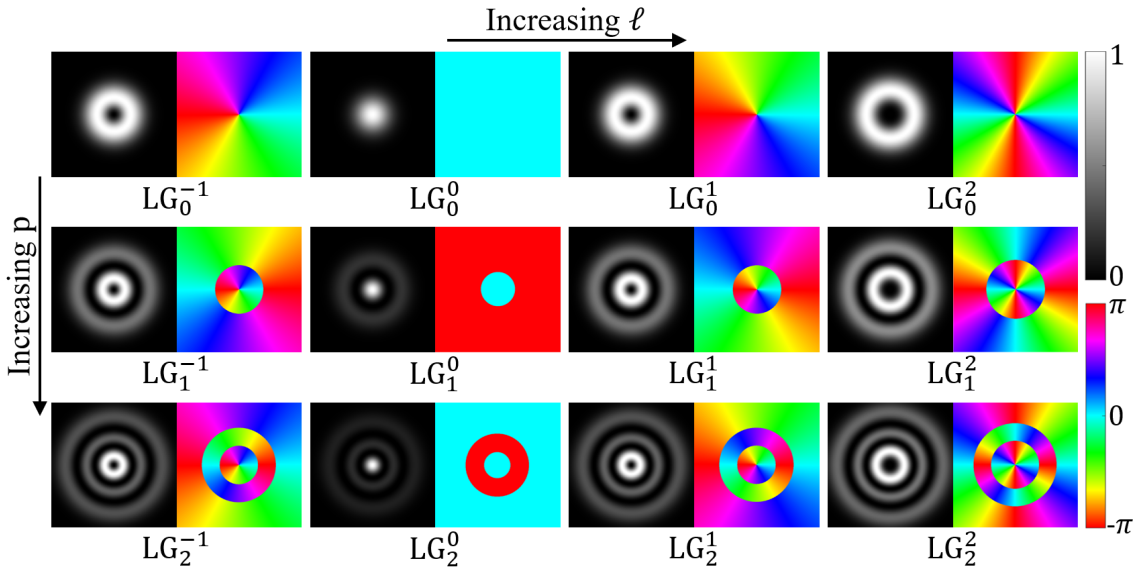

Figure 1.7: Intensity (left) and phase (right) distributions of Laguerre-Gaussian modes LG_p^ℓ, where the intensity has been peak normalised. The intensity and phase colour maps are shown on the far right.

For modes with $p = 0$, LG_0^ℓ, we can also define the radius at which the intensity is maximum,

$$r_0(z) = \sqrt{\frac{|\ell|}{2}} w(z) \tag{1.46}$$

as given in Ref. [61]. This radial distance is indicated by an orange line in Figure 1.8, for an LG_0^3 beam.

For a simple Gaussian beam, the "edge" of the beam, where the intensity I falls to $1/\mathrm{e}^2$ of the maximum intensity $I_{\max}$, is given by the simple expression for the beam size $w(z)$. The radial distance at which the intensity of an LG_0^ℓ beam falls to the same value is not so simple. Additionally, there will be two radii, one at smaller (r_1) and one at larger (r_2) distances, at which the intensity is $I_{\max}/\mathrm{e}^2$. Nevertheless, these radial distances can be calculated from [62],

$$\begin{aligned} r_1(z) &= \sqrt{\frac{\ell}{2}} \sqrt{-\mathcal{W}\left(0, -\frac{(\mathrm{e}^{-\ell-2}\ell^\ell)^{1/\ell}}{\ell}\right)} w(z) \\ r_2(z) &= \sqrt{\frac{\ell}{2}} \sqrt{-\mathcal{W}\left(-1, -\frac{(\mathrm{e}^{-\ell-2}\ell^\ell)^{1/\ell}}{\ell}\right)} w(z), \end{aligned} \tag{1.47}$$

where we have employed the Lambert $\mathcal{W}$ function [63]. The locations of r_1 and r_2 for an LG_0^3 beam are shown as blue and green circles in Figure 1.8, respectively. Knowing the dimensional properties for LG beams, and indeed other spatial light

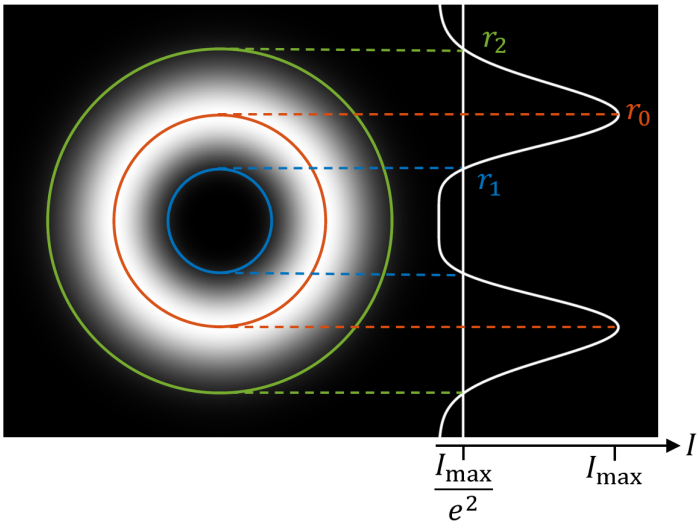

Figure 1.8: Representation of the dimensional properties of an LG beam with $\ell = 3$. On the left is the intensity distribution and on the right a cross-section of the intensity through the beam centre with the $I_{\max}/\mathrm{e}^2$ value indicated by a vertical line. The radial distances described by r_0, r_1 and r_2 are shown by orange, blue and green circles, respectively.

modes, is valuable when considering the superposition of different modes, when a particular spatial overlap may be required.

Both the Hermite- and Laguerre-Gaussian beams form a complete set of solutions to the paraxial wave equation, meaning that any HG mode can be written as a superposition of LG modes and vice versa [42, 48, 64]. Some examples of this are shown in Figure 1.9. Generally, any HG or LG beam with mode order N can be expressed as a superposition of $N+1$ modes from the other mode family, each also of order N. This will come in useful for the consideration of *orbital redirection phases* in Chapter 3.

1.4.3 Gouy phase

Upon propagation, a plane wave acquires a phase shift of e^{ikz}, for wavenumber k and propagation distance z, where $z = 0$ corresponds to the position of the beam waist. For a propagating Gaussian beam, there is also an additional axially-varying phase shift, with respect to the waist location. This is described by the Gouy phase, $\psi(z) = \tan^{-1}(z/z_R)$, where z_R is the Rayleigh range. For higher order Gaussian beams, this becomes,

$$\psi(z) = (N+1)\tan^{-1}\left(\frac{z}{z_R}\right), \tag{1.48}$$

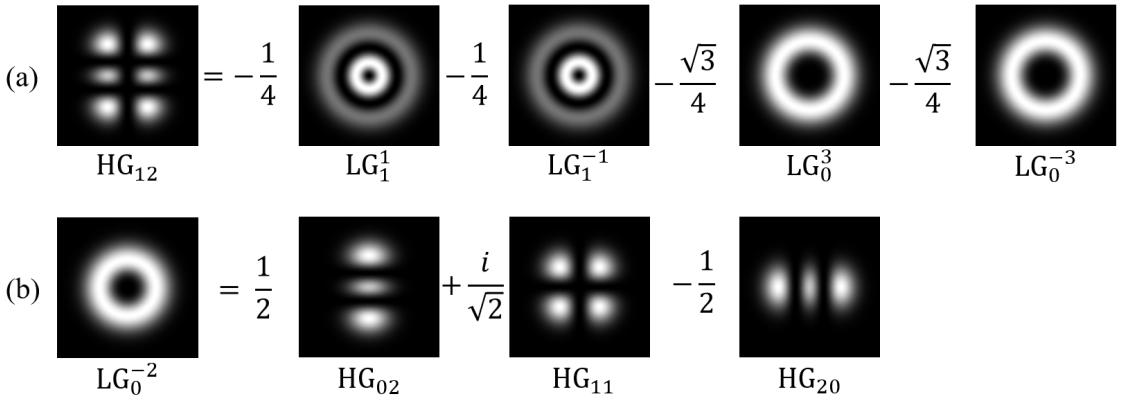

Figure 1.9: Examples of beam mode decomposition. (a) A HG_{12} mode expanded as a sum of LG modes. (b) An LG_0^{-2} mode written in terms of HG modes.

for mode number N. The effect of the Gouy phase on the lowest order Gaussian mode, is of an additional π phase shift on either side of the focus. For higher order modes, this phase shift is larger [53].

The Gouy phase shift can also be seen to be *geometric* in nature. This particular interpretation will be discussed in § 3.2.2.

1.4.4 Propagation

As briefly mentioned in § 1.2, knowing the amplitude and phase of a light beam in any single transverse plane allows the values in any other plane to be determined, arising because the electric field is fundamentally linked along its propagation direction.

To consider the propagation of a light beam, we can employ Fourier optics, which is a useful framework for analysing how light propagates through simple optical components or free space. Fourier optics uses the argument that an arbitrary function can be written as a superposition of harmonic functions of time of unique spatial frequencies [42], i.e. we consider light as a combination of plane waves. In fact, the Fourier plane of a beam corresponds to its plane wave decomposition, such that, each point in the Fourier plane gives the amplitude and phase information of one of its plane wave components [65]. By employing 2-dimensional spatial Fourier transforms, and advancing the phase components appropriately, it is possible to numerically simulate the propagation of any light beam.

By taking the paraxial propagation, we can consider the propagation of a light beam to be entirely in one direction, let's assume this to be the z direction. The plane wave components are characterised by the $\mathbf{k}$-vector, with magnitude given by $k = \frac{2\pi}{\lambda} = \sqrt{k_x^2 + k_y^2 + k_z^2}$. For propagation in the z-direction by a distance Δz (where Δz can be either positive or negative), the phase will advance by $-k_z \Delta z$,

where,

$$k_z(x,y) = \sqrt{\left(\frac{2\pi}{\lambda}\right)^2 - k_x^2(x,y) - k_y^2(x,y)}. \tag{1.49}$$

For a light field $E(x,y,z)$, where a particular transverse plane at $z = z_0$ is known, the propagated field at the $z = z_0 + \Delta z$ plane is therefore given by,

$$E(x,y,z_0+\Delta z) = \mathcal{F}^{-1}\left\{\mathcal{F}\left\{E(x,y,z_0)\right\} \mathrm{e}^{-ik_z \Delta z}\right\}, \tag{1.50}$$

where, $\mathcal{F}$ and $\mathcal{F}^{-1}$ denote the 2D Fourier transform and inverse Fourier transform, respectively. The method summarised by Eq. 1.50 is often referred to as the *angular spectrum method*, *Fourier beam propagation* or *FFT-based angular spectrum method* due to the reliance on Fast Fourier Transforms (FFT) for numerical calculations [42, 65].

Equation 1.50 calculates $E(x,y,z_0+\Delta z)$ from $E(x,y,z_0)$ assuming the beam was not altered in any way between these two planes, i.e. it was propagating in free space. But we can also use it to propagate up to an optical component, apply the action of the optical component, and then use Eq. 1.50 again to propagate further. This recipe can be repeated many times in order to simulate the action of entire optical setups on an input beam. The one condition to this, is that we remain in the paraxial regime. If we instead are interested in non-paraxial propagation, then other methods must be used. For example, the numerical methods introduced by Richards and Wolf [66], for strongly focused light, and described clearly in Ref. [67].

Using FFT for beam propagation is highly advantageous due to its simplicity and numerical speed, but one limiting characteristic occurs when a propagating beam expands close to the full size of the computational grid size, resulting in numerical aliasing. When we have non-zero amplitude regions close to the simulation boundary, the implicit periodicity of the boundary produces false signals in the simulation, producing edge effects and reducing accuracy. This can be overcome by ensuring to create a sufficiently large numerical grid space. However, one other option is to employ adaptive step size methods as outlined in Ref. [68]. For these methods, we propagate a fraction of the required distance multiple times until the total propagation distance is reached. At each step, an absorbing boundary is applied, to suppress the unwanted signals from the periodicity at the edge of the grid space.

For the propagation simulations presented in this thesis, it was generally sufficient to use Eq. 1.50 directly.

1.5 Structured light: scalar and vectorial light fields

The idea of structured light has occupied a prominent position in optical research in recent decades, mainly due to the development of optical technologies which have

allowed the manipulation of the main light field parameters: amplitude, phase, and polarisation [69]. Historically, many examples of shaped light fields only considered scalar beams either by ignoring the polarisation component or by treating it as a degree of freedom. Scalar beams represent solutions to the wave equation (more specifically, the scalar Helmholtz equation, Eq. 1.9) that are independent of the polarisation state, they are spatially structured in amplitude and phase but have a homogeneous polarisation across the beam profile. Examples include the Hermite- and Laguerre-Gaussian modes discussed above.

However, light is intrinsically vectorial in nature - the electric ($\mathbf{E}$) and magnetic ($\mathbf{B}$) field components of an electromagnetic wave are vector quantities, having both magnitude and direction [48].

Vector beams, on the other hand, take into account both the spatial distribution and the polarisation state of light, and are solutions to the full vector form of the Helmholtz equation (Eq. 1.8). They are formed from non-separable combinations of spatial and polarisation modes [70], resulting in non-homogeneous polarisation structures. Additionally, they are not limited to scalar solutions, can exhibit interesting properties [71], and their enhanced modal space offers new effects and applications [48, 72–75].

The presence of either a scalar or a vector beam can be easily experimentally verified by passing the beam through a rotating linear polariser, as shown in Figure 1.10. If only a change in intensity is observed, but the intensity distribution remains constant, then a scalar beam has been revealed (Figure 1.10(a)). However, if a varying intensity pattern for different polariser rotations is observed, then we have a vector beam (Figure 1.10(b)). In this case, the polariser has revealed the spatially varying nature of the polarisation structure.

1.5.1 Vectorial light fields

From Maxwell's equations, and employing the paraxial approximation, the electric field components, $\mathbf{E} = (E_x, E_y)$ in the transverse plane can be selected independently from each other. The combination of the E_x and E_y components with various phase and amplitude weightings gives rise to polarisation, as described in § 1.3. However, if the chosen phase and amplitude weightings are spatially varying, then we end up with a beam whose polarisation profile is also spatially varying [48].

Vector beams can be created from coaxial superpositions of multiple spatial light modes ($u_j(\mathbf{r})$) with different homogeneous polarisations ($\mathbf{e}_j$),

$$\mathbf{E}(\mathbf{r}, t) = \sum_j u_j(\mathbf{r}) \mathrm{e}^{i\phi_j} \mathbf{e}_j. \tag{1.51}$$

The polarisation can be described using any two orthogonal electric field components, therefore, any general vector beam can be written as the superposition of two spatial modes that are orthogonally polarised. It is common to use either

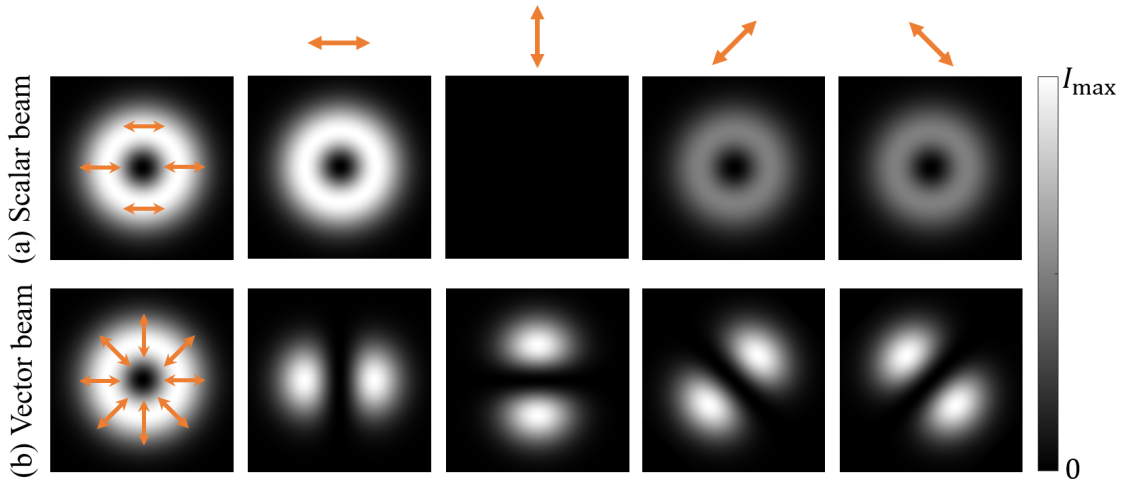

Figure 1.10: Scalar beams vs. vector beams. Examples of the intensity patterns of a homogeneously polarised scalar beam (a) and a (radially polarised) vector beam (b) after passing through a linear polariser. The orientation of the polariser axis in each case is denoted by the arrows above the images, and $I_{\max}$ is the maximum intensity.

the horizontal and vertical linear polarisation basis ($|\hat{h}\rangle$, $|\hat{v}\rangle$) or the right- and left-handed circular polarisation basis ($|\hat{r}\rangle$, $|\hat{l}\rangle$), but any orthogonal basis can be used. This allows a general vector beam, denoted $|\psi\rangle$, to be written as,

$$|\psi\rangle = u_0(\mathbf{r})\,|0\rangle + \mathrm{e}^{i\phi} u_1(\mathbf{r})\,|1\rangle \tag{1.52}$$

where, $|0\rangle$ and $|1\rangle$ represent any two orthogonal polarisations, $u_0(\mathbf{r})$ and $u_1(\mathbf{r})$ the amplitudes of any two spatial modes, and ϕ is the relative phase between them.

The polarisation degree of freedom is confined to a two-dimensional space, however, the spatial degree of freedom extends infinitely. Therefore, it is clear to see that the set of vector beams described by Eq. 1.52 also form an infinite space. Although there are an infinite number of possible vector beams, here I will illustrate some of the most common examples.

First, lets restrict ourselves to a small subset of spatial modes, namely, LG beams with $p = 0$ and $\ell = \pm 1$, relative phase differences of $\phi = \{0, \pi\}$ and the right- and left-handed circular polarisation basis. From combinations of these parameters, we

can obtain four vector modes,

$$|\psi_1\rangle = \frac{1}{\sqrt{2}}\left(\mathrm{LG}_0^1\,|\hat{r}\rangle + \mathrm{LG}_0^{-1}\,|\hat{l}\rangle\right), \tag{1.53a}$$

$$|\psi_2\rangle = \frac{1}{\sqrt{2}}\left(\mathrm{LG}_0^1\,|\hat{r}\rangle - \mathrm{LG}_0^{-1}\,|\hat{l}\rangle\right), \tag{1.53b}$$

$$|\psi_3\rangle = \frac{1}{\sqrt{2}}\left(\mathrm{LG}_0^1\,|\hat{l}\rangle + \mathrm{LG}_0^{-1}\,|\hat{r}\rangle\right), \tag{1.53c}$$

$$|\psi_4\rangle = \frac{1}{\sqrt{2}}\left(\mathrm{LG}_0^1\,|\hat{l}\rangle - \mathrm{LG}_0^{-1}\,|\hat{r}\rangle\right), \tag{1.53d}$$

where I have used that $\mathrm{e}^{i\phi} = \pm 1$ when $\phi = \{0, \pi\}$. The polarisation profiles of these beams are shown in Figure 1.11. The vector modes described by $|\psi_1\rangle$ and $|\psi_2\rangle$ are often referred to as radially and azimuthally polarised beams, the reason for which can clearly be seen from inspection of their polarisation distribution, where as those described by $|\psi_3\rangle$ and $|\psi_4\rangle$ are often referred to as hybrid beams [76].

The polarisation structures shown in Figure 1.11 are in fact well-known as the modes of optical fibres [76, 77]. However, note that although the polarisation structures are identical, their mathematical descriptions differ, since they result from transverse localisation in the fibre due to total internal reflection at the interface between the fibre's core and cladding [78]. Additionally, it is generally difficult to excite these modes in an optical fibre without also exciting the fundamental mode [71].

Here, we can also make use of the fact that both the Laguerre- and Hermite-Gaussian beams form a complete set of solutions to the paraxial wave equation, meaning that one can be written in terms of the other. This allows the 4 vector modes in Eq. 1.53 to be written as superpositions of HG beams, but this time using a linear polarisation basis,

$$|\psi_1\rangle = \frac{1}{\sqrt{2}}\left(\mathrm{HG}_{10}\,|\hat{h}\rangle + \mathrm{HG}_{01}\,|\hat{v}\rangle\right), \tag{1.54a}$$

$$|\psi_2\rangle = \frac{1}{\sqrt{2}}\left(\mathrm{HG}_{01}\,|\hat{h}\rangle - \mathrm{HG}_{10}\,|\hat{l}\rangle\right), \tag{1.54b}$$

$$|\psi_3\rangle = \frac{1}{\sqrt{2}}\left(\mathrm{HG}_{10}\,|\hat{h}\rangle - \mathrm{HG}_{01}\,|\hat{v}\rangle\right), \tag{1.54c}$$

$$|\psi_4\rangle = \frac{1}{\sqrt{2}}\left(\mathrm{HG}_{01}\,|\hat{h}\rangle + \mathrm{HG}_{10}\,|\hat{v}\rangle\right), \tag{1.54d}$$

as illustrated visually in Figure 1.11. The ability to do this can come in useful for some experimental applications where certain superpositions may be more readily performed than others, as will be explored in Chapter 2.

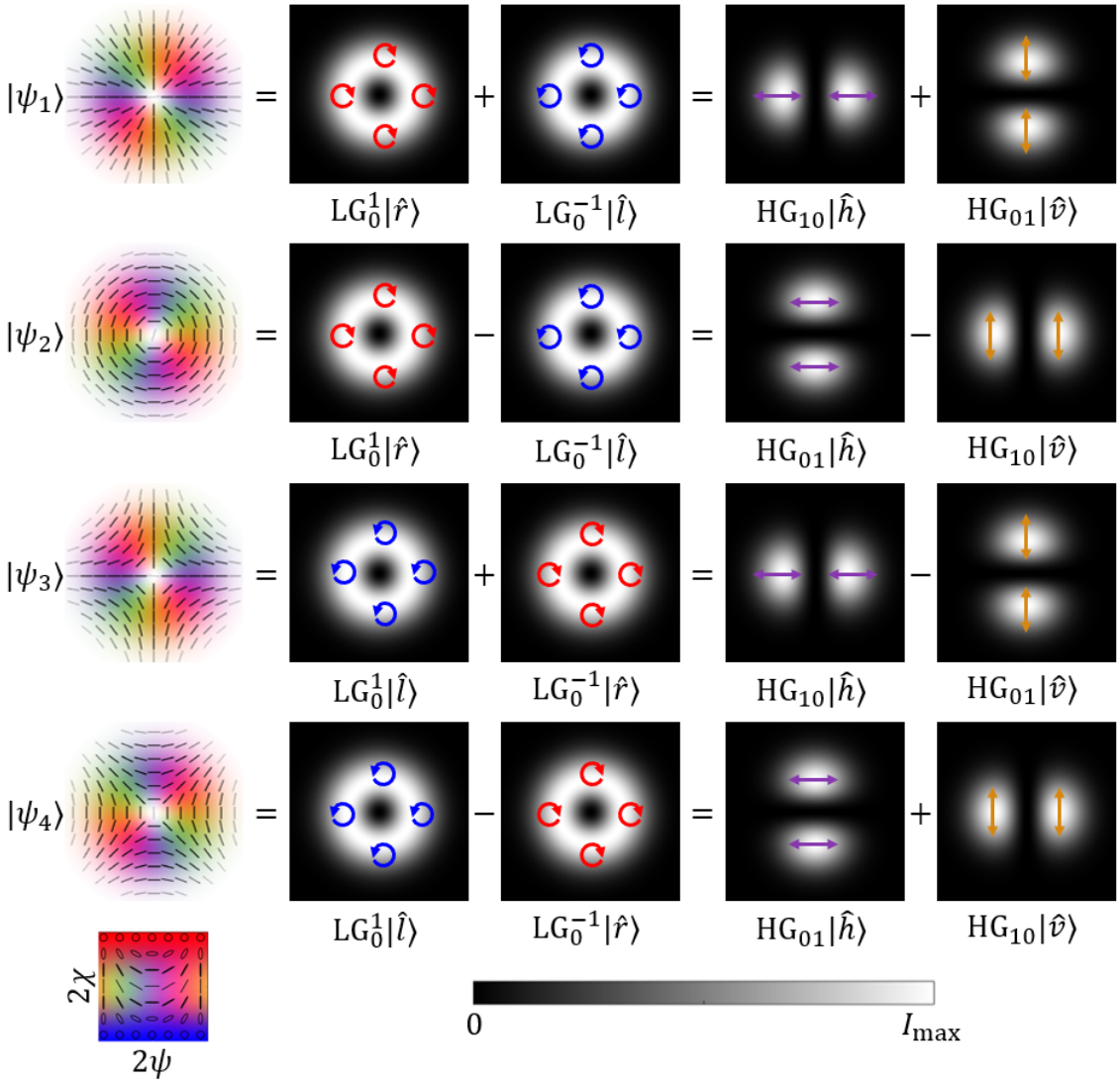

Figure 1.11: Examples of common low-order vector beams, known as radial $|\psi_1\rangle$, azimuthal $|\psi_2\rangle$ and hybrid beams ($|\psi_3\rangle$, $|\psi_4\rangle$). Theoretical polarisation plots are shown on the left along with the required mode superpositions when using either a circular polarisation basis and LG beams or a linear polarisation basis and HG beams. Below the figure, the polarisation and intensity colour maps are shown again for convenience.

1.5.2 A zoo of vector beams and an introduction to their topologies

There is an infinite number of possible vector beams that can be created, leading to some with particularly interesting structures, helping to forge a connection between the fields of topology[5] and structured light.

Recall that light can be described by its electric or magnetic fields. Vector fields, from their mathematical description, are simply collections of vectors, spatially varying continuously and differentiably as functions of position, and are normally "well-behaved". However, in three-dimensions, this is not always the case, and we can end up with singular points or isolated curves in which one (or more) variable is undefined (such as phase or polarisation) [79, 80]. In fact, we have already seen an example one of these singularities, in for form of a phase singularity at the centre of LG beams with non-zero topological charge.

Some vector modes generated using superpositions of LG beams contain singularities known as C points, V points and L lines [79, 81–83]. Consider the orientation of a polarisation ellipse given by $\arctan(S_2/S_1)$ (Eq. 1.35). There exist values of S_1 and S_2 in which the arctan function is undefined, meaning the polarisation does not have a defined orientation. In this case, we must either have a point of zero intensity or a point of pure circular polarisation, in order to satisfy the equation for the ellipticity ($\arcsin(S_3/S_0)$). The points of zero intensity (e.g. at the centre of a radial beam) are known as V-points, whereas, the points of pure circular polarisation are known as C points, and they can occur at areas with or without intensity [84].

In the top left of Figure 1.12, I show two examples of vector beams with right-handed circular polarisation singularities in the centre.

Instead, when the handedness of the polarisation is not defined, i.e. when $S_3 = 0$, it is completely linear and L lines occur [79, 82]. These trace out the points of pure linear polarisation and generally form closed curves, often occurring at the boundary between elliptical polarisation states with opposite handedness [79, 81].

The orientation of the polarisation ellipse can be used to construct polarisation *streamlines* [85]. These continuous lines are created by drawing line segments between the major axes of the polarisation ellipses, resulting in identifiable morphologies. About a C point, three possible morphologies exist [86, 87], called *lemon*, *star* (as shown in Figure 1.12) and *monstar* (not shown here, but see for example Ref. [48, 85]).

In Figure 1.12, I also show some other interesting structures formed from polarisation streamlines, which have adopted named such as spiral, spider, spider web and flower [48, 85].

Another way to reflect on the structures within vector beams is by employing the Poincaré sphere. More specifically, by relating the polarisation states present in the beam to the coverage of the sphere. For example, a radially polarised beam

[5] Topology is the study of the properties of geometrical objects and physical systems that remain invariant under continuous transformations such as bending ans twisting.

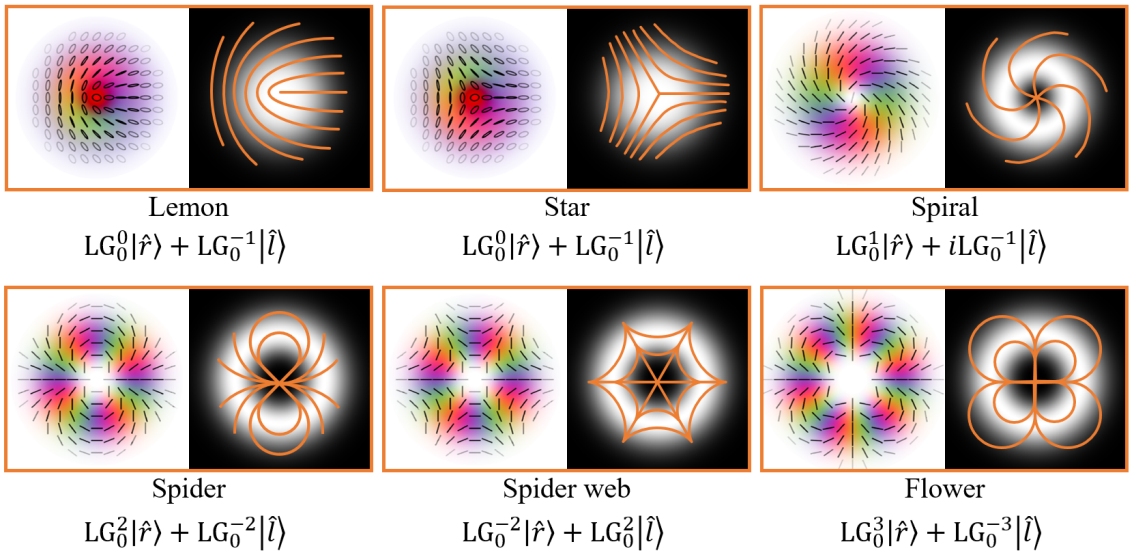

Figure 1.12: Vector beams and their topologies. Polarisation distributions (left) and polarisation streamlines (right) shown on top of the beam intensity. The required beam superpositions are shown below along with the common names for the morphological structures.

(as shown in Figure 1.11), contains all of the polarisation states along the equator of the Poincaré sphere. Indeed, all of the beams shown in Figure 1.11 contain every possible orientation of linear polarisation, and so form great circles around the equator. However, it is also possible to have beams whose polarisation covers a great circle on the Poincaré sphere other than the equator. For example, the other hybrid beams shown in Figure 1.13 also include polarisations along a great circle. E.g. the beams in Figure 1.13(a) and (b) traverse a path including the north and south poles of the Poincaré sphere as well as the points of horizontal/vertical polarisation. Whereas, the beam in Figure 1.13(c) includes the poles and points of diagonal/anti-diagonal polarisation, and (d) shows an example of a beam covering the same great circle as in (c), however, this circle is traversed twice as we travel in an azimuthal direction about the beam's centre.

Rather than just covering a great circle on the sphere, we can generate beams that cover the entire surface of the sphere, i.e. they contain every possible polarisation state. These class of beams are known as *Poincaré beams*, and some examples are the lemon and star beams shown in Figure 1.12. But, we can go one step further, by also filling the entire interior of the sphere. In this case the beams must contain every possible pure polarisation as well as every partially polarised stated. These beams are known as *full Poincaré beams* [88, 89] and can be generated by passing beams through spatially inhomogeneous birefringent materials [90] or using superpositions of temporally incoherent beams [91].

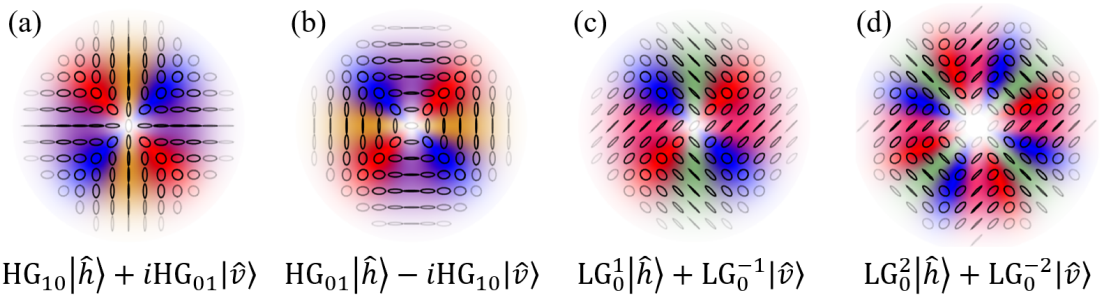

Figure 1.13: Examples of hybrid vector beams whose polarisation distribution traverses a great circle on thee Poincaré sphere. Polarisation plots are shown above and required beam superpositions below.

These are just some of the *hidden structures* that can be found within spatial light fields. An other interesting topological structure - the optical skyrmion - will be introduced and discussed in detail in Chapter 4.

1.6 The angular momentum of light

The vector nature of light means that, even if it is travelling in a straight line, it can exhibit rotation, spinning, or twisting around its own axis, i.e., it can posses angular momentum. This comes in two forms, namely: *spin* and *orbital* angular momentum [41, 92].

Spin angular momentum (SAM) is an *intrinsic* property of the beam relating to the rotation of the electric and magnetic fields about its own propagation axis. Therefore, SAM is associated with the polarisation state of light, in particular the circular polarisation. It has a value of $\pm\hbar$ per photon, depending on the handedness of the circular polarisation (note that the SAM is completely independent of the photon energy [1]). Strictly, a photon's *spin* is always 1 (in natural units, where $\hbar = 1$), and refers to its intrinsic angular momentum, and the photon's *helicity* (often denoted σ) represents the projection of the photon's spin onto its direction of motion [41]. This is either positive, for left-handed circular polarisation, or negative, for right-handed circular polarisation. For linear polarisation, which is an equal combination of left- and right-handed circular polarisation, the SAM is zero.

Whilst the SAM of light has been known about for over a century (discovered by Poynting in 1909 [93, 94]), orbital angular momentum (OAM) is a newer concept, first experimentally verified by Allen, Beijersbergen, Spreeuw, and Woerdman in 1992 [59]. OAM is dependent on a beam's spatial distribution, associated with helical or twisted phase fronts, as seen in the familiar Laguerre Gaussian modes. However, other beams, such as Bessel beams [55, 95], can also carry OAM. The OAM has a value of $\ell\hbar$ per photon, where ℓ is the topological charge (as in Eq. 1.43

for LG beams), denoting the number of helical wavefronts. In comparison to SAM, which is an intrinsic property, depending on the polarisation, OAM is a global, or *extrinsic*, property of a light beam, describing the dynamical rotation of the wavefronts around the beam axis.

The total angular momentum is given by the sum of the spin and orbital components, and is therefore $(\ell + \sigma)\hbar$ per photon. This has importance for many applications, but in this thesis it will become particularly relevant in chapter 3.

1.7 Chapter 1 conclusion

This chapter began by introducing the wave nature of light, demonstrating how it can be described as an oscillation of the electromagnetic field and in terms of its amplitude, phase and polarisation. I then went on to describe polarisation in more detail, providing two different representations (the Jones and Stokes formalisms), both of which are useful in different scenarios, and the corresponding visual representations of polarisation using the Poincaré sphere and polarisation ellipses.

In the second part of this chapter, I provided examples of higher order Gaussian modes, shaped in both intensity and phase, before describing how we can theoretically construct beams with spatially varying polarisation by using superpositions of orthogonally polarised spatial modes. Section 1.5.2 gave a brief introduction to some of the topologies (or "hidden" structures) that can be found within polarisation distributions. This will be explored further in Chapter 4.

The content of this chapter covers the background theory applicable to all of the individual projects undertaken throughout my PhD. More specific theory and background knowledge will be provided in the chapters associated to each project. However, first, it is important to discuss how vector beams can be experimentally generated. This will be presented in the next chapter (chapter 2), along with other relevant experimental considerations and measurement techniques.

Chapter 2

Shaping light and measuring polarisation

2.1 Chapter 2 introduction

In Chapter 1, I introduced the main background theory that is relevant for all of the work that will be presented in this thesis. In this chapter, I will instead focus on the required experimental aspects and analysis techniques that will be used throughout.

I will start off by explaining the mechanisms behind some of the most common optical elements, and their uses, with a particular focus on their effect on the polarisation state of light. The relevant Jones and Mueller matrix representations of these optical elements will be summarised in § 2.2.3. I will then introduce the concept of Stokes tomography, a measurement procedure which can be used to determine the (spatially varying) polarisation state of light, before outlining various image processing and analysis techniques.

In § 2.5, I will outline methods of shaping light with a particular focus on devices for implementing digital holography, such as spatial light modulators (SLMs) and digital micromirror devices (DMDs). Finally, I will describe an experimental setup, incorporating a DMD, which was used extensively for the work in this thesis, for the generation of arbitrary vector beams with spatially varying polarisation.

2.2 Common optical elements and their interaction with polarisation

In this section I will discuss the effects of different optical elements on the polarisation state of light. Here, I will focus on the off-the-shelf optical components that are commonly found in optics laboratories and that will be used extensively for the work presented in this thesis.

2.2.1 Waveplates and polarisers

Waveplates and linear polarisers are perhaps the most common optical elements used for manipulating polarisation. They rely on effects known as dichroism and birefringence, which are two optical properties exhibited by some materials.

Polarisers

Dichroism is the selective absorption of light based on its polarisation. When light passes through a dichroic material, it is absorbed differently depending on its polarisation state. Linear polarisers employ linear dichroism, absorbing one linear polarisation and transmitting the other orthogonal polarisation component of a light beam. The orientation of the transmitted (or absorbed) polarisation can be easily selected by rotation of the polariser [1].

Linear polarisers use linear dichroism, but it is also possible to use circular polarisers [96], which rely on circular dichroism. These filter the circular polarisation components of a light beam.

There are three commonly used materials/mechanisms for linear polarisers: wire-grid polarisers, Polaroid sheets and nano-particle film polarisers [97].

- Wire-grid polarisers are made up of many fine parallel wires, normally sandwiched between glass or silica panels. The electric field component aligned with the wire-grid interacts with electrons in the conducting wires. As the electrons are free to move, a current is induced, transferring energy. However, movement of the electrons is restricted along the width of the wire. As such the component of the electric field perpendicular to the wire orientation is almost fully transmitted [1].

- Polaroid sheets can be used as linear polarisers due to unequal absorption along the orthogonal transmission axes. They are made from a polyvinyl-alcohol which is stretched, creating long chains of hydrocarbon molecules, before being attached to plastic and dipped in an iodine solution to fix the long-chain molecules in place [44]. The long chains of molecules function in a similar way to wire-grid polarisers.

- Nano-particle films are a more modern type of polariser. They are manufactured by embedding elongated, ellipsoidal silver nano-particles in thin glass plates. Nano-particle polarisers offer better extinction ratios between the orthogonal linear polarisation components and higher damage thresholds [97].

Additionally, we can have polarisers not based on absorption, but on splitting orthogonal polarisation components in different directions. This is the case for polarising beam splitters (PBS), which transmit horizontally polarised light and reflect vertically polarised light.

Half- and quarter-wave plates

Optically anisotropic crystals (such as calcite or quartz) exhibit a phenomenon known as birefringence. These crystals have different refractive indices for orthogonal polarisation components (termed the ordinary and extraordinary refractive indices). If a beam is incident on such a material, the two orthogonal polarisation components will travel at different velocities[1], resulting in an acquired phase difference between them [1]. By changing the phase difference between orthogonal polarisation components, the polarisation state can be altered, making the use of birefringence a common method for manipulating polarisation.

By manufacturing slices of birefringent crystals to precise thicknesses, specific phase differences can be obtained leading to controlled polarisation changes. It is most common to find plates of crystalline quartz manufactured to induce phase shifts equal to 1/2 or 1/4 of the wavelength, these are known as half- and quarter-wave plates, respectively (abbreviated to HWP and QWP)[2]. Half-wave plates introduce a π phase shift between the orthogonal polarisation components, rotating the orientation of the polarisation ellipse, and can convert pure circular polarisation to the opposite handedness. Quarter-wave plates, on the other hand, introduce a $\pi/2$ phase shift and change the ellipticity of a polarisation state (in the extreme case, converting from linear to circular polarisation or vice versa).

The decomposition of the input polarisation into orthogonal components differs depending of the orientation of the crystalline quartz axes corresponding to the ordinary and extraordinary refractive indices. Therefore, different changes to the input polarisation can be made by rotation of the waveplate.

There are two types of commercially available waveplate: zero-order and multi-order. A multi-order QWP is manufactured to be a thickness that induces a phase difference of $\Delta\phi = 2\pi m + \lambda/4$, for some integer m and given operation wavelength λ, and similar for a multi-order HWP. This is because it would be impractical to manufacture and handle waveplates that impart phase shifts of only one half or one quarter of a wavelength, as they would be very thin. Zero-order waveplates consist of two multi-order waveplates joined together, but with their axes rotated 90° with respect to each other, such that the differences in their retardance leads to phase differences of exactly $\Delta\phi = \lambda/4$ or $\Delta\phi = \lambda/2$.

It is important to use the correct waveplate for the wavelength being used, as the waveplates retardance depends on λ. This is particularly true for multi-order waveplates, even for a small wavelength deviation, due to the cumulative erroneous phase shifts. The error is less pronounced when using a zero-order waveplate, but these are more expensive. Additionally, the incident angle of the input beam, is important. Waveplates are manufactured for use at normal incidence, and increasing

[1] The speed of light (v) in a medium with refractive index n is given by the ratio $v = \frac{c}{n}$, where c is the speed of light in a vacuum.

[2] Waveplates are also commonly called phase retarders.

the angle of incidence (AOI) increases the distance propagated through the material, resulting in unintended phase shifts. The effects of incident angle on a QWP are investigated in § 5.4.6. Crystalline quartz waveplates are particularly sensitive to AOI, however, it is possible to use polymer waveplates which are fabricated for better stability over a larger range of AOI [98].

The change to an input polarisation state to a polariser or waveplate can be described mathematically using either Jones matrices or Mueller matrices, as mentioned above. The matrices for these common optical elements will be summarised in § 2.2.3.

2.2.2 Mirrors - choosing the right type

Mirrors play a crucial role in optical systems. They allow the easy adjustment of a beam's position and angle, and with as few as two mirrors, one can perform a "beam walk," directing a beam through any point in space.

Reflection from a mirror may seem intuitively simple, but in contrast to common misconceptions, mirrors do not "swap left and right" but instead "near and far". A demonstration of this is shown in Figure 2.1(a) for a beam with initial wave vector $\mathbf{k}_1$ incident on a mirror resulting in a reflected beam with wave vector $\mathbf{k}_2$. By decomposing the wave vectors into two orthogonal components, denoted x and y[3], it can be seen that the direction of $k_{1,y}$ and $k_{2,y}$ are the same whereas $k_{1,x}$ and $k_{2,x}$ are opposite - i.e. the reflection of a beam from a mirror results in the propagation direction perpendicular to the mirror surface being reversed.

Upon reflection, a beam's spin and orbital angular momentum is affected. The angular momentum component perpendicular to the mirror surface is conserved, whereas the parallel component is flipped. This has the effect of reversing the projection of the angular momentum with respect to the propagation direction - i.e., the sign of the OAM number and the photon's spin (helicity) is flipped.

Reflection from a mirror causes a phase shift between the s- and p-polarisation components. These are the polarisation components that are perpendicular and parallel to the plane of incidence (see Figure 2.1(b)). Generally, for a mirror aligned such that the incident and reflected beams remain parallel to the optical table, then the s and p components correspond to the vertical and horizontal polarisations, respectively. However, this is not always the case. A phase shift between the orthogonal s and p components can introduce changes to the polarisation state, changes of which depend on the input polarisation and the mirror normal (which determines the decomposition into the s and p components). Even for an ideal mirror, the p-polarisation component acquires a π phase shift [40]. This can, for example, change diagonal polarisation to anti-diagonal, or left-handed circular to right-handed circular, or vice versa. These phase shifts are not an issue if an input

[3]Note that this notation has been chosen for convenience, the components of $\mathbf{k}$ here do not necessarily correspond to directions along the conventional x and y Cartesian coordinate system.

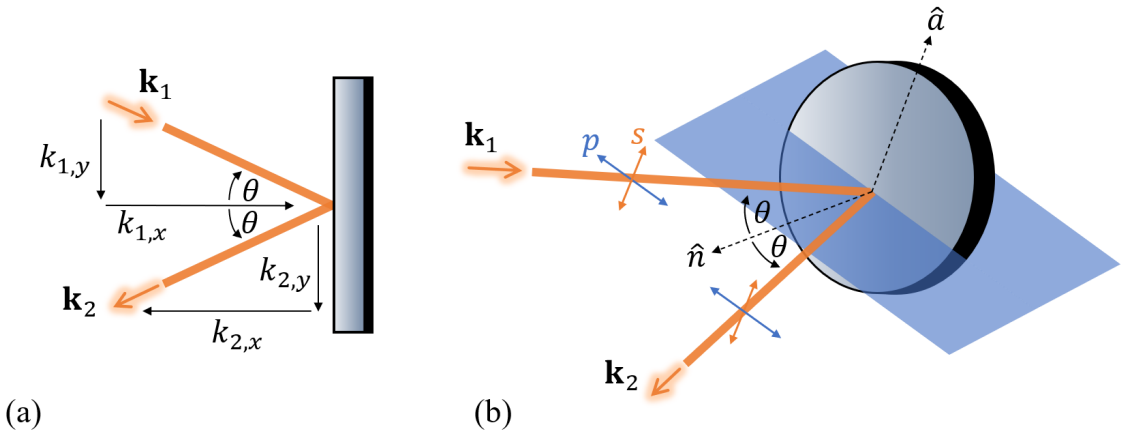

Figure 2.1: Geometry of reflection from a mirror. (a) A beam, with wave vector $\mathbf{k}_1$ incident on a plane mirror surface with angle of incidence θ, resulting in a reflected beam with wave vector $\mathbf{k}_2$. (b) Decomposition into s- and p-polarisation components which are perpendicular and parallel to the plane of incidence, shown in blue. The directions $\hat{n}$ and $\hat{a}$ are the normals to the mirror surface and plane of incidence, respectively.

beam is entirely s or p polarised, they however, pose an issue when we are interested in beams with spatially varying polarisation, especially if the induced phase shift is not predictable.

To investigate the polarisation changes due to reflection a preliminary exploratory experiment was performed. This involved measuring the polarisation before and after two types of mirrors (dielectric and gold metallic) for different angles of incidence (AOI). Full details on how polarisation profiles can be measured are given in § 2.3.

In Figure 2.2(a) and (b), I show measured polarisation profiles of an originally diagonally polarised beam after reflection from a dielectric mirror in (a) and a gold metallic mirror in (b), for AOI ranging from about 8° to 41°. For each of the measurements, the ellipticity and orientation of the polarisation was calculated and averaged over the beam profile, the results of which are given in Figure 2.2(c). From this, and the polarisation plots, it can be seen that the polarisation after the dielectric mirror varies significantly for the different AOI. For the gold mirror, the results are much more consistent. Upon reflection, a π phase shift has been acquired between the horizontal and vertical polarisation components, converting the diagonally polarised light into anti-diagonal, but the resulting ellipticity and orientation of the polarisation are almost constant with AOI, offering more predictable behaviour than the dielectric mirror.

In Figure 2.3 I show equivalent measurements but for a radially polarised beam. Again, after reflection from the dielectric mirror, the polarisation varies greatly, with the radial beam being converted into hybrid beams at certain AOIs. For the

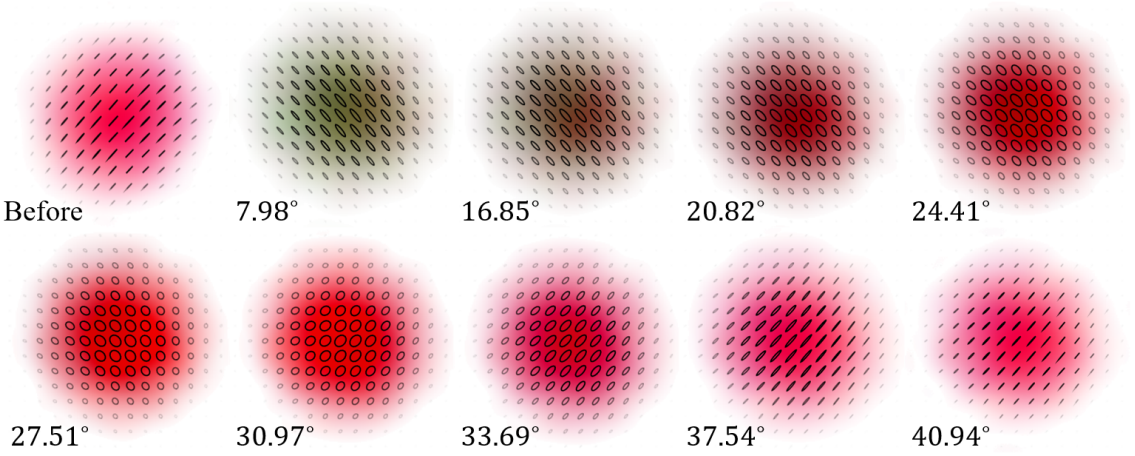

(a) Dielectric mirror

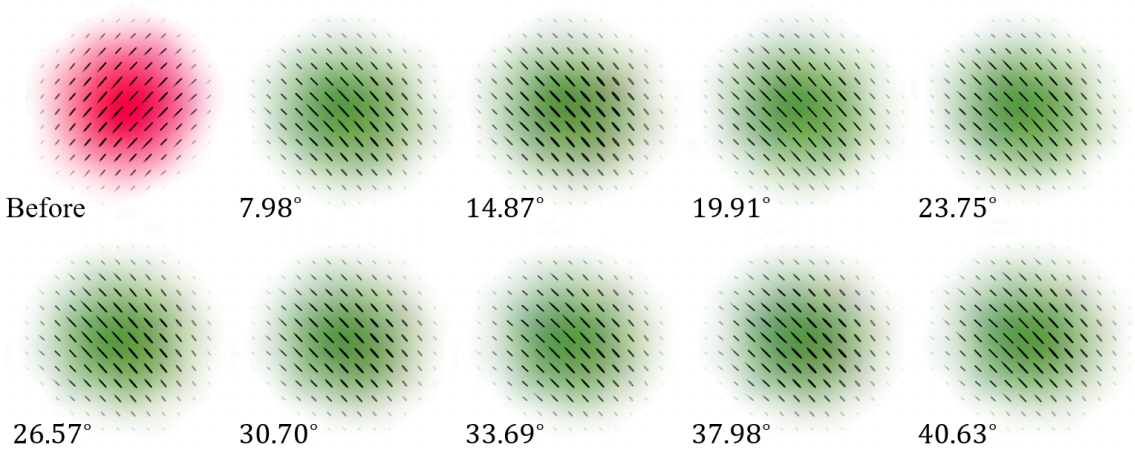

(b) Gold metallic mirror

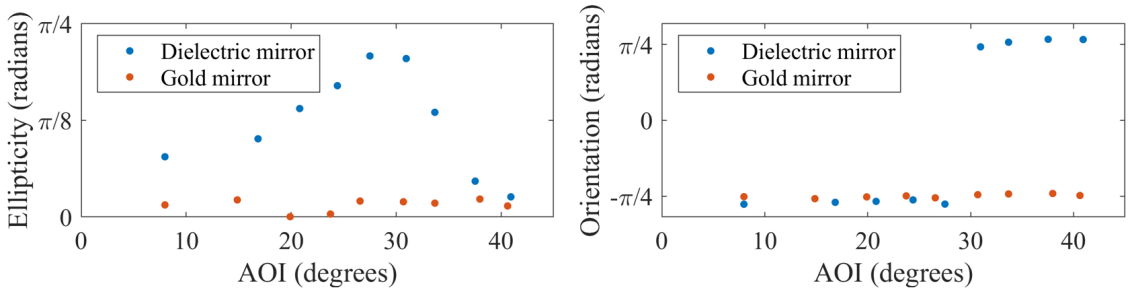

(c) Measured ellipticity and orientation

Figure 2.2: Measured diagonally polarised beam after reflection from a dielectric (a) and gold (b) mirror, for different AOI, as indicated on the plots. The original beams before reflection are shown in the top left of (a) and (b). (c) The measured ellipticity and orientation of the polarisation, averaged over the entire beam profile.

gold mirror, the beam remains radial. This may seem puzzling at first, as above, it was shown that a diagonally polarised beam becomes anti-diagonal after the gold mirror. However, it must be recalled that a mirror will also flip the entire intensity distribution. Therefore, the regions of diagonal (anti-diagonal) polarisation have indeed become anti-diagonal (diagonal), but accompanied with a mirroring of the intensity profile, the radial profile is recovered. This effect is not as clearly observed for a homogeneously polarised Gaussian beam, as shown above, and in fact, it is only seen for a radial beam as it is symmetric about a centred vertical axis. A radial beam is just one example of a subclass of vector beams whose polarisation profile is entirely conserved after reflection (azimuthal beams being another example).

Dielectric mirrors are made up of multiple thin layers of dielectric material, alternating between materials with higher and lower refractive indices. The mirror mechanism is based on the constructive interference of reflections from the different layers, which have thicknesses of multiples of the operating wavelength, allowing for high reflectivity (greater than 99% for a broadband mirror [99]). However, phase shifts occur at each reflection, causing polarisation changes, with the retardance exhibited varying as a function of AOI [100]. This is evident from the results discussed above.

Metallic mirrors consist of a thin metal coating on a substrate. They provide a single reflection from the mirror surface, and, as shown from the experimental results, are insensitive to polarisation and AOI. However, metallic mirrors are more susceptible to damage, they can be scratched easily due to their softer coating. They also have lower heat damage thresholds and lower reflectivity. This can be a problem if using high-powered lasers, or if intensity loss is a concern.

For all of the experimental projects that will be presented in this thesis, polarisation conservation is the main concern. Therefore, gold mirrors will be used.

2.2.3 Jones and Mueller matrices of optical components

As mentioned previously, Jones and Mueller matrices provide a convenient mathematical description for the polarisation changes induced by an optical element, or indeed, an entire optical setup. Whether the Jones or Mueller formalism is used normally depends on the application - Jones matrices are more commonly used for simulations and theoretical calculations when the full electric field information is known, whereas, Mueller matrices are used to describe the true optical activity of an optical element or sample, as they can be easily obtained through intensity measurements.

However, it is often useful to know both representations for the most common optical elements. These are summarised in Table 2.1, for an (ideal) mirror, a linear polariser (LP), a HWP and a QWP. For the waveplates and polariser, the matrices are given in terms of an angle θ, which is the angle of rotation with respect to the horizontal. If instead we wanted to describe a non-idealised mirror, then the s- and

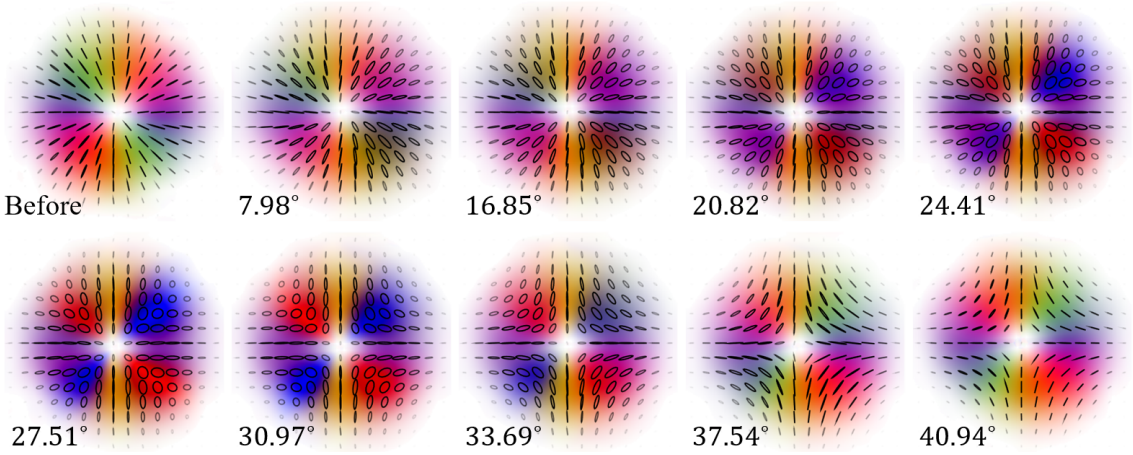

(a) Dielectric mirror

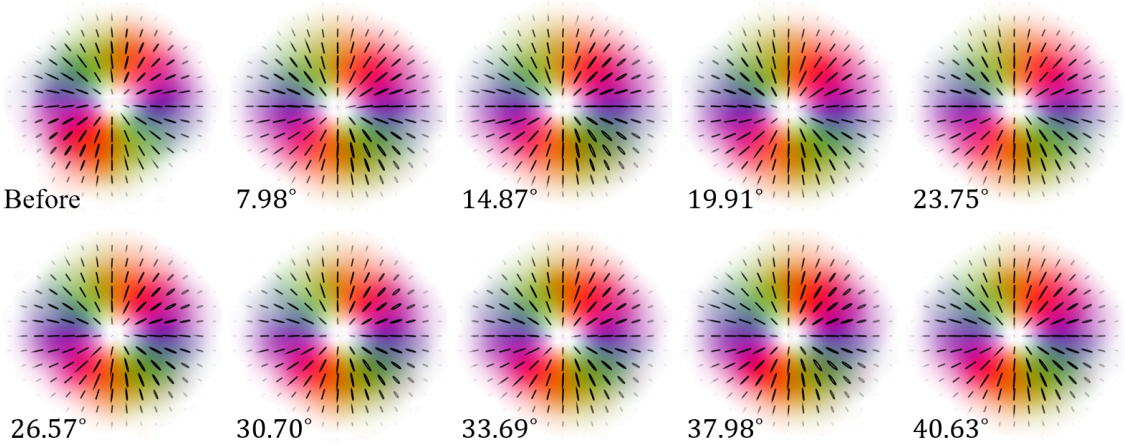

(b) Gold metallic mirror

Figure 2.3: Measured polarisation profiles of a radially polarised beam after reflection from a dielectric (a) and gold (b) mirror, for different AOI, as indicated. The original beams before reflection are shown in the top left of (a) and (b).

Optical element	Jones matrix	Mueller matrix
Ideal mirror	$\begin{bmatrix} -1 & 0 \\ 0 & 1 \end{bmatrix}$	$\begin{bmatrix} 1 & 0 & 0 & 0 \\ 0 & 1 & 0 & 0 \\ 0 & 0 & -1 & 0 \\ 0 & 0 & 0 & -1 \end{bmatrix}$
LP	$\begin{bmatrix} \mathrm{c}^2(\theta) & \mathrm{c}(\theta)\mathrm{s}(\theta) \\ \mathrm{c}(\theta)\mathrm{s}(\theta) & \mathrm{s}^2(\theta) \end{bmatrix}$	$\frac{1}{2}\begin{bmatrix} 1 & \mathrm{c}(2\theta) & \mathrm{s}(2\theta) & 0 \\ \mathrm{c}(2\theta) & \mathrm{c}^2(2\theta) & \mathrm{c}(2\theta)\mathrm{s}(2\theta) & 0 \\ \mathrm{s}(2\theta) & \mathrm{c}(2\theta)\mathrm{s}(2\theta) & \mathrm{s}^2(2\theta) & 0 \\ 0 & 0 & 0 & 0 \end{bmatrix}$
HWP	$\mathrm{e}^{-\frac{i\pi}{2}}\begin{bmatrix} \mathrm{c}(2\theta) & \mathrm{s}(2\theta) \\ \mathrm{s}(2\theta) & -\mathrm{c}(2\theta) \end{bmatrix}$	$\begin{bmatrix} 1 & 0 & 0 & 0 \\ 0 & \mathrm{c}(4\theta) & \mathrm{s}(4\theta) & 0 \\ 0 & \mathrm{s}(4\theta) & -\mathrm{c}(4\theta) & 0 \\ 0 & 0 & 0 & -1 \end{bmatrix}$
QWP	$\mathrm{e}^{-\frac{i\pi}{4}}\begin{bmatrix} \mathrm{c}^2(\theta) + i\mathrm{s}^2(\theta) & (1-i)\mathrm{s}(\theta)\mathrm{c}(\theta) \\ (1-i)\mathrm{s}(\theta)\mathrm{c}(\theta) & \mathrm{s}^2(\theta) + i\mathrm{c}^2(\theta) \end{bmatrix}$	$\begin{bmatrix} 1 & 0 & 0 & 0 \\ 0 & \mathrm{c}^2(2\theta) & \mathrm{c}(2\theta)\mathrm{s}(2\theta) & \mathrm{s}(2\theta) \\ 0 & \mathrm{c}(2\theta)\mathrm{s}(2\theta) & \mathrm{s}^2(2\theta) & -\mathrm{c}(2\theta) \\ 0 & -\mathrm{s}(2\theta) & \mathrm{c}(2\theta) & 0 \end{bmatrix}$

Table 2.1: Jones and Mueller matrices of common optical elements. For the linear polariser (LP), half- and quarter-wave plates (HWP, QWP), θ indicates the angle of the fast axis with respect to the horizontal. The sine and cosine functions have been abbreviated to s and c, respectively.

	General waveplate
Jones	$\mathrm{e}^{-\frac{i\delta}{2}}\begin{bmatrix} \cos^2(\theta) + \mathrm{e}^{-\frac{i\delta}{2}}\sin^2(\theta) & (1-\mathrm{e}^{-\frac{i\delta}{2}})\sin(\theta)\cos(\theta) \\ (1-\mathrm{e}^{-\frac{i\delta}{2}})\sin(\theta)\cos(\theta) & \sin^2(\theta) + \mathrm{e}^{-\frac{i\delta}{2}}\cos^2(\theta) \end{bmatrix}$
Mueller	$\begin{bmatrix} 1 & 0 & 0 & 0 \\ 0 & \cos^2(2\theta) + \sin^2(2\theta)\cos(\delta) & \cos(2\theta)\sin(2\theta)(1-\cos(\delta)) & \sin(2\theta)\sin(\delta) \\ 0 & \cos(2\theta)\sin(2\theta)(1-\cos(\delta)) & \cos^2(2\theta)\cos(\delta) + \sin^2(2\theta) & -\cos(2\theta)\sin(\delta) \\ 0 & -\sin(2\theta)\sin(\delta) & \cos(2\theta)\sin(\delta) & \cos(\delta) \end{bmatrix}$

Table 2.2: Jones and Mueller matrix for a general waveplate rotated by θ and with retardance δ.

p-reflection coefficients of the material would appear along the diagonal entries of the matrices, instead of just ± 1. This would account for any attenuation in the intensity after reflection.

In Table 2.2, I show the matrices for a general waveplate with a phase difference (retardance), given by δ between the two orthogonal polarisation components. From this it can be seen, that if $\delta = \pi$ or $\pi/2$, then these matrices reduce to those for the HWP and QWP respectively.

2.3 Stokes tomography - i.e. measuring polarisation

Generally, the word tomography refers to a technique used to image 3-dimensional objects in sections or slices, using any type of penetrating wave. The full 3D volume can then be reconstructed afterwards. Here, however, the term is perhaps used in a more similar way as to how it was adopted in the field of quantum physics when referring to the process of "quantum state tomography" [101]. This is a process in which a quantum state is reconstructed by performing projective measurements on a number of identical copies of the same state. In this case, we instead want to measure polarisation states, which can be achieved by projecting a beam of light onto different polarisation bases, as described in the following.

The Stokes parameters are a valuable representation of polarisation states and there exist multiple ways in which they can be experimentally measured. Here, I will outline the method used for almost all of the experiments presented in this thesis.

In Figure 2.4, I show a schematic of a simple automated polarimeter. The beam to be measured passes through a quarter-wave plate ($\lambda/4$), a half-wave plate ($\lambda/2$) and and finally a linear polariser (LP) before being detected by a camera. Six intensity measurements are required, corresponding to the six polarisations, $|\hat{h}\rangle, |\hat{v}\rangle, |\hat{d}\rangle, |\hat{a}\rangle, |\hat{r}\rangle$ and $|\hat{l}\rangle$ (see Figure 1.3). These can be obtained from different orientations of the waveplates, as given in Table 2.3. The linear polariser is not rotated, with its axis always orientated along the horizontal. Alternatively, a polarising beam splitter can be used, in place of the LP, with the transmitted intensity being recorded. Each combination of the waveplate angles effectively converts the polarisation state you are interested in measuring the contribution of into horizontal polarisation, such that it now passes through the linear polariser.

In order to efficiently measure the Stokes parameters, an automated system is used. The two waveplates are held in 3D-printed rotation stages. The rotation motion is achieved using a stepper motor, driven by a stepper-driver board and controlled using an Arduino, which is in turn connected to the experiment computer, along with the camera being used. It is then possible to save six camera images at select intervals once the waveplates are at the desired angles, as given in Table 2.3. The technique for this measurement system was previously developed by members of the Optics group at the University of Glasgow, but has since been improved for

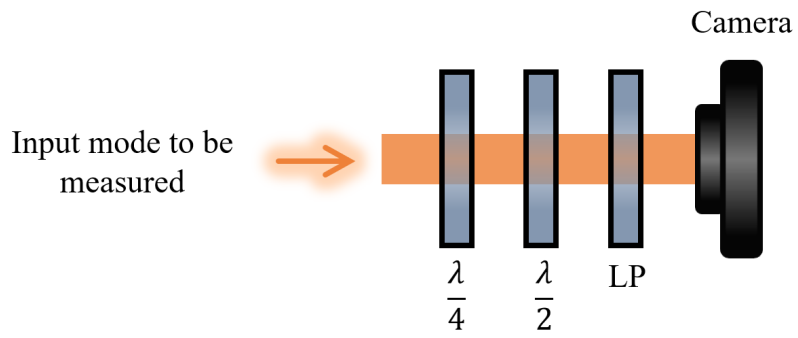

Figure 2.4: Stokes polarimeter measurement system. LP: linear polariser, $\lambda/2$: half-wave plate, $\lambda/4$: quarter-wave plate.

Polarisation State	$\lambda/4$	$\lambda/2$
$\|\hat{h}\rangle$	0°	0°
$\|\hat{r}\rangle$	0°	22.5°
$\|\hat{v}\rangle$	0°	45°
$\|\hat{l}\rangle$	0°	67.5°
$\|\hat{a}\rangle$	45°	67.5°
$\|\hat{d}\rangle$	45°	22.5°

Table 2.3: Waveplate fast axis angles, with respect to the horizontal, for Stokes parameter measurements using the automated setup shown in Figure 2.4.

simpler electronic control by reducing the number of Arduinos required to one. Full details of the automated stages, including schematics of the electronic circuits and 3D-printed designs, can be found in Refs. [102] and [103].

The automation allows the six intensity measurements to be taken more quickly (in a matter of seconds), and with more accuracy than if the waveplates were rotated by hand.

For the automated Stokes measurements, an accurate calibration of the measurement system is needed. A simple and straightforward method for this will now be described. Calibration should be conducted regularly, as the 'zero' position of the stepper motors will eventually change by one or more degrees with frequent use.

To begin with, we use the fact that the first measurement that the automated system takes corresponds to $I_{|\hat{h}\rangle}$, the horizontal state. Therefore, a purely vertically polarised beam should result in zero intensity falling on the camera sensor. A

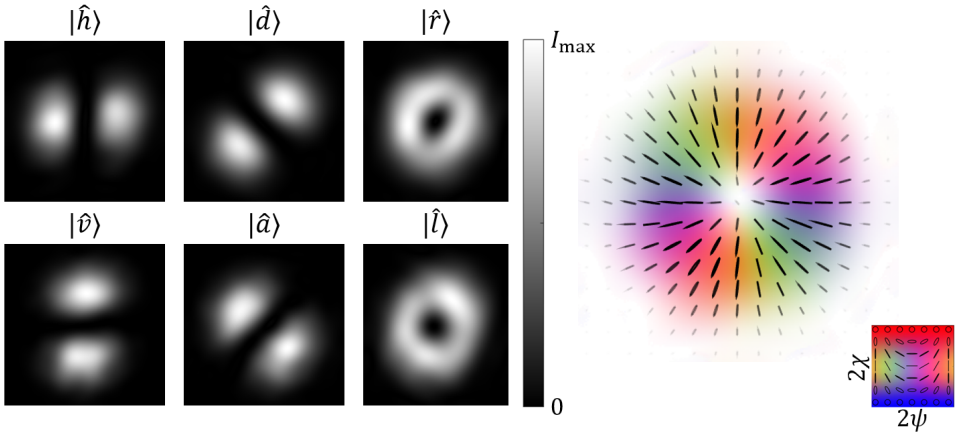

Figure 2.5: Example of polarisation measurement using Stokes tomography. Left: experimentally measured intensity profiles corresponding to the six Stokes measurements in Table 2.3 of a radial beam. Right: the reconstructed polarisation profile, and polarisation colour map in terms of orientation (ψ) and ellipticity (χ) angles. This beam was generated using the setup outlined in § 2.6.

uniformly vertically polarised beam is generated (either using the methods which will be described in § 2.6, another calibrated linear polariser or the reflected output form a polarising beam splitter). Each optical component shown in Figure 2.4 is then placed one by one in the beam path, before the camera. Starting with the linear polariser, the intensity detected by the camera is looked at, with the exposure time set high in order to detect even small values. The polariser is then rotated until an overall intensity minimum (ideally zero total intensity) is achieved. This process is then repeated for the half-wave plate and quarter-wave plate.

Once the six intensity measurements have been made, the Stokes parameters for each point of the beam profile can be calculated using Eq. 1.25. This then allows the orientation and ellipticity to be calculated on a pixel-by-pixel basis (Eq. 1.35).

An example of an experimentally measured polarisation profile for a radially polarised beam can be seen in Figure 2.5, along with the six recorded intensities. This radial beam was generated using the setup and method for arbitrary vector beam generation that will be described in § 2.6.

It is possible to obtain these six projections using only a LP and and QWP. For obtaining the $|\hat{h}\rangle, |\hat{v}\rangle, |\hat{d}\rangle$ and $|\hat{a}\rangle$ polarisation components, the beam is passed through the LP at the angles shown in Table 2.4. For the $|\hat{r}\rangle$ and $|\hat{l}\rangle$ measurements, the beam is passed through the QWP at 45° and LP at 90° and 0°, respectively. This approach should give the same results, and has the benefit of requiring one less optical element. However, it has two disadvantages. The first is that the QWP is only needed for two of the measurements, meaning that it must be added/removed from the beam path. This makes it more difficult to perform automated measurements

Polarisation State	$\lambda/4$	LP
$\|\hat{h}\rangle$	-	0°
$\|\hat{v}\rangle$	-	90°
$\|\hat{d}\rangle$	-	45°
$\|\hat{a}\rangle$	-	−45°
$\|\hat{r}\rangle$	45°	90°
$\|\hat{l}\rangle$	45°	0°

Table 2.4: Waveplate fast axis angles, with respect to the horizontal, for measuring Stokes parameters using only a linear polariser (LP) and quarter-wave plate. For the first four measurements, the beam only passes through the LP, for the remaining two it passes first through the QWP and then the LP.

as we do for the setup in Figure 2.4. The second, is that an unwanted property of the polarisers we use is that they can displace the beam path. This occurs as the polarising film is mounted between two relatively thick plates of glass, which, if the incidence angle is not exactly 0°, can displace the beam due to refraction [104]. We noticed this beam shift even for very small deviations of the angle of incidence. This is not a problem if there is no need to move/rotate the polariser as it can be placed and then any other optics aligned afterwards. However, rotating the polariser changes the beam displacement, so, in this case, will change the position of the beam on the camera. This is undesirable, as it would make it necessary to align the recorded images in post-processing when calculating the Stokes parameters, which, if not done carefully, could lead to errors in the resulting polarisation profiles.

Recall from Eq. 1.29 ($S_0^2 = S_1^2 + S_2^2 + S_3^2$), that for pure polarisation, the Stokes parameters are related to each other, and that only three of the four are independent. Therefore, it is possible to obtain the Stokes parameters from only four intensity measurements. There are multiple ways to do this, but one example is,

$$S_0 = I_0, \qquad S_1 = 2I_{|\hat{h}\rangle} - I_0, \qquad S_2 = 2I_{|\hat{d}\rangle} - I_0, \qquad S_3 = 2I_{|\hat{r}\rangle} - I_0. \tag{2.1}$$

This has the advantage of requiring two fewer measurements, however, as (in this example) only $|\hat{h}\rangle$, $|\hat{d}\rangle$ and $|\hat{r}\rangle$ are directly measured, our measurements only cover one quadrant of the Poincaré sphere, meaning that it is possible for some polarisation states to be favoured. Additionally, for some experimental analysis, we are interested in the normalised Stokes vector $\mathbf{S}^{(N)} = [S_0, S_1, S_2, S_3]^T/S_0$. In theory, the total intensity, S_0, can be found from the addition of any two orthogonal polarisation intensities. However, in practice, there can be slight differences due to imperfect optical components, e.g. some elements may absorb light differently for different

polarisations. Therefore, we can obtain a (at least to some extent) more reliable way of normalisation via,

$$\mathbf{S}_0^N = \left[\frac{I_{|\hat{h}\rangle} - I_{|\hat{v}\rangle}}{I_{|\hat{h}\rangle} + I_{|\hat{v}\rangle}}, \frac{I_{|\hat{d}\rangle} - I_{|\hat{a}\rangle}}{I_{|\hat{d}\rangle} + I_{|\hat{a}\rangle}}, \frac{I_{|\hat{r}\rangle} - I_{|\hat{l}\rangle}}{I_{|\hat{r}\rangle} + I_{|\hat{l}\rangle}} \right]^T, \tag{2.2}$$

which of course requires all six intensity measurements.

However, in Chapter 5, I will present an alternative way of determining polarisation using a minimum number of measurements, that overcomes the problem of non-symmetric Poincaré sphere coverage.

2.4 Image processing and analysis

For experimentally measured intensity profiles, it is common to get unwanted interference fringes appearing, as shown in Figure 2.6(a) for a (rotated) $HG_{1,0}$ mode. This often occurs from self interference of the beam at the surfaces of the camera, and is actually more likely to occur for better alignment. However, it is possible to remove these artefacts in post-processing using a simple Fourier filter.

For this, we start by performing a fast Fourier Transform (FFT) of the raw camera image. The logarithm of the absolute value of the FFT is shown in Figure 2.6(b), in which several bright peaks can be seen. In this plot, the central regions represent the low frequency components of the image and the peripheral regions the higher frequency components. The central largest peak corresponds to the zero frequency component (or DC value), and is the total intensity of the image. The other slightly smaller peaks contain information corresponding to the periodic diagonal fringes seen in the camera image. If we had instead measured a beam with completely horizontal (vertical) fringes, then these additional peaks would only occur as a vertical (horizontal) component in the frequency domain. However, here we have both components.

Finding the location of the peaks, but ignoring the central zero frequency peak, they can be used to create a mask to remove them from the FFT. Figure 2.6(c) shows the FFT with the mask applied, having the effect of setting the unwanted peaks to zero. Finally, the FFT with peaks removed can be inverse Fourier transformed to obtain the final filtered beam, as shown in Figure 2.6(d).

For analysis of experimental data recorded by a camera, we generally want to remove the background intensity occurring from stray light from the surrounding environment, and containing no beam information. This background noise will vary slightly over the camera sensor. To estimate it, we can look at a small region of the recorded image ($\approx 100 \times 100$ pixels) at the edge of the camera sensor, far from the beam profile, and average over this region. This average background value can then be subtracted from the entire image, setting any pixels that now have negative values to zero.

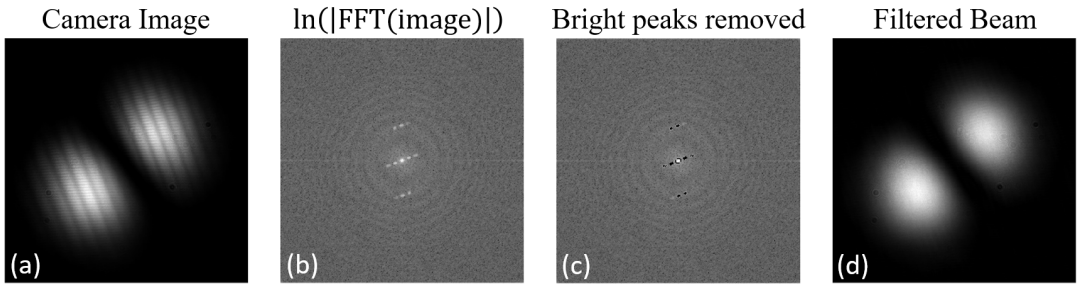

Figure 2.6: Example of low-pass Fourier filtering of an experimentally measured (rotated) $HG_{1,0}$ mode. (a) The original raw camera image. (b) Logarithm of the absolute value of the Fourier transform of the camera image and (c) with the bright peaks corresponding to the fringe information removed. (d) Final filtered beam after inverse Fourier transformation.

Throughout this thesis, where it is stated that Fourier filtering has been performed on the data and a background subtracted, this is the process that has been performed.

One final consideration that must be made in terms of image processing, is the pixel position of the centre of the beam, which is not necessarily at the centre of the camera display. This is particularly important if we want to overlay sequential experimental images on top of each other (e.g. for the Stokes polarimetry described in § 2.3) or find the location of multiple beams that are incident on a single camera sensor at the same time (e.g. for the work that will be described in Chapter 5). A simple way to locate the centre of a beam is by finding the weighted-centroid of a select region of the total image. This will give pixels with higher intensity values a greater "weight" than others within the computation region. This method works well even when trying to find the centre of a beam with zero intensity in the middle (for example those carrying OAM, or some HG modes) as long as there is an even intensity distribution spread equally about the central point. When computing the weighted-centroid, a more accurate centre can be found by only considering pixels with values above a chosen threshold, in order to avoid any background light impacting the results. A threshold of 20% of the peak intensity value proved to be an effective choice.

2.5 Shaping light

As mentioned in Chapter 1, knowing the complex electric field information of a beam in a single transverse plane, at any position along the propagation direction, allows the full three-dimensional structure of the beam to be realised. This includes its phase, intensity and polarisation. We can use this property of paraxial light to our advantage. By controlling the intensity and phase of a laser beam in one plane,

we can shape its entire three-dimensional volume. In fact, engineering the phase profiles and/or intensity of light is at the heart of every optical element, including, for example, the simple lens.

In the following, I will describe two important optical devices that can by used for the dynamic spatial control of a light beam's properties, namely, spatial light modulators and digital micromirror devices. The ability to address these devices with a computer makes them versatile tools in the fields of beam shaping and manipulation.

Furthermore, static light shaping devices exist such as q-plates [105–107], spiral phase plates [108–110] and Fresnel cones [34]. Additionally, static holograms can be constructed using lithography methods on transparent plates or etching techniques [111, 112]. There are advantages and disadvantages to both static and dynamic light shaping tools, e.g. you are limited in the potential structures using static light shaping elements, and with dynamic devices, you can change their action without experimental realignment, however, they are often limited in their resolution in comparison to the static counterpart. Here, the focus will be on the dynamic light shaping devices, and for information on the static devices, the interested reader should refer to the references provided. However, in Chapter 6, I present an experiment that implemented a Fresnel cone, and the details on how a Fresnel cone can be used to modify polarisation will be given therein (specifically in § 6.2).

2.5.1 Spatial light modulators

Reflective liquid crystal spatial light modulators (commonly abbreviated to LC-SLMs or just SLMs) use liquid crystal on silicon (LCOS) technology, relying on the physical properties of liquid crystals to control light beams.

The liquid-crystal state of matter was discovered by Friedrich Reinitzer in 1888 [113], the properties of which are as the name suggests - lying somewhere between those of conventional isotropic liquids and those of solid crystals. Liquid crystal can flow like a liquid, but its molecules (shaped like elongated ellipses) are orientated in a common direction, meaning that they maintain a certain degree of structural organisation akin to crystalline solids [114].

There are various types of liquid crystal phases, characterised both by their optical properties and the type of ordering of the molecules, and occurring for different temperatures and materials [114]. For the context of LC-SLMs, only the *nematic phase* is of relevance. In this case, the molecules lack positional order, but are aligned with their major axes almost completely parallel. The birefringence of the liquid crystal depends on the molecular orientation, which, in turn can be controlled by application of an electric field [115]. This has allowed LC-SLMs to be made based on the principle of the electronically controllable birefringence of liquid crystals.

A schematic showing the working of a typical LC-SLM is shown in Figure 2.7. The device is pixelated, with a liquid crystal layer lying between a cover glass

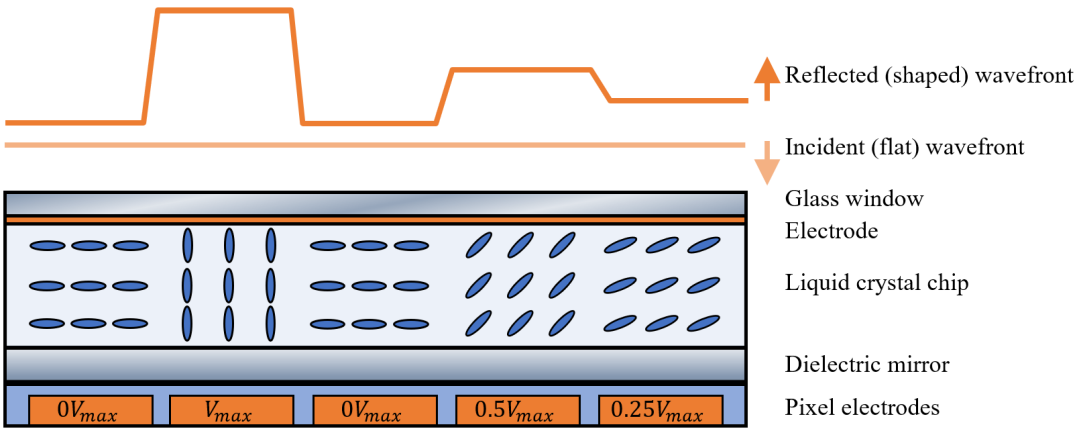

Figure 2.7: Cross-section of the basic structure of a typical LC-SLM working at normal incidence. The crystal molecule orientation is shown as ellipses, and the orientation (hence birefringence) is a function of the applied voltage between the common electrode and pixelated electrodes on the back plane. Minimal birefringence occurs for maximal applied voltage ($V_{\max}$). The wave travelling through the liquid crystal can acquire a spatially dependent phase between 0 and 2π in two passes of the liquid crystal layer, one before and after reflection from the dielectric mirror. Note that in reality, there is a smoother transition between the liquid crystal alignment at the pixel boundaries.

window and a pixelated silicon backplane. Each pixel has electrodes on either side, allowing different electric fields to be applied through them, and the orientation of the molecules (hence birefringence) to be independently chosen [115, 116]. For an incident light wave, the molecule orientation affects the effective optical path through that pixel. For a maximum applied field (denoted $V_{\max}$ in Figure 2.7), the long axis of the crystals are perpendicular to the polarisation direction, minimising the optical path and hence the phase delay. For no applied electric field, the crystal molecules are rotated parallel to the polarisation direction, maximising the optical path and phase retardance [116]. The applied phase retardation to an incoming beam is then simply a function of applied voltage, and can be spatially varying due to the SLM pixelation, as shown in Figure 2.7.

Due to the mechanism for phase modulation, an SLM can only modulate the phase of input light whose polarisation is aligned with the major axis of the liquid crystal molecules. Therefore, for spatial phase modulation, horizontally polarised light is required (or vertical if the SLM is rotated by 90°). However, if diagonally (or anti-diagonally) polarised light is used, then retardation of only the horizontal component occurs, and the phase difference between the horizontal and vertical polarisation components can be changed. This in turn allows for polarisation modulation [117].

A reflective SLM has a mirror at the back surface of the liquid crystal layer. For increased efficiency, this is typically a dielectric mirror, chosen for the specific working wavelength (or wavelength range) of the SLM. This means that the incident wave travels twice through the liquid crystal layer, hence LC-SLMs are manufactured to have a thickness such that the maximal phase retardation (2π) is obtained for two passes through the layer.

For commercial LC-SLM devices, the crystal orientation can be set to one of 256 values. However, this full range may not be required for every wavelength. For example, if we have an SLM that applies the full 0 to 2π phase shift for values of 0 to 255, for a particular wavelength λ, then a wavelength of 0.8λ, would only require values of 0 to 204 to obtain phase modulation between 0 and 2π (although with less resolution). Therefore, it is possible to use an SLM for phase modulation of a light beam with a shorter wavelength than intended, however, not a longer wavelength.

2.5.2 Example SLM setup and hologram calculation for simultaneous phase and amplitude modulation

As discussed, SLMs can be used to spatially modulate the phase of an incident laser beam directly, however, techniques can be employed to also achieve amplitude modulation. Here, I will provide an example of one such method, that will be used in Chapter 7 of this thesis.

Phase-only hologram

One of the simplest ways to obtain both phase and amplitude modulation using an SLM, is to design a hologram that will apply the phase modulation and simultaneously redirect some of the incident light, such that we are left with intensity only in the places that we want. For this we employ a diffraction grating, using the fact that the periodic structure of a diffraction grating can disperse a single light beam into multiple beams travelling in different directions, known as diffraction orders. Using a grating, it is therefore possible to deflect a tunable portion of the light away from the straight reflection from the SLM and direct it into the first diffraction order. Not only that, we can control the specifications of the grating to maximise the intensity directed to the first order. For this we use what is known as a blazed grating.

Blazed diffraction gratings refer to phase gratings with a "sawtooth" profile [118,119]. They are defined by two parameters, their phase *depth* (or height of each "tooth") and their *pitch*, the width of each triangular tooth (see Figure 2.8(b)). If we consider a light beam incident on the SLM with a propagation direction described by wave vector $\mathbf{k}_{\text{in}}$, then a direct reflection would result in a beam with wave vector $\mathbf{k}'_{\text{in}}$ However, the first diffraction order, containing the desired information will propagate in a direction with wave vector $\mathbf{k}_{\text{des}}$, as depicted in Figure 2.8(a).

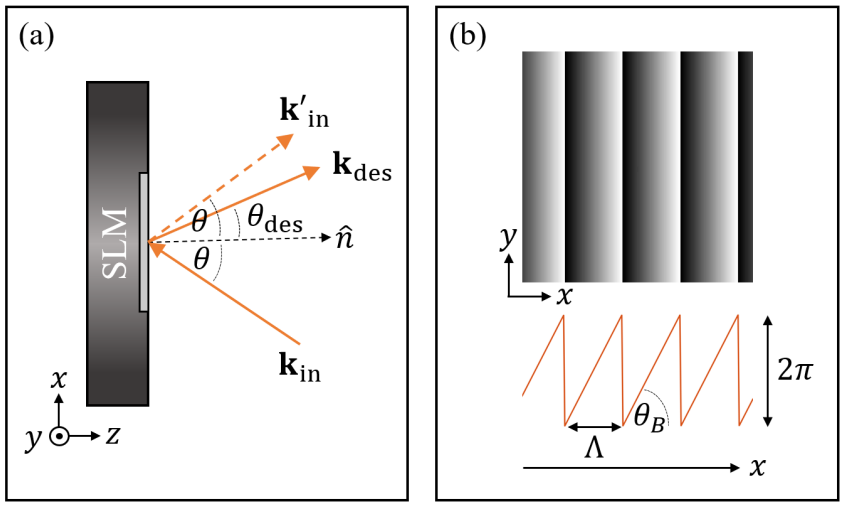

Figure 2.8: Diffraction from an SLM using a blazed diffraction grating. (a) Wave vector directions of the incident beam ($\mathbf{k}_{\text{in}}$), the direct reflection ($\mathbf{k}'_{\text{in}}$) and desired beam in the first diffraction order ($\mathbf{k}_{\text{des}}$) after an SLM, with normal $\hat{n}$. (b) Blazed diffraction grating with pitch Λ, a depth of 2π, resulting in a tilt known as the *blaze angle* θ_B.

The phase grating profile, periodic in the x direction, can be found from,

$$\Phi_g(x, y) = \text{mod}\left(\frac{2\pi x}{\Lambda}, 2\pi\right), \tag{2.3}$$

where Λ is the grating pitch or period, and, in this case, the grating depth has been set to 2π. We want to maximise the purity of the desired field, by increasing the spatial separation between the first and zeroth diffraction orders as much as possible. For this, recall that in the Fourier plane of a periodic diffraction grating the diffraction orders are more spatially separated for gratings with larger grating periods, and vice versa. Experimentally, it has been found that grating periods of $\Lambda \approx 4$ pixels work well [120].

If the grating described by Eq. 2.3 is used directly, then the beam directed along $\mathbf{k}_{\text{des}}$ will have the same intensity distribution as the incident beam. However, by carefully tuning the depth of the phase grating (between 0 and 2π), the intensity in the first diffraction order can be varied, without changing the diffraction angle. Gratings with smaller depth diffract less light into the first order, leaving more in the zeroth order, in comparison to those with a larger depth [119]. Therefore, with spatial control of the grating depth, we can achieve a tunable spatially varying amplitude in the first diffraction order.

This could be achieved by simply multiplying Φ_g with a spatially varying amplitude, corresponding to our desired beam. However, this assumes the incident beam

to be a plane wave with uniform intensity, and in reality, this is not the case. We can then instead take into account the experimental input beam in the calculation of the hologram, by dividing the desired beam by a simulated estimate of the input. An expression for the hologram can then be given by,

$$\begin{aligned} H(x,y) &= f\left(\frac{A_{\text{des}}(x,y)}{A_{\text{in}}(x,y)}\right) \bmod \left[\phi_{\text{des}}(x,y) - \phi_{\text{in}}(x,y) + \Phi_g(x,y), 2\pi\right], \\ &= f\left(A_{\text{rel}}(x,y)\right)\phi_{\text{rel}}(x,y), \end{aligned} \tag{2.4}$$

where A_{rel} and ϕ_{rel} are the relative spatially varying amplitude and phase respectively, which take into account the desired beam, the incident beam and the required blazed grating.

In Eq. 2.4, f represents some function of the relative amplitude, which can be chosen to optimise the experimental results. The simplest choice is $f(A_{\text{rel}}) = A_{\text{rel}}$, which assumes that there is a linear relationship between grating depth and diffraction efficiency, but this is generally not the case for many SLMs. Nonetheless, this simple approach works surprisingly well and is widely used [103, 120].

Reference [120] performs a rigorous comparison of six different options for the function f. One particular option that performed well had f of the form,

$$f(A_{\text{rel}}(x,y)) = 1 - \frac{1}{\pi}\text{sinc}^{-1}(A_{\text{rel}}(x,y)), \tag{2.5}$$

which took inspiration from Davies et al. [119], who found that the amplitude in the first diffraction order had a sinc variation[4].

Together, Eqs. 2.4 and 2.5 form the method for hologram generation used in this thesis. Figure 2.9 offers a pictorial illustration of the hologram generation process. The final hologram is scaled to have values between 0 and 255 (corresponding to 8-bits) before being displayed directly on the SLM, which will convert the 8-bit inputs into the correct voltage and phase retardation.

SLM setup

Figure 2.10 shows a schematic of a simple setup using an SLM for arbitrary beam shaping. A laser beam is expanded and cleaned[5] (using lenses L_1 and L_2 and a pinhole) before being directed onto the front surface of the SLM. Lenses L_1 and L_2 are chosen such that the beam is magnified to overfill the SLM display and to make wavefronts of the incident beam be as close to plane as possible. A linear

[4]Note that a direct inverse for the sinc function does not exist, but it can be defined on the domain $[0, \pi]$. The easiest way to do this is to calculate the ideal $\text{sinc}(x) = \sin x/x$ function and create a "lookup table" to obtain the $\text{sinc}^{-1}(x)$ values.

[5]The output from lasers are often beams with non-perfect quality. By spatially filtering using a pinhole, we can "clean" the beam achieving beam profiles closer to that of an ideal Gaussian.

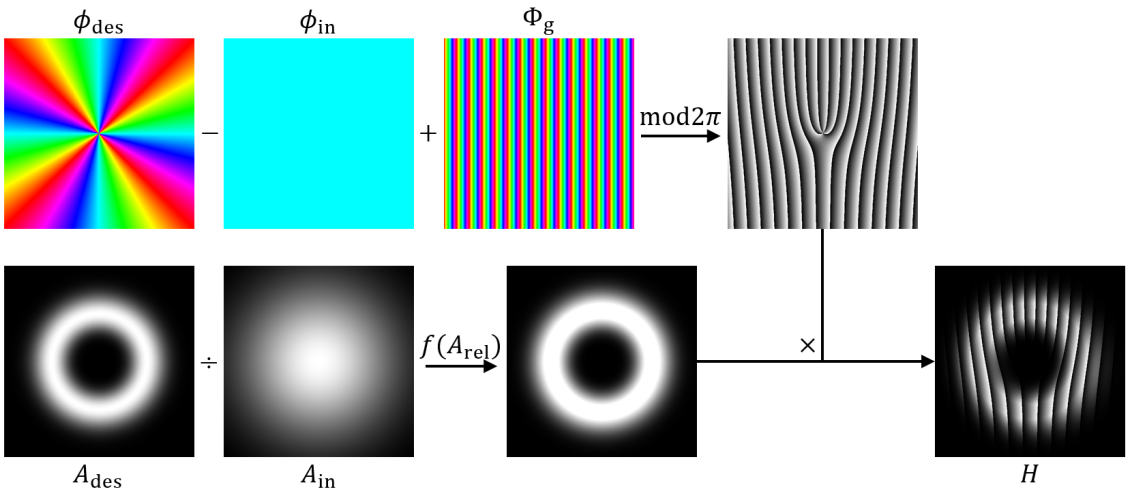

Figure 2.9: Representation of the hologram calculation outlined by Eqs. 2.4 and 2.5. The phase maps are scaled from 0 to 2π, the intensity from 0 to I_{max} and the final hologram H has been scaled to values between 0 and 255, according to the greyscale values accepted by the SLM.

polariser (LP) is also used to ensure linear horizontally polarised light, as the liquid crystals of the SLM display can only modulate horizontal polarisation. The calculated hologram is displayed on the SLM, designed to send our shaped beam to the first diffraction order, as described above. After reflection from the SLM, the beam propagates through a final telescope (lenses L_3 and L_4), allowing the first diffraction order to be selected by placing a variable aperture in the focal plane after L_3, corresponding to the Fourier plane of the SLM. In the top right of Figure 2.10, a simulation of the SLM Fourier plane is shown for an LG_0^1 beam. From this, the desired beam can be seen in the first diffraction order, and the "unwanted" intensity remaining in the zeroth order. The higher diffraction orders have intensity (and phase) distributions equal to higher order LG modes.

2.5.3 Digital micromirror devices

Digital micromirror devices (DMDs) consist of an array of several hundred thousand micron-sized mirrors. These mirrors can be electronically addressed to allow independent switching of the mirror direction. The mirrors can be directed in one of two directions, usually $\pm 12°$, corresponding to an "on" and "off" state. This means that select parts of an incident light beam can be sent towards or away from the intended direction in the experiment (corresponding to the on and off states, respectively), allowing a binary pixel-by-pixel control of the intensity. Therefore, in contrast to SLMs, which provide spatially varying control of the phase, DMDs only

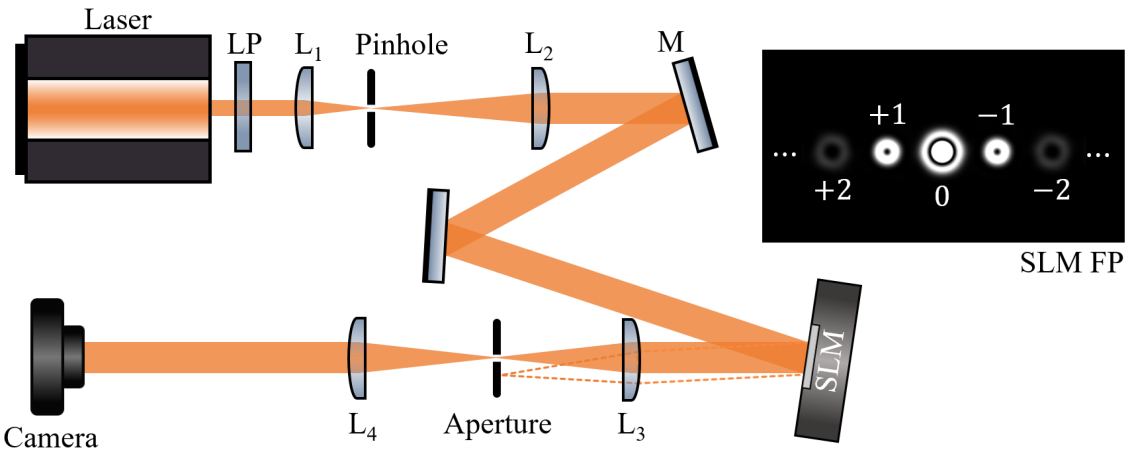

Figure 2.10: SLM setup for phase and amplitude modulation. LP: linear polariser, M: mirror, $L_{1,2,3,4}$ are lenses. The variable aperture sits in the Fourier plane of the SLM and selects the first diffraction order, blocking all other orders. The inset, labelled SLM FP, is a simulation of the SLM Fourier plane when a hologram for an LG_0^1 is used. This image has been saturated in order for the higher orders, with lower intensity, to be more clearly viewed.

act on the amplitude[6].

Figure 2.11 shows a representation of a DMD mirror array along with the specifications for a Texas Instruments DLP3000 LightCrafter DMD [121], which is the model used for the work presented here. Figure 2.11(a) shows a close up of the micro-mirror structure, highlighting their diagonal arrangement. Each individual mirror is square with their axis of rotation being about their diagonal, and the diagonal arrangement means that the spacing between the rows and columns is not equal. In Figure 2.11(b) and (c), I also show photographs of the micromirror array displaying holograms for a checkerboard pattern and a beam with a doughnut intensity distribution.

Digital micromirror devices are known for their speed, and DMD chips where the mirrors can switch at rates of 32.5 kHz or faster, are possible (e.g, DLP7000). Therefore, in applications where hologram changing speed is important, DMDs are often chosen over LC-SLMs, which typically have response rates in the order of tens of milliseconds. Although DMDs can only directly modulate intensity, using diffractive techniques, the phase can also be shaped [17, 122, 123], however, this usually comes with a reduction of efficiency in comparison to LC-SLMs.

[6]Note that, technically, DMDs are a subclass of spatial light modulator, as they offer spatial control of a light beam. As such they are sometimes referred to as binary SLMs or mirror-based SLMs. However, they are more commonly called DMDs, with the term SLM normally kept for reference to the LC-SLMs described above.

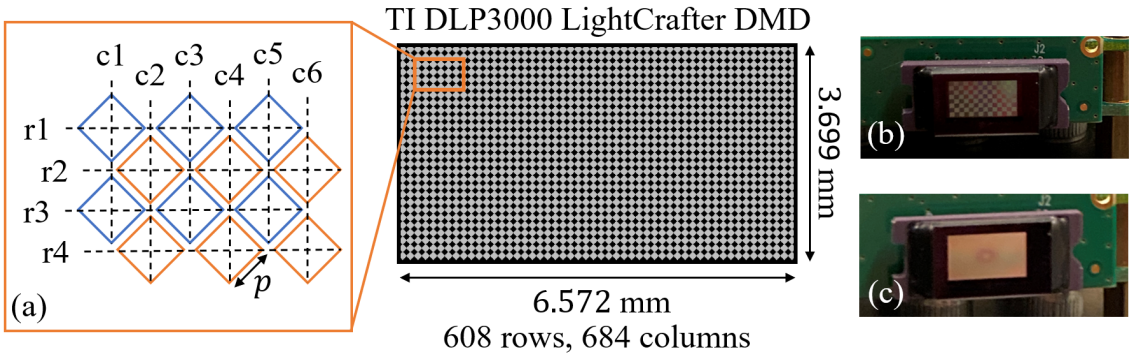

Figure 2.11: Digital micromirror device design. Product specifications for a Texas Instruments DLP3000 LightCrafter DMD and mirror arrangement (a) with rows (r) and columns (c) indicated. The mirrors can be independently rotated about their vertical diagonal to ±12° and the pixel pitch, denoted p, is 7.6 μm. (b) and (c) show photographs of the DMD chip displaying a checkerboard and doughnut beam hologram, respectively.

Binary holograms

In a similar way in which phase-only holograms for SLMs can direct the desired mode into the first diffraction order, it is possible to design binary holograms where the first diffraction order will also contain the desired spatial intensity and phase profile, as first demonstrated in 1966 [124]. Changing the pitch, or width, of the diffraction grating can control the angle of the first diffraction order. By locally varying the grating pitch, we can obtain spatially varying intensity, and by locally varying the lateral offset or position of the grating, a spatially varying phase can be achieved [125]. For example, we will have a π phase difference between two regions of the beam if the "on" parts of the grating in the first region line up with the "off" parts of the grating in the second region.

A binary hologram for obtaining a desired beam in the first diffraction order can be calculated using [103, 125],

$$H(x,y) = \frac{1}{2} + \frac{1}{2}\mathrm{sgn}\left[\cos\left(\phi_{\mathrm{rel}}(x,y)\right) + \cos(\sin^{-1}\left(A_{\mathrm{rel}}(x,y)\right))\right] \tag{2.6}$$

where, A_{rel} and ϕ_{rel} have the same definitions as above, and sgn is the sign function, returning values ±1 and resulting in H having values of 0 or 1, i.e. a binary hologram.

Due to the DMD mirror geometry, specifically, the diagonal layout causing uneven spacing between the rows and columns, and the ±12° tilt of the mirrors, causing a beam at normal incidence to be reflected off at 24°, the resulting shaped beam will display a lateral compression. This can be compensated for by "stretching" the hologram such that the beam in the image plane of the DMD has the desired dimensions.

2.6 Experimental generation of vector beams

Now that the workings of digital micromirror devices and binary holograms have been outlined, I will now describe a way in which they can be used to generate arbitrary beams with spatially varying polarisation.

Due to the mathematical description of a general vector beam (Eq. 1.52), generating beams with spatially varying polarisation boils down to encoding two fields with orthogonal polarisation states into a single beam profile. Multiple methods have been developed to do this, with some being "static", only being able to generate a specific (or a select few) vector beams, and others "active", where arbitrary beams can be generated. The active methods commonly rely on devices such as LC-SLMs and DMDs.

As mentioned in § 2.5.1, LC-SLMs can only modulate a single polarisation, usually horizontal. Nonetheless, it is possible to use them to generate vector beams through either interferometric methods [126–131] (independently shaping two beams and then combining them at a beam splitter, for example) or implementing a double pass of the SLM [132, 133], with a half-wave plate used in between, swapping the vertical and horizontally polarised components, such that a different part of the incident field is modulated each time.

One downside to these experimental systems using SLMs for vector beam generation, is that they often need very precise alignment and/or good interferometric stability to ensure optimal mode overlap. For this reason, for the work presented in this thesis, a DMD was employed to generate vector beams, as they will modulate any incident light, regardless of its polarisation, providing easier polarisation control with a (possibly) simpler setup. The experimental setup that will be explained in the following section was previously developed in collaboration between the Optics group at Glasgow and the University of Witwatersrand [70, 134], and has since been refined to optimise the generation process and resulting measured vector beams.

2.6.1 Experimental setup for vector beam generation and multiplexed holograms

Figure 2.12 shows a schematic of the experimental setup used for arbitrary vector beam generation using a DMD. An initially horizontally polarised laser beam (He-Ne, $\lambda = 633$nm) is expanded and collimated to a spot size that will overfill the active area of the DMD, before being passed through a half-wave plate to create diagonally polarised light. The diagonal beam is split into its horizontal and vertical components using a Wollaston prism (WP), where the resulting orthogonally polarised beams exit the WP with a separation angle of $1^\circ\,20'$. Both the $|\hat{h}\rangle$ and $|\hat{v}\rangle$ polarisation components are directed onto the DMD display using a 4f imaging system (L_1 and L_2), where they overlap spatially (this overlap does not have to be complete, but should be as large as possible and ideally centred on the DMD

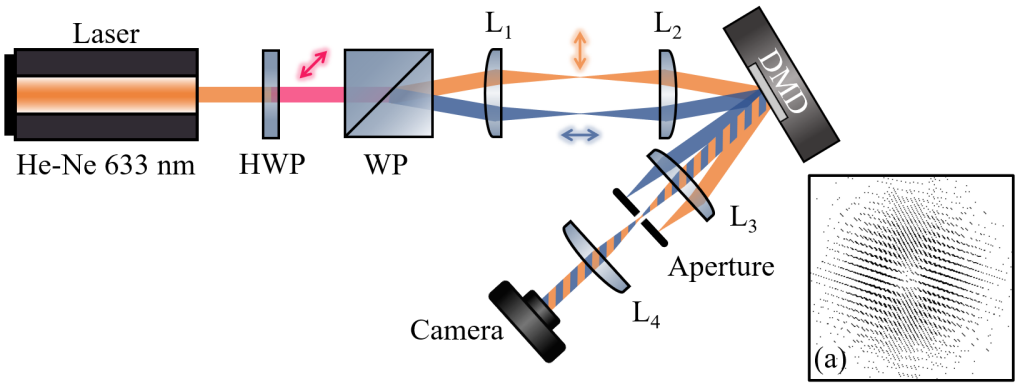

Figure 2.12: Experimental set-up for generating arbitrary vector beams using a DMD. HWP: half-wave plate, WP: Wollaston prism, $L_{1,2,3,4}$: lenses. Here, the pink beam represents diagonal polarisation, blue beams horizontal polarisation, orange vertical polarisation, and a mix of both represent beams with spatially varying polarisation. (a) Example of a binary multiplexed hologram to generate a radially polarised beam, calculated using Eq. 2.7. Black areas represent mirrors tilted to $+12°$ and white areas correspond to mirrors tilted to $-12°$.

display). The DMD will then shape the amplitude and phase of the vertical and horizontal beams independently, using a *multiplexed hologram*.

The multiplexed hologram is designed to diffract light into two different diffraction orders, corresponding to the $|\hat{h}\rangle$ and $|\hat{v}\rangle$ beams, and they are reflected from the DMD surface at two different angles. The hologram consists of the superposition of two independent holograms corresponding to the desired beam profile of each polarisation component. Each hologram is superimposed with a different linear diffraction grating, the period of which is chosen such that, in combination with the different input angles, the first diffraction orders of the shaped horizontal and vertical light fields overlap. Consider that we want to generate a beam from the superposition of a horizontally polarised mode described by $\mathbb{H} = A_h(x,y)\mathrm{e}^{i(\phi_h(x,y)+\Phi_{g,h}(x,y))}$ and a vertically polarised mode described by $\mathbb{V} = A_v(x,y)\mathrm{e}^{i(\phi_v(x,y)+\Phi_{g,v}(x,y))}$, where $\Phi_{g,h}$ and $\Phi_{g,v}$ are the linear diffraction gratings used to specify the direction of each order. To calculate the binary multiplexed hologram we first find the form of a new *multi* beam field, $\mathbb{M}$, given by the weighted complex interferometric sum of $\mathbb{H}$ and $\mathbb{V}$ [125],

$$\mathbb{M}(x,y) = W\mathrm{e}^{i\phi_{\text{global}}}\mathbb{H}(x,y) + (1-W)\mathbb{V}, \tag{2.7}$$

where, W is a relative weighting between the two beams, controlling the fraction of intensity sent into beams $\mathbb{H}$ and $\mathbb{V}$. We will have equal intensity between them when $W = 0.5$ (however, in reality, this is dependent on if the intensity ratio between the horizontal and vertically polarised beams incident on the DMD is equal or not). The phase term ϕ_{global} controls the relative global phase between the two

modes. The expression for $\mathbb{M}$ can then be used in Eq. 2.6 to create the final binary multiplexed hologram, which provides control over the intensity and phase of the two orthogonally polarised beams as well as the position of the diffraction orders. An example hologram for a radially polarised beam is shown in Figure 2.12(a) as well as in Figure 2.11(c) where it can be seen displayed on the DMD itself.

As mentioned, the period of the linear diffraction gratings ($\Phi_{g,h}$ and $\Phi_{g,v}$) are chosen such that the first diffraction orders of the shaped horizontal and vertical light fields overlap spatially, resulting in the desired vector beam appearing immediately after the DMD. This means that after the DMD any unwanted diffraction orders, as well as the zeroth orders, can be removed via spatial filtering. This is achieved by placing an aperture in the Fourier plane of a lens (L_3 in Figure 2.12). The beam is then collimated again before imaging. The polarisation of the resulting beam can be characterised using the Stokes tomography system (as described in § 2.3) by placing it directly after L_4.

During alignment, the spatial overlap of the beams in the first diffraction orders after reflection from the DMD can be observed using a camera, and the overlap fine tuned by varying the period of the gratings in the binary hologram displayed on the DMD. This is most easily performed by looking in the Fourier plane of the DMD, by placing the camera directly behind the aperture. A schematic depicting how the modes are overlapped is shown in Figure 2.13 along with camera images of the DMD Fourier plane.

Here, the generation of vector beams has been described using a superposition of horizontal and vertical polarisation, mainly because these are the two polarisations that a Wollaston prism splits a beam into. However, by simply placing a QWP before (or after) the DMD, with its fast axis at 45° we can generate vector beams using a right- and left-handed polarisation basis. Indeed, by placing a HWP and a QWP before the DMD, we can generate beams using any orthogonal polarisation basis we want.

2.7 Chapter 2 conclusion

In this chapter, I have focused on providing the relevant experimental details for the work carried out for this thesis. This included how common optical elements (e.g. waveplates and polarisers) interact with a light beams polarisation and can be used to control it, and how mirrors can impart unwanted polarisation changes. The Jones and Mueller matrix representations of these optical elements were provided, which can be used to understand how a series of optical components will modify a polarisation state.

In § 2.3, I described how polarisation can be experimentally measured via Stokes tomography. For all of the work presented in this thesis polarisation is determined using a simple automated set up consisting of two rotating waveplates and a sta-

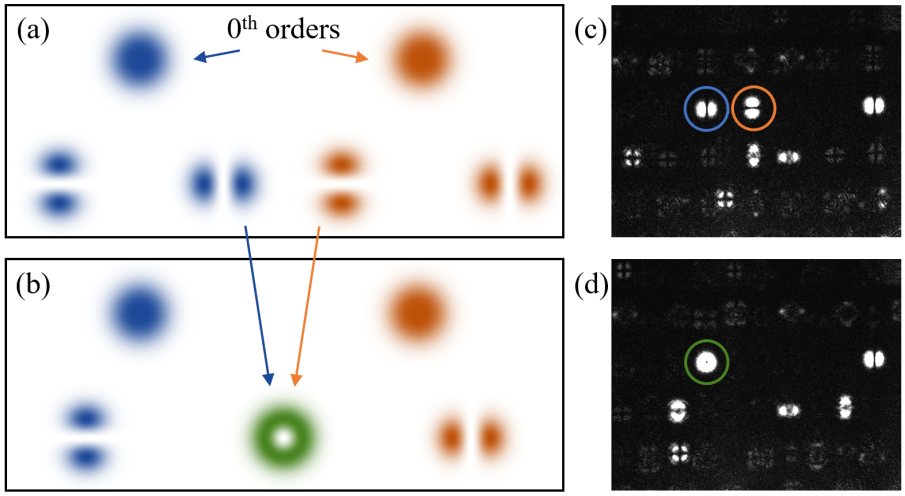

Figure 2.13: DMD Fourier plane when generating a radially polarised beam. Horizontally polarised beams are shown in blue and vertical in orange. A depiction of the Fourier plane before and after spatial overlap is shown in (a) and (b) respectively, with the superimposed beam shown in green. (c) and (d) show equivalent experimentally recorded images, where higher diffraction orders can also be seen. In these images the zeroth order has been blocked to avoid over saturation of the camera.

tionary linear polariser.

A large part of this chapter concentrated on the ways in which light beams can be shaped using dynamic digital devices. The workings of LC-SLMs were explained and an experimental system and phase-only hologram calculation presented for arbitrary phase and amplitude modulation of light beams using LC-SLMs. A description of digital micromirror devices, how they work, the concept of binary holograms and how they can be used to shape light was given in §2.5.3.

Finally, the knowledge of light shaping and DMDs was combined in § 2.6 where I detailed the experimental setup used at Glasgow for the generation of arbitrary vector beams. This is perhaps the most important experimental setup presented in this thesis, as it is the way in which the vector beams required for the other experimental projects are generated.

Chapter 3

Angular momentum redirection phase and non-planar beam propagation

3.1 Chapter 3 introduction

The experiment and theory contained within this chapter is what I worked on at the very start of my PhD (and during the peak of Covid lockdowns). As my first project, it is probably the one I learnt the most from, particularly in terms of experimental techniques and analysis, and it is this project that led to my first, first-author publication (Ref. [135]), and as such, I always think back to this experiment fondly.

For this work, we began with an interest in looking into what happens when structured beams propagate along strange and unusual paths and linking this to geometric phases. We started by investigating experimentally the propagation of beams along an out of plane trajectory, connecting the rotations seen individually in the intensity patterns and polarisation to separate geometric phases. It has previously been shown that that geometric phases are independently linked to spin-redirection, resulting in the rotation of polarisation [136–138], and to spatial mode transformation, resulting in intensity rotation [139–142]. However, by looking at the non-planar propagation of vector beams, we could study these rotations together. By doing so, we discovered that these geometric phases can be linked to a more general geometric phase, allowing us to introduce the concept of the *angular momentum redirection phase*.

Here, I will discuss the concept of geometric phase, giving some common examples found in optics, before outlining the experiment, results and theoretical explanations of our non-planar propagation investigations.

The work outlined in this chapter was completed in collaboration with my primary and secondary supervisors, Sonja Franke-Arnold and Robert Bennett, and Claire M. Cisowski. My specific contributions to the work included setting up the

beam generation system (Figure 2.12), building and aligning the non-planar system, acquiring all the experimental data and performing the data analysis. I also performed some of the simulations, including the simulated results shown in the final section of this chapter. R. Bennett and C. M. Cisowski worked on the theoretical framework, and R. Bennett also assisted with some of the simulations. S. Franke-Arnold led the project and provided experimental guidance.

3.2 Geometric phase

A propagating electromagnetic field can be characterised by its amplitude and phase. For a light beam travelling in free space, the phase advances by 2π in each cycle of the oscillation, meaning that phase information can tell us what part of the oscillation cycle the electric field is in. As the phase of a light beam varies as a function of time, it is often referred to as the *dynamic phase*, and it is directly proportional to the optical path length.

However, additional finite phase differences can also be acquired due to transformations in either the state or parameter space. In 1984, Berry reported on the phase that a physical system can acquire if it travels a path in state space, and is directly related to the geometry of the path formed [143]. It is for this reason, that these phase shifts are termed *geometric phases*.

The concept of geometric phase was first discovered in tandem, both in the field of optics (by Pancharatnam in 1956) [144] and in molecular electronic degeneracies (by Longuet-Higgins et al in 1958) [145], however, it was Sir Michael Berry who generalised these ideas in his landmark paper [143], and in the decades that have followed, the discovery has impacted many areas of both quantum and classical physics, such as plasma [146,147], nuclear physics [148], condensed matter [149,150], photonic crystals [151,152] and optics [28,153–155]. In optics alone, there are many examples of geometric phases that occur due to the geometry of the system in which a beam propagates. These include, the well-known Gouy phase [156], the Pancharatnam-Berry phase, where an additional phase results from a cycling of polarisation states [144,157], the spin-redirection phase[1], where the phase shift arises from variations of the wave vector direction [158,159] and phase shifts can also occur from the cyclic manipulation of squeezed light [160,161]. Some of these phenomena will be detailed in the sections below.

Initially, the idea of geometric phases seemed only to be relevant from a theoretical perspective [28], but they have been observed in many different areas, leading to various applications [162], such as within molecular and condensed matter physics [163] and for quantum computations [164,165]. Although, it is perhaps in optics that the concept has had the greatest impact, with applications in wave-

[1]This geometric phase was named the spin-redirection phase for the first time by Jiao et al. in [136], although it had been discovered by others before.

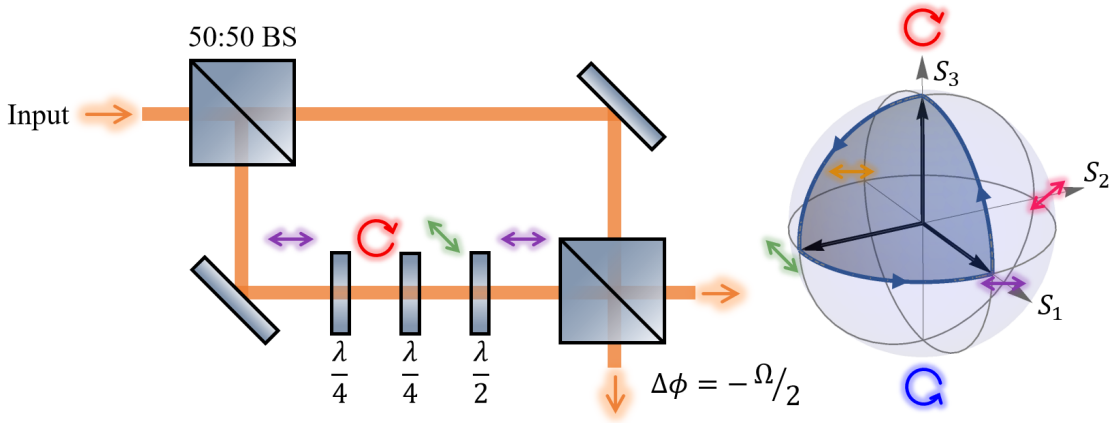

Figure 3.1: Simple example of an experimental setup for measuring the PBP. Left: Mach-Zehnder interferometer with arms of equal optical path length. In one arm the beam passes through two QWPs (fast axes at $3\pi/4$ and $\pi/2$) and a HWP (at $\pi/8$), resulting in polarisation state changes, as depicted, and the acquisition of a phase difference ($\Delta\phi$) between the arms of the interferometer. Right: Path of the polarisations traced on the Poincaré sphere, giving geometric interpretation. The solid angle Ω is shown as a shaded area.

front shaping arising [166, 167]. Examples include structured metasurfaces [168], Q-plates [105, 106], beam shaping elements based on liquid crystals [169–171], frequency shifters [172, 173], phase compensators in interferometric sensors [174], and the birefringent materials used to modulate polarisation [167, 175].

3.2.1 Pancharatnam-Berry phase

In 1956, the Pancharatnam phase was introduced by Shivaramakrishnan Pancharatnam. He discovered this geometric phase (although not called this at the time) while investigating the interference of beams with different polarisations, where he found that a beam would acquire a phase dependent on the path travelled by the polarisation on the Poincaré sphere [144]. After Berry introduced the concept of geometric phase, providing a quantum interpretation, Ramaseshan and Nityananda in 1986 [176] pointed out that the Pancharatnam phase is an early example of Berry phase, and as such, it is now often referred to as the Pancharatnam-Berry phase (PBP hereafter).

It is straightforward to realise the PBP experimentally, as it is simply based on polarisation transformations. Consider the setup shown in Figure 3.1. Here, an initially horizontally polarised beam is used as the input to a Mach-Zehnder interferometer with arms of equal optical path length. Normally, if the interferometer is balanced, then there is no additional phase acquired by one of the beams ($\Delta\phi = 0$), leading to only one output. However, in one of the interferometer arms in Fig-

ure 3.1, we have introduced a series of state transformations using waveplates. The beam passes through two QWPs and a HWP, converting the polarisation first to circular polarisation, then to anti-diagonal polarisation and finally returning back to horizontally polarised light.

As mentioned above in 3.2, the geometric phase of a system depends on the path travelled in state space. As we are considering polarisation states here, we employ the Poincaré sphere as the state space, which allows for a comprehensive visualisation of the phenomenon. The evolution of the polarisation from $|\hat{h}\rangle$ to $|\hat{r}\rangle$ to $|\hat{a}\rangle$ and then back to $|\hat{h}\rangle$ can be traced out on the Poincaré sphere as shown in Figure 3.1, where it is clear that the path forms a closed curve. Pancharatmun [144], Berry [157] and others [136, 177] have all shown that the geometric phase acquired by a beam after travelling a closed cycle on the Poincaré sphere is given by,

$$\Delta\phi = -\frac{\Omega_P}{2}. \tag{3.1}$$

where Ω_P is the solid angle subtended by the closed path on the sphere (depicted by the shaded area in Figure 3.1).

Pancharatnam first observed this phase when he was studying interference in bi-axial crystal plates [144], but it wasn't until 1988 that it was first observed in both a Mach-Zehnder [177] and Michelson interferometer [178]. Since then, it has been measured in many different experimental setups, including a non-planar interferometer [136], using Young' double slit interference [179] and using non-interferometric methods [180].

For the example given in Figure 3.1, waveplates were employed to impose a geometric phase, however, geometric phases can be observed in birefringent materials by themselves. As an example, we can consider a HWP (which is simply a slice of birefringent material, cut to a thickness such that it induces a relative phase shift of half a wavelength, or π, between the two polarisation components aligned with the fast and slow axes of the wave plate, respectively). For a linearly polarised beam incident on a HWP, the resulting beam is also linearly polarised, but rotated by 2θ, where θ is the angle between the HWPs fast (or slow) axis and the angle of the input polarisation. For an circularly polarised input beam, the handedness of the polarisation flips after passing through the HWP, independent of the orientation of the HWPs fast axis. However, the beam still acquires a global phase of 2θ. This is the same as the geometric phase that was noted by Pancharatnum when a polarisation state evolves from right-handed circular to left-handed circular or vice-versa [154].

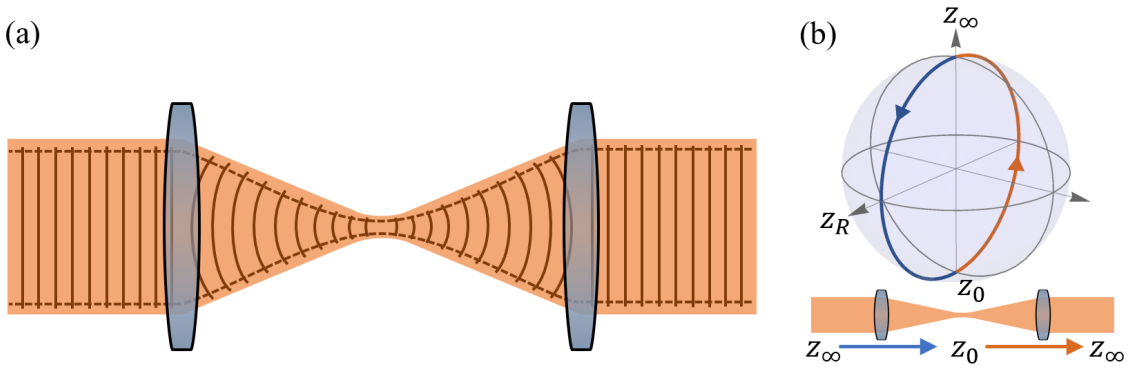

Figure 3.2: Focusing of a Gaussian beam between two lenses of equal focal length f. A geometric phase, the Gouy phase, is acquired upon focusing when the complex radius of curvature is cycled in its parameter space. (a) Representation of the radius of curvature which is weak both very close to and far from the focus. (b) Path on the focusing sphere for a 4f imaging system.

3.2.2 Gouy phase

The Gouy phase is a well-known $n\pi/2$ phase shift[2] that is gradually acquired by a converging beam as is passes through a focus propagating from $-\infty$ to $+\infty$ (where $n = 1$ for cylindrical waves and 2 for spherical waves) [53, 181]. Although it has been over a century since Gouy made his discovery in 1890 [182], it has still been a focus of work in recent years to provide a simpler and perhaps more satisfying physical interpretation to this phase anomaly [181]. It was Simon and Mukunda in 1993 [183] and Subbarao in 1995 [156] who were among the first to suggest that the Gouy phase shift is a manifestation of a general Berry phase.

As a Gaussian beam is focused, a Gouy phase shift is acquired and its spot size changes, as shown in Figure 3.2(a). We know that for the existence of an additional phase of a geometric nature, there has to be a cyclic evolution of the system in its parameter space. In the case of the Gouy phase, the parameter that is cycled is the complex wave-front radius of curvature, q. For a beam propagating in the z direction, $q(z) = z + iz_R$, however, it is often more useful to consider the reciprocal of this complex beam parameter, given as,

$$\frac{1}{q(z)} = \frac{1}{R(z)} - i\frac{\lambda}{\pi w^2(z)}, \tag{3.2}$$

which depends on the radius of curvature ($R(z)$) and beam size ($w(z)$), allowing for a simplified version of the equation for the Gaussian beam amplitude (previously

[2]Note that this phase shift is only for the fundamental Gaussian beam. The Gouy phase is increased by an additional factor of $N + 1$, for higher order modes with mode number N, as described in § 1.4.3.

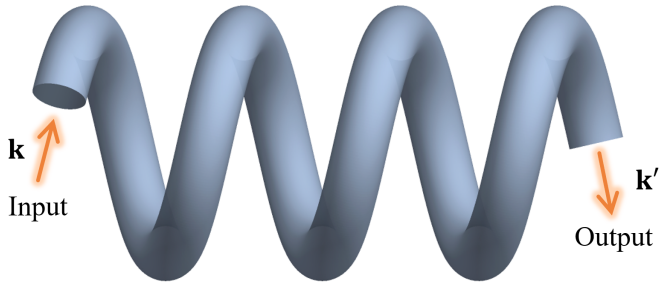

Figure 3.3: Propagation through a helically-wound optical fiber. A spin-redirection phase can arise from the cycling in the direction of the wave-vector in its parameter space.

given as Eq. 1.40 in § 1.4) to be written as,

$$E(r,z) = \frac{1}{q(z)} \exp\left(-ik\frac{r^2}{2q(z)}\right). \tag{3.3}$$

To visualise the state space, the "focusing sphere" of unit diameter is employed. This is just the Riemannian sphere, which is a stereographic projection of the extended complex plane, and hence can also be considered to be a representation of the complex q-plane. Considering the stereographic projection, the south pole of the focusing sphere corresponds to the origin of the q-plane. This point also corresponds to the focusing of a point, whereas the north pole corresponds to the complete defocusing of a Gaussian beam and represents the infinity point of the q-plane. The points that lie on the unit circle of the q-plane will lie on the equator of the focusing sphere. The equator then represents plane wave-fronts with constant beam width [156]. A representation of this is shown in Figure 3.2(b) for a 4f imaging system. It can clearly be seen that the path traced on the focusing sphere subtends a solid angle of $\Omega = -2\pi$, thus making the Berry phase factor $\Delta\phi = -\pi$ (cf. Eq. 3.1), which is equal to the Gouy phase [156, 184].

3.2.3 Spin-redirection phase

As mentioned above, the spin-redirection phase is a phase shift of geometric origin that results from the cycling of the wave vector direction, $\mathbf{k}$, of a light beam. It was first observed in 1938 by Rytov [185] in inhomogeneous media and again shortly afterwards by Vladimirskiy [137]. A few decades later, the effect was witnessed in optical fibres [158, 186]. A schematic is given in Figure 3.3 demonstrating how the wave vector direction can be changed using a helically-wound fiber.

In both of these cases, we have examples of *adiabatic* transformations, i.e. a gradually changing system. For example, if we had a photon with its spin initially aligned with its wave vector, then, the spin will remain aligned with the wave vector

at all times as its direction is cycled. The geometric phase acquired in this instance, is given by $-\sigma\Omega_{\mathbf{k}}$, where $\Omega_{\mathbf{k}}$ is the solid angle subtended by the path traced out on the sphere of wave vector directions, or the $\mathbf{k}$-sphere, and σ is the photons helicity which represents the projection of the photon's spin onto the wave vector. The helicity can either be 1 or -1 for left- or right-handed circular polarisation, respectively [140].

However, later work [136, 187, 188] has also shown that a geometric phase can be acquired for *nonadiabatic* changes in a wave vector's direction (i.e. discontinuous changes). This means that this additional phase shift can be observed in discrete optical systems containing no waveguides, for example using mirror reflections. In this case, we have a nonadiabatic transformation because a photon's helicity will flip upon reflection from a mirror (see § 1.6). To account for this, a slightly different parameter space was introduced, focusing on the evolution of the direction of the spin vector ($\mathbf{S}$) [187, 188]. Due to this, this geometric phase is now termed the spin-redirection phase and is given by,

$$\Delta\phi = -\sigma\Omega_{\mathbf{S}}, \tag{3.4}$$

where $\Omega_{\mathbf{S}}$ is the solid angle enclosed on the spin-redirection sphere - the sphere representing all the possible directions of the spin vector in real space [136, 166].

For both adiabatic and non-adiabatic transformations, we have the same effect for cyclic re-directions of $\mathbf{k}$ (or $\mathbf{S}$), after its original orientation is recovered, that is, the initial polarisation state will be rotated. This can be related to the concept of circular birefringence, as the right- and left-circular polarisation components acquire equal and opposite geometric phase, leading Berry to refer to this effect as *geometric* circular birefringence [189, 190]. This will be discussed further in § 3.5.

Here, and in § 3.2.1, I have outlined the concepts of the PBP and the spin-redirection phase separately. However, Jiao et al. looked at the combined effects of both of these using a nonplanar Mach-Zehnder interferometer, and in the process, discovered that the two geometric phases are additive [136]. The experiment outlined in the remainder of this chapter took inspiration from Jiao et al.'s work but we also consider the geometric phases linked to mode transformations allowing us to look in detail into the geometric phases acquired by beams with spatially varying polarisation.

3.3 Experimental setup for non-planar beam propagation

The optical setup used to investigate intensity and polarisation rotation, and as a result, the acquired geometric phase, is shown in Figure 3.4(a). This system was inspired by earlier work [136, 188], and simply consists of four mirror reflections, arranged such that the initial and final wave vectors, $\mathbf{k}_0$ and $\mathbf{k}_4$ point in the same direction. This provides an axis around which to define rotations. Mirrors M_2,

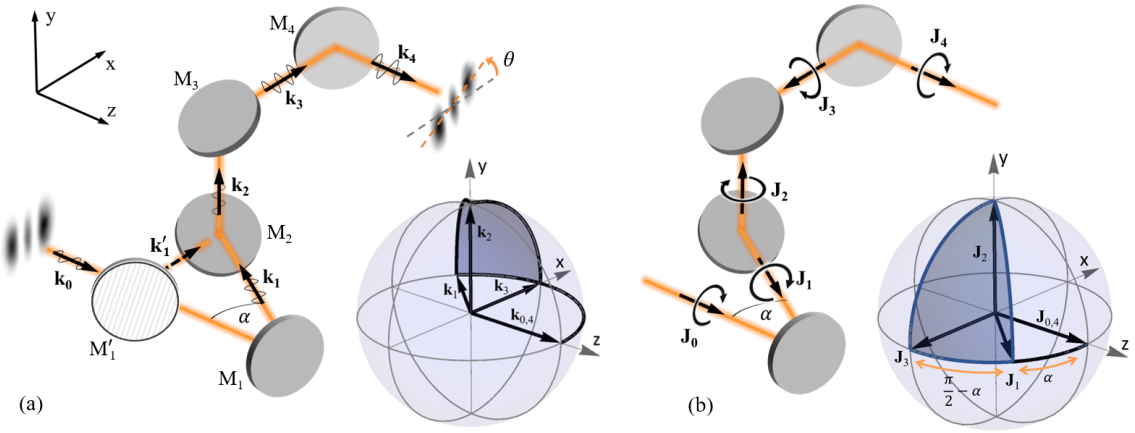

Figure 3.4: Schematic of non-planar trajectory. (a) Optical setup comprising of a series of mirror reflections to propagate a beam along a non-planar path, where $\mathbf{k}_n$ label the wave vectors after reflection from mirror n ($\mathrm{M_n}$). Experimentally, we can adjust the non-planarity of the beam path, parameterised by α, by moving the position of $\mathrm{M_1}$ along the z-axis, as indicated by $\mathrm{M'_1}$. The corresponding $\mathbf{k}$-sphere shows how the $\mathbf{k}$ vectors change along the beam path. (b) Shows the same optical setup as in (a) but interpreted in terms of the total angular momentum, $\mathbf{J} = \mathbf{L} + \mathbf{S}$, for the case where the initial angular momentum vector, $\mathbf{J}_0$, is aligned with $\mathbf{k}_0$. Shown as inset is the angular momentum redirection sphere, where the rotation θ is equal to the solid angle enclosed by the path. Figure adapted from [135].

$\mathrm{M_3}$ and $\mathrm{M_4}$ form a (vertical) plane, and we choose to parameterise the degree of non-planarity of the system by the angle,

$$\theta_{\mathrm{NP}} = \frac{\pi}{2} - \alpha, \tag{3.5}$$

where, α is the angle between $\mathbf{k}_0$ and $\mathbf{k}_1$, as indicated in Figure 3.4, and corresponds to twice the angle of incidence on $\mathrm{M_1}$. Experimentally, α can be changed by moving $\mathrm{M_1}$ along the z-axis. An example of another possible position of the first mirror, and resulting beam path, is indicated by $\mathrm{M'_1}$ in Figure 3.4.

As discussed previously in § 2.2.2, mirror coatings can cause unwanted optical activity, leading to unwanted polarisation changes. To prevent this, we ensure to use gold mirrors, which for the incidence angles used in the setup, do not alter the polarisation, meaning that any polarisation change occurs directly from the system geometry.

This setup is used to look at the non-planar propagation of homogeneously polarised beams with various intensity profiles, as well as vector beams, with more complex spatially varying polarisation structures. All of these beams are generated using an optical system incorporating a digital micromirror device (DMD), as shown in Figure 2.12, and detailed fully in § 2.6.

The polarisation profiles of the beams can be measured using Stokes tomography, which allows polarisation rotation to be determined (as detailed previously in § 2.3). For image rotation, we can simply analyse the intensity measurements obtained from the CMOS camera. The coordinate system indicated in Figure 3.4 is used throughout. Therefore, when defining rotations, a positive rotation angle θ corresponds to a clockwise rotation when looking in the direction of beam propagation (+ve z-direction). The rotation then appears anticlockwise when observed on the camera, looking against the propagation direction.

3.4 Image rotation

Beams with structured intensity profiles were allowed to propagate along the non-planar trajectory shown above. By choosing non-rotationally symmetric patterns, any rotation can be easily observed. Examples of Hermite-Gaussian (HG) modes before and after the setup are shown in Figure 3.5. Figure 3.5(a) shows a HG_{30} mode for multiple non-planar configurations, as indicated, and (b) shows various HG modes for a fixed α. It was found that the amount of rotation did not depend on the spatial mode, and the angle of rotation θ would always be equal to $\pi/2 - \alpha$. This is the same as the non-planarity angle of our system, θ_{NP}, described in Eq. 3.5.

3.4.1 Describing image rotation using geometric phase

By considering the propagation of an intensity profile along the non-planar path, it is straightforward to see how this rotation occurs due to the direct mirror reflections. However, it is also possible to interpret this rotation in terms of geometric phase.

Consider an arbitrary mode, $\psi(r, \phi)$, where r and ϕ are cylindrical coordinates. A rotation of this will simply give the resulting mode, $\psi'(r, \phi) = \psi(r, \phi + \theta)$, for any angle θ. If we want to understand this in terms of geometric phase, it becomes convenient to rewrite the expression in terms of Laguerre-Gaussian (LG) beam modes. As LG modes form a complete basis, it is possible to write any intensity profile in terms of them, doing this for the original mode we obtain,

$$\psi(r, \phi) = \sum_{p,\ell} \langle \mathrm{LG}_p^\ell | \psi(r, \phi) \rangle \, \mathrm{LG}_p^\ell, \tag{3.6}$$

where $\langle a|b\rangle$ denotes the inner product which can be evaluated from the mode overlap and $\mathrm{LG}_p^\ell = u_p^\ell(r) \exp(i\ell\phi)$, for radial and azimuthal indices p and ℓ. Similarly, we can write the rotated mode as,

$$\psi'(r, \phi + \theta) = \sum_{p,\ell} \langle \mathrm{LG}_p^\ell | \psi(r, \phi + \theta) \rangle \, \mathrm{LG}_p^\ell. \tag{3.7}$$

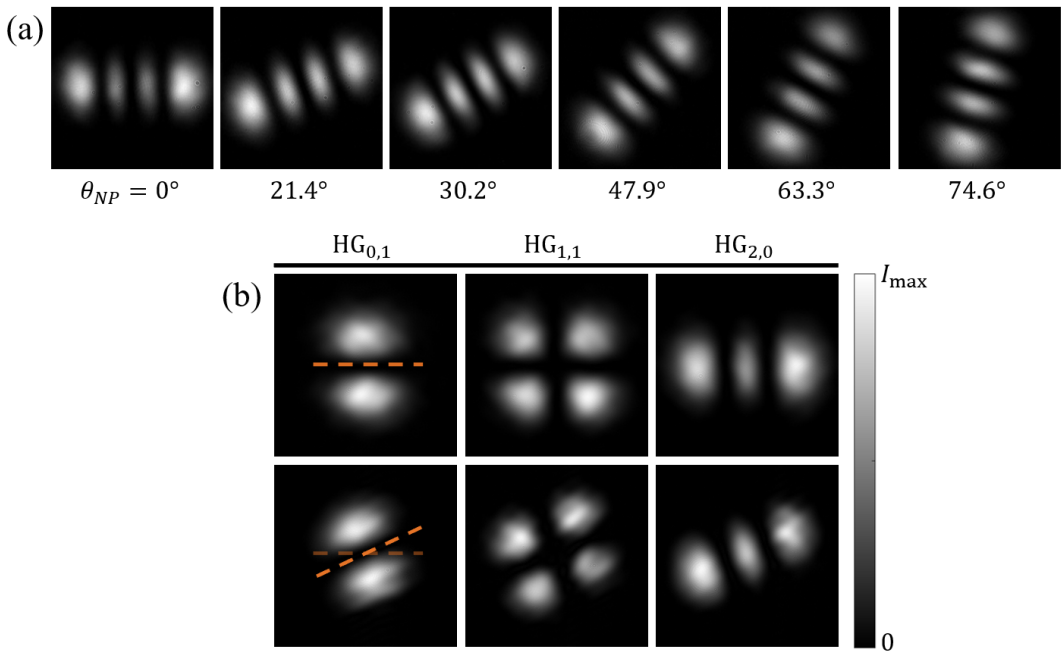

Figure 3.5: Sample of experimental intensity measurements of HG modes showing image rotation. (a) Rotation of a HG_{30} mode for different non-planarity angles, as indicated. The original un-rotated mode can be seen on the left for $\theta_{NP} = 0°$. (b) Rotation of a selection of HG modes for a fixed non-planarity angle $\theta_{NP} = (21.4 \pm 0.5)°$, indicated by dashed line. The top row shows the original beam profiles and the bottom row shows rotated modes after propagation through the system. (b) adapted from [135].

We can directly evaluate the inner product as,

$$\begin{aligned}\langle \mathrm{LG}_p^\ell|\psi(r,\phi+\theta)\rangle &= \langle u_p^\ell(r)\mathrm{e}^{i\ell\phi}|\psi(r,\phi+\theta)\rangle \\ &= \langle u_p^\ell(r)\mathrm{e}^{i\ell(\phi-\theta)}|\psi(r,\phi)\rangle \\ &= \mathrm{e}^{-i\ell\theta}\,\langle \mathrm{LG}_p^\ell|\psi(r,\phi)\rangle\,,\end{aligned} \tag{3.8}$$

where the second line results from relabelling the angular variables, allowing us to write Eq. 3.7 as,

$$\psi'(r,\phi) = \sum_{p,\ell} \mathrm{e}^{-i\ell\theta}\,\langle \mathrm{LG}_p^\ell|\psi(r,\phi)\rangle\,\mathrm{LG}_p^\ell. \tag{3.9}$$

By comparing this to Eq. 3.6, we can see that a rotation by an angle θ is associated with a phase $-\ell\theta$. Namely, a spatial mode with a given orbital angular momentum (OAM) acquires a phase proportional to its topological charge, ℓ. For this reason, we refer to it as the *orbital*-redirection phase.

From this, it can perhaps be seen that choosing to rewrite the arbitrary spatial mode, ψ, in terms of LG modes was a convenient choice, as we end up with a somewhat simple expression where we can identify the geometric phase acquired by the mode. This was in fact a conscious choice, as LG modes are eigenmodes of the angular momentum operator ($-i\hbar\partial_\theta$), which is the generator of rotations, hence, making the modes themselves convenient for describing rotations.

Redirection phases occur from a cycling in the direction of a light beam. They depend on the geometry of the path formed on the relevant sphere of angular momentum directions, consequently, these phase shifts are said to be geometric. For a paraxial propagating light beam, its spin ($\mathbf{S}$) and orbital angular momentum ($\mathbf{L}$) vectors and hence the total angular momentum, $\mathbf{J} = \mathbf{L}+\mathbf{S}$ are aligned with the wave vectors, $\mathbf{k}$. Upon reflection from a mirror, a photons helicity flips, and the direction of OAM reverses. Hence, the component of $\mathbf{J}$ perpendicular to the mirror does not change orientation, as indicated in Figure 3.4(b). Considering this, the $\mathbf{k}$-redirection sphere (as described in § 3.2.3), shown in Figure 3.4(a) can be translated into an angular momentum redirection sphere, as shown in Figure 3.4(b). The solid angle, Ω, traced out by $\mathbf{J}$ on the angular momentum redirection sphere, and indicated by the blue curve, is equal to $\pi/2-\alpha$. This is equivalent to the rotation angles, θ, seen here.

3.4.2 Rotation of Hermite-Gaussian modes

For simple illustration of the orbital-redirection phase we can consider the rotation of HG modes. These modes, defined by the positive integers n and m ($\mathrm{HG}_{n,m}$) and LG modes can be characterised by a mode number, $N = n+m = 2p+|\ell|$.

Let a HG mode rotated by an angle θ be denoted as HG$'$. As described above, it is easy to interpret the rotation of an LG mode in terms of an acquired orbital-redirection phase, $-\ell\theta$, and as HG and LG modes both form their own complete

orthonormal basis, one can be written as a superposition of the other via [191],

$$\begin{aligned} |\mathrm{HG}_{n,m}\rangle &= \sum_{p,\ell} \langle \mathrm{LG}_p^\ell | \mathrm{HG}_{n,m}\rangle \, |\mathrm{LG}_p^\ell\rangle \\ |\mathrm{LG}_p^\ell\rangle &= \sum_{n,m} \langle \mathrm{HG}_{n,m} | \mathrm{LG}_p^\ell\rangle \, |\mathrm{HG}_{n,m}\rangle \,. \end{aligned} \tag{3.10}$$

By calculating the overlaps directly, the mode transformations can be described by mode conversion matrices, B. Generally, any transverse spatial mode of mode order N can be expressed as a superposition of $N+1$ modes from a different mode family with the same mode order, i.e. the relevant square matrix B will have dimensions of $N+1$.

Using this, the rotation of a HG mode can be described as a superposition of fundamental HG modes by first expressing it in terms of the LG basis, applying a rotation matrix, $R_{\mathrm{LG}}(\theta)$ then returning to the HG basis [191],

$$|\mathrm{HG}'\rangle = B_{\mathrm{HG}\leftarrow\mathrm{LG}} \cdot R_{\mathrm{LG}}(\theta) \cdot B_{\mathrm{LG}\leftarrow\mathrm{HG}} \, |\mathrm{HG}\rangle \,, \tag{3.11}$$

where, $R_{\mathrm{LG}}(\theta) = \mathrm{diag}(\mathrm{e}^{-i\ell_1\theta}, \mathrm{e}^{-i\ell_2\theta}, \ldots, \mathrm{e}^{-i\ell_{N+1}\theta})$. This rotation matrix results in the rotation of each LG component with topological charge ℓ by imparting an orbital-redirection phase of $-\ell\theta$.

As an example, we can consider the first order mode $\mathrm{HG}_{0,1}$ rotated by θ in the clockwise direction (as defined with beam propagation). An experimental measurement of this is shown in the first column of Figure 3.5(b). For first order modes, the explicit forms of the matrices describing the mode transformation are,

$$\mathrm{B}^{\mathrm{N=1}}_{\mathrm{HG}\leftarrow\mathrm{LG}} = \frac{1}{\sqrt{2}}\begin{pmatrix} 1 & 1 \\ i & -i \end{pmatrix}, \; \mathrm{R}^{\mathrm{N=1}}_{\mathrm{LG}}(\theta) = \begin{pmatrix} e^{-i\theta} & 0 \\ 0 & e^{+i\theta} \end{pmatrix}, \; \mathrm{B}^{\mathrm{N=1}}_{\mathrm{LG}\leftarrow\mathrm{HG}} = \frac{1}{\sqrt{2}}\begin{pmatrix} 1 & -i \\ 1 & i \end{pmatrix}, \tag{3.12}$$

allowing the rotated mode to be expressed as,

$$\begin{aligned} \mathrm{HG}'_{0,1} &= \frac{i}{\sqrt{2}}(\mathrm{LG}_0^{-1}\mathrm{e}^{i\theta} - \mathrm{LG}_0^{+1}\mathrm{e}^{-i\theta}) \\ &= \cos\theta \mathrm{HG}_{0,1} - \sin\theta \mathrm{HG}_{1,0}, \end{aligned} \tag{3.13}$$

in the LG basis and HG basis, respectively[3].

Similarly, for second order modes ($N = 2$), the mode transformation matrices

[3]The expression given here in Eq. 3.13 is different to that given in [135], where a typo has been corrected.

are,

$$\mathrm{B}^{\mathrm{N=2}}_{\mathrm{HG}\leftarrow\mathrm{LG}} = \begin{pmatrix} \frac{1}{2} & -\frac{1}{\sqrt{2}} & \frac{1}{2} \\ \frac{i}{\sqrt{2}} & 0 & -\frac{i}{\sqrt{2}} \\ -\frac{1}{2} & -\frac{1}{\sqrt{2}} & -\frac{1}{2} \end{pmatrix}, \; \mathrm{R}^{\mathrm{N=2}}_{\mathrm{LG}}(\theta) = \begin{pmatrix} e^{-i2\theta} & 0 & 0 \\ 0 & 1 & 0 \\ 0 & 0 & e^{+i2\theta} \end{pmatrix}, \tag{3.14}$$

$$\mathrm{B}^{\mathrm{N=2}}_{\mathrm{LG}\leftarrow\mathrm{HG}} = \begin{pmatrix} \frac{1}{2} & -\frac{i}{\sqrt{2}} & -\frac{1}{2} \\ -\frac{1}{\sqrt{2}} & 0 & -\frac{1}{\sqrt{2}} \\ \frac{1}{2} & \frac{i}{\sqrt{2}} & -\frac{1}{2} \end{pmatrix}.$$

This allows us to write an expression for a rotated $\mathrm{HG}_{2,0}$ mode, as shown in the last column of figure 3.5(b),

$$\begin{aligned} \mathrm{HG}'_{2,0} &= \frac{1}{2}(\mathrm{LG}_0^{+2}e^{-i2\theta} - \sqrt{2}\mathrm{LG}_1^0 + \mathrm{LG}_0^{-2}e^{+i2\theta}) \\ &= \cos^2(\theta)\mathrm{HG}_{2,0} + \frac{\sin(2\theta)}{\sqrt{2}}\mathrm{HG}_{1,1} + \sin^2(\theta)\mathrm{HG}_{0,2}. \end{aligned} \tag{3.15}$$

3.4.3 Experimental confirmation of image rotation

Experimentally, we confirm the relationship between the non-planarity of the system and image rotation by setting α to various angles between 0° and 70° and identifying the rotation of HG modes. For each angle, 14 separate $\mathrm{HG}_{n,m}$ modes, with mode numbers $N = n + m \leq 4$ were used, with images recorded before and after propagation through the system. The camera images were low-pass Fourier filtered to remove artefacts due to diffraction and then converted to polar plots. The rotation of each mode can then be easily realised from the angular offset between the input and output beam profiles. A schematic displaying an example of the analysis procedure for a $\mathrm{HG}_{1,0}$ mode is shown in Figure 3.6. From this, it was seen that the rotation did not depend on the input beam mode, as expected. Due to this, the rotation angle θ observed for each setup angle α could be determined by averaging over the rotations found for each of the HG modes, and an error found from the standard deviation. By plotting the measured θ for each α, shown as the blue data points in Figure 3.7, the rotation relation, $\theta = \theta_{\mathrm{NP}} = \pi/2 - \alpha$ could be confirmed, and hence, that the image rotation is directly related to the degree of non-planarity of the beam trajectory.

3.5 Polarisation rotation

In this section, I will now consider polarisation rotation after non-planar propagation and link this effect to geometric phases.

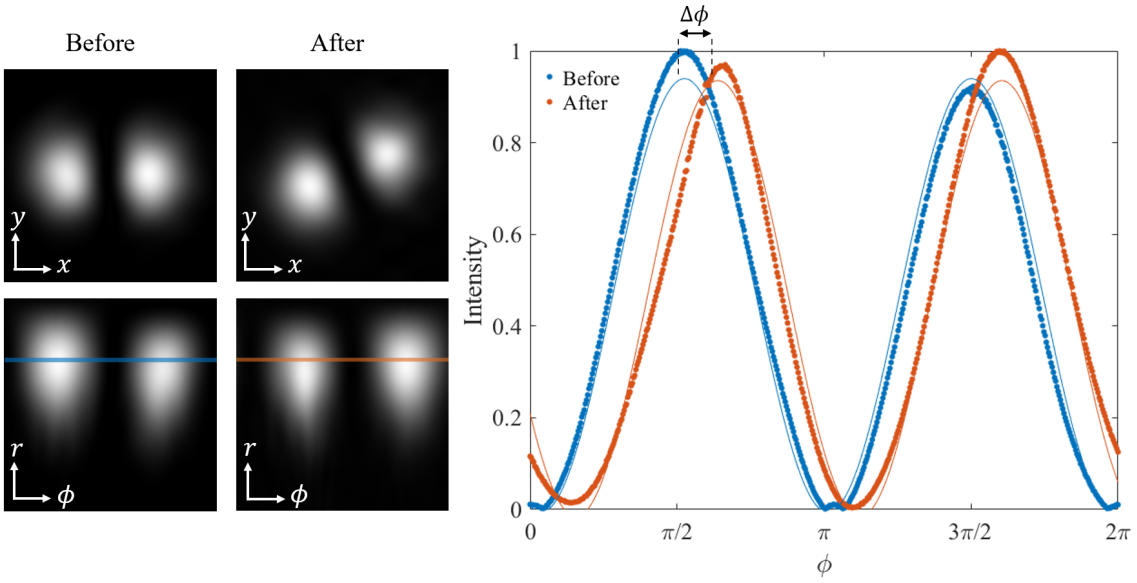

Figure 3.6: Example of intensity rotation analysis for a $HG_{1,0}$ mode. Left: Measured intensity before and after non-planar propagation in both Cartesian (x, y) and polar (r, ϕ) co-ordinates. Right: Plot of normalised intensity against polar angle for the beam before (blue) and after (orange) rotation. The intensity is taken as an average over 10 rows either side of the location of maximum intensity, as indicated by the lines on the polar intensity plots. The rotation of the intensity angle can be found from the angular offset between the two profiles ($\theta = \Delta\phi$).

Gaussian beams that were initially horizontally polarised were used as the inputs to the system, again, for various non-planarity angles of $\theta_{NP} = \pi/2 - \alpha$. Examples of the resulting rotated polarisation profiles are given in Figure 3.8(a), where it can be seen that the polarisation remains uniform across the beam profile. Additionally, an initially horizontally polarised $HG_{1,1}$ mode is given in Figure 3.8(b), showing that polarisation rotation is independent of the spatial mode and that polarisation and intensity rotate by the same angle, as expected.

To determine polarisation rotation, spatially resolved Stokes measurements are performed on the beams before and after non-planar propagation. This was achieved by implementing the rotating waveplate setup previously shown in Figure 2.4 and discussed in § 2.3. As we can assume that the polarisation remains uniform over the beam after propagation through the system, we average the measured polarisation over the entire Gaussian beam profile. The rotation θ is then found from the orientation angle[4] of the polarisation and the error in θ given by the standard deviation.

[4]Here, the polarisation orientation angle is the same as discussed in § 1.3, denoted by ψ, and defined by Eq. 1.35.

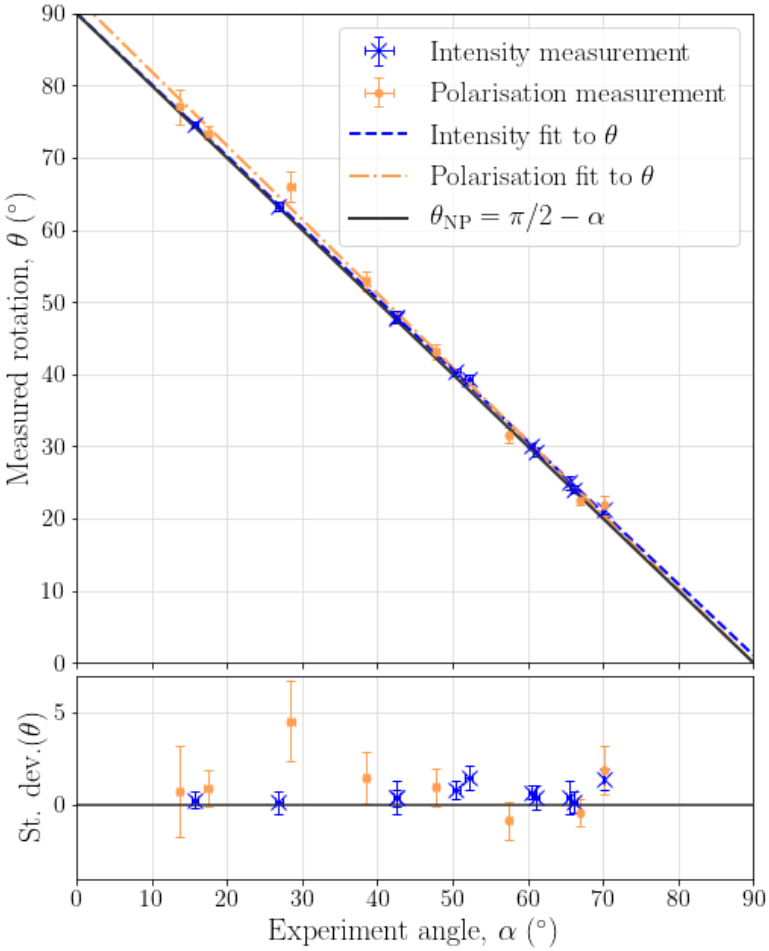

Figure 3.7: Image and polarisation rotation for non-planar trajectories. Experimental measurements of intensity (blue) and polarisation (orange) rotation and the theoretical prediction (black) of the relationship between the non-planarity of the system set by α and the rotation angle θ. The lower plot shows the difference between the measured θ and the theoretically expected θ_{NP}. The error in α is estimated to be smaller than 0.5°. Figure adapted from [135].

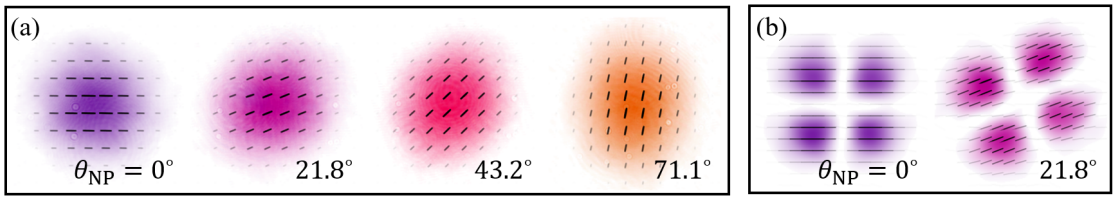

Figure 3.8: Polarisation rotation. (a) Experimental measurements of the rotation of an initially horizontally polarised Gaussian beam (left) for different θ_{NP}. (b) Measured polarisation of an initially horizontally polarised $HG_{1,1}$ mode before (left) and after (right) non-planar propagation.

The orange data points in figure 3.7 show measured α against measured polarisation rotation, θ. This confirms that polarisation rotation is equal to the non-planarity angle, given by the relation $\theta = \theta_{NP} = \pi/2 - \alpha$, and also demonstrates that polarisation and image rotation is the same.

3.5.1 Three-dimensional polarisation ray tracing approach

One way to understand the origin of polarisation rotation is to first consider the propagation of light through the non-planar trajectory in terms of Jones vectors [46], which allows the action of each mirror on the incident polarisation vector to be described by a Jones matrix. The advantage of using Jones matrix formalism is that a single matrix describing the overall effect of an optical system on an input polarisation state can simply be found from multiplication of the Jones matrix of each optical component.

As we are considering non-planar propagation, we have a 3D geometry and therefore, write the electric field in the form $\mathbf{E} = E_h\mathbf{e}_h + E_v\mathbf{e}_v + E_z\mathbf{e}_z$, where $\mathbf{e}_h$, $\mathbf{e}_v$ and $\mathbf{e}_z$ are unit vectors in the horizontal, vertical and propagation direction. To begin to describe the effect of each mirror, we need three orthogonal vectors: the incident wave vector, $\mathbf{k}$, and two orthogonal polarisation components, one in the plane of the mirror, $\mathbf{p}$, and one perpendicular to it, $\mathbf{s}$. However, the Jones matrix of an optical element acts on the local Jones vectors. As we are considering an out of plane path, the direction of the $\mathbf{p}$ and $\mathbf{s}$ vectors change at each mirror. Therefore, for each mirror, we have to change from a global to a local coordinate system, apply the action of the Jones matrix, and then transform back to the global coordinates.

Here, I will apply this three-dimensional polarisation ray tracing approach, as also discussed in [192], to obtain a matrix describing the effect of our non-planar system.

Let the action of an arbitrary optical element q on a polarisation vector $\mathbf{e}_q$, be written as,

$$\mathbf{e}_q = P_q \cdot \mathbf{e}_{q-1}, \tag{3.16}$$

where P_q is a 3×3 matrix to be found, which describes the action of element q. This equation is written using a *global* coordinate system, but can similarly be written using a *local* coordinate system, leading to an equivalent equation, namely,

$$w_q = J_q \cdot w_{q-1}. \tag{3.17}$$

As P_q is a 3×3 matrix, it has 9 elements, and hence we require a set of 9 linear equations to uniquely define it. For this, we can start from the fact that any polarisation state can be written in terms of two orthogonal basis states. Let's call these a and b. Therefore, Eq. 3.16 can be written as a pair of statements, each one describing the change to one of the orthogonal polarisation components,

$$\mathbf{e}'_a = P_q \cdot \mathbf{e}_a, \quad \mathbf{e}'_b = P_q \cdot \mathbf{e}_b, \tag{3.18}$$

which gives us a total of 6 equations.

To get the last 3 equations required to define P_q, we use the matrix form of the law of reflection,

$$\mathbf{k}_q = P_q \cdot \mathbf{k}_{q-1}, \tag{3.19}$$

written in global coordinates, which simply describes the change in direction of the wave vector at each mirror interface. With Eqs. 3.18 and 3.19 together, we now have our set of 9 linear equations with 9 unknowns, which can be solved to find the elements of P_q.

As mentioned above, a Jones matrix describing an optical element acts on the local Jones vectors, requiring transformations between the global and local coordinate systems in order to apply the Jones matrix. This process should all be contained within the matrix P_q, so we can write it in form,

$$P_q = O_{G\leftarrow L} \cdot J_q \cdot O_{L\leftarrow G}, \tag{3.20}$$

where $O_{L\leftarrow G}$ transforms from global to local coordinates, $O_{G\leftarrow L}$ from local to global and J_q is the Jones matrix describing q.

To find the matrix $O_{L\leftarrow G}$, we use the orthogonal coordinate system before the element, which is $\{\mathbf{s}_q, \mathbf{p}_q, \mathbf{k}_{q-1},\}$, and project it onto the local z direction for the element. This kind of basis transformation can be obtained using a matrix whose rows are the coordinate vectors of the new basis vectors (local, $\{\mathbf{s}_q, \mathbf{p}_q, \mathbf{k}_{q-1},\}$) in the old basis (global, $\{\mathbf{x}, \mathbf{y}, \mathbf{z},\}$). Therefore, $O_{L\leftarrow G}$ is of the form,

$$O_{L\leftarrow G} = \begin{pmatrix} s_{x,q} & s_{y,q} & s_{z,q-1} \\ p_{x,q} & p_{y,q} & p_{z,q-1} \\ k_{x,q} & k_{y,q} & k_{z,q-1} \end{pmatrix}. \tag{3.21}$$

Instead, to get the matrix describing the local to global coordinate transformation, we can take take the inverse of this, replacing the basis vectors with those after

the element, resulting in,

$$O^{-1}_{G\leftarrow L} = O^{T}_{G\leftarrow L} = \begin{pmatrix} s'_{x,q} & p'_{x,q} & k_{x,q} \\ s'_{y,q} & p'_{y,q} & k_{y,q} \\ s'_{z,q} & p'_{z,q} & k_{z,q} \end{pmatrix}. \tag{3.22}$$

Here, the relation $A^{-1} = A^T$ was used, where A is any orthogonal matrix. This could be done as we know that we must be dealing with orthogonal matrices as the basis vectors $\{\mathbf{s}_q, \mathbf{p}_q, \mathbf{k}_{q-1},\}$ are orthogonal to each other. This means that P_q can be determined if the Jones matrix of the optical element and the basis vectors $\{\mathbf{s}_q, \mathbf{p}_q, \mathbf{k}_{q-1},\}$ are known. However, the information needed can be simplified further, as it turns out that the $\mathbf{s}$ and $\mathbf{p}$ polarisation components can be written in terms of $\mathbf{k}_q$ and $\mathbf{k}_{q-1}$,

$$\begin{aligned} \mathbf{s}_q &= \frac{\mathbf{k}_{q-1} \times \mathbf{k}_q}{|\mathbf{k}_{q-1} \times \mathbf{k}_q|} & \mathbf{s}'_q &= \mathbf{s}_q \\ \mathbf{p}_q &= \mathbf{k}_{q-1} \times \mathbf{s}_q & \mathbf{p}'_q &= \mathbf{k}_q \times \mathbf{s}'_q. \end{aligned} \tag{3.23}$$

One advantage to this method of describing the action an optical element has on a polarisation state, is that the effect of Q optical elements acting sequentially on a beam can be combined into an overall matrix P, by multiplying the individual P_q matrices together in order,

$$P = P_Q \cdot P_{Q-1} \cdot \cdots \cdot P_q \cdot \cdots \cdot P_2 \cdot P_1. \tag{3.24}$$

All of this together means that to describe an entire system, all we need are the Jones matrices of each element and the $\mathbf{k}$ vectors after each optical component. In our case, $\mathbf{k}$ can be determined by the direction of each mirror.

For an ideal mirror, the 3D Jones matrix describing reflection is,

$$J_q = \begin{pmatrix} 1 & 0 & 0 \\ 0 & -1 & 0 \\ 0 & 0 & 0 \end{pmatrix}, \tag{3.25}$$

and our 3D geometry, as shown in Figure 3.4, comprises of 4 mirrors, and 5 $\mathbf{k}$ vectors given as,

$$\mathbf{k}_0 = \begin{pmatrix} 0 \\ 0 \\ 1 \end{pmatrix}, \ \mathbf{k}_1 = \begin{pmatrix} \sin\alpha \\ 0 \\ -\cos\alpha \end{pmatrix}, \ \mathbf{k}_2 = \begin{pmatrix} 0 \\ 1 \\ 0 \end{pmatrix}, \ \mathbf{k}_3 = \begin{pmatrix} 1 \\ 0 \\ 0 \end{pmatrix}, \ \mathbf{k}_4 = \begin{pmatrix} 0 \\ 0 \\ 1 \end{pmatrix} = \mathbf{k}_0, \tag{3.26}$$

where, α is the angle between the first and second $\mathbf{k}$ vectors ($\mathbf{k}_0$ and $\mathbf{k}_1$), and we have used the same coordinate system as indicated in Figure 3.4.

Using Eqs. 3.20 to 3.26, we can obtain P matrices for each element, and hence the combined P matrix,

$$P = P_4 \cdot P_3 \cdot P_2 \cdot P_1 \cdot = \begin{pmatrix} \sin\alpha & -\cos\alpha & 0 \\ \cos\alpha & \sin\alpha & 0 \\ 0 & 0 & 1 \end{pmatrix}. \tag{3.27}$$

Above, we defined $\theta = \frac{\pi}{2} - \alpha$, which described the non-planarity and rotation angle. Substituting this in Eq. 3.27, results in,

$$P = \begin{pmatrix} \cos\theta & -\sin\theta & 0 \\ \sin\theta & \cos\theta & 0 \\ 0 & 0 & 1 \end{pmatrix}. \tag{3.28}$$

This matrix is in the form of a rotation matrix, representing a rotation in the xy plane, about the z axis by an angle θ. From our coordinate system, we have defined the beam as travelling in the positive z direction, hence we will observe a clockwise direction when the rotation is viewed along the propagation axis of the beam. However, when viewed against the propagation direction the rotation will appear to be in the anticlockwise direction, as shown in Figure 3.8.

3.5.2 Interpreting polarisation rotation using geometric phase

Using the results of the previous section, we can now begin to interpret the polarisation rotation after non-planar propagation in terms of geometric phase. Any uniformly linearly polarised paraxial light beam, propagating in the z direction can be written in terms of its horizontal and vertical polarisation components as,

$$|\mathbf{E}\rangle = E_0(r,\phi)\left(\cos\theta_0\,|\hat{h}\rangle + \sin\theta_0\,|\hat{v}\rangle\right), \tag{3.29}$$

where $E_0(r,\phi)$ is the transverse spatial mode and $0 \leq \theta_0 \leq 2\pi$ is the angle of the linear polarisation to the horizontal. If the beam described by Eq. 3.29 is allowed to propagate along the non-planar trajectory, then an expression for the rotated polarisation can be obtained by applying the rotation matrix given in Eq. 3.28,

$$|\mathbf{E}'\rangle = E_0(r,\phi)\left(\cos(\theta_0+\theta)\,|\hat{h}\rangle + \sin(\theta_0+\theta)\,|\hat{v}\rangle\right). \tag{3.30}$$

However, as will be shown, it becomes simpler to consider this in terms of circular polarisation when looking at geometric phase. Converting to the circular polarisation basis using, $|\hat{r}\rangle = (|\hat{h}\rangle - \mathrm{i}\,|\hat{v}\rangle)/\sqrt{2}$ and $|\hat{l}\rangle = (|\hat{h}\rangle + \mathrm{i}\,|\hat{v}\rangle)/\sqrt{2}$ we have,

$$|\mathbf{E}\rangle = (E_0(r,\phi)/\sqrt{2})\left(\mathrm{e}^{\mathrm{i}\theta_0}\,|\hat{r}\rangle + \mathrm{e}^{-\mathrm{i}\theta_0}\,|\hat{l}\rangle\right), \tag{3.31}$$

$$|\mathbf{E}'\rangle = (E_0(r,\phi)/\sqrt{2})\left(\mathrm{e}^{\mathrm{i}(\theta_0+\theta)}\,|\hat{r}\rangle + \mathrm{e}^{-\mathrm{i}(\theta_0+\theta)}\,|\hat{l}\rangle\right), \tag{3.32}$$

for the initial and rotated fields, respectively. From this, it can be seen that for a rotation of θ, the right and left handed polarisation components, with a spin angular momentum of $\mp\hbar$ per photon, have acquired a phase factor of $\exp(\pm i\theta)$. Therefore, we can link polarisation rotation by an angle θ, to a spin-redirection phase of $-\sigma\theta$ to each circularly polarised mode with helicity σ. Furthermore, θ is equal to the solid angle enclosed by the path traced out by the spin vector on the spin redirection sphere, as shown in Figure 3.4(b). Naturally, this result also holds for initial beams with any arbitrary elliptical polarisation.

3.6 Rotation of vector beams

In sections 3.4 and 3.5 the rotation of intensity and homogeneous polarisation was discussed. In this section, we will look at these two effects simultaneously by considering the non-planar propagation of vector beams, with an inhomogeneous polarisation distribution.

A general beam with structured polarisation can be formed from the superpostion of two orthogonally polarised spatial modes. Here, to easily follow on from the discussion in § 3.5.2, we choose to express the vector beams using a right- and left-handed circular polarisation basis, $|\boldsymbol{\psi}\rangle = \psi_l(r,\phi)\,|\hat{l}\rangle + \psi_r(r,\phi)\,|\hat{r}\rangle$, and restrict ourselves, for simplicity, to LG spatial modes, such that we consider beams of the form,

$$|\boldsymbol{\psi}\rangle = \mathrm{LG}_{p_1}^{\ell_1}\,|\hat{l}\rangle + \mathrm{e}^{\mathrm{i}\varphi}\mathrm{LG}_{p2}^{\ell_2}\,|\hat{r}\rangle\,. \tag{3.33}$$

Above, in § 3.4 and § 3.5 it was shown that non-planar propagation results a mode with OAM $\ell\hbar$ acquiring an orbital redirection phase factor of $\exp(-i\ell\theta)$ and a mode with a spin of $\sigma\hbar$ along the propagation direction gaining a spin redirection phase of $\exp(-i\sigma\theta)$. To consider the effect of non-planar propagation of a general vector beam, we can apply the known acquired phases to Eq. 3.33, leading to the simultaneous rotation of the intensity pattern and polarisation by an angle θ,

$$|\boldsymbol{\psi'}\rangle = \mathrm{e}^{-\mathrm{i}(\ell_1+1)\theta}\mathrm{LG}_{p_1}^{\ell_1}\,|\hat{l}\rangle + \mathrm{e}^{\mathrm{i}\varphi}\mathrm{e}^{-\mathrm{i}(\ell_2-1)\theta}\mathrm{LG}_{p2}^{\ell_2}\,|\hat{r}\rangle\,. \tag{3.34}$$

Therefore, it can be seen that the total geometric phase acquired is proportional to the total angular momentum number, $j = \ell + \sigma$.

From further inspection of Eq. (3.34), we can see that if $j = \ell + \sigma = 0$, then after rotation, the original beam is recovered and the input and output beams will be indistinguishable. The helicity, σ, can only take values of ± 1, meaning that we obtain $j = 0$ only for LG modes $\ell_1 = -1$ and $\ell_2 = 1$. As these modes are unchanged after non-planar propagation through the system, they can be considered as eigenmodes of the system and therefore, conserved quantities. This is true for all values of $p_{1,2}$ and φ. For $p_{1,2} = 0$, we obtain beams with rotationally symmetric intensity and radial polarisation for $\varphi = 0$, azimuthal polarisation for $\varphi = \pi$ and rotationally symmetric polarisation with orientations in between radial and azimuthal for $0 < \varphi < \pi$.

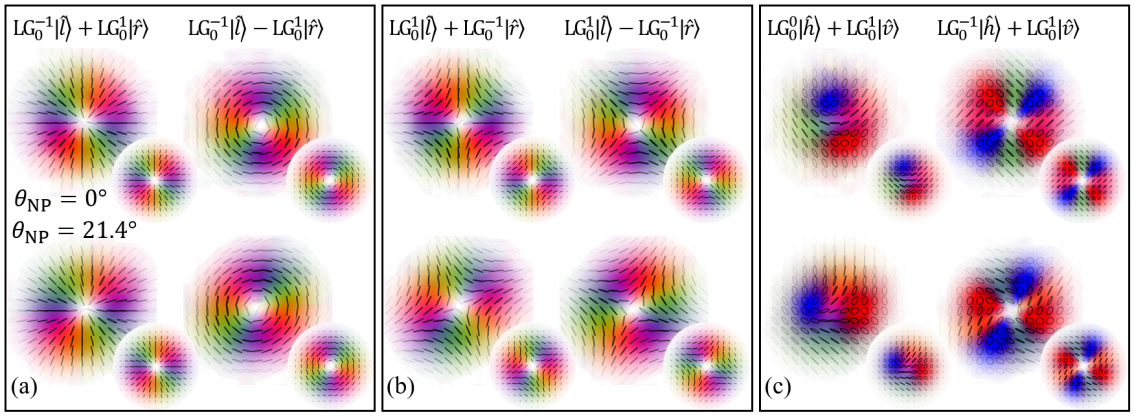

Figure 3.9: Vector beam rotation. Polarisation plots of experimentally measured vector beams before (top row) and after (bottom row) non-planar propagation through the system, for a fixed rotation angle of $\theta = (24.1 \pm 0.5)°$. Beams shown in (a), and (b) are of the form $\mathrm{LG}_0^{\pm 1}|\hat{l}\rangle + \mathrm{e}^{-\mathrm{i}\varphi}\mathrm{LG}_0^{\pm 1}|\hat{r}\rangle$ for $\varphi = (0, \pi)$. The first column in (c) is a Poincaré beam, containing all possible polarisations, and the second column shows a beam containing polarisations along a great circle on the Poincaré sphere. The corresponding theory plots are given as smaller inserts. Figure adapted from [135].

Examples of radially and azimuthally polarised beams are given in Figure 3.9(a), showing that they do appear unchanged. However, for all other values of j, we have a non-zero angular momentum redirection phase, resulting in a visible rotation of the beam. Some examples of the rotation of general vector beams with $j \neq 0$ are given in Figure 3.9(b) and (c). In Figure 3.10, I provide examples of the recorded camera intensities obtained from Stokes measurements of a $\mathrm{LG}_0^0|\hat{h}\rangle + \mathrm{LG}_0^1|\hat{v}\rangle$ beam, both before, and after non-planar propagation. The corresponding spatially varying polarisation profile reconstructed from these measurements can be seen on the left column of Figure 3.9(c). From inspection of these intensity measurements, it can clearly be seen that the location of the individual polarisation components is rotated clockwise about the beam centre.

3.7 Chapter 3 conclusion

Throughout this chapter, I have discussed some of the common geometric phases found in optics and outlined an experiment looking at the non-planar propagation of vector beams, and linking the rotations seen to geometric phases.

For this work, a closed out of plane optical trajectory was devised, consisting solely of four mirror reflections, and the rotation of intensity, polarisation and vector beam profiles was investigated, both experimentally and theoretically. With this simple experiment, it was demonstrated (and confirmed through excellent agreement

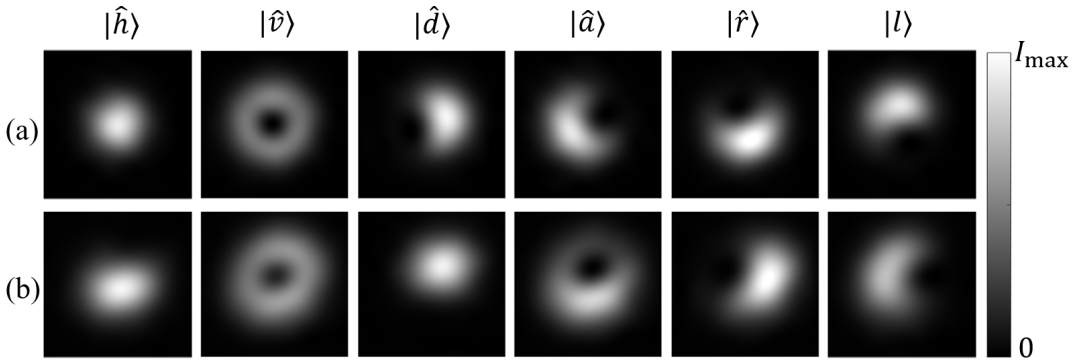

Figure 3.10: Experimental intensities obtained from Stokes measurements of an $\mathrm{LG}_0^0 |\hat{h}\rangle + \mathrm{LG}_0^1 |\hat{v}\rangle$ beam before (a) and after (b) non-planar propagation, for a rotation angle of $\theta = 24.1°$. From left to right, we have the intensities corresponding to horizontal, vertical, diagonal, antidiagonal, right- and left-handed circular polarisation components, respectively. These intensity measurements were used to construct the polarisation profiles shown on the left of Figure 3.9(c).

between theory and experimental results) that polarisation and intensity rotate in the same direction and by the same angle, dependent on the solid angle enclosed by the traversed path on the associated redirection sphere.

We have seen that propagating a light beam along a non-planar trajectory affects both the orbital and spin angular momentum in the same way, by adding a geometric phase factor proportional to the observed rotation. This is perhaps surprising, as the orbital and spin angular momentum are fundamentally different properties of light. OAM is an extrinsic property, arising from twisted phase fronts, whereas SAM is an intrinsic property, relating to the vector nature of electromagnetic fields (or, more specifically, the handedness of their circular polarisation).

By looking at the rotation of vector modes, we saw that, to the overall light beam, non-planar propagation has the affect of adding an angular momentum redirection phase factor of $\mathrm{e}^{-ij\theta_{\mathrm{NP}}}$, where θ_{NP} characterises the non-planrity of the light path, and $j = \ell + \sigma$ is the total angular momentum number of the beam, combining both the spin and orbital components. When $j = \ell + \sigma = 0$, no geometric phase is acquired, and the polarisation profile appears unchanged by the experimental system. This is the case for the popular radial and azimuthally polarised modes, and as such, can be considered as eigenmodes of the system.

The findings presented here have some potential applications. For example, the robustness of the radial and azimuthally polarised vector beams against aplanarity, means that they could be ideal candidates for use within optical communication using fibres, which are inherently subject to twisting and bending [193], and also within microscopy systems, which often contain many redirections of a light beam. Additionally, these particular vector modes can be tightly focused [194], again, making

them useful for microscopy applications. The results are also relevant for twisted optical cavities, mirror-based resonators [195–197] and quantum metrology [198]. Looking at intensity/polarisation rotations also provides a way to measure the acquired geometric phase without the need for a reference beam, and infer the planarity of a surface.

Chapter 4

Optical skyrmions

4.1 Chapter 4 introduction

There are many types of interesting structures and topological features that can be found in structured light beams such as the phase vortex singularities seen in beams carrying orbital angular momentum [92, 199] and polarisation singularities [200]. One such topological structure that has become of interest of late is known as the skyrmion. It was as recent as 2020 when certain paraxial vector beams were shown to have skyrmionic structures embedded within their polarisation profiles [201]. In fact, this work was completed by members of the Quantum Theory Group here, at the University of Glasgow. As part of my PhD, I collaborated with the Quantum Theory Group to continue this project, where my main task was to experimentally generate and analyse optical skyrmions, as well as aid in the development of a new method by which they can be characterised.

Topology is a branch of mathematics which aims to quantify the geometric properties of objects and physical systems, which are conserved under continuous transformations e.g. actions such as bending, twisting and stretching [202]. Topologies and singularities appear in many different physical systems from the small scale vortex singularities in Bose-Einstein condensates [203], to the other end of the length scale, where they are seen in black holes [204]. Singularities are also present in day-to-day life, existing in fingerprints [205], tornadoes [206] and hurricanes [207, 208]. Of late, optics has become a field in which interesting topologies are being studied. This is mainly due to the development of tools such as digital micromirror devices, spatial light modulators and q-plates over recent decades, which allow complex structures to be created at will through the control of a light beam's amplitude, phase and polarisation.

One such topological structure, known as the skyrmion, has been observed in many areas of physics, but the accessible skyrmionic constructs are often limited due to physical constraints of the system. However, paraxial optics offers an easily re-configurable platform for the investigation of skyrmionic structures, made even

more appealing by the accessible nature of experimental intensity and polarisation measurements.

In this chapter, I will start by giving a brief history and introduction into the concept of skyrmions as a whole before focusing on the field of optical skyrmions, where I will discuss how they can be constructed and classified, using a topological index known as the skyrmion number. In § 4.4 I outline a new topological method that we derived to characterise optical skyrmions solely via their polarisation singularities, and associated winding numbers, motivated by the difficulties that can arise when evaluating skyrmion numbers by conventional means. Additionally, the new proposed topological method provides interesting and intuitive geometrical insights into the underlying skyrmionic structures.

In § 4.5 I present experimental results of the simplest skyrmionic beams, and the propagation of such beams under weak focusing (in § 4.7), before outlining an investigation performed to evaluate the performance of the different methods of calculating skyrmion numbers in response to noise. I will then, finally, present a new way in which optical multi-skyrmions can be generated, leading to the investigation of interesting topologies in optics.

For this work, I had the role of experimentally generating the optical skyrmions, acquiring experimental data, processing and analysing the data, evaluating skyrmion numbers and I contributed to the development of the new topological approach to determining skyrmion numbers. I performed simulations of skyrmion beams, in order to test different analysis procedures and test the response when applying simulated noise, and I also suggested the new way of generating optical multi-skyrmions with tunable polarisation textures. Members of the Quantum Theory group at the University of Glasgow, including, Claire M. Cisowski, Zhujun Ye, Fiona C. Speirits, Jörg B. Götte, and lead by Stephen M. Barnett, contributed to the theoretical aspects of the work, focusing on the development of the underlying theory behind the new topological method and the fundamental properties of the skyrmion field. Sonja Franke-Arnold guided the research and helped to integrate the theoretical and experimental aspects.

Some of the work presented in this chapter can be seen in Refs. [209], [210], [211] and [212].

4.2 Skyrmions

In 1961, Tony Skyrme proposed the idea of using a topological model to describe the excitations in the non-linear field of the nucleon [213] . He believed that the stability of hadrons could be explained by topological features and as such, interpreted them as topological solitons due to their particle-like continuous 3D field. Today, these structures are known as skyrmions.

Topological features, defects or solitons are field configurations that cannot be

deformed into a simple smooth shape using continuous transformations and are often characterised by their stability. They can take on many forms, such as points, lines or surfaces [214]. Therefore, in their most basic form, skyrmions can be considered as knots of twisting field lines [215,216], in which it is impossible to separate or untangle these field lines without destroying the skyrmion. In the case of skyrmions, they are often characterised by an integer topological number known as the skyrmion number, n, which will not change through any deformation of the field unless the skyrmion is destroyed [217–219].

In Skyrme's model, he mapped the 3D real space onto the hypersphere (the unit sphere in 4-dimensions [220]) in order to parameterise the continuous pion field. The skyrmion configuration wraps around the hypersphere an integer number of times, with the integer number of wrappings being equal to the skyrmion number. His theory gave spatial structure to the protons and neutrons inside nuclei and a topological explanation to the conservation of baryon number (an important principle in physics preventing proton decay) [221], with each singularity in the field contributing one unit to the baryon number [213]. By fixing the radius of the nucleus, Skyrme was able to model low energy configurations of nucleons to a reasonable accuracy [222]. However, the theory struggled with some aspects of nuclear behaviour (e.g. overestimating nuclear binding energies and sometimes failing to match the clustering structures in some nuclei [223]), and as such, the field of quantum chromodynamics (QCD), which has been more successful at modelling subatomic particles, has superseded Skyrme's theories.

Although Skyrme's ideas were never adopted for their intended purpose of describing sub-atomic particles, these topological quasi-particles have since been studied in many areas of physics, including the study of mesons and baryons, quantum liquids [224], spintronics [225], string theory [226], Bose-condensates and atoms [227, 228], and perhaps most notably, in magnetic materials [229–231]. More recently, the optical analogue to skyrmions has become of interest where they have been observed in evanescent fields [232] and paraxial beams [201, 233, 234].

For many of these other fields of physics, the focus is on the simplest version of the skyrmion configuration, the 2D counterpart of the 3D Skyrmion model, often termed "baby skyrmions", the study of which is much more developed in both theory and experiments. In this case, instead of considering a mapping from a real 3D space to the 4D hypersphere, we are interested in mapping a real 2D space to the unit sphere in 3D [233]. This is in fact the case for the skyrmionic structures typically seen in magnetic materials and in paraxial optics, as will be discussed in the following sections[1]. It should be noted that the stereographic projection of the unit sphere in 3D on to a 2D plane misses out a single point, i.e. at large radii $\rho \to \infty$.

[1]It may be interesting to note that, although "baby" magnetic skyrmions are widely researched, it is possible for magnetic skyrmions to extend into 3D in the form of skyrmion strings [235, 236].

4.2.1 Magnetic skyrmions

As mentioned briefly above, magnetism is perhaps the area in which Skyrme's ideas have had the most prominent impact. The construction of paraxial optical skyrmions has features in common with magnetic skyrmions, and as such, a discussion of these provides a natural starting point.

In magnetism, skyrmions are a type of topological defect formed on the surface of a suitable magnetic material [237] (such as manganese monosilicide (MnSi) [238] or thin films). They have shown promise for applications in the fields of magnetic storage and spintronics [239–241]. These magnetic skyrmions have configurations where the magnetisation is orthogonal to the plane of the sample, with the exception of a finite region region in which the magnetic spins progressively rotate, leading to the direction of the magnetisation being opposite at the centre and outskirts of the skyrmion [229] - i.e. for a single skyrmion, the spin points up (down) at $\rho = 0$ and down (up) at $\rho = \infty$ with only one "flip" of the spin direction between $\rho = 0$ and $\rho = \infty$. A schematic representing a one-dimensional cross-section of the magnetic spin directions is shown in Figure 4.1 (or indeed any 1D skyrmion).

In order to visualise these two-dimensional skyrmionic structures, the Bloch sphere is employed, on which, the local magnetisation direction is mapped, with every possible direction present at least at one point in space. Therefore, we have a stereographic projection from the 3D Bloch sphere onto the 2D plane of the magnetic surface [242–245]. Allowing $\mathbf{M}$ to describe the local direction of the magnetisation, the mathematical form of the skyrmion number can be quoted as [237, 246],

$$n = \frac{1}{4\pi} \int_A \mathbf{M} \cdot \left(\frac{\partial \mathbf{M}}{\partial x} \times \frac{\partial \mathbf{M}}{\partial y} \right) \mathrm{d}x\mathrm{d}y, \tag{4.1}$$

where the integration is performed over the entire plane of the magnetic surface A, (here assumed to be at position $z = 0$). Physically, n counts the number of rotations of $\mathbf{M}$ around the Bloch sphere as we traverse a closed circuit around the centre of the Skyrmion. Note that $\mathbf{M}$ is a normalised vector field, hence, Eq. 4.1 depends only on the *direction* of the magnetisation, not its magnitude.

The configurations of spin alignment observed within magnetic skyrmions arises due to certain physical constraints defined by the film structure, such as energy minimisation and conservation laws. This results in structures with circular symmetry, often subdivided into different categories (e.g. Néel-type, Bloch-type, anti-skyrmions ($n = -1$), merons (or half-skyrmions with $n = 1/2$) and bimerons) depending on the parameters describing them, namely, their vorticity and helicity [247]. However, as will be seen, in optics, we do not have such limitations, therefore here, I will not focus too much on the different subcategories of skyrmion. If the reader is interested in the different categories of skyrmion permissible in magnetism and their topological properties then, I refer them to Refs. [247], [248] and [249].

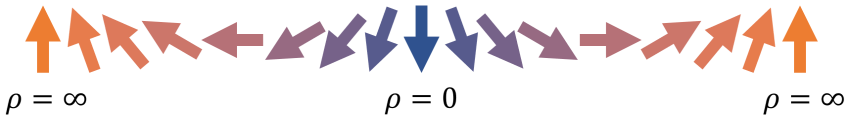

Figure 4.1: Representation of the skyrmion field directions for a 1D skyrmion with radial distance ρ. This also stands as an example of one possible configuration of the spin directions through a cross section of a magnetic skyrmion.

4.3 Optical skyrmions

Recently, the idea from the topology of skyrmions has been translated into the field of optics, where they were first seen as skyrmion lattices generated using evanescent fields and demonstrated using surface plasmon polaritons [232]. However, skyrmionic structures can also be found in paraxial optics, more specifically, in vector beams with spatially varying polarisation.

The first paraxial skyrmions [201] closely followed the ideas of the skyrmionic structures seen in the field of magnetism. To make this transition from magnetism into optics, we replace the vector field representing the magnetic spin direction $\mathbf{M}$, with the vector field $\mathbf{S}$, which is the spatially resolved reduced Stokes vector, written as, $\mathbf{S} = [S_1, S_2, S_3]^T$. This vector field is composed of the normalised Stokes parameters ($S_i^{\mathrm{N}} = S_i/S_0$, for $i \in \{1, 2, 3\}$, where I have dropped the N superscript for simplicity, as for the remainder of this chapter, only normalised Stokes parameters will be considered) and it represents the direction of the Stokes vector describing the polarisation on the Poincaré sphere.

Therefore, instead of utilising the Bloch sphere as the parameter space onto which to map the magnetic spin directions and to visualise the skyrmionic structures, the Poincaré sphere is considered. The expression for the skyrmion number (Eq. 4.1) can be re-written as,

$$n = \frac{1}{4\pi} \int_A \mathbf{S} \cdot \left(\frac{\partial \mathbf{S}}{\partial x} \times \frac{\partial \mathbf{S}}{\partial y} \right) \mathrm{d}x\mathrm{d}y, \tag{4.2}$$

where the surface A is now the entire transverse plane perpendicular to the propagation direction. Equation 4.2 counts the number of times the transverse polarisation wraps the Poincaré sphere. For a beam to be considered an optical skyrmion and to obtain an integer skyrmion number of $n = 1$, there must exist every possible polarisation state at least once in its transverse profile, in order to satisfy a complete wrapping of the sphere. To obtain a higher integer skyrmion number of n, then the polarisation distribution must wrap the Poincaré sphere n times, with each possible polarisation state appearing at least n times in the beams transverse profile.

From these relations, the reader may see a link between optical skyrmions and Poincaré beams, which are a class of structured beam containing every possible polarisation state [250]. And, while it is true that every optical skyrmion is a

Poincaré beam, the reverse is not. As well as containing every polarisation, the polarisation profile of an optical skyrmion must be continuously varying, with the distribution of the polarisation obeying a set of topological rules as discussed in Ref. [251] and which will become more apparent as I continue these discussions throughout this chapter.

The polarisation profiles of structured paraxial beams can take on many forms. It is possible for the polarisation distribution between different beams to appear very different, but have identical skyrmion numbers - n describes the underlying topology. Therefore, the skyrmion number provides one way in which structured light beams can be characterised, especially since the spatially varying Stokes vectors $\mathbf{S}(x, y)$ are easily experimentally accessible. Explicit examples showing how we can construct optical skyrmions with equal n but different polarisation profiles will be given in § 4.3.1 and 4.5, and examples covering ways in which we can change or deform the polarisation distribution, but keep the skyrmion number constant will be § 4.7 and § 4.8.

The optical skyrmions that will be discussed in this thesis all (ideally) have integer skyrmion number. However, in reality, it often happens that the simulated or experimentally measured skyrmion number is smaller than the true number due to an incomplete mapping from the transverse plane to the Poincaré sphere. The incomplete mapping must always occur because of the missing singular point at $\rho \to \infty$, but is exaggerated in numerical simulations due to the chosen grid resolution and finite grid space over which integration is performed. For experimental measurements, under estimation of n occurs due to numerical apertures that limit the accessible area, with further errors resulting from noise (particularly in low-intensity regions), and insufficient measurement resolution that limits the ability to capture small polarisation variations. All of this will be discussed in more detail in § 4.5.

The skyrmion field

For a paraxial light beam, we can also introduce the concept of the *skyrmion field*, which we will denote $\mathbf{\Sigma}$. The skyrmion field is defined in terms of the normalised Stokes parameters S_1, S_2 and S_3, with the direction of the field lines of $\mathbf{\Sigma}$ pointing in the direction of the Stokes vector [201, 252]. The i-th component of the skyrmion field is,

$$\Sigma_i = \frac{1}{2}\varepsilon_{ijk}\varepsilon_{pqr}S_p\frac{\partial S_q}{\partial x_j}\frac{\partial S_r}{\partial x_k}, \tag{4.3}$$

or similarly, employing the vector notation of the Stokes parameters,

$$\Sigma_i = \frac{1}{2}\varepsilon_{ijk}\mathbf{S}\cdot\left(\frac{\partial \mathbf{S}}{\partial x_j}\times\frac{\partial \mathbf{S}}{\partial x_k}\right) \tag{4.4}$$

where ε_{ijk} is the alternating or Levi-Civita symbol and we have employed the Einstein summation convention over multiple indices.

The form of $\mathbf{\Sigma}$ ensures that it is transverse ($\nabla \cdot \Sigma = 0$)[2], meaning that it has no sources or sinks - i.e. the polarisation must be continuously spatially varying. As a consequence, the associated skyrmion field lines must either form loops, or extend to infinity, resulting in the integrated flux of the skyrmion field through any closed surface being zero [201].

Using the definition of the skyrmion field, the skyrmion number can be expressed as,

$$n = \frac{1}{4\pi} \int \mathbf{\Sigma} \cdot \mathrm{d}\mathbf{A}, \tag{4.5}$$

where $\mathbf{A}$ is, again, the entire transverse plane. Therefore, the skyrmion number is in fact a property of the underlying skyrmion field of paraxial beams.

For paraxial beams, we are always concerned with a beam propagating in a defined direction. Lets assume propagation in the z-direction, therefore, the transverse polarisation varies only in the x- and y-directions. It then becomes useful to consider one of the Cartesian components of $\mathbf{\Sigma}$,

$$\begin{aligned} \Sigma_z &= \frac{1}{2}\varepsilon_{pqr} S_p \left(\frac{\partial S_q}{\partial x}\frac{\partial S_r}{\partial y} - \frac{\partial S_r}{\partial x}\frac{\partial S_q}{\partial y} \right) \\ &= S_1 \left(\frac{\partial S_2}{\partial x}\frac{\partial S_3}{\partial y} - \frac{\partial S_3}{\partial x}\frac{\partial S_2}{\partial y} \right) + S_2 \left(\frac{\partial S_3}{\partial x}\frac{\partial S_1}{\partial y} - \frac{\partial S_1}{\partial x}\frac{\partial S_3}{\partial y} \right) \\ &\qquad + S_3 \left(\frac{\partial S_1}{\partial x}\frac{\partial S_2}{\partial y} - \frac{\partial S_2}{\partial x}\frac{\partial S_1}{\partial y} \right) \end{aligned} \tag{4.6}$$

from which it can be seen that each term of the z-component depends on the variation of all three Stokes parameters. In each transverse plane, the polarisation distribution can form a skyrmion, with n in each z plane simply given by,

$$n(z) = \frac{1}{4\pi} \int \Sigma_z \mathrm{d}x\mathrm{d}y. \tag{4.7}$$

Before we conclude this subsection on the skyrmion field, there is one other interesting (and, as will become evident, important) property of $\mathbf{\Sigma}$: it is independent of the choice of physical coordinate system. We can rewrite Eq. 4.3 as a sum of determinants [219],

$$\Sigma_i = \frac{1}{2}\varepsilon_{ijk} \det \begin{bmatrix} S_x & S_y & S_z \\ \partial_j S_x & \partial_j S_y & \partial_j S_z \\ \partial_k S_x & \partial_k S_y & \partial_k S_z \end{bmatrix}, \tag{4.8}$$

[2] A proof of this can be seen in Ref. [212].

from which it is clear that the Skyrmion field is closely related to the scalar triple product[3]. From this relation, we can infer an important symmetry. Changing the global orientation of $\mathbf{S}$, obtained by multiplication of a global rotation matrix R, does not affect $\mathbf{\Sigma}$, as the determinant of a rotation matrix is one. This means that $\mathbf{\Sigma}$ is not affected by the choice of physical coordinate system. An alternative way to think about this, is that the Skyrmion field is invariant under a global rotation of the polarisation on the Poincaré sphere, leading to many forms of polarisation distributions with identical skyrmion fields [212].

4.3.1 Constructing optical skyrmions - the simplest case

In this section, I have chosen to begin with a discussion of an intuitive way to think about the construction of optical skyrmions, by considering the properties that we now know skyrmions must have, before moving on to more general polarisation structures.

To begin this discussion into optical skyrmion construction, we first consider a generic vector beam of the form,

$$|\Psi\rangle = u_0 |0\rangle + \mathrm{e}^{i\varphi} u_1 |1\rangle , \tag{4.9}$$

where $|0\rangle$ and $|1\rangle$ represent any two orthogonal polarisations, u_0 and u_1 are spatial modes and φ is the global phase difference between them. Here, I have employed braket notation for the polarisation, drawing on the mathematical similarity between the Poincaré sphere describing polarisation and the Bloch sphere.

In order to construct a vector beam that is also a skyrmion beam, first recall that skyrmionic beams must have a continuously varying polarisation structure. Using our knowledge of spatial light modes and vector beams accumulated so far, one may speculate that spatial modes with a continuously varying spatial feature pose as convenient building blocks. Perhaps the most obvious of these are the Laguerre Gaussian modes, with their azimuthal phase profiles, superpositions of which will always result in a polarisation distribution with spatial dependence as long as two orthogonal polarisations are used for the constituent LG modes, and that these two modes are not the same.

Also, recall that optical skyrmions are required to contain every possible polarisation state, Therefore, if LG modes are used for the superposition, then their intensity must not entirely spatially overlap, such that the chosen orthogonal polarisations can dominate in some regions of the beam profile. As a simple example of this, we could consider an LG_0^0 and an LG_0^1, the first of which has a Gaussian intensity profile with on-axis intensity, and the latter has zero on-axis intensity, due

[3]Recall that the scalar triple product is unchanged after a circular shift of the three vectors ($\mathbf{a} \cdot (\mathbf{b} \times \mathbf{c}) = \mathbf{b} \cdot (\mathbf{c} \times \mathbf{a}) = \mathbf{c} \cdot (\mathbf{a} \times \mathbf{b})$), and is also invariant under a global rotation of the three vectors, as the volume described by them does not change.

to the optical vortex, and a larger effective radius. A vector beam generated using a superposition of these modes can therefore be written as,

$$|\Psi\rangle = \frac{1}{\sqrt{2}}\left(\mathrm{LG}_0^0\,|0\rangle + \mathrm{LG}_0^1\,|1\rangle\right), \tag{4.10}$$

where I have now included a normalisation factor. An example polarisation distribution for a choice of $|0\rangle = |\hat{l}\rangle$ and $|1\rangle = |\hat{r}\rangle$ is shown in Figure 4.2(a) and Figure 4.2(b) shows the polarisation distribution for a choice of $|0\rangle = |\hat{h}\rangle$ and $|1\rangle = |\hat{v}\rangle$.

From inspection of the polarisation profiles, it can be observed that they do indeed contain every polarisation state, with one polarisation dominating in the centre and the opposite polarisation dominating on the outside. These two polarisations correspond to the basis used to generate the beam. Due to the rate of fall off of intensity at the beam periphery, it is difficult to observe the purely right-handed circular (vertical) polarisation state in Figure 4.2(a) (4.2(b)). However, from the plotted Stokes parameter distributions, specifically S_3 in (a) and S_1 in (b), it can be seen that we reach values of ± 1 at the edges of the distributions, and hence, these polarisations are truly present far from the beam centre.

The beams presented here also satisfy the condition of possessing a continuously varying polarisation distribution, as, if we pick any point in the beam, and travel in any transverse direction, the polarisation state will have changed. This is not always the case for vector beams. For instance, taking the example of a radially polarised beam, if we start in the centre of the beam profile and travel upwards (or downwards) in the transverse plane, then the polarisation is always vertical. In this case the polarisation distribution is *spatially* varying but not *continuously* varying.

Of course, to be a skyrmion beam, the distribution of the polarisation states must obey a set of topological rules, as mentioned above and explained fully in Ref. [251]. But, to test whether these are skyrmion beams, it is perhaps easiest to apply Eq. 4.2. By doing this, we find that both beams shown in Figure 4.2, and in fact any beam described by Eq. 4.10 for any two orthogonal polarisations, are indeed skyrmion beams with $n = 1$. These are perhaps the simplest examples of optical skyrmions, the polarisation structure of which can be easily imprinted within free-space paraxial light beams.

Link between optical skyrmions and OAM

To start to consider more general forms of optical skyrmion construction, and show how they are linked to OAM, it becomes useful to rewrite Eq. 4.9 into a locally normalised form,

$$|\Psi^{(\mathrm{N})}\rangle = \frac{|0\rangle + \mu(\mathbf{r})\,|1\rangle}{\sqrt{1+|\mu(\mathbf{r})|^2}} \tag{4.11}$$

as the skyrmion field and skyrmion number only depend on the spatial variation of the local polarisation direction, and not its magnitude. Here, $\mu(\mathbf{r}) = \mathrm{e}^{i\varphi}u_1(\mathbf{r})/u_0(\mathbf{r})$,

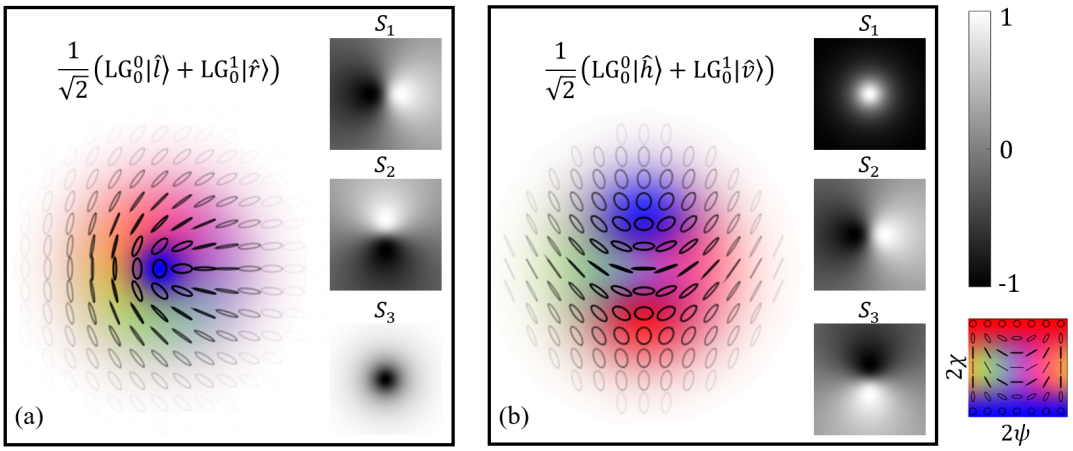

Figure 4.2: Polarisation profiles and Stokes parameter distribution of vector beams described by Eq. 4.10 for the choice of $|0\rangle = |\hat{l}\rangle$, $|1\rangle = |\hat{r}\rangle$ in (a) and $|0\rangle = |\hat{v}\rangle$, $|1\rangle = |\hat{v}\rangle$ in (b). These are examples of some of the simplest optical skyrmions, with $n = 1$. On the right is the polarisation colour scheme in terms of orientation ψ, and ellipticity χ, and the grey scale used to represent the value of the Stokes parameters.

is the ratio between the two complex spatial mode amplitudes, and the superscript N is used to denote the locally normalised version of $|\Psi\rangle$.

Still considering a superposition of two LG modes, with all parameters kept the same between them (e.g. wavelength, beam waist and radial index p) except the OAM number ℓ (see Eq. 1.43), then $\mu(\mathbf{r})$ can be written in terms of two functions f and Φ, depending on the variables ρ, ϕ and z,

$$\mu(\mathbf{r}) = f(\rho, z)\mathrm{e}^{i\Phi(\rho,\phi,z)}, \tag{4.12}$$

or equivalently in terms of the functions f and Θ as,

$$\mu(\mathbf{r}) = f(\rho, z)\mathrm{e}^{i\Theta(\rho,z)}\mathrm{e}^{i(\ell_1-\ell_0)\phi}, \tag{4.13}$$

From the above expression, it can be seen that $\mu(\mathbf{r})$ carries the azimuthal phase dependence, $\mathrm{e}^{i\Delta\ell\phi}$, where $\Delta\ell = \ell_1 - \ell_0$ is the difference between the OAM values of each mode u_0 and u_1.

The Stokes vectors describing the local direction of the polarisation of the normalised beam $|\Psi^{(N)}\rangle$ can be obtained from the expectation value with the familiar Pauli matrices $\boldsymbol{\sigma}$,

$$\mathbf{S} = \langle\Psi^{(N)}|\boldsymbol{\sigma}|\Psi^{(N)}\rangle \tag{4.14}$$

as described in § 1.3.2. This results in three Stokes parameters with the following

form,

$$\begin{aligned} S_x &= \frac{2f\cos\left[\Theta + (\ell_1 - \ell_0)\phi\right]}{1+f^2} \\ S_y &= \frac{2f\sin\left[\Theta + (\ell_1 - \ell_0)\phi\right]}{1+f^2} \\ S_z &= \frac{1-f^2}{1+f^2}. \end{aligned} \tag{4.15}$$

Using these Stokes parameters in the equation for the skyrmion number (Eq. 4.2) and simplifying, we get the following expression,

$$n(z) = (\ell_1 - \ell_0)\left(\frac{1}{1+f^2(0,z)} - \frac{1}{1+f^2(\infty,z)}\right). \tag{4.16}$$

Further details of this calculation can be seen in Ref. [201], [219] and [212].

From inspection of Eq. 4.16, it can be seen that the skyrmion number of vector beams of this form depends only on the polarisation that is dominant at the centre of the beam ($\rho = 0$) and at large distances from the centre ($\rho = \infty$). If the mode u_0 dominates on the optic axis, then $\lim_{\rho\to 0}\mu(\mathbf{r}) = 0$ and therefore $f(0,z) = 0$, and instead if mode u_1 dominates at the centre, then $\lim_{\rho\to 0}\mu(\mathbf{r}) = \infty$, giving $f(0,z) = \infty$. Similarly, considering distances far from the beam centre, we find $f(\infty,z) = 0$ or ∞ depending on what mode dominates. It is always true that $f(0,z)$ and $f(\infty,z)$ will both be either 0 or ∞ unless $\ell_0 = -\ell_1$ (i.e. $\Delta\ell = 0$), as in this case the beams have the same effective radius and so completely spatially overlap (see § 1.4.2).

Typically, beams generated using a superposition of LG_0^ℓ modes will have an integer skyrmion number of $n = \pm(\ell_1 - \ell_0) = \pm\Delta\ell$ or zero, determined by the mode (u_0 or u_1) that dominates at these two extreme locations. We obtain non-zero n if the polarisations at $\rho = 0$ and $\rho \to \infty$ are orthogonal to each other (as shown in the examples in Figure 4.2), and will obtain $n = 0$ if either a single mode dominates in both locations, or if the both modes have equal contribution[4].

Using this relation, between skyrmion number and $\Delta\ell$, we can generate simple optical skyrmions with any integer skyrmion number n using the superposition of a Gaussian with an orthogonally polarised Laguerre-Gaussian with indices $\ell = n$ and $p = 0$,

$$|\Psi_n\rangle = \frac{1}{\sqrt{2}}\left(\mathrm{LG}_0^0|0\rangle + \mathrm{LG}_0^n|1\rangle\right). \tag{4.17}$$

The orthogonal polarisations $|0\rangle$ and $|1\rangle$ used in the generation make up the Schmidt basis [253] of the beam (using the same mathematical ideas as the Schmidt decomposition from the study of entangled states in quantum theory, which allows the

[4]There is an exception to this that occurs when neither mode u_0 or u_1 is sufficiently dominant at $\rho = 0$, in this case a non-integer skyrmion number is obtained. Examples of these optical skyrmions will not be covered in this thesis, but theoretical details can be seen in Ref. [212].

entanglement between the basis states to be quantified [254]). The relevance of the Schmidt basis in reference to skyrmion number calculation will to touched upon later in this chapter.

4.4 Topological definition of the skyrmion number

The skyrmion number of paraxial light beams can be evaluated using Eq. 4.2, which involves integrating over the entire transverse plane, A. However, directly applying this equation has two main difficulties: The first is that the experimentally accessible region of A is limited, we clearly cannot image infinitely far from the beam centre with a camera sensor. The second is that derivatives are inherently sensitive to noise, particularly in low intensity regions, that can be dominated by noise, resulting in the spatial derivative of fluctuating noise levels overwhelming the signal. Both of these factors can make experimental evaluation challenging.

To try and over come these problems, we derived a new topological method for calculating skyrmion numbers, avoiding the use of polarisation gradients. Instead, the method is based on polarisation singularities and associated winding numbers, providing an intuitive geometric insight into skyrmionic structures allowing for a deeper understanding of their underlying topology. We verified this method by evaluating n for a variety of experimentally generated optical skyrmions, with results presented in § 4.5. In § 4.6 I will discuss the performance of the proposed method in the presence of noise by applying noise to simulated data, and comparing results to those obtained using the surface integral equation, Eq. 4.2, showing that the topological approach does indeed outperform Eq. 4.2, and provides a robust and accurate way to determine n. However, first, in this section, I will provide an overview of the derivation of the new method.

To begin this discussion, we recall that the skyrmion number can be calculated as a surface integral over the entire transverse plane A, utilising either the skyrmion field, or Stokes parameters directly,

$$n = \frac{1}{4\pi}\int_A \boldsymbol{\Sigma}\cdot \mathrm{d}\mathbf{A} = \frac{1}{4\pi}\int_A \mathbf{S}_R \cdot \left(\frac{\partial \mathbf{S}_R}{\partial x}\times\frac{\partial \mathbf{S}_R}{\partial y}\right)\mathrm{d}x\mathrm{d}y. \tag{4.18}$$

The only difference between this expression and those quoted above, is that I have now chosen to employ a generalised Stokes vector $\mathbf{S}_R = R\mathbf{S} = [S_x, S_y, S_z]^T$ that relates to the conventional, normalised and spatially resolved, reduced Stokes vector, $\mathbf{S} = [S_1, S_2, S_3]^T$ through an arbitrary rotation described by the matrix R. The reason that we are free to use a generalised Stokes vector here, is that a property of the skyrmion field is that it is invariant under rotations (as discussed above in § 4.3). This means, that it does not matter how we orient our Poincaré sphere, or choose the three orthogonal directions to describe the Stokes parameters, we will still obtain the same correct skyrmion number.

We can also exploit the fact that the skyrmion field is divergenceless ($\nabla \cdot \mathbf{\Sigma} = 0$). This transverse property of $\mathbf{\Sigma}$ allows it to be expressed as the curl of a vector field, which I will call $\mathbf{V}$, such that $\mathbf{\Sigma} = \nabla \times \mathbf{V}$. To draw analogies with the field of magnetism, I will refer to $\mathbf{V}$ as the skyrmion vector potential[5].

By applying Stokes's theorem we can rewrite the above expression from a surface integral of the curl of a vector field, to a line integral of the vector field. From this we obtain,

$$n = \frac{1}{4\pi}\int_A \mathbf{\Sigma}\cdot \mathrm{d}\mathbf{A} = \frac{1}{4\pi}\int_A (\nabla \times \mathbf{V})\cdot \mathrm{d}\mathbf{A} = \frac{1}{4\pi}\oint_C \mathbf{V}\cdot \mathrm{d}\boldsymbol{l}. \tag{4.19}$$

where C is a suitably chosen integration path across the transverse plane that avoids any singularities in $\mathbf{V}$.

The idea of writing the skyrmion field in terms of a curl of a vector field has previously been exploited in the field of superfluids, where skyrmionic structures have also been observed (although, in this area the language used is often different, with the topological structures characterised by the quantised value *circulation*, however the mathematical expressions are identical) [255–259]. The form of $\mathbf{V}$ is not unique, but by turning to the study of superfluids, we can obtain a form of $\mathbf{V}$ thanks to the Mermin and Ho relation [255, 260]. The i-th component of the skyrmion potential is thus,

$$V_i = \mathbf{m}\cdot\frac{\partial}{\partial x_i}\mathbf{n} \tag{4.20}$$

where $\mathbf{m}$ and $\mathbf{n}$ are any two orthogonal unit vectors that satisfy $\mathbf{m}\times\mathbf{n} = \mathbf{S}$, i.e. $\mathbf{S}$, $\mathbf{m}$ and $\mathbf{n}$ form an orthonormal triad. This non-uniqueness of the form of $\mathbf{V}$ means that we have freedom in the choice of $\mathbf{m}$ and $\mathbf{n}$, changing the vector potential but not the skyrmion field [212].

One suitable choice is [212, 219],

$$\begin{aligned}\mathbf{m} &= \frac{1}{\sqrt{S_x^2+S_y^2}}(S_y\hat{\mathbf{x}} + S_x\hat{\mathbf{y}})\\ \mathbf{n} &= \frac{1}{\sqrt{S_x^2+S_y^2}}\left[-S_zS_x\hat{\mathbf{x}} - S_zS_y\hat{\mathbf{y}} + (S_x^2+S_y^2)\hat{\mathbf{z}}\right]\end{aligned} \tag{4.21}$$

allowing Eq. 4.20 to be written as,

$$V_i = \frac{S_z}{S_x^2+S_y^2}\left(S_y\frac{\partial}{\partial x_i}S_x - S_x\frac{\partial}{\partial x_i}S_y\right), \tag{4.22}$$

or equivalently in polar coordinates,

$$V_\phi = \frac{S_z}{S_x^2+S_y^2}\frac{1}{\rho}\left(S_y\frac{\partial}{\partial \phi}S_x - S_x\frac{\partial}{\partial \phi}S_y\right). \tag{4.23}$$

[5] In electromagnetism, the curl of the magnetic vector potential ($\mathbf{A}$) is equal to the magnetic field, $\mathbf{B} = \nabla\times\mathbf{A}$.

It is now possible to define the skyrmion number as a line integral of the skyrmion potential. However, the line integration path much be chosen carefully. We want to include as much of the transverse plane as possible, but, as we shall explain, we cannot simply choose an integration path with a suitably large radius centred on the skyrmion. By inspection of Eq. 4.23, it can be seen that if the term in brackets does approach zero as $\rho \to 0$, then V_ϕ will diverge. To exclude these singular points from the integration we use the same technique as to what is employed in complex contour integration, where poles in the complex plane are avoided. An example of this integration path is shown in Figure 4.3(a), where the chosen path passes from large radii, towards the singular point, circles the singularity (in the opposite direction), and then returns back to the larger circular contour, in order to close the integration. If this integration is carried out, then the integrals along the two straight lines cancel, leaving us with the difference of two circular line integrals, one at large radii (denoted α) and small radii (β), both centred at the origin. Performing this integration takes into account that Σ_z is finite everywhere. That is, the same value for n is obtained if Σ_z is integrated over a surface, A, $\int_A \Sigma_z \mathrm{d}x\mathrm{d}y$, which omits a very small region around $(x, y) = (0, 0)$.

However, it is possible for the skyrmion field to have more than one singular point, thus, the line integration of $\mathbf{V}$, must exclude all of these points. An example of a possible integration path when multiple singularities are present is shown in Figure 4.3(b), following the same technique as before.

The skyrmion number can now be re-expressed as the difference between two (or more) circular line integrals of $\mathbf{V}$,

$$n = \frac{1}{4\pi}\left(\oint_\alpha \mathbf{V}\cdot \mathrm{d}\boldsymbol{l} - \sum_j \oint_{\beta_j} \mathbf{V}\cdot \mathrm{d}\boldsymbol{l}\right), \tag{4.24}$$

where α is the integration path evaluated (counter-clockwise) at large radii and β_j is the integration path evaluated (clockwise) around the j-th singularity located at (x_j, y_j).

It turns out that the previous equation can be simplified further in order to remove the need for integration, or the direct calculation of $\mathbf{V}$. To do this, we start by introducing a pair of complex Stokes parameters, also referred to as the complex Stokes field,

$$S_\pm = S_x \pm iS_y = |S_\pm| e^{\pm i\Phi}, \tag{4.25}$$

allowing us to write,

$$\begin{aligned} S_x &= S\cos\Phi \\ S_y &= S\sin\Phi \end{aligned} \tag{4.26}$$

where the $\pm$ subscript has been dropped for simplicity. From the above, we can read off a phase term for this complex quantity, Φ, which is commonly termed the

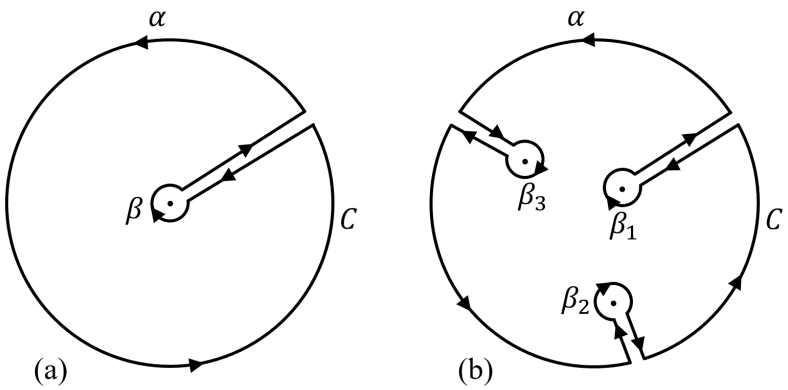

Figure 4.3: Illustration of possible line integration paths for evaluation of n using Eq. 4.19, excluding the singular points in $\mathbf{V}$.

Stokes phase and can be explicitly written as,

$$\Phi = \arctan\left(S_y/S_x\right). \tag{4.27}$$

By direct substitution of Eq. 4.26 into Eq. 4.22, the i-th component of the skyrmion field can be simply rewritten as,

$$\begin{aligned} V_i =& \frac{S_z}{S_x^2 + S_y^2}\Big\{ - S^2 \sin^2\Phi \nabla_i \Phi - S^2 \cos^2\Phi \nabla_i \Phi \Big\} \\ =& - S_z \nabla_i \Phi, \end{aligned} \tag{4.28}$$

resulting in,

$$\mathbf{V} = -S_z \nabla \Phi. \tag{4.29}$$

This allows us to express the skyrmion number as,

$$n = \sum_j \frac{1}{4\pi} \oint_{\beta_j} S_z \nabla\Phi \cdot \mathrm{d}\boldsymbol{l} - \frac{1}{4\pi} \oint_{\alpha} S_z \nabla\Phi \cdot \mathrm{d}\boldsymbol{l}, \tag{4.30}$$

At the location (x_j, y_j), the position of the j-th inner singularity, we can simply take the value of the local Stokes parameter $S_z^{(j)}$, and, as such, it can be taken out of the integral. At the outside of the beam, the Stokes parameter converges to a single value, $\bar{S}_z^{(\infty)}$, therefore, this can also be removed from the integral. The remaining integrals are related to the polarisation winding number, given by [79, 81],

$$N = \frac{1}{2\pi} \oint \nabla\Phi \cdot \mathrm{d}\boldsymbol{l} \tag{4.31}$$

which counts the number of turns S completes on the Poincaré sphere when following the respective circular paths. From the definition, N, must be an integer, therefore, it has the benefit of being free from noise.

Inserting all of this into the previous equation, we obtain our final topological definition for the Skyrmion number [209, 212],

$$n = \frac{1}{2}\left(\sum_j S_z^{(j)} N_j - \bar{S}_z^{(\infty)} N_\infty\right), \tag{4.32}$$

which depends only on the Stokes vector at the position of the singularities and at the beam periphery, and the corresponding integer winding numbers on the Poincaré sphere, around the singularity positions.

The derived expression for the skyrmion number given in Eq. 4.32 was obtained using a generalised Stokes vector $\mathbf{S}_R = [S_x, S_y, S_z]^T$. As the Skyrmion field, $\mathbf{\Sigma}$, is invariant under rotations, the orientation of the Poincaré sphere is irrelevant, and any $\mathbf{S}_R$ can be chosen when calculating n, as long as S_x, S_y and S_z are orthogonal, giving us unlimited options.

In the following subsection, I will give a detailed illustration of how to apply the derived topological approach to evaluate skyrmion numbers. For this, I will use the examples of $n = 1$ and $n = 2$ skyrmion beams, and in the process, illustrate how Eq. 4.32 links to the topology of the polarisation profile and how the choice of $\mathbf{S}_R$ can make the topological features more apparent.

4.4.1 Simple illustration of using the topological approach for finding skyrmion numbers

To highlight the simplicity and subtleties of the previously derived topological approach to finding skyrmion numbers, and how it links to the topology of the polarisation texture, let us consider two examples.

Firstly, let's take the example of an $n = 1$ optical skyrmion of the form $|\Psi_1\rangle$ of Eq. 4.17 and a polarisation profile as shown in the top left of Figure 4.4. In the top row of Figure 4.4, I also show the corresponding vectorial representation of $\mathbf{S}(x, y)$, indicating the local direction of the Stokes vector on the Poincaré sphere and a representation of the mapping of the unitary Stokes vectors onto the Poincaré sphere. This in theory demonstrates a full coverage of the sphere, however, for clarity, not every vector on the sphere has been plotted.

If we choose $\mathbf{S}_R = [S_1, S_2, S_3]^T$, then $\Phi = \arctan(S_2/S_1)$, the profile of which is displayed in Figure 4.4(a). This choice results in a singularity in the centre at the left-handed circular polarisation position, and a delocalised singularity at the beam periphery, as we approach the orthogonal right-handed circular polarisation state. To avoid the singularity locations in this case, we use an integration path (C) as shown on the left of (a). At the central singularity location, $S_3 = -1$ and as $\rho \to \infty$, $S_3 = 1$, and the polarisation winding number, $N = -1$ in both cases, allowing Eq. 4.32 to be evaluated as $n = \frac{1}{2}\{(-1)(-1) - (1)(-1)\} = 1$.

Alternatively, we can choose $\mathbf{S}_R = [S_2, S_3, S_1]^T$, as illustrated in Figure 4.4(b). This choice results in two singularities, located at the positions of the horizontal

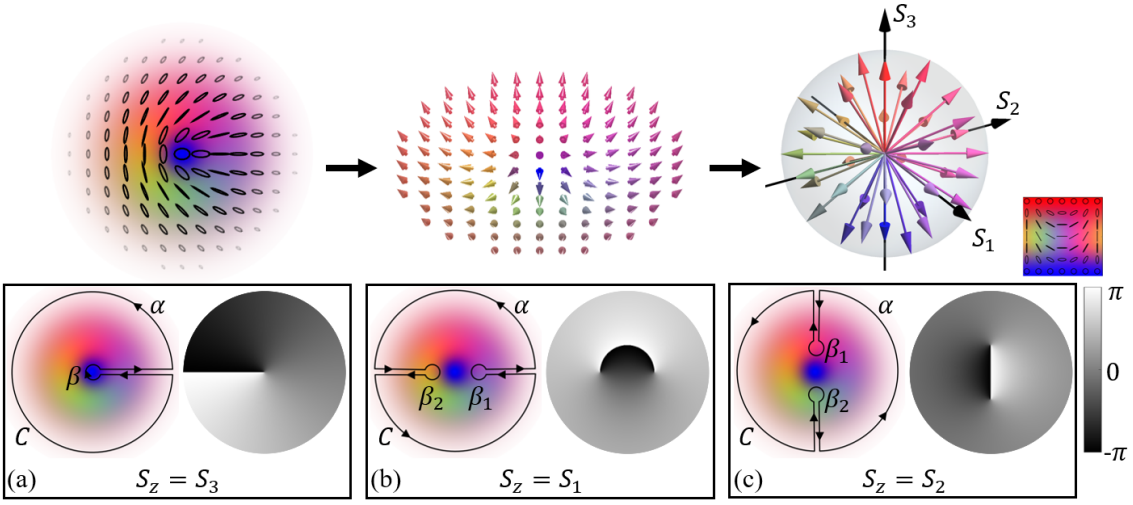

Figure 4.4: Illustration of the topological measurement of the skyrmion number for an $n = 1$ beam. Top row shows the polarisation profile of an $n = 1$ skyrmion beam represented as polarisation ellipses (left) and unitary Stokes vectors (centre) and on the right is a representation of the Stokes vectors mapped onto the Poincaré sphere, along with the polarisation colour scheme. (a), (b) and (c) show integration paths (left) and Stokes phase profiles Φ (right) when evaluated for a choice of $S_z = S_1$, S_2 and S_3. Parts of this figure have been adapted from [211].

and vertical linear polarisation states. To avoid the singularities in this instance, we choose an integration path as shown in Figure 4.4(b), where we now have two inner circular line integrals. Following the same procedure as before and using this integration path gives $n = \frac{1}{2}\{[(1)(1) + (-1)(-1)] - 0\} = 1$. That is, we obtain the same correct skyrmion number. Here, we have used that, for this choice, $S_1 = 1$ at β_1, $S_1 = -1$ at β_2, and $N = 0$ around the beam periphery.

In Figure 4.4(c) I provide an illustration for a choice of $\mathbf{S}_R = [S_3, S_1, S_2]^T$, where, again, two singularities are obtained, this time at the locations of diagonal and anti-diagonal linear polarisations. If the same procedure is followed and Eq. 4.32 evaluated, $n = 1$ will again be obtained.

In order to demonstrate how the number of singularities present in Φ changes with skyrmion number and choice of $\mathbf{S}_R$, and to more explicitly show how the polarisation winding number N is related to the path on the Poincaré sphere, we will now consider the example of an $n = 2$ optical skyrmion. The polarisation distribution of a beam of the form $|\Psi_2\rangle$ of Eq. 4.17 is shown in Figure 4.5(a), and below it is the corresponding vectorial representation of $\mathbf{S}(x, y)$.

Figure 4.5(b) displays Φ when a choice of $\mathbf{S}_R = [S_1, S_2, S_3]^T$ is made, resulting in a singularity in the centre. A chosen suitable integration path is also shown, which yields contributions from the central singularity ($S_3 = -1$) and at $\rho \to \infty$

($S_3 = +1$). By plotting the integration path on the Poncaré sphere (as shown on the right of (b)), we can clearly see that the paths wind twice (backwards) around the South and North pole, respectively, giving a visual representation of the winding number in terms of the varying polarisation states. Substituting this information into Eq. 4.32 as above results in $n = \frac{1}{2}\{(-1)(-2) - (1)(-2)\} = 2$.

It may have been noticed that the singularity location is the same as in Figure 4.4(a), appearing at the point of pure left-handed circular polarisation. This is in fact a consequence of the Schmidt decomposition of the beam. Both of these optical skyrmions were generated using Eq. 4.17 and a left- and right-handed circular polarisation basis, i.e. $|0\rangle = |\hat{l}\rangle$ and $|1\rangle = |\hat{r}\rangle$. From Eq. 4.29, we can see that the S_z component is singled out in the form of $\mathbf{V}$, meaning that if we choose $\mathbf{S}_R$ such that S_z corresponds to the polarisation of the Schmidt basis of the beam ($S_z = S_3$ in this case), then we obtain one singularity at the beam centre, with the magnitude of the winding equal to $|n|$. This is true at least for skyrmion beams of the form of Eq. 4.17.

Figure 4.5(c) provides an illustration of evaluating the $n = 2$ skyrmion beam using a choice of $\mathbf{S}_R = [S_2, S_3, S_1]^T$, resulting in four singularities located at the horizontal and vertical linear polarisations. The corresponding integration path is shown on the Poincaré sphere, however, this time it is traversed twice, alternatingly winding around $S_1 = 1$ (β_1 and β_3) and $S_1 = -1$ (β_2 and β_4), with positive and negative winding numbers respectively. At the periphery, $N = 0$, therefore giving no contribution. This again results in the correct $n = 2$.

From these simple examples, it can be seen, that unlike the surface integral form of the skyrmion number, given in Eq. 4.2, our topological definition does not require any derivatives or integration and instead can be read directly from inspection of the polarisation profile. In the following sections, I will provide experimental results and further simulations, demonstrating that this new skyrmion number definition can provide a significant increase in accuracy and precision.

4.5 Experimental evaluation of the skyrmion number

In this section, I will present measurements of optical skyrmions and compare the skyrmion number measurement methods of Eq. 4.2 and Eq. 4.32 (the surface integral and topological methods, respectively).

For experimental demonstration, we will consider beams with integer skyrmion number n created using superpositions of orthogonally polarised Laguerre-Gaussian modes,

$$|\Psi_n\rangle = \frac{1}{\sqrt{2}}\left(\mathrm{LG}_0^0\,|0\rangle + \mathrm{LG}_0^n\,|1\rangle\right). \tag{4.33}$$

This beam equation is equivalent to that given and discussed above, but is quoted again here for convenience.

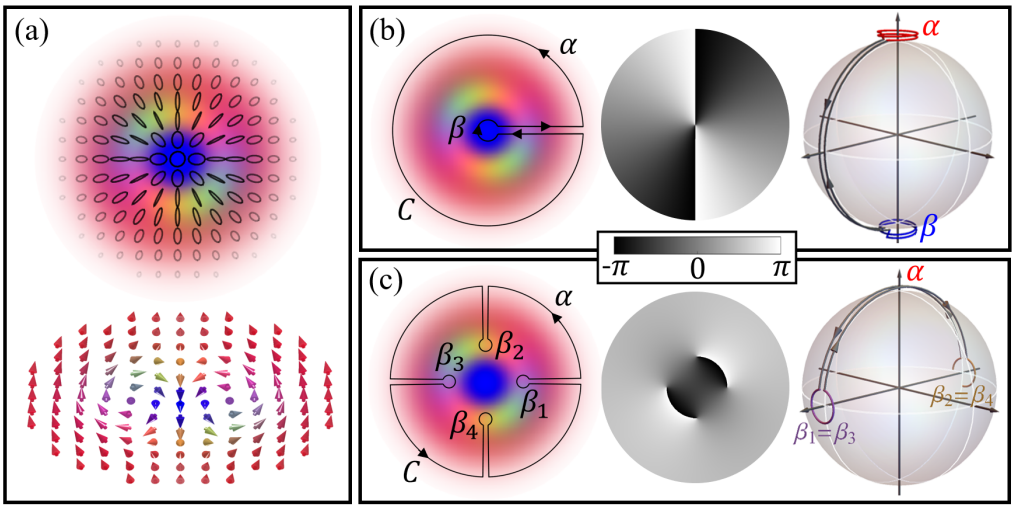

Figure 4.5: Illustration of the topological measurement of the skyrmion number for an $n = 2$ beam. (a) Polarisation profile of an $n = 2$ skyrmion beam and corresponding distribution of unitary Stokes vectors $\mathbf{S}(x, y)$. (b) and (c) show path integrals (left) phase profiles Φ (centre) and Poincaré spheres (right) with corresponding path indicated when evaluated using either $S_z = S_3$ (b) or $S_z = S_1$ (c). Parts of this figure have been adapted from [209].

Beams of the form of Eq. 4.33 were generated using the DMD setup (Figure 2.12) described previously in § 2.6, and the spatially resolved Stokes parameters obtained by performing a full Stokes tomography using a rotating waveplate setup (see § 2.3, Figure 2.4). We chose to generate beams using either a circular ($|0\rangle = |\hat{l}\rangle$, $|1\rangle = |\hat{r}\rangle$) or linear ($|0\rangle = |\hat{h}\rangle$, $|1\rangle = |\hat{v}\rangle$) polarisation basis, resulting in polarisation textures with either a skyrmionic or a bimeronic structure [261]. This choice of polarisation basis could be made by either including, or not including, an additional quarter-wave plate immediately after the DMD in the beam generation setup shown in Figure 2.12. The measured polarisation profiles can be seen in Figure 4.6 for beams with $n = 1$ to 5 where the top row shows the beams with skyrmionic structure and bottom row bimeronic structures. The polarisation profiles show good qualitative agreement with the corresponding theoretical profiles. On the right of Figure 4.6, I provide simulated $n = 5$ profiles for comparison.

In Figure 4.7, I provide examples of the raw intensity images obtained from Stokes measurements for two different skyrmion beams. Figure 4.7(a) shows polarisation projections of an $n = 5$ optical skyrmion of the form,

$$|\Psi_5\rangle = \frac{1}{\sqrt{2}}\left(\mathrm{LG}_0^0\,|\hat{l}\rangle + \mathrm{LG}_0^5\,|\hat{r}\rangle\right), \tag{4.34}$$

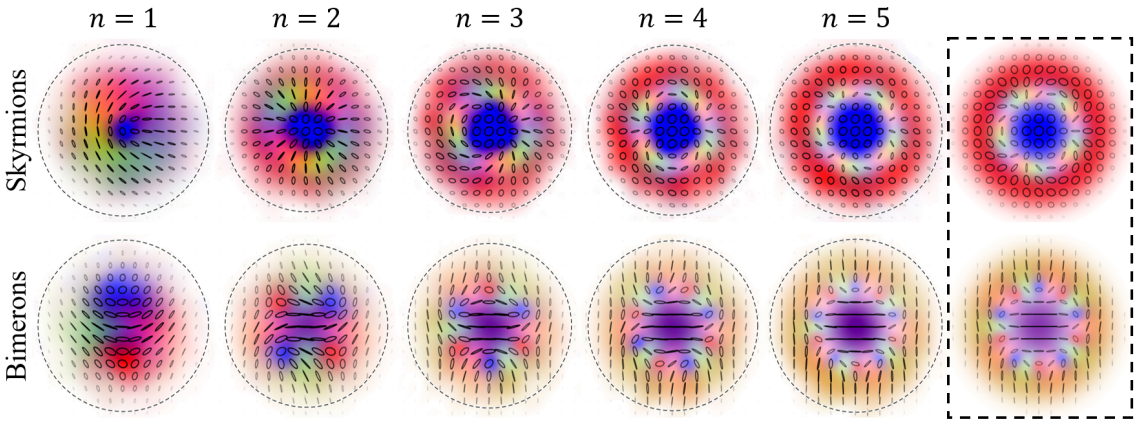

Figure 4.6: Experimentally measured polarisation profiles of skyrmion beams with $n = 1$ to 5 and of the form of Eq. 4.33. The top row shows skyrmions generated in the circular basis ($|0\rangle = |\hat{l}\rangle$, $|1\rangle = |\hat{r}\rangle$) and the bottom row shows beams (bimerons) generated using a linear basis $|0\rangle = |\hat{h}\rangle$, $|1\rangle = |\hat{v}\rangle$. The insert on the right shows the theoretical polarisation profiles for the corresponding beams with $n = 5$. The dashed circles around indicate the radius where the intensity falls to 5% of the peak intensity. Figure adapted from [209].

and Figure 4.7(b) shows the experimental intensities for a beam of the form,

$$|\Psi_2\rangle = \frac{1}{\sqrt{2}}\left(\mathrm{LG}_0^0\,|\hat{h}\rangle + \mathrm{LG}_0^2\,|\hat{v}\rangle\right). \tag{4.35}$$

The reconstructed polarisation profile using the intensity measurements in (a) is shown in the top row of Figure 4.6 under $n = 5$, and the corresponding polarisation for Figure 4.7(b) can be seen in the bottom row of Figure 4.6 under $n = 2$.

4.5.1 Analysis process and results

As well as providing us with information in order to plot the polarisation profiles, the measured spatially resolved Stokes vectors $\mathbf{S}(x, y)$, also form the foundation for the quantitative analysis on n using the two different approaches.

The Stokes parameters are obtained from six intensity images corresponding to horizontal, vertical, diagonal, anti-diagonal, right and left circular polarisations. The background intensity (of approximately 1.5% of the peak intensity) was subtracted from each of these images, with its exact value obtained by averaging over a small number of camera pixels far from the beam. Fourier filtering is then applied to each intensity image, to remove artefacts due to diffraction. Additional details of this image processing can be found in § 2.4. To retrieve the spatially resolved normalised reduced Stokes vector, we need to divide by the total intensity. This, in theory, can be obtained the from addition of any two images corresponding to orthogonal

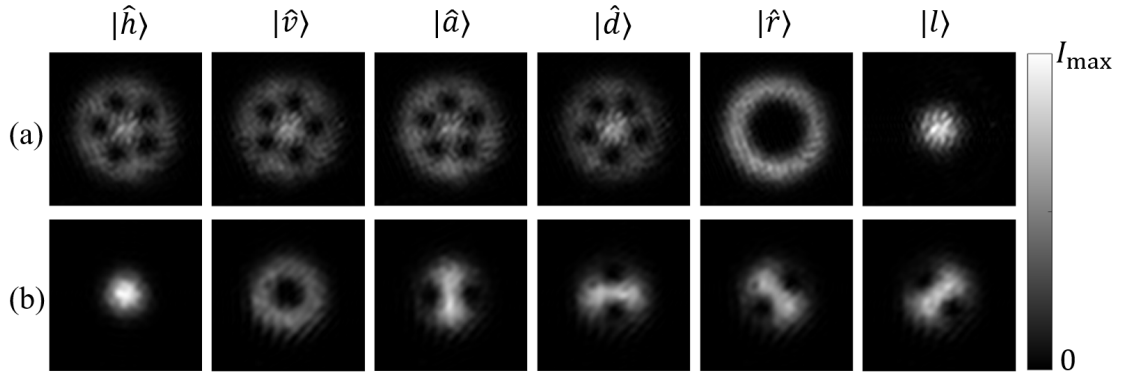

Figure 4.7: Raw experimental intensities obtained from Stokes measurements of optical skyrmions. From left to right, we have the intensities corresponding to horizontal, vertical, antidiagonal, diagonal, right- and left-handed circular polarisation, respectively. (a) Measurements of an $n = 5$ beam of the form of Eq. 4.34. (b) Measurements of an $n = 2$ beam of the form of Eq. 4.35.

polarisation measurements. However, measured values may differ slightly depending on the chosen basis, due to imperfect optical elements. Consequently, $\mathbf{S}(x, y)$ is obtained by dividing each parameter by the total intensity obtained from the sum of the corresponding polarisation states,

$$\mathbf{S}(x,y) = \left[\frac{I_{|\hat{h}\rangle} - I_{|\hat{v}\rangle}}{I_{|\hat{h}\rangle} + I_{|\hat{v}\rangle}}, \frac{I_{|\hat{d}\rangle} - I_{|\hat{a}\rangle}}{I_{|\hat{d}\rangle} + I_{|\hat{a}\rangle}}, \frac{I_{|\hat{r}\rangle} - I_{|\hat{l}\rangle}}{I_{|\hat{r}\rangle} + I_{|\hat{l}\rangle}} \right]^T, \tag{4.36}$$

where $I_{|\hat{i}\rangle}(x, y)$ are the spatially resolved intensity measurements for each on the six Stokes images, and the (x, y) has been left out of the equation for simplicity.

Before I discuss the remaining details of experimental evaluation on n, I would like to point out the considerations that must be made when choosing a suitable integration path for the topological approach, guided by both fundamental and practical criteria. To obey Stokes's theorem, the outside circular line integral should ideally cover the entire transverse plane. Of course, in practice this is not possible, but it should contain as much as possible of the beam profile. For practical reasons, we want to choose a path that avoids very low intensity regions right at the beam periphery, where the intensity measurements are dominated by noise, as well as the immediate neighbourhood of the singularities.

To account for this, and to ensure a fair comparison between the evaluation methods, the analysis was performed over a disk, outside of which the intensity falls below 5% of the peak intensity. The size of these disks are indicated in Figure 4.6 as dashed circled on top of the polarisation profiles. The reasoning behind the chosen intensity cut-off value will be given in the following subsection.

Table 4.1: Comparison of experimentally measured skyrmion numbers for the beams shown in Figure 4.6 evaluated using the surface integral method Eq. (4.2) and the topological method Eq. (4.32), respectively.

Type	Method	$n=1$	$n=2$	$n=3$	$n=4$	$n=5$
skyrmion	Eq. (4.2)	0.918	1.921	2.994	4.007	4.924
	Eq. (4.32) ($S_z = S_3$)	0.913	1.910	2.925	3.891	4.884
	Eq. (4.32) ($S_z = S_1$)	1.000	1.998	2.994	3.989	4.976
bimeron	Eq. (4.2)	0.927	1.941	2.971	3.999	4.991
	Eq. (4.32) ($S_z = S_1$)	0.915	1.931	2.970	3.966	4.972
	Eq. (4.32) ($S_z = S_3$)	1.000	1.998	2.992	3.989	4.993

Equation 4.2 evaluates n directly using the numerical gradients of the measured $\mathbf{S}(x, y)$ and performing the surface integral over the chosen disk centred on the beam origin. The obtained skyrmion numbers using Eq. 4.2 are given in Table 4.1.

The topological method, Eq. 4.32, requires the identification of $\bar{S}_z^{(\infty)}$, $S_z^{(j)}$ and the corresponding winding numbers about these points. For this we need to identify the location of the singularities. Recall that the winding numbers N in Eq. 4.32 describe the number of turns completed by S on the Poincaré sphere along a path surrounding a singularity. Plotting the Stokes phase ($\Phi = \arctan(S_y/S_x)$) visually gives the location of each singularity and the corresponding winding numbers, as shown in Figures 4.4 and 4.5. However, computationally, the singularities can be found at the positions where $S_z \to \pm 1$, or equivalently, where S_x and $S_y \to 0$.

To evaluate $S_z^{(j)}$, an average of the S_z values is performed over a square of 3×3 pixels, centred on the location of the j-th singularity. The contribution from the outside, $\bar{S}_z^{(\infty)}$, is taken taken to be the edge of the disk, as such the value of $\bar{S}_z^{(\infty)}$ is calculated by averaging the values of S_z lying along the circular path, where intensity falls to 5% of the peak. By converting a small area about the j-th singularity into a polar plot and integrating along the angular direction, the magnitude of the winding number N_j can be obtained, with the sign of the gradient giving the sign of N_j. For experimental data, N is calculated by averaging over 10 rows of the polar plot. To find N_∞, the entire grid space is converted into a polar plot and and the same analysis performed near the edge of the beam profile. Alternatively, it is possible to find $|N|$ without the need for integration by simply numerically counting the number peaks in the angular direction of the polar plots.

In Table 4.1, I present the results obtained using the topological approach to evaluate the beams shown in Figure 4.6, for a choice of $[S_x, S_y, S_z] = [S_1, S_2, S_3]$ and $[S_x, S_y, S_z] = [S_2, S_3, S_1]$.

From Table 4.1 it is clear that for both methods, we obtain skyrmion numbers that closely match the target n for each beam. Considering the results from the topological approach, we obtain the highest accuracy when Eq. 4.32 is evaluated using a choice of $\mathbf{S}_R$ such that S_z is orthogonal to the Schmidt basis that defines the skyrmion in Eq. 4.33, i.e. using $S_z = S_1$ for the skyrmions generated in the left- and right-handed polarisation basis, and using $S_z = S_3$ for the bimerons generated in the horizontal and vertical polarisation basis. The reason for this, is that this choice of generalised Stokes vector shifts the relevant path integrals away from beam areas of low intensity where noise could compromise the evaluation of the relevant Stokes parameters. For the beams discussed here so far, this means that the outside circular integral (previously labelled α) has a contribution of zero, as explicitly demonstrated in the examples given at the end of § 4.4.1.

The Skyrmion number is a global property. Ideally, both calculation methods should be evaluated over the entire transverse plane, extending to infinity. As such any measurement (or indeed any simulation over a finite grid space) will be an approximation, leading to one of the reasons for the inaccuracies seen in Table 4.1. Differences from the target skyrmion number also arise from inaccuracies in the experimental generation process and Stokes tomography, where imperfect optical elements are undoubtedly used, as well as from the numerical evaluation.

It may be noticed from Table 4.1, that accuracy generally improves for higher skyrmion numbers, particularly for Eq. 4.2. The is an artefact of our particular skyrmion 'recipe' as defined in Eq. (4.33), as the intensity profile of the two constituting spatial modes LG_0^n and LG_0^0 overlap less for higher n, so that $S_z^{(\infty)}$ is better defined.

For the beams shown in Figure 4.6, we managed to achieve measured skyrmion numbers with high accuracy, due to the high fidelity optical skyrmions we were able to generate with the experimental beam generation techniques used here. However in many situations one may not have this luxury, for example, when working at extremely low light levels, or when investigating light after propagation through noisy environments. Comparisons of the response of the various calculation methods to increasing noise levels are given in § 4.6, where it was confirmed that the topological method proves more effective. This is perhaps no surprise, as noise amplification is an inherent property of derivatives which are required for the surface integral method Eq. 4.2.

Example of an $n = 0$ Poincaré beam

All of the beams shown so far have been optical skyrmions that are also Poincaré beams, evident as they contain every possible polarisation state, and the relation between Poincaré beams and the coverage of the Poincaré sphere has been discussed by others including in Ref. [259]. However, as mentioned, not all Poincaré beams are skyrmions, as the distribution of the polarisation must also follow a set of topological

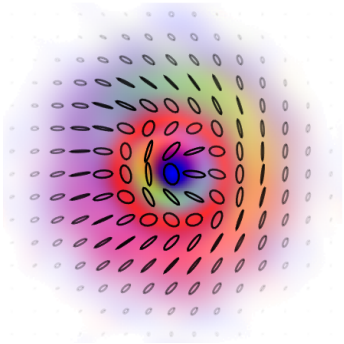

Figure 4.8: Polarisation profile of a beam with skyrmion number 0.

rules [251]. Here, I will provide an example showing that Poincaré beams and skyrmion beams are not equivalent.

In Figure 4.8 I show the experimentally measured polarisation profile of a beam of the form,

$$\mathrm{LG}_1^0 \left|\hat{l}\right\rangle + \mathrm{LG}_0^1 \left|\hat{r}\right\rangle \tag{4.37}$$

where we are now considering an LG mode with a non-zero p index.

This beam contains every possible polarisation state and is therefore a Poincaré beam. By inspection of the polarisation profile and considering a path starting at the centre of the beam and travelling radially outwards, then we traverse a path on the Poincaré sphere staring at the south pole, moving up to the north pole, and back to the south pole again, such that an entire great circle is traversed. No matter what radial direction is considered, a great circle is always traversed on the Poincaré sphere, but corresponding to a different line of longitude. Therefore, the polarisation of the beam presented here does indeed cover the Poincaré sphere.

However, if the skyrmion number is calculated using either of the methods mentioned above, then we obtain $n = 0$, and as such, this beam is not a skyrmion.

4.5.2 Variation of the skyrmion number with evaluation area

As the skyrmion number is a global property of a beam, relying on evaluation over an infinite transverse plane, any measurement outcome will always be an approximation. In this section, I will illustrate this by evaluating the numerical and measured skyrmion number over a restricted circular region of the transverse plane, accomplished by varying the radii ρ of the disk over which the evaluation is performed.

In Figure 4.9, I compare the response of the surface integral and topological methods when ρ was increased from 0.1 up to 2.5 times the beam waist w_0.

For this investigation, it was chosen to evaluate optical skyrmions of the form of Eq. 4.33 generated in a circular polarisation basis ($|0\rangle = \left|\hat{l}\right\rangle$, $|1\rangle = \left|\hat{r}\right\rangle$), corresponding to the beams in the top row of Figure 4.6. However, similar results would have been

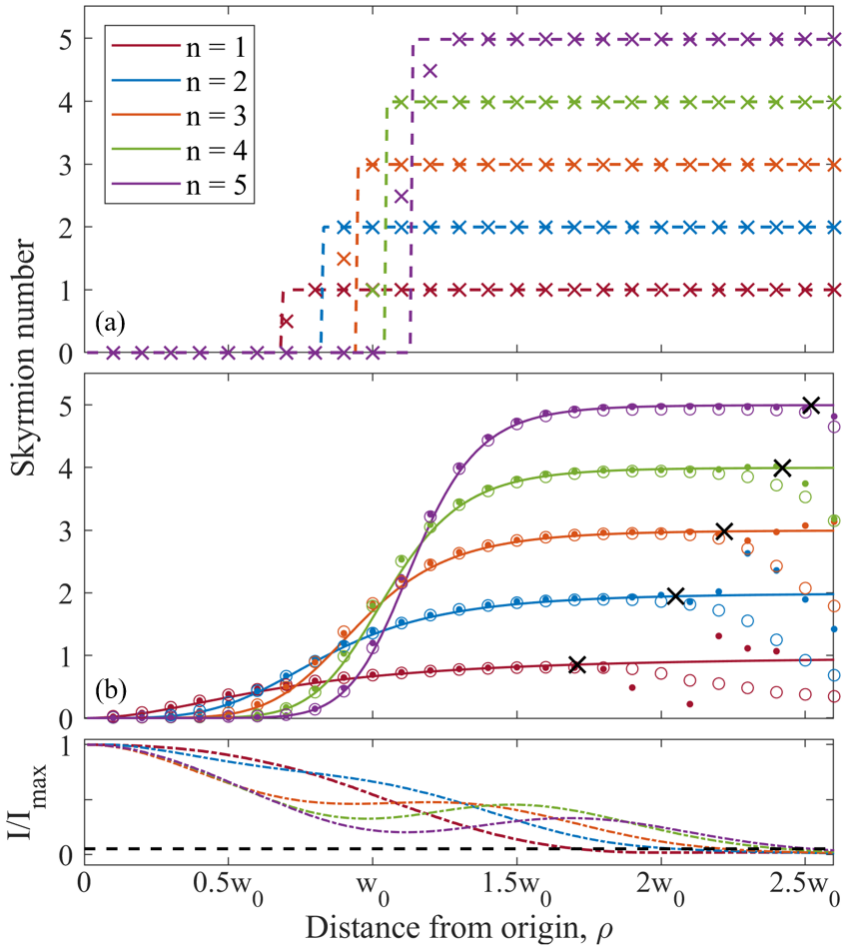

Figure 4.9: Comparison of skyrmion numbers obtained from the integral (Eq. 4.2) and topological (Eq.4.32) definition calculated over varying evaluation areas with radii ρ. We evaluate skyrmions of the form of Eq. 4.33 with $|0\rangle = |\hat{l}\rangle$, $|1\rangle = |\hat{r}\rangle$ and for skyrmion numbers $n = 1$ to 5. (a) Displays simulated (dashed lines) and experimentally (crosses) obtained skyrmion numbers when using the topological method and evaluating in an orthogonal polarisation basis ($S_z = S_1$). (b) Compares the two methods when choosing S_z to correspond to the Schmidt basis ($S_z = S_3$). Simulations are shown as solid lines, and experimental data as closed (Eq. 4.2) and open (Eq. 4.32) data points. The lower plot shows the peak-normalised beam intensity of the experimentally measured beams. The dashed line marks 5% of $I_{\max}$, and the beam radii where the various beams reach this intensity are indicated by black crosses in (b). Figure adapted from the Supplemental material of [209].

obtained if we used the horizontal/vertical linear polarisation basis, or indeed any other orthogonal polarisation basis.

In Figure 4.9(a), the topological method, Eq. 4.32, has been used to evaluate skyrmion beams with $n = 1$ to 5, with simulation shown as dashed lines and experimental measurements as crosses. Here, $\mathbf{S}_R = [S_2, S_3, S_1]^T$ was chosen, such that in the calculation was performed using a polarisation basis orthogonal to the Schmidt basis of the beam. From Figure 4.9(a), it can clearly be seen from the simulated results that the measured skyrmion number remains zero for restricted circular regions, with lower radii. Once all the singularities are included within the evaluation area, the correct skyrmion number is identified. The experimental results match the simulation with very little deviation.

In Figure 4.9(b) the same investigation is performed, however, using the surface integral method (Eq. 4.2) and again the topological method but this time evaluating in using the Schmidt basis of the beam ($S_Z = S_3$) by choosing the generalised Stokes vector to be $\mathbf{S}_R = [S_1, S_2, S_3]^T$. The simulations are shown as solid lines, where it was found that simulations based on both Eqs. 4.2 and 4.32 were indistinguishable. The corresponding measured data using Eq. 4.2 is shown as solid data points, and the measurements using Eq. 4.32 are given as open data points. The simulations indicate that the obtained skyrmion numbers indeed approach their target values when we increase the area of the beam used in the evaluation, where we have better approximations to the transverse plane.

For both methods used in Figure 4.9(b), the experimental results initially very closely follow simulation and approach the expected skyrmion number. However, as we increase the evaluation area further, beyond certain values of ρ, the measurement results are compromised by noise in the low intensity regions. Equation 4.2 can be observed to produce fluctuating numbers for n, mainly due to the noise amplification caused by the derivatives. For Eq. 4.32, the values steadily decrease. We observed that the measurements began to deviate from simulation when a beam radius ρ is reached where at which point the intensity falls to around 5% of the of the peak intensity $I_{\max}$. Due to this, this 5% intensity cut-off was used in the analysis process outlined in § 4.5.1, and for the results presented in Table 4.1.

Additionally, the investigations presented here show that the response to noise of the topological approach is more consistent. The skyrmion number is always underestimated in the areas dominated by noise due to $\left| \lim_{\rho \to \infty} \bar{S}_z(\rho) \right| \leq 1$ always being true. Therefore, it is possible for the true value of n to be obtained by identifying the radius where n is maximum and rounding to the nearest integer (if indeed we are dealing with a scenario in which integer skyrmion numbers are expected).

4.5.3 Characterisation of a multi-skyrmion ring

One way in which we can highlight the geometric nature of the proposed topological method is to apply it in the evaluation of multi-skyrmions.

From the results presented above, it has been seen that through a rotation of the Poincaré sphere, i.e. via a different choice of $\mathbf{S}_R$, we can obtain different interpretations of the skyrmion spin texture and its polarisation singularities. For multi-skyrmions, using the topological method can lead to the identification of sub-skyrmion structures and their corresponding attributions. I will choose to illustrate this with a multi-skyrmion ring[6] of the form,

$$|\Psi_{\text{ring}}\rangle = \frac{1}{\sqrt{2}}\left(\text{LG}_0^2\,|\hat{h}\rangle - \text{LG}_0^5\,|\hat{v}\rangle\right), \tag{4.38}$$

which should have a skyrmion number of $\Delta\ell = 3$. An experimentally measured polarisation profile of this beam is shown on the left of Figure 4.10. While it may be true that in the field of magnetism, it would be impossible to generate a multi-skyrmion with this spin texture, in optics we are only restricted by Maxwell's equations, and therefore have the luxury and ability to generate more exotic skyrmionic structures. In magnetism however, it is common to have skyrmion lattices consisting of periodic structures with $n = 1$ [231], and the subsequent discussion also extends to these scenarios.

Using the surface integral method, a skyrmion number of $n = 2.918$ for the measured multi-skyrmion ring was obtained, which is close to the expected value. However, using the topological method, more accurate values of $n = 2.958$, 2.996 and 2.998 were obtained for the choices of $S_z = S_1$, S_2 and S_3, respectively. The Stokes phase profiles, Φ, and integration paths associated with these calculations are given in Figure 4.10(a - c).

The choice of $S_z = S_1$, as shown in Figure 4.10(a), correspond to evaluating in the Schmidt basis of the beam, with only one singularity appearing in the centre of the profile. In Figure 4.10(b), the beam is interpreted in terms of winging numbers about polarisation singularities located at the diagonal/antidiagonal linear polarisations and in (c), we instead have the singularities at the positions of right/left handed circular polarisations, each time occurring where $S_z \to \pm 1$. In both cases we have six singularities in Φ, where the polarisation winging number is either $N = \pm 1$, and each singularity represents the location of a meron, contributing a skyrmion number of 1/2 to the total skyrmion number. For the choices of $S_z = S_2$ and S_3, the contribution from the beam periphery to the total n is zero.

The experimentally measured skyrmion numbers obtained when evaluating using the topological method and polarisation bases orthogonal to the beams Schmidt basis deviate form the expected n only by an order of about 1/1000. This is an

[6] Named due to the similarity in structure with the *intensity* optical ring lattices used for atom trapping.

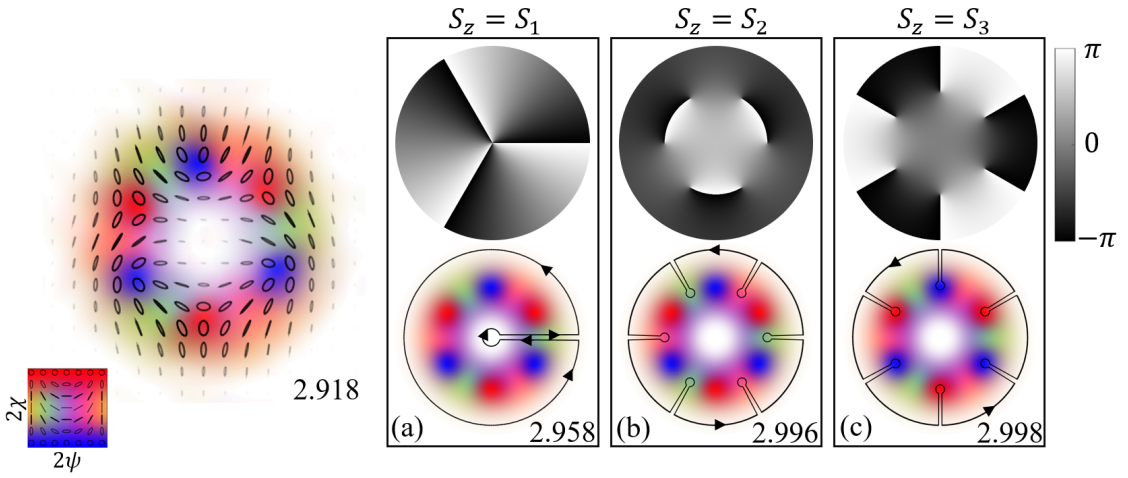

Figure 4.10: Interpretation of an optical multi-skyrmion in terms of different polarisation bases. An experimentally measured polarisation profile of $|\Psi_{\text{ring}}\rangle$ is shown on the left and the measured skyrmion number, using Eq. 4.2, indicated. (a) The phase of the complex Stokes field, Φ, when evaluated in the horizontal/vertical ($S_z = S_1$) polarisation basis, and the path of the chosen contour displayed on top of the polarisation map. (b, c) Equivalent to (a) but evaluated in the diagonal/antidiagonal basis (b) and the right/left circular polarisation basis (c), by setting $S_z = S_2$ and $S_z = S_3$, respectively. In each case, the skyrmion number determined from the experiment measurement and Eq. 4.32 is indicated. The polarisation colour map is shown as an insert on the left. Figure adapted from [209].

error reduced by an order of magnitude compared to evaluating in the Schmidt basis (or indeed using the surface integral method). The reason for the improved values results from the improved accuracy in determining S_z at locations of higher beam intensity. This is particularly evident for the beam considered here, as, in addition to the low intensity at the beams periphery, we also have a low intensity region at the centre. These results provide further evidence that a careful and thought out choice of generalised Stokes vector $\mathbf{S}_R$ can allow for optimised measurements, as will be confirmed in the next section through the application of artificial noise to a simulated multi-skyrmion ring of the same form as $|\Psi_{\text{ring}}\rangle$.

In this section, I have presented results considering choices of $S_z = S_1, S_2$ or S_3, but of course, it is possible to evaluate using any arbitrary polarisation basis we want.

4.6 Investigations into evaluating the skyrmion number in the presence of noise

Regions of low intensity directly affect the skyrmion number as the polarisation in these areas (particularly at the beam periphery for the optical skyrmions presented so far) can determine whether the mapping of the Poincaré sphere is complete over the transverse profile. One of the aims of deriving the topological method was to have a more robust way of finding skyrmion numbers compared to the surface integral method, by removing the need for derivatives in which noise amplification is an inherent property. To confirm that the topological identification of n proves more effective in tackling noise, simulations were performed to analyse noisy data.

The experimental measurements contain two main sources of noise: artefacts due to diffraction and background noise. Diffraction artefacts can be easily removed using a low pass Fourier filter, however, background noise is more difficult to account for, as it is challenging to ensure that only background noise, and no signal information, is being removed. Due to this, we will consider the application of background noise to simulated data.

To attempt to resemble the effects of background noise, random values ranging between 0 and $\gamma I_{\max}$ were added to simulated Stokes intensity images (corresponding to $|\hat{h}\rangle$, $|\hat{v}\rangle$, $|\hat{d}\rangle$, $|\hat{a}\rangle$, $|\hat{r}\rangle$ and $|\hat{l}\rangle$ polarisation projection measurements). Here, $I_{\max}$ is the maximum intensity in the entire beam, and γ is a parameter to control the noise level. We choose to apply levels of artificial background noise ranging from 0 to 2% of $I_{\max}$, i.e. for $0 \leq \gamma \leq 0.02$.

Figure 4.11 compares the different methods at calculating skyrmion numbers after applying noise to beams with $n = 1$ to 5 of f the form of Eq. 4.33 with $|0\rangle = |\hat{l}\rangle$ and $|1\rangle = |\hat{r}\rangle$, equivalent to the beams shown in the top row of Figure 4.6. For a fair comparison, for each method we evaluate over a disk, the size which is given by the radial distance from the beam centre at which the intensity falls to $0.05I_{\max}$, corresponding to the distances marked by crosses in Figure 4.9. The values found using Eq. 4.2 are displayed using solid lines and the dotted and dashed lines indicate the values calculated using the topological approach either in the Schmidt basis of the beam or an orthogonal polarisation basis.

From inspection of Figure 4.11, it was found that increasing noise levels leads to an underestimation of n using both the surface integral method and the topological method evaluated in the Schmidt basis, although, this underestimation is less so in the latter case, particularly for higher skyrmion numbers. However, the simulation indicates that by choosing to evaluate Eq. 4.32 in an orthogonal polarisation basis to the Schmidt basis, we can obtain an almost noise-free skyrmion number (as shown by the dashed lines). Additionally, it can be seen that there is an offset that is present for low skyrmion numbers, which disappears for evaluation in an orthogonal polarisation basis.

To provide additional insights, I will also show the response of the different

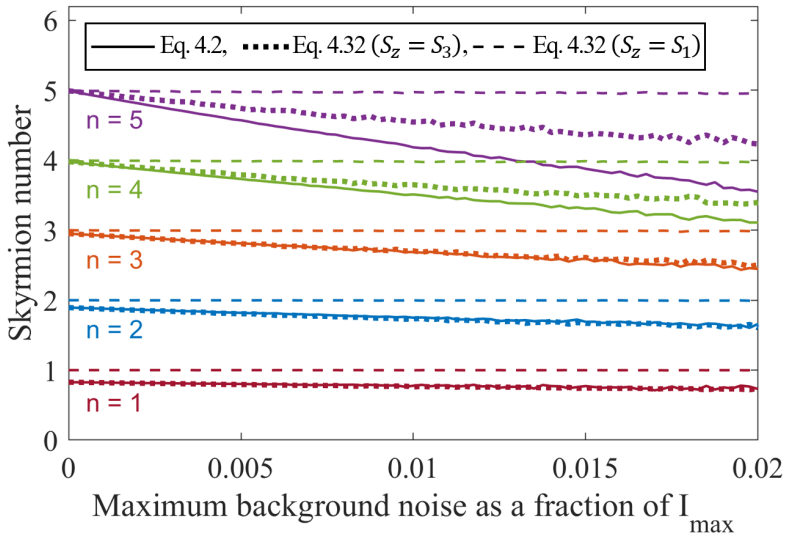

Figure 4.11: Comparison of the performance of skyrmion measurement methods for increasing noise levels. Increasing levels of background noise applied to simulated skyrmions with $n = 1$ to 5 of the form of Eq. 4.33 with $|0\rangle = |\hat{l}\rangle$ and $|1\rangle = |\hat{r}\rangle$, equivalent to the beams shown in the top row of Figure 4.6. Evaluation is performed over a disk outside of which intensity falls to 5% of the peak intensity. The solid lines indicate values calculated using Eq. 4.2. Dotted lines correspond to values calculated using Eq. 4.32 in the Schmidt basis of the beam ($S_z = S_3$) and dashed lines when evaluating Eq. 4.32 using an orthogonal polarisation basis ($S_z = S_1$). Figure adapted from [209].

methods to a simulated multi-skyrmion with applied background noise. For this, the same multi-skyrmion ring as described by $|\Psi_{\text{ring}}\rangle$ in Eq. 4.38 and shown in Figure 4.10, is used and background noise applied to the six simulated Stokes intensity measurements as before. Figure 4.12 displays the calculated skyrmion numbers for increasing levels of background noise ($0 \leq \gamma \leq 0.02$), and again evaluating using either the surface integral approach (Eq. 4.2), or the topological approach with $S_z = S_1$, S_2 or S_3. We applied 100 iterations of each noise level, with n being calculated each time, allowing the average of the obtained values to be plotted in Figure 4.12. The standard deviation of the average is shown as error bars.

For each method, n was evaluated over a disk, outside of which intensity falls to 5% of I_{max}. From the circle data points and corresponding error bars, it can be seen that the surface integral method can either greatly under- or overestimate the measured skyrmion number, with a large standard deviation being obtained even over the 100 iterations used here. This large variation can mainly be attributed to the low intensity region in the centre of $|\Psi_{\text{ring}}\rangle$. Due to this, it was decided to repeat the analysis, but this time also excluding the central region, with intensity values $\leq 0.05 I_{\text{max}}$, from the performed integration. This was again repeated 100 times and

the average values are shown as crosses in Figure 4.12, where it can again be seen that the skyrmion number still deteriorates with increased nose, but we do this time have a smaller standard deviation, and n is no longer overestimated at any point.

When the Eq. 4.32 is used to evaluate the multi-skyrmion and performed in the Schmidt basis of the beam, the measured n was also found to deteriorate with increased noise (as shown by the blue dashed line), with a steeper deterioration than applying Eq. 4.2. However, with this method, there was less variation in the obtained n, as evident from the negligible standard deviation after the 100 iterations. The true advantage of the topological method is seen when choosing to evaluate using an orthogonal polarisation basis to the Schmidt basis (orange and green dashed lines in Figure 4.12). With this calculation it was possible to correctly identify the skyrmion number of the multi-skyrmion ring for all levels of noise investigated here.

The simulations discussed and presented in this section indicate that the topological method is advantageous when dealing with noisy experimental data for a suitable choice of S_z.

4.7 Propagation of paraxial skyrmionic beams under weak focusing

In this section, I will present a discussion around the propagation of optical skyrmions and corresponding measurement results, demonstrating the invariance of the skyrmion number. For the purpose of this, I chose to observe the beam propagation under weak focusing, still remaining within the paraxial regime, allowing any changes in the beam profile to be observed over shorter distances rather than propagating to the far field.

Consider the simplest case of a beam with a skyrmion number of 1 of the form,

$$|\Psi_1\rangle = \frac{1}{\sqrt{2}}\left(\mathrm{LG}_0^0\,|0\rangle + \mathrm{LG}_0^1\,|1\rangle\right). \tag{4.39}$$

This beam was generated as before using either a circular ($|0\rangle = |l\rangle$, $|1\rangle = |r\rangle$) or linear ($|0\rangle = |h\rangle$, $|1\rangle = |v\rangle$) polarisation basis, resulting in polarisation textures with either a skyrmionic or a bimeronic structure. To view the propagation of such structures with focusing, a 150 mm lens was used along with a camera mounted on a motorised translation stage, allowing precise measurement of the transverse polarisation at different propagation planes.

In Figure 4.13(a) and (b) I show the experimentally measured polarisation profiles of the focusing of the two $n = 1$ beams considered here at different transverse planes after the 150 mm lens. The optical skyrmion generated in the circular polarisation basis is shown in (a) and (b) shows the bimeron, generated using the horizontal/vertical linear polarisation basis. At a propagation distance of $z = 0$ cm, we have the original skyrmion beam (c.f. Figure 4.6) and at 15 cm ($z = f$), we have

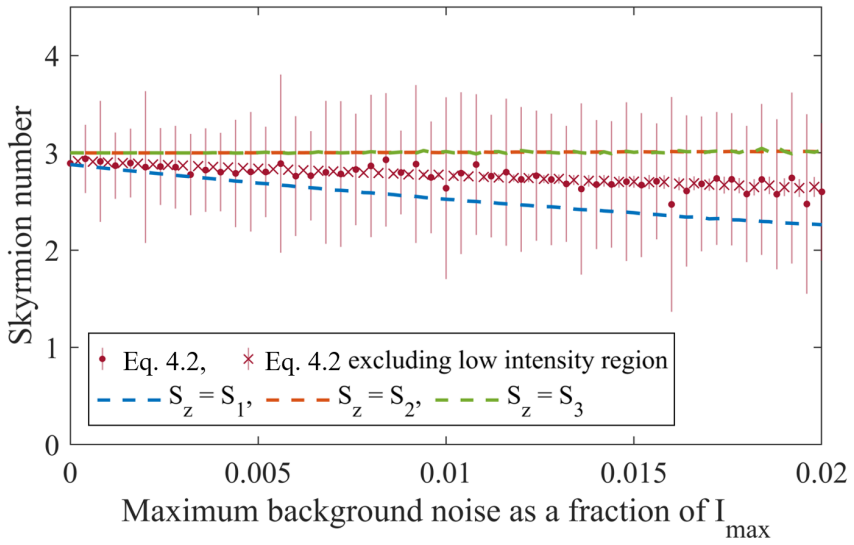

Figure 4.12: Comparison of performance of the skyrmion measurement methods at evaluating the multi-skyrmion ring (given by $|\Psi_{\text{ring}}\rangle$) for simulated increasing background noise levels. The red points show the average of 100 n values calculated using Eq. 4.2 directly over a disk, outside of which intensity falls to 5% of I_{max}, whereas red crosses show n calculated using Eq. 4.2, but omitting the central region of the beam where intensity is also below $0.05I_{\text{max}}$. Error bars indicate the standard deviation of the 100 values. The three dashed lines show n evaluated using Eq. 4.32, when using the Schmidt basis of the beam (blue), and the two orthogonal polarisation bases (orange and green). The standard deviation when using Eq. 4.32 re too small to be seen, however, was calculated to be less than 0.04 for the maximum noise level. Figure adapted from the Supplemental material of [209].

the polarisation profile at the focus. In Figure 4.13, the experimental images have been cropped to different beam waist multiples, as indicated on each measurement, to reflect the change in beam size with focusing, allowing the polarisation to be resolved clearly.

From inspection of Figure 4.13, a continuous rotation can be seen in the polarisation profiles as the beam propagates. This can be explained by the different relative Gouy phase,

$$\psi(z) = (N+1)\tan^{-1}\left(\frac{z}{z_R}\right), \tag{4.40}$$

between the constituent modes used to construct the beam, arising due do the different mode numbers of the Gaussian ($N = 0$) and LG_0^1 mode ($N = 1$).

For both the skyrmion and bimeron, the entire polarisation profile rotates by $\pm\frac{\pi}{2}$ as it propagates from the far field to the focus, with the majority of the rotation happening close to the focal point, within about two Rayleigh ranges (z_R). This is,

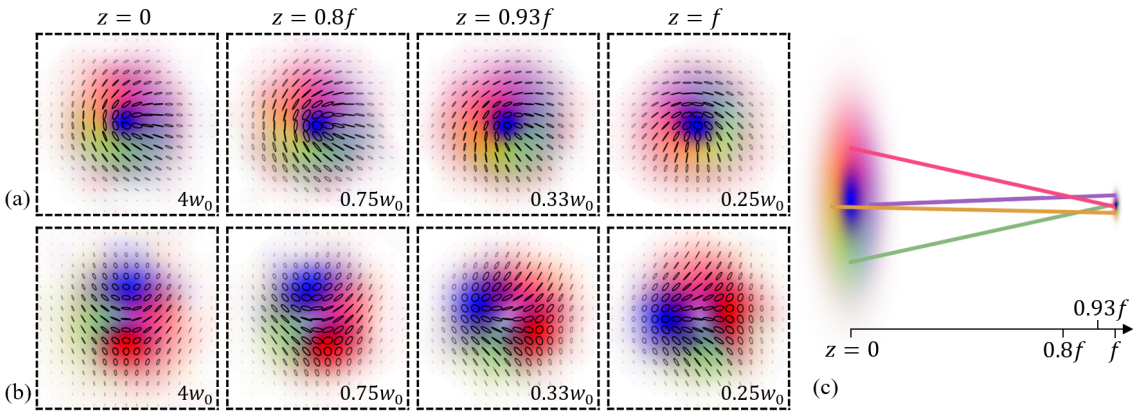

Figure 4.13: Propagation of optical skyrmions. Experimentally measured transverse polarisation profiles of focusing using a 150 mm lens. (a,b) Optical skyrmions (bimerons) with $n = 1$ generated using Eq. 4.17 and a circular polarisation basis ($|0\rangle = |l\rangle$, $|1\rangle = |r\rangle$) (a) or a linear polarisation basis ($|0\rangle = |h\rangle$, $|1\rangle = |v\rangle$) (b). The propagation distance after the lens is indicated on the top row as a fraction of focal length (f) and the numbers on the bottom right of each beam profile represent the the real width and height of the images as a multiple of the original beam waist (w_0). (c) Trace of the lines of constant polarisation for the focusing skyrmion beam given in (a). Figure adapted from [211].

of course, due to the dependence of the Gouy phase on $\tan^{-1}(z/z_R)$ [53]. However, despite the visual change in the polarisation pattern, the skyrmion number should remain unchanged. Interestingly, it is possible to trace out lines of constant polarisation, as shown in Figure 4.13(c), where they can be seen to twist together as we approach the focus, and it has recently been demonstrated in Ref. [252] that these constant polarisation lines are equivalent to skyrmion field lines (Σ).

To show the invariance of the skyrmion number with propagation under weak focusing, n was evaluated using the spatially resolved Stokes parameters and both Eq. 4.2 and our topological method (Eq. 4.32). The results are summarised in Table 4.2. Both evaluation methods are carried out in the same way as before - the background noise is subtracted, unwanted diffraction artefacts are removed via Fourier filtering of the camera images, with the images then cropped to a disk, outside of which, the intensity is $\leq 5\%$ of the peak intensity. For Eq. 4.2, the surface integral was performed over the entire grid space in order to find the skyrmion number. For Eq. 4.32 it was chosen to perform the evaluation by assigning either $S_z = S_3$ or $S_z = S_1$.

For both methods, we achieve experimental skyrmion numbers close to 1 for every propagation distance, as can be seen in Table 4.2, demonstrating the invariance of the skyrmion number under paraxial propagation. In all cases, the highest accuracy in the skyrmion number was attained when using the topological approach Eq. 4.32,

Table 4.2: Comparison of experimentally measured skyrmion numbers at different propagation distances for the $n = 1$ skyrmion and bimeron shown in Figure 4.13 and evaluated using Eqs. 4.2 and 4.32.

Type	Method	Propagation distance			
		0	$0.8f$	$0.93f$	f
skyrmion	Eq. 4.2	0.915	0.942	0.930	0.929
	Eq. 4.32 ($S_z = S_3$)	0.914	0.946	0.947	0.943
	Eq. 4.32 ($S_z = S_1$)	0.999	0.998	0.988	0.998
bimeron	Eq. 4.2	0.922	0.931	0.921	0.905
	Eq. 4.32 ($S_z = S_1$)	0.955	0.964	0.960	0.949
	Eq. 4.32 ($S_z = S_3$)	0.999	0.985	0.971	0.995

and evaluating it using a mutually unbiased basis to the Schmidt basis used to define the beam in Eq. 4.39 (i.e. assigning $S_z = S_1$ for the skyrmion shown in Figure 4.13(a) and $S_z = S_3$ for the bimeron shown in Figure 4.13(b)). The reason for this improved accuracy is the same as discussed earlier in this chapter - it is due to the relocation of the relevant path integrals away from beam areas with low intensity, which are dominated by noise, to higher intensity areas with better signal-to-noise ratios.

Side note on propagation under weak focusing: A comparison to non-planar propagation

In Figure 4.13(b) I show the weak focusing of a $\mathrm{LG}_0^0 |\hat{h}\rangle + \mathrm{LG}_0^1 |\hat{v}\rangle$ beam, upon which a rotation in the over all polarisation profile is observed, of course due to the differing Gouy phase between the two LG modes.

Previously, back in Chapter 3, I also presented the rotation of vector beams but through a different mechanism: Non-planar propagation. In fact, in Figure 3.9(c), the result of the non-planar propagation of this same skyrmion beam was shown. Interestingly, if we only look at the polarisation profiles of the beams shown in Figure 3.9 and Figure 4.13, in both cases we observe a rotation, but you cannot tell directly from the measurements themselves what process has occurred. For non-planar propagation, the rotation occurs from physically moving the beam, and is related to the total geometry of the propagation path and hence can be interpreted in terms of an additional geometric phase. During focusing, the propagation direction instead remains constant, and the rotation occurs due to differences in Gouy phase of the two contributing modes. However, both of these acquired phases leading to the observed effects are geometric in nature, as discussed in Chapter 3.

4.8 Generation of tunable optical multi-skyrmions

Typically, optical skyrmions are generated such that the centre and periphery of their transverse polarisation distributions have orthogonal polarisations, with all other polarisation states appearing in a winding arrangement in the regions in between. This has been the case for all the optical skyrmion examples shown in this chapter so far and also for the optical skyrmions investigated in other work [233, 234, 262–264]. The reason for this is, perhaps, due to the resemblance of the skyrmion field of this class of beam and that seen in the more familiar magnetic skyrmions, which formed the basis under which paraxial optical skyrmions were first modelled [201]. As discussed in § 4.2.1, magnetic skyrmions are subject to certain physical constraints (e.g. energy minimisation and conservation laws), resulting in circularly symmetric configurations in magnetic films where the spins are all aligned orthonormal to the plane of the film, with the exception of a specific, finite region in which the spins progressively rotate [229]. However, unlike magnetic skyrmions, paraxial beams are limited only by Maxwell's equations, so, in principle, it is possible to generate arbitrary polarisation patterns, embedded with any type of structure that we desire. This freedom could allow the field of free space optics to provide a versatile platform for investigating interesting topological structures.

In this section, I will present a new way of generating optical skyrmions using split-vortex beams and show how the skyrmion number and its topology is related to the OAM of the constituent beam. To begin this discussion, I will start by giving a brief introduction to the concept of split vortex beams in the following section.

4.8.1 Split vortex beams

It is known that the coherent mixture of an LG_0^1 mode with a Gaussian beam can displace the location of the phase vortex singularity from the centre of the beam [265,266], as is shown in Figure 4.14(a). This addition of the two beams results in us no longer having a doughnut intensity distribution commonly associated with beams carrying orbital angular momentum, instead leaving us with intensity that is not rotationally symmetric. One interesting application of these beams is that, due to their non rotationally symmetric intensity distributions, they have been used to observe the mechanical rotational motion of beams carrying OAM about their propagation axis [265], of course, resulting from the fact that a rotation of a non-rotationally symmetric distribution can be easily observed.

However, if we consider the addition of a Gaussian beam to LG modes with higher OAM values, we have the effect of vortex splitting, where an LG beam with a single central vortex of order ℓ will now have $|\ell|$ vortices of order 1 (or -1). This behaviour is shown in Figure 4.14(b-d) for $\mathrm{LG}_0^\ell +$ Gaussian beams, for $\ell = 2$, 3 or 5. From the corresponding phase profiles, we can see the individual phase vortex singularities, resulting in the same number of null intensity regions. Additionally,

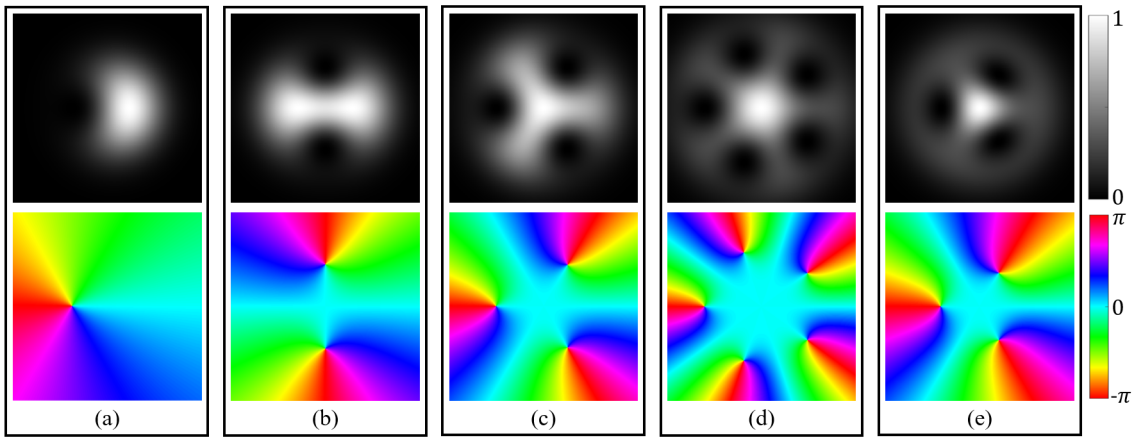

Figure 4.14: Intensity (top row) and phase distributions (bottom row) of equal superpositions of LG_0^ℓ modes and a Gaussian. (a-d) show the superposition of an LG_0^1, LG_0^2, LG_0^3 and LG_0^5 with a Gaussian of equal waist w_0, respectively, whereas in (e) an LG_0^3 mode is superimposed with a Gaussian with a beam waist of $0.7w_0$. The intensity and phase maps used are shown on the right. Figure adapted from [211].

as shown by the example in Figure 4.14(e), by changing the ratio between the beam waists of the two superimposed beams, we can control the vortex singularity positions in reference to the beam centre.

4.8.2 Optical multi-skyrmions generated using split-vortex beams

We can now consider what happens if we try to make optical skyrmions using these split-vortex beam. It turns out, that it is simple to create beams with integer n by employing a similar recipe as before,

$$|\Psi_{\mathrm{multi}}\rangle = \mathrm{LG}_0^0(w_0)\,|0\rangle + \mathrm{e}^{i\varphi_0}\left(\mathrm{LG}_0^\ell(w_0) + \mathrm{e}^{i\varphi_1}\mathrm{LG}_0^0(\delta w_0)\right)|1\rangle\,, \tag{4.41}$$

where the term in the bracket now corresponds to a split vortex beam with $|\ell|$ singularities, instead of an LG beam with a single vortex or order ℓ. Here φ_0 is an overall phase factor between the two orthogonally polarised beams, φ_1 is a phase factor between the modes used to create the split vortex beam and δ is the ratio between the beam waist of the additional Gaussian beam used to create the split vortex beam and the other LG modes which have the same waist w_0. This provides control over the position of the polarisation singularities, as will become evident in § 4.8.3.

Here, we will restrict ourselves slightly in the form of these beams, only considering those created using a circular polarisation basis. Figure 4.15 shows simulated polarisation profiles of beams of the form,

$$|\Psi_{\mathrm{multi}}\rangle = \mathrm{LG}_0^0(w_0)\,|\hat{l}\rangle + \left(\mathrm{LG}_0^\ell(w_0) + \mathrm{LG}_0^0(\delta w_0)\right)|\hat{r}\rangle\,, \tag{4.42}$$

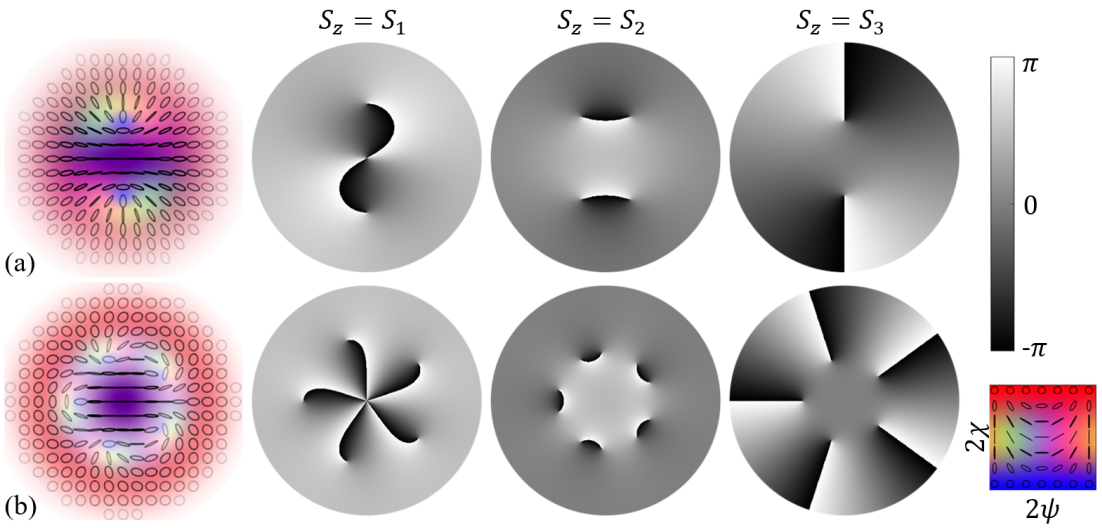

Figure 4.15: Simulated polarisation profiles and Stokes phase (Φ) distributions of optical skyrmions generated using split vortex beams as described by Eq. 4.42. The left of (a) shows an $n = 2$ skyrmion created using $\ell = 2$ and $\delta = 0.7$ in Eq. 4.42 and (b) shows an $n = 5$ skyrmion created using $\ell = 5$ and $\delta = 0.7$. On the right of (a) and (b), the relevant Φ is displayed when interpreting the skyrmion in different polarisation bases by assigning $S_z = S_1,\ S_2,\ S_3$, as indicated. Figure adapted from [211]

with skyrmion numbers 2 and 5 in (a) and (b) respectively. In Figure 4.15 I also show the associated Stokes phase profiles Φ for interpretation in different polarisation bases by assigning $S_z = S_1$, S_2 or S_3 in the generalised Stokes vector $\mathbf{S}_R$. The polarisation profile of these beams are reminiscent of the multi-skyrmions created using rational maps as seen in Ref. [251].

From inspection of the polarisation in Figure 4.15(a) and comparing it to the $n = 1$ beams shown in Figures 4.2(a), 4.4 or 4.6, we can see that it appears similar to two partially overlapping $n = 1$ optical skyrmions. Indeed, if we choose to calculate the skyrmion number of this beam using the topological method and a choice of $\mathbf{S}_R = [S_1, S_2, S_3]^T$, as shown in the far right of Figure 4.15(a), we can see that Φ contains two singularities located at the left handed circular polarisation locations (the Φ distribution has pick up the centre locations of the two components reminiscent of $n = 1$ beams). Both of these areas contribute a value of 1/2 to the overall skyrmion number and the outside contributes a value of 1. This shows how the topological approach to finding n can allow multi-skyrmions to be interpreted as a combination of individual skyrmion structures (as also demonstrated for the example of a multi-skyrmion ring above in § 4.5.3).

4.8.3 Tuning the polarisation singularity positions

In § 4.8.1 above, I discussed how it is possible to move the position of the vortex phase singularities in a split vortex beam in relation to the beam centre by changing the relative beam waists between the Gaussian and LG mode used. We can now consider using this characteristic of split vortex beams to make optical multi-skyrmions with interesting polarisation textures.

In Figure 4.16, I show the effect of changing the ratio between the beam waists δ on the resulting polarisation distributions and the singularities in Φ for a beam of the form of Eq. 4.42 with $\ell = 3$. On the bottom row of Figure 4.16 I show the corresponding Stokes phase profiles Φ when setting $S_z = S_3$, for each of the polarisation textures shown on the top row for each indicated δ. From this, it can be seen that the singularities in Φ move further from the beam centre, along with the pure left-handed circular polarisation components, as δ increases from 0 to 1. In fact, the location of these singularities is, perhaps to no surprise, the same as the location of the phase singularities in the split vortex beam, displaying the link between skyrmionic structures and the underlying differential OAM of the contributing modes [201]. Despite the difference in appearance of the polarisation patterns, all of the beams shown in Figure 4.16 have the same skyrmion number of $n = 3$, confirmed by both application of the surface integral method for evaluating skyrmion numbers Eq. 4.2, and the topological approach Eq. 4.32.

As well as being able to control the radial positions of the polarisation singularities relative to the beam centre, we can also choose to control where they appear azimuthally. This can simply be done by altering the φ_1 term in Eq. 4.41, which has the effect of rotating the locations of the phase singularities in the split vortex beam around its axis.

Beams of the form of those shown throughout this section (in Figures 4.15 and 4.16) and described by Eq. 4.42 give a further example of beams that can be added to the growing field of paraxial optical skyrmions. Additionally, they provide an example of ways in which optics can be used to investigate topologies not permitted in other fields.

4.9 Chapter 4 conclusion

I began this chapter by introducing the concept of a particular interesting topological structure, the skyrmion, often characterised by an integer topological number, known as the skyrmion number. These topological features have been seen in many areas of physics, but the work presented in this thesis has centred around an area of physics in which they have been more recently demonstrated - paraxial optics.

In § 4.3, I provided the theoretical details and properties of paraxial skyrmionic beams, describing how skyrmionic structures can lie within the spatially varying polarisation of vector beams, ultimately showing that optical skyrmions fall into a

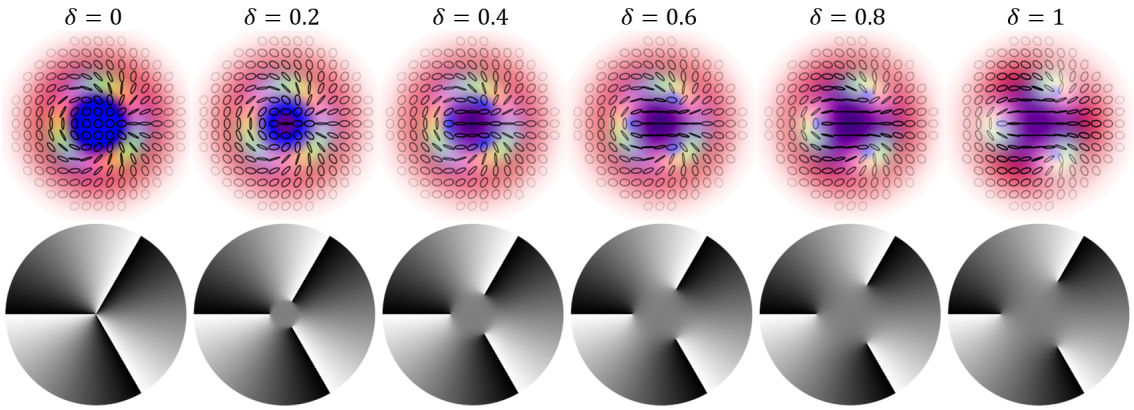

Figure 4.16: Simulated $n = 3$ optical skyrmions of the form of Eq. 4.42 for $\ell = 3$ and varying δ. The top row shows the polarisation profiles and the bottom row the Φ profiles when $S_z = S_3$ is chosen. Figure adapted from [211].

specific category of structured light beams. I then went on to describe the ways in which they can be created. In their simplest from, optical skyrmions can be constructed from the superposition of orthogonally polarised coaxial Gaussian and LG modes, with indices $\ell = n$ and $p = 0$. More generally, they can be constructed using the superposition of two orthogonally polarised LG_0^ℓ modes, with the resulting skyrmion number given by $\Delta\ell$.

The skyrmion number is a global property, dependent on the underlying skyrmion field, which points in the direction of the local Stokes vectors, $\mathbf{S}$. It counts the number of complete wrappings of $\mathbf{S}$ around the Poincaré sphere. From evaluation of the skyrmion number, we can examine the topological properties of paraxial beams, as such, accurate determination is crucial. In previous work, n has been evaluated using Eq. 4.2, which relies on the the surface integral of polarisation gradients over the entire transverse plane. Here, I introduced a novel method that we derived for calculating skyrmion numbers, with the full derivation outlined in § 4.4, and first published in [209]. This simple method is based on polarisation singularities and associated polarisation winding numbers, removing the need for derivatives and surface integration. Additionally, we find that the method provides an intuitive geometric insight into optical skyrmions by capturing the topological texture via contours along which the analysis is performed. This allows individual skyrmionic structures to be identified within multi-skyrmions, rather than just providing a single topological number to characterise the full transverse profile.

The topological method was confirmed by analysing an array of experimentally measured optical skyrmions and bimerons with different theoretical skyrmion numbers, as well as beams propagating under weak focusing, showing excellent agreement with theory, and compared to results obtained by applying the surface integral method.

One of the main incentives which inspired this new topological approach to skyrmion numbers was the inherent sensitivity of Eq. 4.2 to noise. In § 4.6, I presented an investigation based on applying background noise to simulated data to confirm that the new method is indeed more robust and predictable when evaluating noisy data. It was demonstrated, that by choosing a suitable basis in which to evaluate the topological method, then it becomes possible to obtain the correct skyrmion number for noise levels under which the surface integral method would fail.

Towards the end of this chapter, in § 4.8, I introduced a new way of generating optical multi-skyrmions with tunable polarisation textures using split-vortex beams. By superimposing oppositely polarised Gaussian and split-vortex beams of different waists, it was found that the skyrmion number is conserved as a function of waist scaling. For the examples of these beams, it could again be shown that the topological approach to finding n allows the individual skyrmion structures to be easily identified.

Research within the field of optical skyrmions is still in its infancy, but we believe that our new method to identify skyrmion numbers could directly benefit the growth of the discipline, particularly due to its performance in the presence of noise and the intuitive understanding it brings. Additionally, we believe that the tunable multi-skyrmions presented here could be an interesting addition to the growing research field.

Chapter 5

Polarisation tomography using generalised measurements

5.1 Chapter 5 introduction

The tomography of vector beams is generally performed using projection measurements (for example using Stokes polarisation tomography as discussed previously in § 2.3) and is carried out to determine both polarisation and the constituent spatial modes. In this chapter, I am going to focus on another way in which vector light beams can be characterised by performing positive operator valued measurements (POVMs) using interferometric systems, and give details of a potential application.

Throughout this chapter, I will adopt a quantum language to emphasis the strong connection with quantum tomography. Even though the experiments that will be discussed here were performed entirely for classical light, the techniques could also be applied to single photons, and the theory presented is valid in both the classical and quantum domains.

The work that will be presented here started with an interest in previous theoretical work on minimal qubit tomography [267], which proposed a highly efficient scheme for the determination of a single-qubit state. This scheme implementing a minimal POVM was later carried out experimentally for uniformly polarised beams by Ling et al [268]. Within the Optics group at the University of Glasgow, it became an aim to employ some of the ideas presented in the previous work to design an experimental system which could perform spatially dependent POVMs, allowing the determination of the spatially varying polarisation of vector beams with a single camera image [269]. This research was undertaken in collaboration with a visiting professor, Sebastião Pádua, from the Universidade Federal de Minas Gerais and was successful in accurately characterising vector beams, with superior data acquisition speeds in comparison to traditional Stokes tomography. However, the experimental setup used for this project had some issues in terms of stability, as will be discussed.

As part of my PhD research, I became involved in this project, where the desire

was now to redesign the experimental setup in order to improve stability. As measurements were already obtained with a single camera frame, an improved stability over time would allow the possibility of time-resolved measurements, for example investigating temporal changes in optical activity.

This chapter is split into three main parts. The first part outlines the theoretical concept of generalised measurements and provides a summery of the previous work. The second part introduces the new improved experimental setup for single-shot[1] vector beam characterisation employing POVMs and details the experimental procedures and features. Finally, the third part will present a possible application in the form of dynamic Mueller matrix polarimetry.

The work that will be outlined in parts two and three of this chapter was completed in collaboration with my supervisor, Sonja Franke-Arnold, visiting professor, Sebastião Pádua from the Universidade Federal de Minas Gerais, and fellow PhD students form the University of Glasgow Optics group, Mustafa A. Al Khafaji and Sphinx J. Svensson. For the project, I was responsible for building and aligning the optical setup and improving on initial designs of the system, the beam generation, acquiring and processing experimental data, developing the dynamic Mueller matrix method with accompanying analysis process and error calculation. I also performed theoretical simulations, both for the vector beam characterisation and Mueller matrix determination. M. A. Al Khafaji helped with the initial optical system design and provided insights from the previous work performed within the group, S. J. Svensson assisted with acquiring some of the experimental data, S. Franke-Arnold lead the project, providing ideas for improving and building on the previous work, and S. Pádua also helped guide the project, bringing theoretical insights, and assisted with the first iteration of building the experimental system.

Some of the work presented in this chapter can be seen in Ref. [270].

5.2 Chapter 5 Part 1: Generalised measurements

Before I discuss the the implementation of generalised measurements to characterise polarisation, it is beneficial to first visit the idea of measurements in quantum mechanics. Some of the basics of this are covered in the following subsection. I will then show how these concepts can be taken and applied within the field of polarisation tomography, by considering a polarisation state as a qubit, with the benefit of reducing the required number of measurements from 6 to 4. Finally, I will start the discussion of how this can be implemented experimentally.

[1]Note that throughout this chapter, whenever the term single-shot is used, we are referring to experimental measurements obtained from an individual camera frame.

5.2.1 Measurements in quantum mechanics

In quantum mechanics, it is important to be able to create, encode and manipulate quantum states, and it is equally important to be able to characterise them. This has implications in areas of research such as quantum computing, quantum cryptography and communications [271–275]. A feature of quantum mechanics is that the outcomes of measurements are probabilistic, and that the process of taking a measurement is *active* - i.e. the post-measurement state will be changed.

In quantum theory, we are often interested in using measurements to determine the properties of a system. It is usually assumed that we have access to a large enough quantity of identically prepared systems on which repeat measurements can be performed in order to build up statistics, and obtain a reasonable approximation of the quantum state of the system. Therefore, expectation values are normally used (the weighted average of all the possible outcomes, as weighted by their probability) [254, 276].

However, the expectation value is only meaningful in the limit of a large number of measurements on identically prepared quantum systems. In some applications (such as in quantum information) you only have access to one copy of the state you would like to characterise, or very few copies, meaning that the choice of measurement becomes important. Ideally, the goal is to extract maximal information from as few measurements as possible, with the minimum number of measurements determined by the size of the state space [254, 277].

Projective measurements

The simplest form of measurements are referred to as *projective measurements* or *von Neumann measurements* after the mathematician[2] who gave gave the approach its mathematical formulation [254].

For an operator $\hat{A}$, its relationship with its eigenstates and eigenvalues can simply be expressed using the eigenvalue equation,

$$\hat{A}\left|\lambda_i\right\rangle = \lambda_i \left|\lambda_i\right\rangle . \tag{5.1}$$

When dealing with a small numbers of states, we are now instead interested only in probability distributions (P) rather than expectation values. In terms of a set of projectors, $\hat{P}_i = \left|\lambda_i\right\rangle \left\langle\lambda_i\right|$, the probability distribution of obtaining an outcome λ_i is,

$$P(\lambda_i) = \mathrm{Tr}(\hat{\rho}\hat{P}_i), \tag{5.2}$$

where $\hat{\rho}$ is the density operator and Tr represents the trace operator.

[2] As well as being a mathematician, John von Neumann was also a physicist, computer scientist, engineer and polymath.

The projectors $\hat{P}_i$ can be thought of as operators that project onto the basis vector corresponding to the measurement outcomes and have the following properties [254],

Table 5.1: Properties of projectors

1. Hermitian	$\hat{P}_i^\dagger = \hat{P}_i$
2. Positive	$\hat{P}_i \geq 0$
3. Complete	$\sum_i \hat{P}_i = \hat{I}$
4. Orthonormal	$\hat{P}_i \hat{P}_j = \hat{P}_i \delta_{ij}$

From property 4, the projectors form an orthonormal basis for the Hilbert space describing the physical system, with each possible outcome of that measurement corresponding to one of the vectors comprising the basis.

As an example, we can relate this to polarisation, which can be represented in a two-dimensional Hilbert space, visualised using the Poincaré sphere (or Bloch sphere), and Stokes parameters. Physically, these parameters directly correspond to a select pair of projective measurements [276],

$$S_0 = P_{|\hat{h}\rangle} + P_{|\hat{v}\rangle} \tag{5.3}$$

$$S_1 = P_{|\hat{h}\rangle} - P_{|\hat{v}\rangle} \tag{5.4}$$

$$S_2 = P_{|\hat{d}\rangle} - P_{|\hat{a}\rangle} \tag{5.5}$$

$$S_3 = P_{|\hat{r}\rangle} - P_{|\hat{l}\rangle} \tag{5.6}$$

This is equivalent to the form of the Stokes parameters written before in § 1.3.2, but rewritten using the notation used in this section, and to make it clear that these are probabilities obtained as a result of projective measurements.

Therefore, using projective measurements to fully determine a polarisation state requires 6 individual projections - i.e. 2 measurements for each of the 3 orthonormal bases which comprise a set of mutually unbiased bases (MUBs) fully describing the 2d Hilbert space.

The number of MUBs required scales with the dimension of the Hilbert space, however, the relation between the two is not simple. In fact, the maximal set of MUBs is only known for Hilbert spaces with certain dimensions d. More specifically, it is only known when we have a prime-power dimension, $d = p^m$, where p is a prime number and m a positive integer. For more details, the reader is referred to [278].

Generalised measurements

Another useful way of performing measurements in quantum information uses probability operators π_i, the set of which is known as a positive operator value measure (POVM). The set of operators $\{\hat{\pi}_i\}$ are defined by the following properties outlined in Table 5.2,

Table 5.2: Properties of POVM operators

1. Hermitian	$\hat{\pi}_i^\dagger = \hat{\pi}_i$
2. Positive	$\hat{\pi}_i \geq 0$
3. Complete	$\sum_i \hat{\pi}_i = \hat{I}$

The POVM element $\hat{\pi}_i$ is associated with an outcome i, and the probability of obtaining i, when performing a measurement on a system prepared in a state described by the density operator $\hat{\rho}$ is,

$$P(i) = \mathrm{Tr}(\hat{\rho}\hat{\pi}_i). \tag{5.7}$$

These types of probability measurements are often termed generalised measurements as they are a *generalisation* of projective measurements. The main difference between projective measurements and POVM measurements is that the POVM operators need not be orthogonal. As such, there is no restriction on the number of elements in a POVM (it can be greater or less than the dimension of the state space), whereas the number of projectors cannot exceed the dimension of the state space [254].

One way to obtain the full tomography of a quantum state by employing generalised measurements [254, 279, 280], is by ensuring the use of informationally complete POVMs (IC-POVMs) [281–283]. However, we may want to be able to uniquely determine a state using a minimum number of measurements. For this, the measurements are chosen to form a minimum informationally complete positive operator value measure (MIC-POVM) [283, 284]. An IC-POVM and a MIC-POVM are related in that, if we have d-dimensional Hilbert space, then an IC-POVM is said to be a MIC-POVM if it contains exactly d^2 linearly independent elements [277].

5.2.2 Applying generalised measurements to polarisation

Due to the fact that the polarisation degree of freedom can be represented by a two-dimensional Hilbert space, there exists an entire class of experiments that use a photon's polarisation state as the carrier of the quantum bit, or qubit [267, 285–287]. In fact, it can be argued that the first experimental technique for determining the state of a quantum system was devised in 1852 by George Stokes, as his well-known four Stokes parameters allow the easy experimental determination of a polarisation state [47].

As well as quantum optics and quantum information applications [288], polarisation profiling also plays a crucial role in various metrological applications, such as the characterisation and stress analysis of materials [289–291], ellipsometry [292, 293], pharmaceutical ingredient analysis [294] and biological microscopy [295,296]. Therefore, accurate determination of polarisation is important in both classical as well as quantum optics.

As mentioned above, a state belonging to a Hilbert space of dimension d requires a minimum of d^2 measurements for the state reconstruction. Therefore, polarisation requires a minimum of $d^2 = 4$ measurements for reconstruction [271], which are associated with the 4 parameters of a Stokes vector. For experimental convenience[3], Stokes parameters are generally obtained using six measurements, corresponding to projections into the horizontal, vertical, diagonal, anti-diagonal, right- and left-handed circular polarisation bases ($|\hat{h}\rangle$, $|\hat{v}\rangle$, $|\hat{d}\rangle$, $|\hat{a}\rangle$, $|\hat{r}\rangle$ and $|\hat{l}\rangle$). These projections form an overcomplete set of measurements composed from three pairs of mutually unbiased bases.

We can instead adopt the mathematical ideas from the measurements used in quantum mechanics to identify a quantum state, to polarisation tomography. By applying generalised measurements in the form of MIC-POVMs to polarisation determination, the number of required measurements can be reduced from 6 to 4. For this we must have operators that satisfy the conditions outlined in Table 5.2 and are written in the form of projection operators as $\hat{\pi}_i = \frac{1}{d} |\phi_i\rangle \langle\phi_i|$, where $|\langle\phi_i|\phi_j\rangle|^2 = (d\delta_{ij} + 1)/(d + 1)$, for associated states $|\phi_i\rangle$. Here, $|\phi_i\rangle$ are the states associated with the POVM outcomes, often referred to as *POVM states* from here on.

To satisfy these requisites, we choose 4 POVM states that correspond to the four corners of a tetrahedron lying on the surface of the Poincaré sphere, as the equally spaced and symmetric distribution of the states ensures no privilege in the reconstruction. The chosen states are given by,

$$\begin{aligned} |\phi_1\rangle &= a\,|\hat{h}\rangle + b\,|\hat{v}\rangle\,, \quad |\phi_2\rangle = a\,|\hat{h}\rangle - b\,|\hat{v}\rangle\,, \\ |\phi_3\rangle &= b\,|\hat{h}\rangle + ia\,|\hat{v}\rangle\,, \quad |\phi_4\rangle = b\,|\hat{h}\rangle - ia\,|\hat{v}\rangle\,, \end{aligned} \tag{5.8}$$

where,

$$a = \sqrt{\frac{1}{2} + \frac{1}{2\sqrt{3}}}, \quad b = \sqrt{\frac{1}{2} - \frac{1}{2\sqrt{3}}}. \tag{5.9}$$

These are the same states introduced by [267] and implemented by [268] for the tomography of homogeneously polarised beams using an optimal polarimeter. The polarisations associated with these states and their related locations on the Poncaré sphere are shown in Figure 5.1.

[3]Indeed, this is what is used for all the other polarisation measurements throughout this thesis.

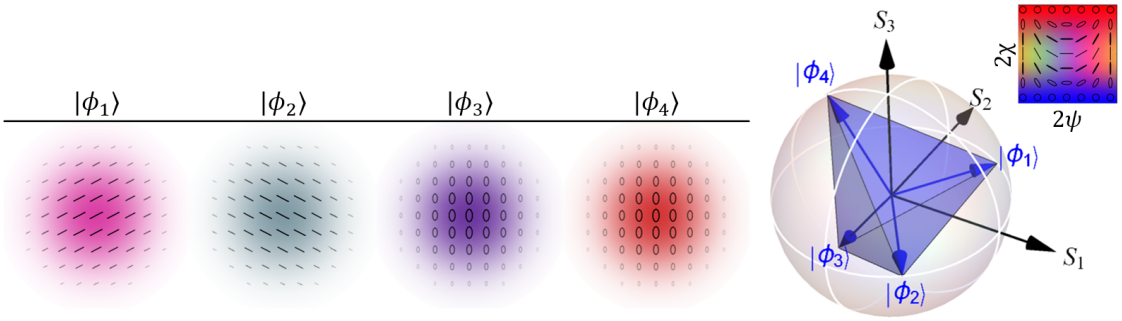

Figure 5.1: Polarisation profiles of the four POVM states described by Eq. 5.8 and their positions on the Poincaré sphere. The states form a tetrahedron on the sphere, as indicated in blue. The polarisation colour map is shown in the top right where ψ and χ represent the polarisation orientation and ellipticity angles, respectively, and intensity is shown as opacity. Figure adapted from [270].

There exist an infinite number of possible tetrahedrons, but from Figure 5.1, it can be seen that two of the polarisation states are linear, (they lie on the equator of the Poincaré sphere) and can be accessed relatively easily using conventional polarisation optical elements. Keeping two of the states located on the equator offers experimental convenience, but still provides a large selection of the infinitely possible tetrahedral configurations to choose from.

The probability of obtaining an outcome i on a system that is prepared in state $|\psi\rangle$ is then simply given by,

$$P_i = \langle\psi|\hat{\pi}_i|\psi\rangle = \mathrm{Tr}(\hat{\pi}_i\hat{\rho}). \tag{5.10}$$

In Eq. 5.8, 5.10 and throughout this chapter, I have adopted a quantum notation to describe the polarisations to emphasise the strong connection with quantum tomography. Even though here we will only be dealing with classical light beams, in theory, this could also be applied to single photons.

In order to perform measurements on the *non-orthogonal* POVM states $|\phi_i\rangle$, a common strategy is to form a Naimark extension of the measurement [254, 279] by increasing the Hilbert space of the input states with the addition of an auxiliary state. This action is carried out such that the extended Hilbert space now contains a set of *orthogonal* projection operators. The Naimark extension has the physical interpretation of the extended Hilbert space being a combination of the states we want to measure and another known system (the auxiliary state) [297]. Here we use the path degree of freedom [268, 280, 298], such that the input state has two propagation directions available. Full details on how the process of a Naimark extension can lead to the four necessary outcomes of the POVM measurement can be seen in Ref. [269] and the associated Supplementary Documentation [299].

In the case of spatially resolved light beams, performing a measurement imple-

menting the desired POVM will result in four output intensity profiles, I_i, which can be detected by a camera. This allows the normalised four component intensity vector,

$$\mathbf{I}^{(\mathrm{N})} = (I_1, I_2, I_3, I_4)^T / I_t, \tag{5.11}$$

to be obtained, where I_t is the total intensity given by $I_t = \sum_{i=1}^{i=4} I_i$.

These four intensities are all that is needed to determine the Stokes vector of the state. First, we need an expression for the density operator, which, for a single-qubit, can be written in terms of the normalised Stokes vector ($\mathbf{S}^{(\mathrm{N})}$) as [276],

$$\hat{\rho} = \frac{1}{2}\sum_{i=0}^{3} S_i \hat{\sigma}_i = \frac{1}{2}\begin{pmatrix} 1 + S_1^{(\mathrm{N})} & S_2^{(\mathrm{N})} - iS_3^{(\mathrm{N})} \\ S_2^{(\mathrm{N})} + iS_3^{(\mathrm{N})} & 1 - S_1^{(\mathrm{N})} \end{pmatrix}, \tag{5.12}$$

where σ_i are the Pauli matrices and $\mathbf{S}^{(\mathrm{N})} = (S_0, S_1, S_2, S_3)/S_0$. Recalling Eq. 5.10, we can now obtain a relationship between the intensity distribution and the (normalised) Stokes vector of the polarisation to be measured by,

$$\mathbf{I}^{(\mathrm{N})} = \Pi \cdot \mathbf{S}^{(\mathrm{N})}, \tag{5.13}$$

where Π is the 4×4 instrumentation matrix, given by

$$\Pi = \frac{1}{4}\begin{pmatrix} 1 & \sqrt{\frac{1}{3}} & \sqrt{\frac{2}{3}} & 0 \\ 1 & \sqrt{\frac{1}{3}} & -\sqrt{\frac{2}{3}} & 0 \\ 1 & -\sqrt{\frac{1}{3}} & 0 & -\sqrt{\frac{2}{3}} \\ 1 & -\sqrt{\frac{1}{3}} & 0 & \sqrt{\frac{2}{3}} \end{pmatrix}, \tag{5.14}$$

for an ideal experimental polarimeter. The horizontal entries of Π correspond to the Stokes vectors of each of the POVM states, $|\phi_i\rangle$. By inverting Eq. 5.13, spatially varying Stokes vectors can be recovered from the four spatially varying intensity measurements.

The first experimental implementation of these POVM states to measure polarisation was realised by Ling et al [268], where they made use of a custom partially polarising beam splitter. This work only concerned homogeneously polarised states. In section § 5.2.4, I will give an overview of the work previously carried out within the Optics group in order to perform the tomography of vector beams implementing the same POVM states. But first, it is useful to visit the idea of a partially polarising beam splitter in more detail, and how it is possible to build these using standard optical elements. This will be covered in the following section.

5.2.3 Concept of a partially polarising beam splitter

There are two main types of beam splitter that are readily available commercially: a non-polarising beam splitter (NPBS), which transmits 50% of the input intensity

and reflects the other 50%, and a polarising beam splitter (PBS), which is a crucial element for spatially splitting or extracting the horizontal and vertical polarisation components of a beam by transmitting one (horizontal), and reflecting the other (vertical).

However, there exist applications, particularly within quantum optics, in which a particular set of transmission and reflection coefficients are required for each of the horizontal and vertical polarisation components. Examples of this include, quantum logic gates [300–302], quantum walks [303, 304], techniques for quantum state estimation [268, 269, 305] and even experimental studies into wave-particle duality [306, 307]. For these applications an element known as a partially polarising beam-splitter (PPBS) is used.

To illustrate the properties of a PPBS, first consider a diagonally polarised beam (with equal $|\hat{h}\rangle$ and $|\hat{v}\rangle$ components) incident on an arbitrary beam splitter, as shown in Figure 5.2. The outputs from both arms will depend on the polarisation dependent transmission (T) and reflection (R) coefficients. For a PBS (Figure 5.2(a)), all of the input horizontally polarised light is transmitted and the vertically polarised light reflected, therefore, to satisfy this, we must have $T_h = R_v = 1$ and $R_h = T_v = 0$. If instead, $T_h = T_v = R_h = R_v = \frac{1}{2}$, as in Figure 5.2(b), then both the horizontally and vertically polarised components of the light are equally transmitted and reflected, leaving us with a non-polarising beam splitter[4]. However, in theory, we can choose any splitting ratio, $T\!:\!R$, between the two beam splitter output ports for the horizontal and vertical polarisations independently. An example of this is illustrated in Figure 5.2(c) for $T_h = R_v = \frac{2}{3}$ and $R_h = T_v = \frac{1}{3}$. Therefore, two-thirds and one-third of the horizontal and vertical light, respectively, is transmitted, with the rest reflected. In this case, we have *partially* split the individual polarisation components, creating a PPBS.

It is possible to make PPBS using layers of dielectric coatings with different T and R coefficients for each polarisation. However, such optical elements must be custom made and are therefore expensive, and once fabricated, the coefficients cannot be changed. Nevertheless, it turns out that it is possible to make a simple optical setup using widely available components that performs the same as a PPBS [308]. A schematic of which is given in Figure 5.3 and is based on a Mach-Zehnder interferometer.

Consider, as an input to PBS_1 in Figure 5.3, a beam with horizontal and vertical polarisation components of the form,

$$\mathbf{E}_{\text{in}} = \begin{pmatrix} E_{\text{in}}^{h} \\ E_{\text{in}}^{v} \end{pmatrix}.$$

The PBS will divide the beam into its horizontal and vertical components, so we

[4] It should be noted that Figure 5.2(b) depicts an idealised version of a non-polarising beam splitter. Real NPBSs that are often used in optics labs will transmit/reflect half of the intensity, but the polarisation is not necessarily conserved.

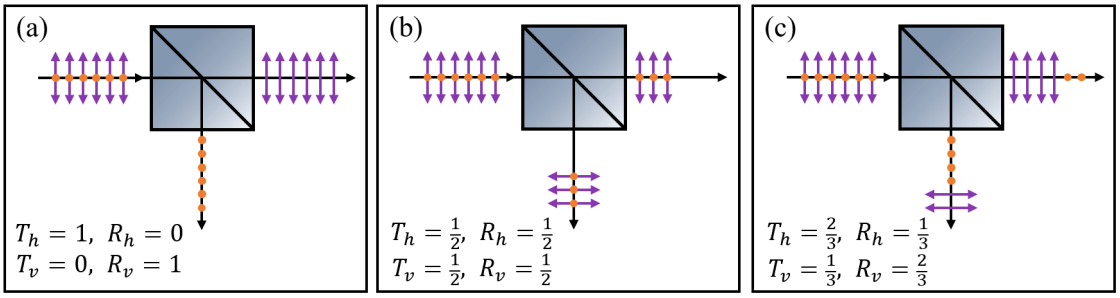

Figure 5.2: Illustration of a partially polarising beam splitter and the dependence on transmission and reflection coefficients. (a) For $T_h = R_v = 1$, we have a PBS, with all horizontally (vertically) polarised light transmitted (reflected). (b) When all transmission and reflection coefficients are $\frac{1}{2}$, we have a NPBS with half of all intensity transmitted and the other half reflected[4]. However, if $T_h = R_v = \frac{2}{3}$ and $R_h = T_v = \frac{1}{3}$, as in (c), then we have a PPBS, with two-thirds of the horizontal and one-third of the vertical light transmitted, and the rest reflected.

will deal with the transmitted and reflected paths separately, labelled as A and B in Figure 5.3 respectively. Following path A up until the second PBS we get,

$$\begin{aligned}\mathbf{E}_{\mathrm{A}} &= \mathbf{J}_{\mathrm{HWP}}(\alpha)\mathbf{J}_{\mathrm{M}}\begin{pmatrix} E^h_{\mathrm{in}} \\ 0 \end{pmatrix}, \\ &= iE^h_{\mathrm{in}}\begin{pmatrix} \cos(2\alpha) \\ \sin(2\alpha) \end{pmatrix},\end{aligned} \tag{5.15}$$

where $\mathbf{J}_{\mathrm{M}}$ is the Jones matrix of a mirror, $\mathbf{J}_{\mathrm{HWP}}(\alpha)$ is the Jones matrix of a half-wave plate with its fast axis rotated to an angle α. Both of these matrices are given in § 2.2.3.

Now following path B up until the second PBS, in a similar manner, but first applying a $\pi/2$ phase shift to the reflected beam from the input PBS, we obtain,

$$\begin{aligned}\mathbf{E}_{\mathrm{B}} &= \mathbf{J}_{\mathrm{HWP}}(\beta)\mathbf{J}_{\mathrm{M}}\begin{pmatrix} 0 \\ iE^v_{\mathrm{in}} \end{pmatrix}, \\ &= E^v_{\mathrm{in}}\begin{pmatrix} \sin(2\beta) \\ -\cos(2\beta) \end{pmatrix},\end{aligned} \tag{5.16}$$

where, in this case, the HWP is at an angle β.

To get output 1, we combine the transmitted (horizontal) component of the beam from path B, the reflected (vertical) component of the beam from path A and apply HWP_3 which is set to 45°,

$$\begin{aligned}\mathbf{E}_{\mathrm{out},1} &= \mathbf{J}_{\mathrm{HWP}}(45^\circ)\begin{pmatrix} E^v_{\mathrm{in}}\sin(2\beta) \\ -E^h_{\mathrm{in}}\sin(2\alpha) \end{pmatrix}, \\ &= \begin{pmatrix} -E^h_{\mathrm{in}}\sin(2\alpha) \\ E^v_{\mathrm{in}}\sin(2\beta) \end{pmatrix}.\end{aligned} \tag{5.17}$$

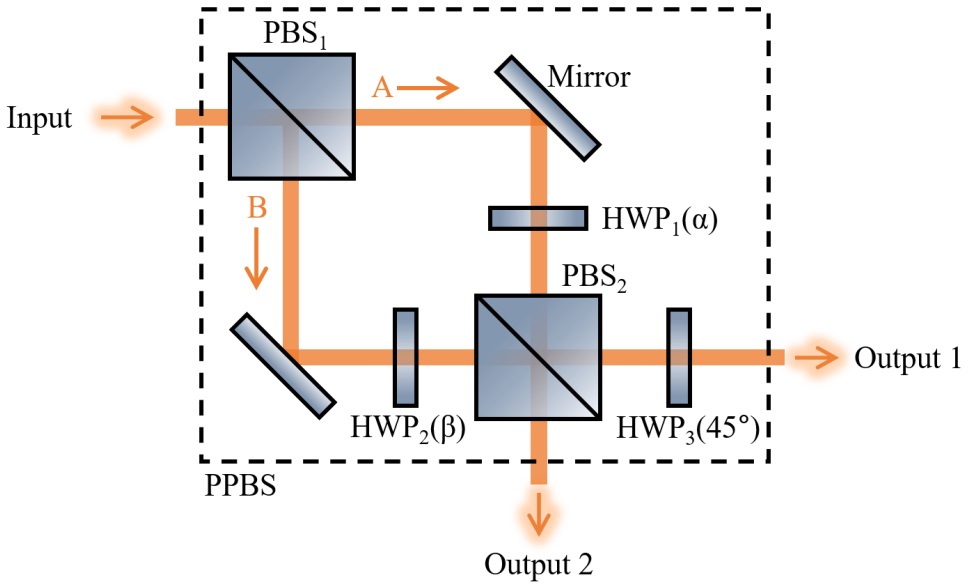

Figure 5.3: Schematic of a partially polarising beam splitter (PPBS) based on a Mach-Zehnder interferometer configuration and constructed using readily available polarisation beam splitters (PBS) and half-wave plates (HWP). HWP_1 is rotated to an angle α, HWP_2 to an angle β and HWP_3 to 45°. The angles α and β can be chosen to individually control the proportion of horizontal and vertical polarisation at outputs 1 and 2.

Finally, to obtain output 2, we need to combine the transmitted (horizontal) component from path A and the reflected (vertical) component of path B, giving us,

$$\mathbf{E}_{\text{out},2} = i \begin{pmatrix} E_{\text{in}}^{h} \cos(2\alpha) \\ -E_{\text{in}}^{v} \cos(2\beta) \end{pmatrix}. \tag{5.18}$$

By inspection of $\mathbf{E}_{\text{out},1}$ and $\mathbf{E}_{\text{out},2}$ and comparing them to $\mathbf{E}_{\text{in}}$, it is evident that each output has a horizontal and vertical polarisation component, the magnitude of which is completely dependent on the angle of the HWPs within the interferometer. Therefore, the HWPs have introduced polarisation-dependent phases between the two paths, and the simple setup shown in Figure 5.3 provides an example of a way in which a partially polarising beam splitter can be constructed using common optical components.

A similar example of a PPBS but implemented using NPBSs instead of PBSs can be seen in Ref. [308].

The ideas described in this section will be applied to the experimental designs presented later in this chapter used to implement generalised measurements.

It should be noted, that it is possible in some cases to use a normal PBS to extract and measure a single POVM element, however, afterwards, only the orthogonal

component of the state remains, making it impossible to measure later elements. This is one of the reasons that PPBS's are useful for quantum state estimation, as they make possible the partial projection onto each element, leaving the remaining state mostly unaltered [305].

5.2.4 Summary of previous work

As I mentioned in the introduction of this chapter, the generalised measurements discussed above were performed within the Optics group to characterise vector beams [269]. This work was the first time that spatially dependent POVM measurements have been demonstrated. Additionally, the measurements were implemented such that all the required information could be acquired with a single camera image, providing improved data acquisition speeds in comparison to Stokes tomography which is often carried out using six sequential images.

In this section, I will give a brief overview of the experimental system used for this work, in order to provide a baseline for my own work that will be discussed in § 5.3 and § 5.4.

Figure 5.4 shows a schematic of the setup used in Ref. [269] to experimentally realise the instrumentation matrix given in Eq. 5.14 and perform spatially dependent POVM measurements using a Mach-Zehnder interferometric design. The experimental system follows the general outline of the polarimeter for homogeneously polarised states in Ref. [268], however applied to beams with spatially varying polarisation. Additionally, this experimental system does not use a custom PPBS but instead builds a PPBS using common optical elements using the methods described above in § 5.2.3.

For this experiment, arbitrary vector beams of the form,

$$|\psi\rangle = |u_h\rangle\,|\hat{h}\rangle + \mathrm{e}^{i\phi}\,|u_v\rangle\,|\hat{v}\rangle\,, \tag{5.19}$$

were generated using the same DMD beam generation setup as described in § 2.6. The polarisation of the beam was confirmed using Stokes polarimetry, which also provided a control over which to assess the performance of the POVM polarisation tomography.

The generated vector beams were directed towards the measurement system in Figure 5.4 where a polarising beam splitter (PBS_1) splits the beam into its $|\hat{h}\rangle$ and $|\hat{v}\rangle$ components. The light now travels along two paths (α and β), introducing a path degree of freedom, and hence realising the Naimark extension as mentioned above. After PBS_1, the state can now be represented as,

$$|u_h\rangle \otimes |\hat{h}\rangle \otimes |k_\alpha\rangle + \mathrm{e}^{i\phi}\,|u_v\rangle \otimes |\hat{v}\rangle \otimes |k_\beta\rangle\,, \tag{5.20}$$

where $|k_\alpha\rangle$ and $|k_\beta\rangle$ are the linear momenta along the associated paths. The first Mach-Zehnder interferometer in Figure 5.4, consisting of PBS_1, HWP_1, HWP_2 and

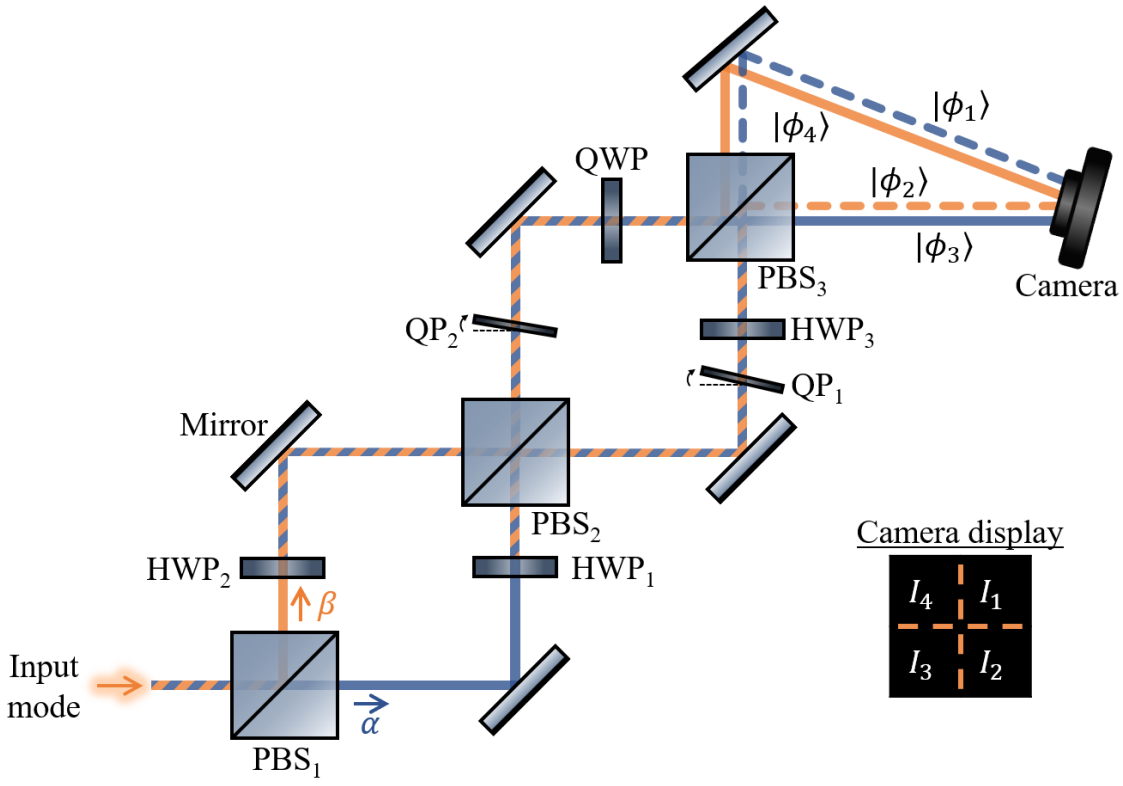

Figure 5.4: Schematic of experimental setup for single-shot spatially dependent POVM measurements using a Mach-Zehnder interferometer. The colour of the beams represent the polarisation, blue for horizontal, orange for vertical and a mix for a superposition of both. HWP and QWP are half- and quarter-wave plates. PBS are polarising beam splitters and QP are quartz plates, rotated about their vertical axis. HWP$_1$ and HWP$_2$ are rotated to angles $\theta_1 = \frac{1}{2}\sin^{-1}(a)$ and $\theta_2 = \frac{1}{2}\sin^{-1}(b)$, respectively. HWP$_3$ is at 67.5° and the QWP is at 45°. The insert of the camera display shows the arrangement of the four quadrants recording the intensities of the POVM projections.

closed by PBS_2 makes up the PPBS (with the aid of HWP_3 on one of the outputs). HWPs 1 and 2 are rotated to angles,

$$\begin{aligned}\theta_1 &= \frac{1}{2}\sin^{-1}(a)\\ \theta_2 &= \frac{1}{2}\sin^{-1}(b),\end{aligned} \tag{5.21}$$

where a and b are the coefficients given in Eq. 5.9. This ensures that the $\hat{h} : \hat{v}$ amplitude ratio becomes $a{:}b$ in path α and $b{:}a$ in path β. Experimentally, this can be checked by measuring the respective intensities at the two outputs[5].

The half-wave plate in path α (HWP_3) has its fast axis rotated to 67.5°, and prepares states $|\phi_1\rangle$ and $|\phi_2\rangle$. States $|\phi_3\rangle$ and $|\phi_4\rangle$ are prepared by the QWP in path β which is rotated to 45°.

Therefore, the full state transformation is realised by the four waveplates in the system and can be written as,

$$\begin{aligned}
|\hat{h}\rangle \otimes |k_\alpha\rangle &\mapsto \left(-ia\frac{\sqrt{2}}{2}\left(|\hat{h}\rangle + |\hat{v}\rangle\right) \otimes |k_\alpha\rangle - ib\frac{\sqrt{2}}{2}\left(|\hat{h}\rangle - i\,|\hat{v}\rangle\right) \otimes |k_\beta\rangle\right) \mathrm{e}^{i\phi_\alpha}\\
|\hat{v}\rangle \otimes |k_\alpha\rangle &\mapsto \left(ib\frac{\sqrt{2}}{2}\left(|\hat{h}\rangle - |\hat{v}\rangle\right) \otimes |k_\alpha\rangle - a\frac{\sqrt{2}}{2}\left(|\hat{h}\rangle + i\,|\hat{v}\rangle\right) \otimes |k_\beta\rangle\right) \mathrm{e}^{i\phi_\beta}\\
|\hat{h}\rangle \otimes |k_\beta\rangle &\mapsto \left(a\frac{\sqrt{2}}{2}\left(|\hat{h}\rangle - |\hat{v}\rangle\right) \otimes |k_\alpha\rangle + b\frac{\sqrt{2}}{2}\left(-i\,|\hat{h}\rangle + |\hat{v}\rangle\right) \otimes |k_\beta\rangle\right) \mathrm{e}^{i\phi_\beta}\\
|\hat{v}\rangle \otimes |k_\beta\rangle &\mapsto \left(-b\frac{\sqrt{2}}{2}\left(|\hat{h}\rangle + |\hat{v}\rangle\right) \otimes |k_\alpha\rangle + a\frac{\sqrt{2}}{2}\left(|\hat{h}\rangle - i\,|\hat{v}\rangle\right) \otimes |k_\beta\rangle\right) \mathrm{e}^{i\phi_\alpha}
\end{aligned} \tag{5.22}$$

Here, ϕ_α and ϕ_β are additional phases that are acquired due to the differing optical path length of the two interferometer arms. Experimentally, these phase shifts can be cancelled by tilting the quartz plates (QP in Figure 5.4) about their vertical axes.

Lastly, PBS_3 performs the final projection measurement by splitting the horizontal and vertical components from paths α and β and thus separating $|\phi_1\rangle$ and $|\phi_2\rangle$ from path α and $|\phi_3\rangle$ and $|\phi_4\rangle$ from path β. The four resulting intensity profiles from the projection are directed onto a single camera sensor, where they are recorded in for separate quadrants, as shown in the inset of Figure 5.4. This allows the POVM measurements of the input beam to be measured in a single-shot, and the spatially varying polarisation to be recovered using the inverse of Eq. 5.13.

[5]When measuring the ratio between the horizontal and vertical intensities at the outputs of the PPBS, recall that intensities are amplitudes squared, i.e. we are interested in the values a^2 and b^2. We expect to obtain 79% : 21% of $\hat{h}{:}\hat{v}$ after HWP_3 in path α and 21% : 79% after PBS_2 in path β.

Before measurements could be taken, the interferometric system must be calibrated to remove any unwanted phase shifts and the experimental instrumentation matrix measured. The process of this is very similar to that which is used for the updated experimental system introduced in Chapter 5 Part 2, and as such, the calibration process will be discussed in detail in § 5.3.2.

A selection of vector beams were used to test the performance of the spatially resolved POVM measurements using the setup in Figure 5.4, with the resulting polarisation compared to both the polarisation measured using Stokes tomography and theoretically simulated polarisation distributions. The polarisation obtained using the POVM measurements showed excellent agreement to both. The full results of this can be seen in [269]. Although the experiment discussed here provided a good tomography, and proof of principle demonstration of the technique, achieving interferometric stability was challenging. It was found to be particularly challenging for the case of the spatially extended beams we are interested in here, as a greater transverse coherence needs to be maintained throughout the entire setup, compared to that required for homogeneously polarised beams with much smaller waists. The inherent sensitivity of the Mach-Zehnder interferometer to phase shifts (caused by, for example, vibrations or air currents) meant that the system needed frequent realignment and a new instrumentation matrix measured each time. This poses an issue if stability over time would be required, for example, when taking time resolved measurements.

To try and overcome these problems, improvements to the experimental setup were proposed, by replacing the Mach-Zehnder interferometer with a Sagnac interferometer configuration. This new experimental system will be discussed in the next section, measurement results presented and the stability assessed.

5.3 Chapter 5 Part 2: Experimental realisation using an improved system

As part of my PhD research, it became my task to work on building an updated experimental system for performing POVM measurements, with the main aim of improving stability, such that it could then be used for some potential applications (see § 5.4). In the following sections, I will outline the new setup and give full details of the experimental calibration process and in § 5.3.3 I will discuss an experimental investigation performed in order to asses the stability of the new setup. The underlying theory to this experiment is identical to that discussed above (with some slight differences to account for differing mirror reflections) and hence will not be repeated here. Finally, in § 5.3.4, I will present the polarisation tomography results using the updated system.

5.3.1 Sagnac interferometer for spatial POVM tomography

If we consider the geometric beam path of an interferometer as a means of characterisation[6], then we end up with two main classes of interferometer, namely, double path and common path. The difference between these two types of interferometer is exactly as the names suggest: A double path interferometer, is one in which the reference and sample beams travel along different physical paths before being recombined (examples include Michelson, Mach-Zehnder and Twyman–Green [311] interferometers), whereas, in a common path interferometer, the two beams traverse the same geometric trajectory (for example, Sagnac interferometers and the fibre optic gyroscope [312]). Although the beams travel the same path, depending on the interferometer type and application, they may travel in opposite directions, or in the same direction but with orthogonal polarisations.

Generally, common path interferometers are more robust to environmental vibrations than their double-path analogues, as each beam experiences the same physical path in space and any noise that comes with it. Double-path interferometers are extremely sensitive to any optical path length changes between the two paths, which does make them useful for applications involving the measurement of small displacements (e.g. gravitational wave detection [313] and surface quality testing [314,315]). However, there are some instances in which this sensitivity is not desirable, such as the POVM measurements discussed above. For this reason it was decided to try to improve the stability of the POVM measurement system by redesigning it to be based on a Sagnac configuration rather than a Mach-Zehnder interferometer. The final experimental design is shown in figure 5.5 where we use a path-displaced Sagnac interferometer. Strictly speaking, this path-displacement violates the common path criterion, but it is expected that the differences between the two paths should be minimal in comparison to a Mach-Zehnder interferometer.

Again, vector beams with spatially varying polarisation are generated using the DMD setup discussed in § 2.6 and shown in Figure 2.12, and enter the interferometer via PBS_1. This separates the horizontal and vertical polarisation components, allowing them to propagate in opposite directions around the split path Sagnac interferometer, before exiting again through PBS_1. Within the Sagnac are two half waveplates (HWP_1 and HWP_2), each only intersecting one of the beam paths, as shown in Figure 5.5. These waveplates are rotated to control the ratio of horizontal to vertical polarisation exiting each arm of the interferometer. The rotation angles θ_1 and θ_2 are equivalent to those given in Eq. 5.21 and depend on the coefficients a and b as given in Eq. 5.9. This has the overall effect of transforming the initial PBS into a partially polarising beam splitter (PPBS) (along with the help of HWP_3). The resulting $\hat{h}:\hat{v}$ amplitude ratios are the same as before, $a:b$ at output 1 and $b:a$

[6]Of course, there exist several other ways in which we can categorise interferometer techniques, such as homodyne vs. heterodyne (same vs. different wavelength interference) or amplitude vs. wavefront splitting [309,310].

at output 2.

The beam from output 1 of the interferometer passes through a HWP (HWP_3) with its fast axis set to 67.5°, and the beam from output 2 is directed through a QWP, with its fast axis set to −45°. These four waveplates (HWP_1, HWP_2, HWP_3 and the QWP), perform the full state transformation, with POVM states $|\phi_1\rangle$ and $|\phi_2\rangle$ being prepared along the path of output 1 and $|\phi_3\rangle$ and $|\phi_4\rangle$ prepared after the QWP on the path of output 2. All that is left to do is separate these states from each other. In the same way as in Figure 5.4, PBS_2 in Figure 5.5 performs the final projection by splitting the horizontal and vertical components of the two beams. The resulting four intensity profiles are directed onto four quadrants of a single camera sensor (as shown in Figure 5.5(a)), to allow a complete and spatially dependent polarisation tomography in a single-shot measurement.

It will be noticed that the setup in Figure 5.5 includes some additional optical elements in the form of a quartz plate (QP) and glass microscope slides withing the Sagnac interferometer. These are used to aid in the experimental calibration by adjusting for optical path length differences. This process is discussed in the following section.

5.3.2 Experimental calibration

The change in the experimental design from using a Mach-Zehnder to a Sagnac interferometer was carried out with the aim to improve stability and remove unwanted phase shifts. The difference in path lengths in a Mach-Zehnder interferometer, means that phase differences in the two beams have to be corrected. Additionally, as the beams travel spatially different paths, any noise experienced by one beam (for example, table or optical element vibrations or air currents) is not necessarily experienced by the other. Therefore, the system requires frequent realignment. However, in a Sagnac interferometer, both beams travel the same physical path (although in opposite directions), helping to eliminate optical path differences to first order, and improves the resilience to common noise, as any vibration experienced by one beam is experienced by the other.

Nevertheless, due to the split path utilised within the interferometer presented here, experimentally, we found that there is a small difference between the clockwise and anticlockwise optical path lengths, requiring periodic calibration and measurements of the instrumentation matrix Π. The calibration procedure for this is outlined below.

Firstly, homogeneously polarised beams with polarisations orthogonal to the POVM states are generated. These orthogonal states, $|\overline{\phi_i}\rangle$, can be expressed by,

$$\begin{aligned} |\overline{\phi_1}\rangle &= b\,|h\rangle - a\,|v\rangle\,, \quad |\overline{\phi_2}\rangle = b\,|h\rangle + a\,|v\rangle\,, \\ |\overline{\phi_3}\rangle &= a\,|h\rangle - ib\,|v\rangle\,, \quad |\overline{\phi_4}\rangle = a\,|h\rangle + ib\,|v\rangle\,. \end{aligned} \tag{5.23}$$

For an ideal, perfectly aligned interferometer, measurement of each orthogonal

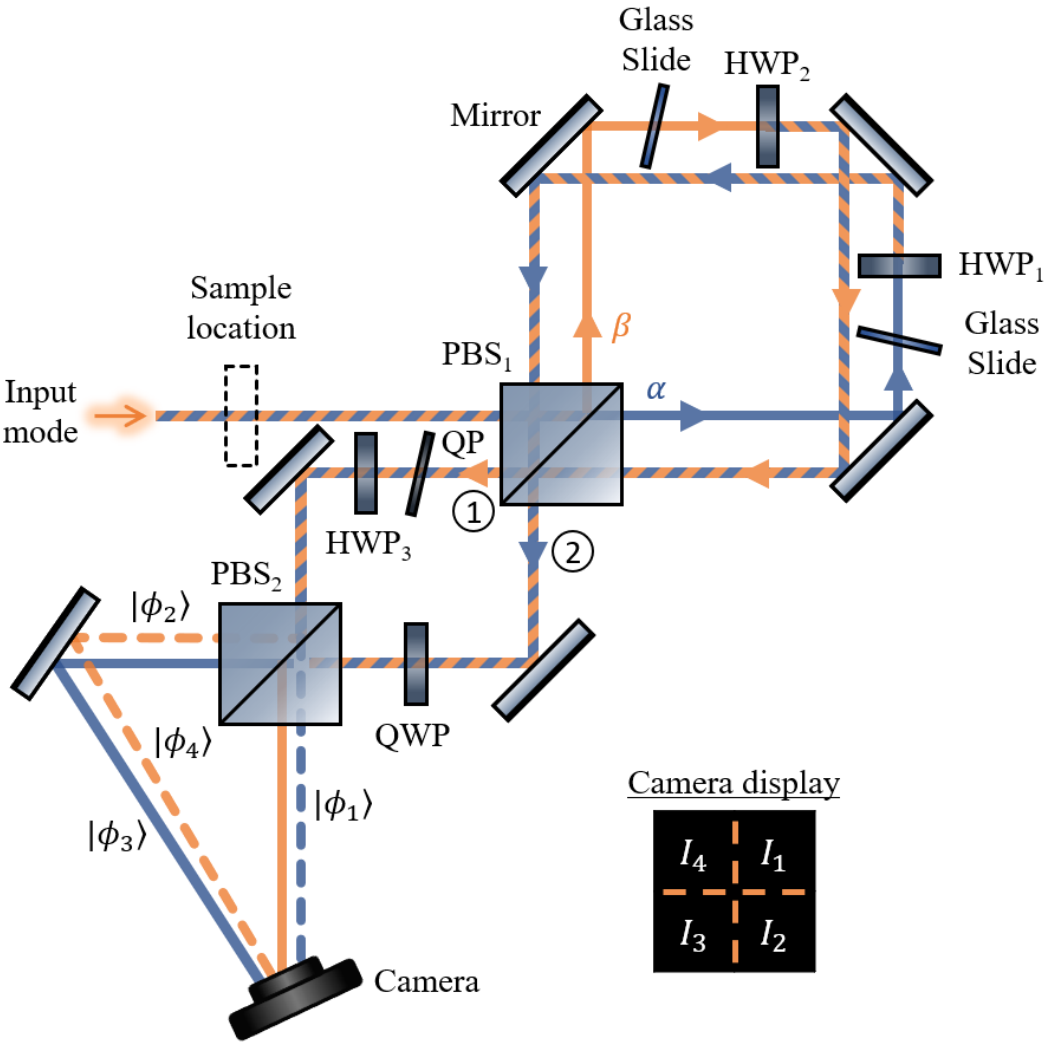

Figure 5.5: Experimental design for single-shot, spatially dependent polarisation tomography and Muller matrix determination using POVM measurements. PBS: polarising beam splitter, HWP: half waveplate, QWP: quarter waveplate, QP: quartz plate. The outputs from PBS$_1$ are indicated by the numbers in circles and the inset shows the arrangement of the four quadrants on the camera display. The colour of the beams represent the polarisation state, blue for horizontal, orange for vertical and a mix for a superposition of both.

state $|\overline{\phi_i}\rangle$ should result in $I_i = 0$, and equal intensities in the other 3 camera quadrants, as $P_i = \langle\overline{\phi_i}|\,\hat{\pi}_i\,|\overline{\phi_i}\rangle = 0$ for $i \in \{1, 2, 3, 4\}$. The observation and minimising of the intensity levels therefore allows for an easy way to calibrate the instrument. The main aim of the calibration process is to remove any phase difference between the clockwise and anticlockwise arms of the interferometer which can be achieved by tilting one of the glass microscope slides within the interferometer and the quartz plate (QP), as labelled in Figure 5.5. In theory, only having a glass slide in one of the interferometer arms is sufficient to compensate for path differences, however, it is beneficial to have identical glass slides in each arm to balance any intensity loss, especially as the intensity ratio of the Sagnac outputs are important for constructing the PPBS.

When a light beam passes from one medium into another, the direction of propagation changes due to the different light propagation speeds of the two medium. As glass has a higher refractive index than air, light travels slower within it. For this reason, the use of a thin piece of glass can remove unwanted phase differences by increasing the optical path length in one interferometer arm such that it matches the other. This is possible within the interferometer as the beam has been split into its horizontal and vertical components and we want to apply a phase shift to the entire beam. However, once we exit the interferometer, we now have two of the POVM states travelling along the same path (one encoded in the horizontal polarisation and the other in the vertical). If we need to implement phase compensation between these two beams, then we can no longer rely on a simple glass slide, as we now require polarisation dependent calibration. For this we employ a quartz plate, which, for normal incidence, introduces a $\pi/2$ phase difference between the orthogonal wavefronts. But, by simply rotating the quartz plate about its vertical axis, and thus varying the angle of incidence, we can vary the phase difference introduced between the $\hat{h}$ and $\hat{v}$ components, therefore compensating for any unwanted optical path differences.

The calibration process is simple and is as follows: We start by tilting only one of the glass slides (the choice of which shouldn't matter) until the I_3 (I_4) camera quadrant records minimum intensity when measuring $|\overline{\phi_3}\rangle$ $\left(|\overline{\phi_4}\rangle\right)$, while the other glass slide is kept stationary, at normal incidence. Afterwards, the quartz plate is tilted to ensure minimum intensity in the I_1 (I_2) camera quadrant for $|\overline{\phi_1}\rangle$ $\left(|\overline{\phi_2}\rangle\right)$. Experimental images of the orthogonal states after calibration can be seen in the top row of Figure 5.6.

After calibration, an experimental instrumentation matrix Π can be obtained. From Eq. 5.13, we know that Π relates normalised Stokes vectors to the normalised output intensities. We generate the 4 POVM states (Eq. 5.8) as the input beams, and record the resulting intensity profiles, as shown in the bottom row of Figure 5.6. The normalised intensities, $\mathbf{I}_i^{(\mathrm{N})} = (I_1, I_2, I_3, I_4)/I_t$ are found for each beam by summing over each camera quadrant and dividing by the total intensity incident on the camera. As the ideal Stokes vectors $\mathbf{S}^{(N)}$ are known, the experimental Π can

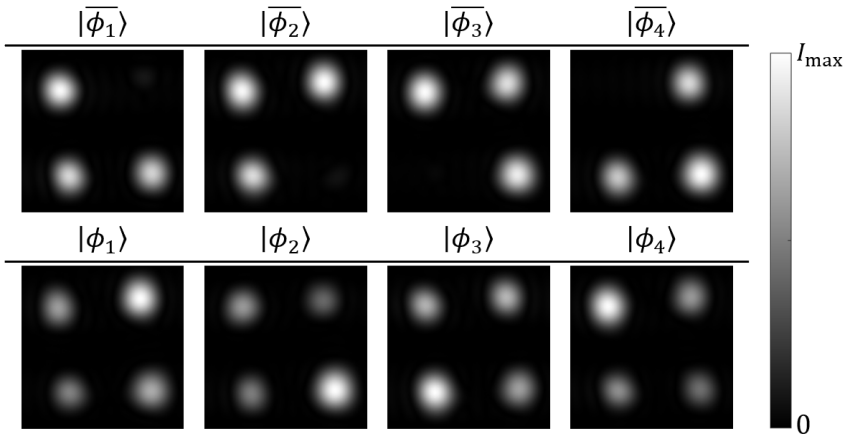

Figure 5.6: Experimental calibration measurements. Camera images of the homogeneously polarised orthogonal states, $|\overline{\phi_i}\rangle$ (top row) and POVM states, $|\phi_i\rangle$ (bottom row). The intensity measurements I_i ($i \in \{1, 2, 3, 4\}$) are in the positions as indicated in the insert of Figure 5.5. Figure adapted from [270].

simply be found by inverting Eq. 5.13. An example of an experimentally measured instrumentation matrix is,

$$\Pi_{\text{exp}} = \frac{1}{4}\begin{pmatrix} 0.950 & 0.826\sqrt{\frac{1}{3}} & 0.786\sqrt{\frac{2}{3}} & -0.015 \\ 1.041 & 0.867\sqrt{\frac{1}{3}} & -0.804\sqrt{\frac{2}{3}} & -0.017 \\ 0.955 & -0.810\sqrt{\frac{1}{3}} & 0.007 & -0.875\sqrt{\frac{2}{3}} \\ 1.053 & -0.883\sqrt{\frac{1}{3}} & 0.008 & 0.915\sqrt{\frac{2}{3}} \end{pmatrix}. \tag{5.24}$$

Comparison with the ideal instrumentation matrix Eq. 5.14, it is evident that Π_{exp} is not exactly the same as theoretically expected, suggesting that there exist some imperfections in the optical components and the alignment. From the discrepancy between Π and Π_{exp}, it can be assumed that the experimental system just projects the input state onto slightly different polarisation states than the intended tetrahedral POVM states. However, polarisation tomography can still be performed as long as a mapping between the Stokes vectors and measured POVM states exists and there is a large enough coverage of the Poincaré sphere.

In addition, it should be noted that the calibration method is also sensitive to any discrepancies in beam generation Therefore, care has to be taken to ensure high fidelity operation of the DMD-based vector beam generation. The beam generation was always calibrated using the methods outlined in § 2.6, and the POVM polarisation states measured and confirmed using Stokes polarisation tomography before completing the calibration process, to ensure a system with optimal alignment and instrumentation matrix as possible.

5.3.3 Investigation of experimental stability

As mentioned previously, a Sagnac-based interferometric setup was developed to perform one-shot polarisation tomography using generalised measurements, with the aim of improving the stability over the previous setup incorporating a Mach-Zehnder interferometer. Having a stable system over time removes the need for frequent re-calibration and has benefits when wanting to take time-resolved measurements of slowly varying processes, which requires the system to be optically stable during the entire evaluation process. This longer term stability becomes more relevant for the application of Mueller matrix polarimetry, which will be discussed in § 5.4.2, and is useful for measuring changes in optical activity over time (e.g. investigation of bio-chemical samples).

In this section, I will briefly outline an experimental investigation that was performed in order to assess the stability of the experimental setup.

As for the experimental calibration, we can make use of the orthogonal states $|\overline{\Phi_i}\rangle$. Recall that, in theory, for a perfectly aligned system, these states should produce zero intensity in the corresponding camera quadrant. Therefore, if the alignment of the interferometer drifts over time, the intensities in these camera quadrants are expected to increase. By taking periodic measurements of $|\overline{\Phi_i}\rangle$ over time the stability of the interferometer can be inferred. The findings of this simple experimental investigation are shown in Figure 5.7.

The data points in Figure 5.7 show measured $P_i = \langle\overline{\phi_i}| \hat{\pi}_i |\overline{\phi_i}\rangle$, in the corresponding camera quadrant as the fraction of the total intensity, with the dashed black line showing a smoothing spline fit to the average. The main figure shows measurements taken over 8 hours at 30 minute intervals in a quiet laboratory, and in the inset over 3 hours at 15 minute intervals during times of intense activity and traffic next to the experiment. After initial alignment and calibration, we typically achieve probabilities as low as $P_i \approx 2\%$. In a quiet laboratory, the calibration quality does change slightly over the whole 8 hour period, but these changes are insignificant. Whereas, in a busy laboratory calibration deteriorated markedly, as can be seen in the inset graph in Figure 5.7. This gradual misalignment is assumed to be attributed to slight shifts of the glass slides due to vibrations in the laboratory. This may be further suppressed in a custom-built monolithic interferometer setup, however, for the measurements reported in here, in § 5.3.4 and 5.4.2, the stability is entirely sufficient.

5.3.4 Results of single-shot polarisation tomography

Once the setup has been calibrated, and instrumentation matrix measured, the system can be used to measure the spatially varying polarisation of any vector

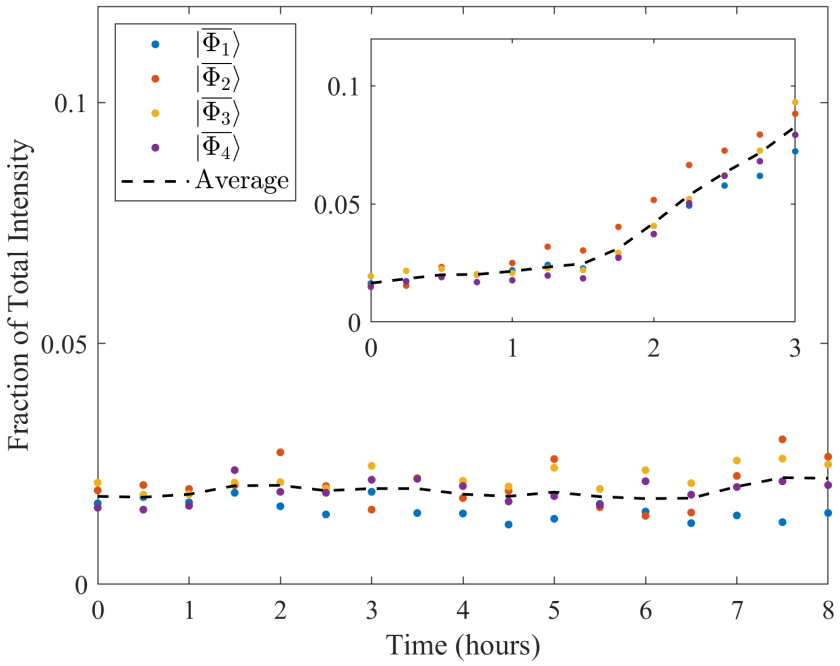

Figure 5.7: Investigating the stability of the Sagnac interferometer with time using the alignment states. The data points show the normalised total intensity, $I^{(\mathrm{N})}$ in camera quadrant I_i for the measured orthogonal state $|\overline{\phi_i}\rangle$, where $i \in \{1, 2, 3, 4\}$, and the black dashed line shows a smoothing spline fit to their average. The main plot shows data taken at 30 minute intervals over a total time of 8 hours during a quiet time in the laboratory. Stability decreases when there is a lot of traffic in the laboratory, as indicated in the inset, showing data taken at 15 minute intervals over 3 hours. Figure adapted from [270].

beam. Here, the results of three beams of the form,

$$\begin{aligned} |\psi_1\rangle &= \mathrm{HG}_{1,0}\,|\hat{h}\rangle + \mathrm{HG}_{0,1}\,|\hat{v}\rangle\,, \\ |\psi_2\rangle &= \mathrm{HG}_{0,2}\,|\hat{h}\rangle + \mathrm{HG}_{2,0}\,|\hat{v}\rangle\,, \\ |\psi_3\rangle &= \mathrm{LG}_1^0\,|\hat{h}\rangle + \mathrm{LG}_0^2\,|\hat{v}\rangle\,, \end{aligned} \tag{5.25}$$

will be presented, where $\mathrm{HG}_{n,m}$ are Hermite-Gaussian modes with indices n and m, and LG_p^ℓ Laguerre-Gaussian modes with radial index p and and topological charge ℓ. The equations for these higher order Gaussian modes can be found as Eqs. 1.41 and 1.43 in Chapter 1.

Single-shot camera images are acquired of the three vector beams, resulting in four intensity profiles from the four camera quadrants. The experimentally measured intensities can be seen in the odd columns of Figure 5.8, along with the theoretically expected results (even columns), for comparison. The total intensity distributions

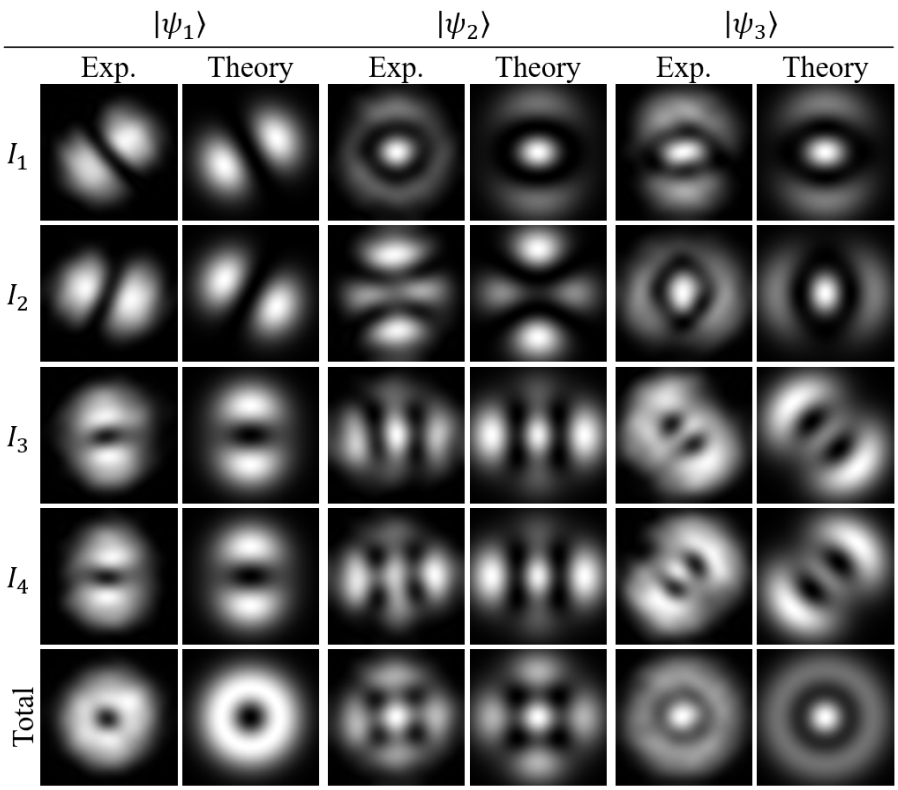

Figure 5.8: Experimental (odd columns) and simulated (even columns) intensity measurements of the POVM states for the three vector beams described by $|\psi_1\rangle$, $|\psi_2\rangle$ and $|\psi_3\rangle$ in Eq. 5.25. The bottom row shows the total intensity distributions.

are obtained by overlapping the four individual projections. These are shown in the bottom row of Figure 5.8.

From the measured intensities and experimental instrumentation matrix, we can invert Eq. 5.13 to obtain the spatially varying Stokes vectors, hence, allowing the reconstruction of the vector beam. The resulting polarisation profiles obtained from the POVM state projection measurements are given in Figure 5.9 along with the theoretical profiles, showing excellent agreement. Additionally, the results are of equal quality to those presented in Ref. [269], confirming that the new Sagnac-based setup performs as well as the Mach-Zehnder-based setup, but with an improved stability.

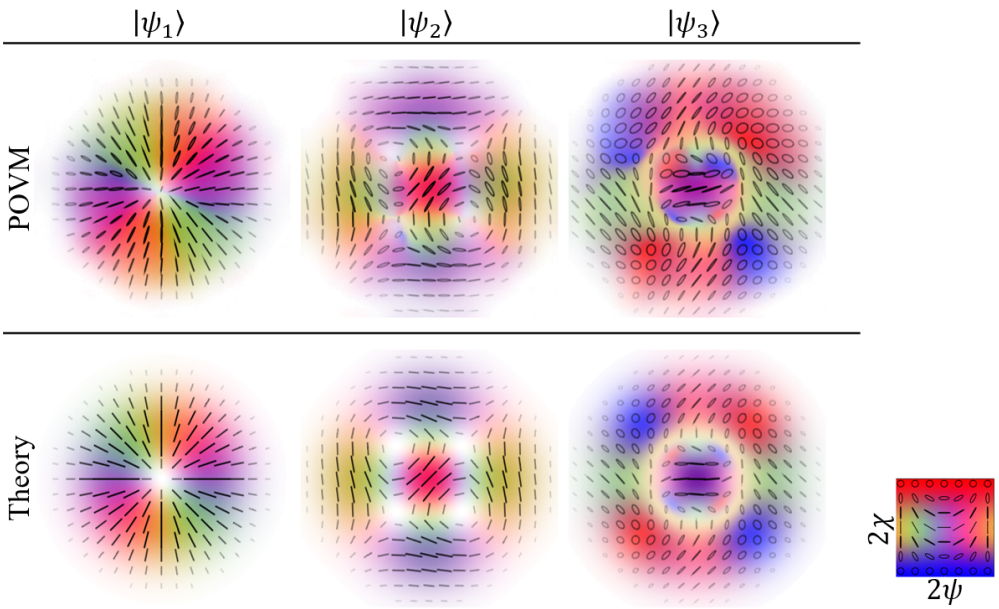

Figure 5.9: Polarisation distributions of the three vector beams described by $|\psi_1\rangle$, $|\psi_2\rangle$ and $|\psi_3\rangle$ in Eq. 5.25. Top row: Experimental polarisation profiles obtained using POVM tomography and the resulting measured intensities shown in Figure 5.8. Bottom row: Simulated polarisation profiles.

5.4 Chapter 5 Part 3: Application: Dynamic Mueller matrix polarimetry using generalised measurements

Now that we have an experimental system that is able to perform POVM measurements in a single-shot and with a proven inerferometric stability over a time scale of hours, thought can be put towards potential applications.

There are many fields in which polarisation determination plays a crucial role. This is partly due to one interesting characteristic of polarisation in particular - it contains information regarding a light beam's source as well as any interaction with materials that it has encountered. Additionally, polarisation information can be acquired without the need for invasive techniques. Therefore, it is perhaps not surprising that this feature of light is utilised for a variety or metrological applications. Some examples of possible applications include the characterisation and stress analysis of materials [289–291], ellipsometry [292, 293], astronomy [316–318], pharmaceutical ingredient analysis [294], monitoring of soil conditions and crop growth [319], chiral symmetry [320], biomedical studies and clinical applications [321–328], biological microscopy [295, 296] and quantum optics and quantum information [285, 288, 329–332].

Mueller matrix polarimetry is a powerful experimental technique often used to determine the optical activity of a material or medium (such as its linear/circular

birefringence or dichroism), by identifying the changes it makes to polarisation. Of late, the dynamic determination of Muller matrices has attracted attention as a tool for studying rapid phenomena which are polarisation sensitive [333–338]. For this reason, we decided to apply the POVM measurement system described above to perform single-shot Mueller matrix measurements using a Poincaré beam.

In the following sections, I will describe how a Mueller matrix is commonly measured, how our polarimetry is performed to obtain the Mueller matrix of a homogeneous sample and why using generalised measurements could be advantageous. I will then use the examples of tilted and rotated wave plates to illustrate the working of our Mueller matrix polarimetry, where we find excellent agreement with predictions as well as alternative Stokes measurements.

5.4.1 Overview of common techniques for Mueller matrix polarimetry

Any fully or partially polarised state of light can be expressed in terms of a 4×1 Stokes vector $\mathbf{S}$. The optical behaviour of an optical element or sample is fully described by a 4×4 (real) Mueller matrix, such that, in a similar way onto which a Jones matrix acts on a Jones vector, an initial polarisation state $\mathbf{S}_{\text{in}}$ becomes $\mathbf{S}_{\text{out}} = \mathbf{M}\mathbf{S}_{\text{in}}$ after passing through a sample described by the Mueller matrix $\mathbf{M}$ [52]. A simple way to measure a Mueller matrix uses 36 intensity measurements. This is accomplished by generating uniformly polarised beams of $|\hat{h}\rangle$, $|\hat{v}\rangle$, $|\hat{d}\rangle$, $|\hat{a}\rangle$, $|\hat{r}\rangle$ and $|\hat{l}\rangle$ before the element to be investigated, and then analysing $|\hat{h}\rangle$, $|\hat{v}\rangle$, $|\hat{d}\rangle$, $|\hat{a}\rangle$, $|\hat{r}\rangle$ and $|\hat{l}\rangle$ polarisations after the element [292,339]. However, as we have a 4×4 matrix, with 16 elements, taking 36 measurements results in an over-complete determination[7]. Indeed, we only require (at least) 16 measurements, taken with linearly independent combinations of settings of the polarisation state generator before the sample and the analyser after the sample, to determine the elements of $\mathbf{M}$.

There exist three common approaches to polarimetry - using either spatial splitting, temporal modulation or encoding information into different degrees of freedom. Polarimetry achieved by temporal modulation requires sequential measurements, such as the rotating wave plate approach, which is the technique most commonly found in commercial polarimeters. However, the sequential nature of temporal modulation techniques deems them inadequate if the optical activity of the sample varies with time. In contrast, the techniques based on spatial splitting divide the beam and analyse each part using different polarisation optics at once, but deliver inferior signal to noise ratios. Hence, spatial splitting techniques are less suitable for applications requiring weak probe light.

Some other noteworthy developments into polarimeters include the recent work on ellipsometers based on photoelastic modulators [340] which, due to their quick

[7] However, if the number of measurements is not a concern then this over-complete determination of the components of $\mathbf{M}$ allows further analysis and reduction of errors in relation to experimental determination of a Mueller matrix.

switching time, allow rapid sequences of individual Stokes measurements, leading to time resolutions in the range of microseconds [341].

As mentioned, another method for Mueller matrix polarimetry uses additional degrees of freedom, such as spectral encoding [342], where different polarisation states of different wavelength are used and Stokes measurements simultaneously carried out at the different wavelengths, with time resolutions feasible at tens of nanoseconds [343]. Other methods use spatial information as the additional degree of freedom, relying on vector light beams with a spatial polarisation dependence, allowing polarisation information to be deduced from spatial intensity measurements [344–346]. If we are interested in analysing a sample with homogeneous optical activity, then it is possible obtain a Mueller matrix using only one probe beam. The only requirement of this, is that the beam must contain at least 4 linearly independent polarisation states that together span the complex polarisation space. Poincaré beams are a class of beams that contain every possible polarisation across their transverse profile (therefore, must satisfy this requirement), and there have been two recent examples of work on Poincaré based polarimetry: Ref. [347] sequentially analysed 4 regions of the Poincaré beam, corresponding to 4 linearly independent polarisations, with a commercial polarimeter, and Ref. [348] used a CCD camera and Stokes tomography to analyse the Poincaré beam after passing through the sample. The work outlined in both of these papers reduced the number of required probe beams but still needed multiple measurements of the resulting beam.

By using a Poincaré beam as a probe beam, and the POVM measurement system described previously in § 5.3.1, we can realise single-shot polarimetry of homogeneous samples. This enables dynamic Mueller matrix measurements with potential applications in the investigation of fast physical, chemical or biological processes as well as material stress analysis. The time resolution of the optical activity evolution is therefore only limited by the camera frame rate.

5.4.2 Dynamic Mueller matrix determination using generalised measurements and a full Poincaré beam

As mentioned, the optical behaviour of any optical element or unknown sample can be described by a 4×4 Mueller matrix $\mathbf{M}$, such that the transformation of an initial polarisation state passing through the sample can be described by [52],

$$\mathbf{S}_{\text{out}} = \mathbf{M}\,\mathbf{S}_{\text{in}} \tag{5.26}$$

This relation holds for any input polarisation, $\mathbf{S}_{\text{in}}$, thus, every point across the transverse profile of the input probe beam. Therefore, while Eq. 5.26 is almost always applied to homogeneously polarised light, it can equally be applied to spatially varying vector light, so that we can now write,

$$\mathbf{S}_{\text{out}}(x, y) = \mathbf{M}\,\mathbf{S}_{\text{in}}(x, y), \tag{5.27}$$

where x and y are the spatial coordinates on the transverse plane.

Here, a Poincaré beam will be used as the probe beam, as it contains every possible polarisation, including the POVM polarisation states, allowing us to observe the way a material alters every polarisation state at once. We could choose to analyse selected areas of the resulting Poincaré beam corresponding to 4 linearly independent polarisations (such as the POVM polarisations themselves, or any rotated POVM tetrahedron), similar to the work performed in Ref. [347]. However, we instead choose to maximise the information obtained from our measurement by using all polarisations of the probe beam, and analysing its components using the POVM strategy.

The intensity profile, and hence Stokes parameters of the beam are continuous, however, measurement performed with a camera (in this case, a CMOS camera with 1920×1200 pixels) has the effect of parameterisation by pixel number. Consequently, for N camera pixels used to measure the input and output beams, the measured Stokes vectors can be arranged into $4\times N$ matrices $\mathcal{S}$, with matrix entries $\mathcal{S}_{i,n}$. Here, $i \in \{1,2,3,4\}$ denote the Stokes parameter and $n \in \{1, N\}$ the pixel number. This allows us to obtain a set of $4N$ linear equations:

$$\mathcal{S}_{\text{out}} = \mathbf{M}\,\mathcal{S}_{\text{in}}. \tag{5.28}$$

The matrices $\mathcal{S}_{\text{in}}$ and $\mathcal{S}_{\text{out}}$ can be easily acquired from spatially resolved intensities by implementing POVM measurements before and after the sample and obtaining the corresponding Stokes parameters using the methods described previously.

In order to find $\mathbf{M}$, we follow a similar procedure as outlined in [348]. By inspection of Eq. 5.28, we notice that we require an inverse for $\mathcal{S}_{\text{in}}$, but, $\mathcal{S}_{\text{in}}$ is a non-square matrix. However, as a Poincaré beam is used as the input beam, then it is possible to find a set (or multiple sets) of 4 polarisation states across the beam profile which are linearly independent. Therefore, $\mathcal{S}_{\text{in}}(\mathcal{S}_{\text{in}})^T$ must be invertible, allowing the right Moore-Penrose pseudo-inverse of S_{in} to be calculated via [349],

$$(\mathcal{S}_{\text{in}})^\dagger = (\mathcal{S}_{\text{in}})^T \left[\mathcal{S}_{\text{in}}\,(\mathcal{S}_{\text{in}})^T\right]^{-1}. \tag{5.29}$$

Following on from Eqs. 5.28 and 5.29, the Mueller matrix can be obtained using,

$$\mathbf{M} = \mathcal{S}_{\text{out}}(\mathcal{S}_{\text{in}})^\dagger. \tag{5.30}$$

The benefits of Eq. 5.30 is that it uses the full information contained within the Poincaré beams which can be analysed simultaneously by projecting into the 4 POVM polarisations with the interferometric setup.

5.4.3 Experimental single-shot Mueller matrix measurement procedure

For the experimental determination of the Mueller matrix, we need to know how the sample to be measured will affect input polarisation. This requires measurement of the Stokes parameters of the beam itself and after interaction with the sample.

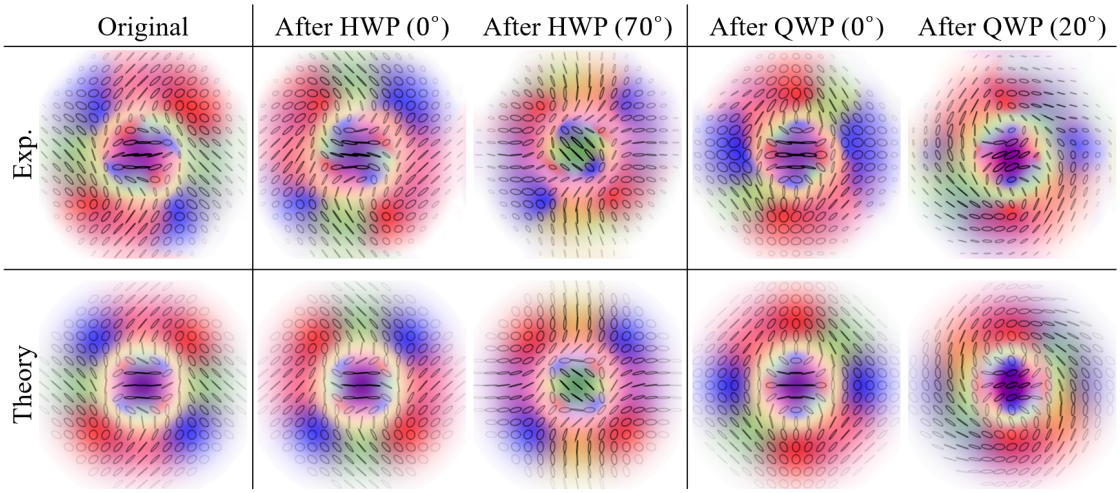

Figure 5.10: Experimentally measured with the Sagnac interferometer (top) and simulated (bottom) polarisation profiles $\mathbf{S}_{\text{in}}$ of an $\text{LG}_1^0 |\hat{h}\rangle + \text{LG}_0^2 |\hat{v}\rangle$ Poincaré beam before (left) and $\mathbf{S}_{\text{out}}$ after passing through either a half waveplate or quarter waveplate with their fast axis rotated with respect to the horizontal to the angle indicated in the figure. Figure adapted from [270].

To test the proposed Mueller polarimetry method, we choose to use a Poincaré beam generated from a superposition of horizontally and vertically polarised Laguerre Gaussian (LG_p^ℓ) modes, of the form,

$$|\Psi\rangle = \text{LG}_1^0 |\hat{h}\rangle + \text{LG}_0^2 |\hat{v}\rangle \,, \tag{5.31}$$

where p and ℓ are the radial and azimuthal mode numbers, respectively. The equation for the LG modes is given in § 1.4.2 as Eq. 1.43. This particular Poincaré beam was chosen as the mode orders of the two contributing LG modes are identical, $N = 2p + |\ell| = 2$, so they have the same Gouy phase. This means that upon propagation the beam maintains its shape (apart from an overall change of size) and there is no rotation of the polarisation distribution due to differing Gouy phases (see § 1.4.3). The experimentally measured polarisation profile $\mathbf{S}_{\text{in}}$ of $|\Psi\rangle$ is shown in the top left of Figure 5.10, with the simulated ideal polarisation profile displayed below.

Now that we have a measurement of $\mathbf{S}_{\text{in}}$ (and hence $\mathcal{S}_{\text{in}}$), we can detail the single-shot procedure for Mueller matrix determination. The sample to be analysed is placed in the beam path, before the beam enters the interferometric system, as indicated by the dashed box in Figure 5.5, and the resulting Stokes parameter $\mathcal{S}_{\text{out}}$ is obtained as before. The Mueller matrix of the sample can then be obtained from Eq. 5.30.

As we are utilising a Poincaré beam including every polarisation state, the resolved Stokes vectors provide an overcomplete measurement, allowing us the ability

to eliminate from the calculation camera pixels at low intensities that may be compromised by noise. This is acceptable, and will not affect the resulting matrix as long as the remaining sections of the Poincaré beam still span the full polarisation state space. Specifically, we choose to only include camera pixels in the analysis with an intensity greater than 5% of the peak intensity.

5.4.4 Mueller matrix measurement of rotated waveplates

As an illustration of the single-shot Mueller matrix polarimetry, it was chosen to use half and quarter waveplates at various angles as the samples to be measured, for the simple reason that the theoretical matrices describing these components are readily available, providing a benchmark for which to compare results.

The theoretical Mueller matrix $\mathbf{M}_\mathrm{T}$ of a waveplate can be found using,

$$\mathbf{M}_\mathrm{T}(\delta,\theta)=\begin{bmatrix} 1 & 0 & 0 & 0 \\ 0 & \cos^2(2\theta)+\sin^2(2\theta)\cos(\delta) & \cos(2\theta)\sin(2\theta)(1-\cos(\delta)) & \sin(2\theta)\sin(\delta) \\ 0 & \cos(2\theta)\sin(2\theta)(1-\cos(\delta)) & \cos^2(2\theta)\cos(\delta)+\sin^2(2\theta) & -\cos(2\theta)\sin(\delta) \\ 0 & -\sin(2\theta)\sin(\delta) & \cos(2\theta)\sin(\delta) & \cos(\delta) \end{bmatrix}, \quad (5.32)$$

where δ is the phase difference between the fast and slow axis and θ is the angle of the fast axis with respect to the horizontal. For a HWP and QWP, $\delta = \pi$ and $\pi/2$, respectively.

Measurements were taken for normal incidence on a HWP and QWP for different fast axis angles of $\theta = 0°$ to $90°$ in $10°$ increments and the Mueller matrices obtained as described above. A selection of the measured polarisation profiles of the chosen Poincaré beam after passing through the waveplates at different θ are shown in Figure 5.10 along with the corresponding theoretical plots.

The results of measured Mueller matrix entries $m_{i,j}$ against waveplate fast axis angle are plotted as data points in Figure 5.11(a) for the HWP and in Figure 5.11(b) for the QWP. In both figures, the theoretically expected values are given as solid blue lines, showing that the measured values follow theory well, with just some slight deviations for some fast axis angles.

In Figure 5.12, a bar chart representation is provided of a selection of the measured Mueller matrices and comparison to theoretically expected matrices, where theoretical values are given as transparent columns, and measured values as narrower opaque columns. The results given here are for the same waveplates and fast axis angles as shown in Figure 5.10 with the bar charts in Figure 5.12(a) and (b) showing results for the HWP results and 5.12(c) and (d) showing the QWP results.

To asses the performance of the single-shot Mueller matrix measurements we calculate an error value that quantifies the discrepancy between the Mueller matrices obtained using the single-shot POVM measurements and the theoretically predicted quantities. One possible way to globally quantify the error of the 16 Mueller matrix

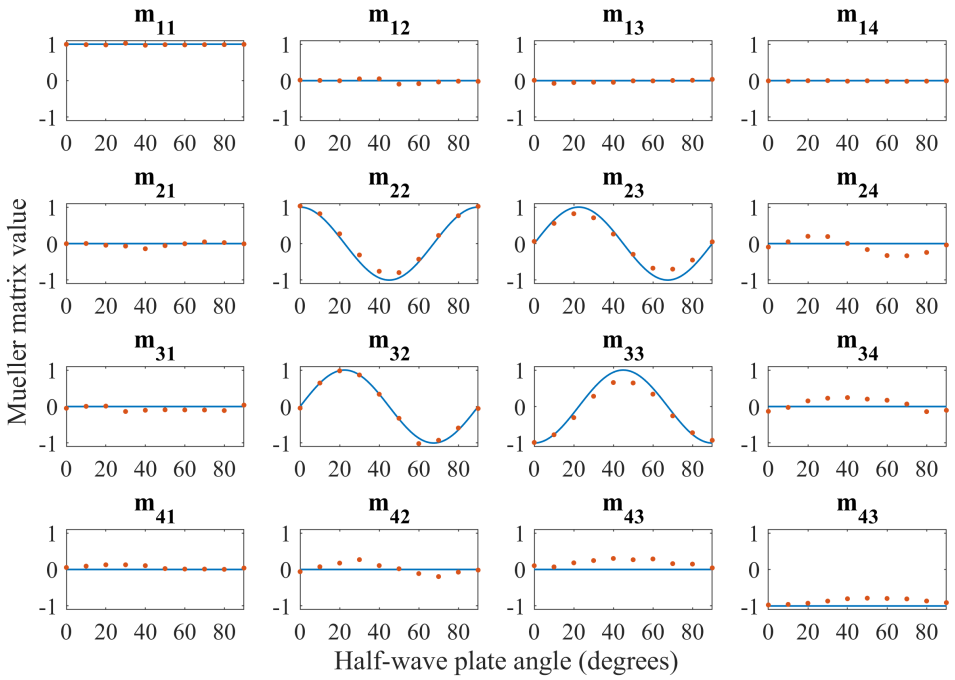

(a)

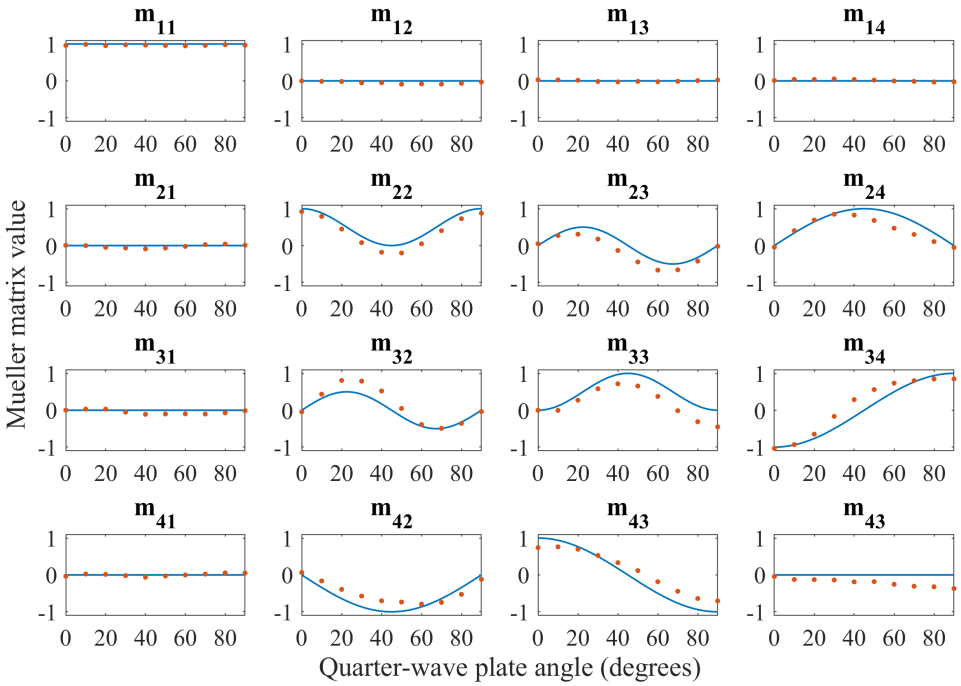

(b)

Figure 5.11: Measured Mueller matrix entries $m_{i,j}$, where $i, j \in \{1, 2, 3, 4\}$, against HWP (a) and QWP (b) angle. Orange data points show values obtained using the single-shot procedure and solid blue lines are theoretical values.

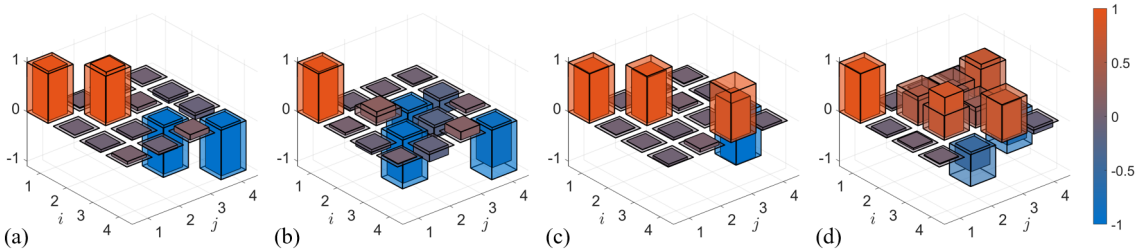

Figure 5.12: Comparison of experimental and theoretical Mueller matrices. The bar graphs show the $m_{i,j}$ entries of Mueller matrices where $i, j \in \{1, 2, 3, 4\}$ are the row and column indices, respectively. Theoretical values are indicated by the transparent columns and experimental values given by narrower opaque columns. The positive and negative values are indicated by an orange-to-blue colour gradient as indicated on the right. Examples are given for a HWP with fast axis at 0° (a) and 70° (b) and a QWP at 0° (c) and 20° (d). Figure adapted from [270].

entries is to evaluate the root mean square (rms) of the individual errors as [348],

$$\mathrm{rms}(\widehat{\delta M}) = \frac{1}{4}\sqrt{\sum_{i,j=1}^{4} |\delta M_{ij}|^2}, \tag{5.33}$$

where, $\widehat{\delta M} = \widehat{\delta M_E} - \widehat{\delta M_T}$ is the difference between the experimentally measured Mueller matrix and the theoretically expected matrix, and i and j are the row and column indices. Note that the obtained error from Eq. 5.33 not only includes a measure of uncertainty between the experimental and expected Mueller matrix but also includes small uncertainties in determining the exact rotation angle of the retardation plates θ (encompassing both errors in the calibrated fast axis position and in the manual rotation to the correct θ under investigation).

The $\mathrm{rms}(\widehat{\delta M})$ of the single-shot Mueller matrix measurements are shown as green data points in Figure 5.13(a) for the HWP and Figure 5.13(b) for the QWP.

Comparison to different Mueller matrix measurement techniques

To asses the performance of the single-shot POVM measurements, the obtained error values were compared to $\mathrm{rms}(\widehat{\delta M})$ values of Mueller matrices acquired using two other experimental techniques. For both, the resulting light beam after the waveplate was analysed using sequential Stokes measurements, projecting into each of the $|\hat{h}\rangle$, $|\hat{v}\rangle$, $|\hat{d}\rangle$, $|\hat{a}\rangle$, $|\hat{r}\rangle$ and $|\hat{l}\rangle$ polarisation bases in turn. These measurements were performed using a rotating wave plate setup consisting of a rotating QWP, HWP and stationary polariser, as described in § 2.3.

For the first technique, the sequential Mueller analysis was performed using the same Poincaré beam used above, and as described by Eq. 5.31, as the probe

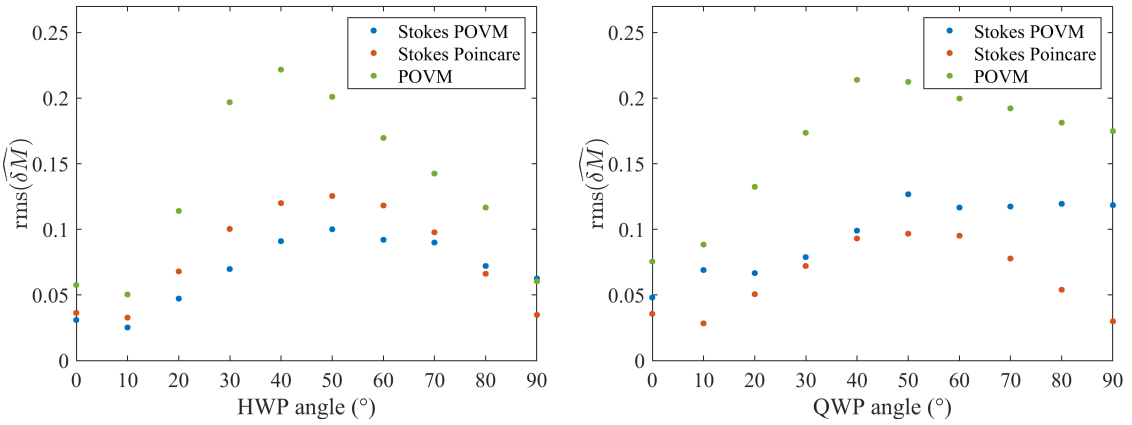

Figure 5.13: Comparison of calculated errors of the measured Mueller matrices of a HWP (a) and QWP (b) for the different methods used. Green data points show errors for the single shot POVM measurements, blue and orange data points are the errors when Stokes measurements are used either using the 4 POVM states as input beams (blue) or a Poincaré beam (orange). The errors are calculated using Eq. 5.33. Figure adapted from [270].

beam. The beam was first measured before the sample and then again afterwards, requiring 12 intensity measurements in total, but 6 for the Mueller analysis. From the resulting intensities, we obtain spatially resolved Stokes parameters, with one Stokes vector associated to each camera pixel, from which the Mueller matrices could be calculated using Eq. 5.30. This is analogous to the data processing for the single-shot measurements. The corresponding rms($\widehat{\delta M}$) values were calculated using Eq. 5.33, and are shown as orange data points in Figure 5.13(a) and (b).

The second technique used four homogeneously polarised beams as the probe beams, as this is the minimum number of required linearly independent polarisations. For this, we choose the four POVM polarisations themselves (as shown in Figure 5.1). Again, the polarisations of the beams were measured before the sample, and after interaction with the sample. Cycling through the four beams and recording the Stokes projections requires a series of 24 (4×6) consecutive images per sample. Stokes parameters were acquired for each of the four homogeneously polarised beams by averaging over the entire intensity profiles, resulting in four input and output Stokes vectors, allowing us to construct two 4×4 matrices, and solve $\mathbf{S}_{\text{out}} = \mathbf{M}\,\mathbf{S}_{\text{in}}$ directly. The corresponding error values were calculated for the resulting matrices, and are shown as blue data points in Figure 5.13(a) and (b).

The comparison of the rms($\widehat{\delta M}$) in Figure 5.13 shows that the Mueller matrices obtained using single-shot POVM approach have an error of similar magnitude

(within a factor of two) as those measured with traditional Stokes polarimetry, despite the large gain in measurement speed. It is not surprising that the Stokes tomography based analysis executed here performs slightly better, given that it consists of a simple sequence of three optical elements (where slight shifts of the beam path should not affect the results) compared to the Sagnac setup shown in Figure 5.5, which requires more optical components. Additionally, the Sagnac setup features more alignment challenges, and any slight shift in the overall beam path that could be caused by the Mueller sample has the possibility to change the alignment and overlap of the beams within the interferometric system. By inspection of the graphs in Figure 5.13, it is noticed that there appears to be a fast axis angle dependence on the accuracy of the measured Mueller matrix. This dependence is present for all three measurement techniques, with a maximal error occurring in the range $\theta = 40°$ to $50°$ depending on the technique and waveplate used. This suggests a possible alignment error, potentially caused by a slight tilt of the waveplates relative to the beam path (therefore changing the effective δ of the waveplates).

5.4.5 Dynamic measurements

All of the above Mueller matrix results were obtained from stationary images. However, as only one image is required for each measurement, it is possible to apply this method to time resolved analysis (e.g. for the investigation of time varying chemical or biological processes). To give a controllable demonstration of this application, we looked at the continuous rotation of a HWP. A HWP was mounted in a rotation mount controlled by a stepper motor and placed in the sample location, as highlighted in Figure 5.5. The stepper motor allowed the automation of the waveplate rotation, in turn allowing a live video to be recorded. A video was recorded of the probe beam passing through the HWP as it rotated a full 360°. The raw video can be seen in Ref. [270] as Visualisation 1 which also shows a video of the reconstructed polarisation profile.

The camera and exposure time that were used meant that we recorded 39.68 frames per second and the stepper motor rotated the entire 360° in 1.13 seconds. This meant that each frame of the video shows the altered intensity distributions after the HWP had advanced by 8°. Here, we are clearly only limited by the frame rate of the camera, and employing a faster camera, with higher sensitivity, allowing for a lower exposure time, would provide more time resolution. Visualisation 1 in Ref. [270] shows the recorded video slowed down by a factor of 10, in order to clearly view the changes to the recorded intensity and reconstructed polarisation profiles.

5.4.6 Measuring the retardance of a tilted quarter waveplate

In the previous section, Mueller matrices of waveplates were measured as they provided an easy way to asses the performance of the proposed experimental setup and

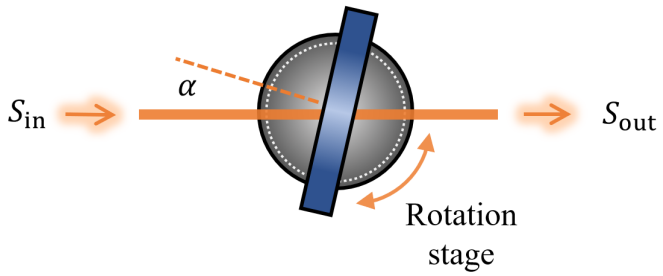

Figure 5.14: Schematic of experimental setup for retardance measurements. Mounting a quarter waveplate on a rotation stage allows for easy change of the incident angle of the input beam.

method. Here, I will provide a slightly more practical example of how we can use these measurements, by measuring the retardance of a birefringent material in relation to the material thickness. For this, a QWP with its fast axis set to 0° is used, and the angle of incidence (AOI) of the probe beam changed by tilting the QWP about its vertical axis by an angle α, as indicated in Figure 5.14. By tilting the QWP in this way, we increase the optical path length through the material, hence allowing variations of material thickness to be investigated.

Birefringent materials impart a phase shift between two orthogonal polarisation components of incident polarised light. For this reason, they are commonly used to make HWPs and QWPs to allow easy polarisation modulation. This phase shift (or retardance) depends on the properties of the material, such as the thickness, and the ordinary (n_o) and extraordinary (n_e) refractive indices at the relevant wavelength. Due to the dependence on material thickness, birefringent waveplates are designed for use at normal incidence, as increasing the AOI increases the distance travelled through the material. With increased distance, the optical path difference between the ordinary and extraordinary rays changes, imparting an unintended phase shift between the rays. The significance of the this change in retardance with incident angle is material dependent. For example, polymer waveplates are fabricated to allow better stability for a large range of AOI, whereas waveplates made of crystalline quartz are less stable, with the greater retardance changes for smaller AOI [98].

The Mueller matrix of a waveplate with its fast axis at 0° and arbitrary retardance (δ) is,

$$M_T(\delta, \theta = 0) = \begin{bmatrix} 1 & 0 & 0 & 0 \\ 0 & 1 & 0 & 0 \\ 0 & 0 & \cos(\delta) & -\sin(\delta) \\ 0 & 0 & \sin(\delta) & \cos(\delta) \end{bmatrix}. \tag{5.34}$$

For a matrix of the form of Eq. 5.34, the correct sign and magnitude of the retardance can be obtained, simply using the fact that $\delta = \tan^{-1}(\sin(\delta)/\cos(\delta))$. Therefore,

from a measured Mueller matrix, there are 4 ways to compute the retardance,

$$\begin{aligned} \delta_1 &= \tan^{-1}\left(-\frac{m_{34}}{m_{33}}\right), \quad \delta_2 = \tan^{-1}\left(-\frac{m_{34}}{m_{44}}\right), \\ \delta_3 &= \tan^{-1}\left(\frac{m_{43}}{m_{33}}\right), \quad \delta_4 = \tan^{-1}\left(\frac{m_{43}}{m_{44}}\right), \end{aligned} \tag{5.35}$$

where, $m_{i,j}$ are the matrix elements of M_T with row and column indices i and j respectively.

A multi-order crystalline quartz quarter waveplate (ThorLabs WPMQ05M-633) was used for testing the Mueller matrix procedure for measuring retardance. The fast axis of the QWP was set to 0° and it was mounted on a rotation stage to allow varying incidence angles (see Figure 5.14). The same Poincaré beam as described by Eq. 5.31 was used as the probe beam allowing the same procedure as described above to be implemented in order to find the Mueller matrix for incident angles ranging from 0° to 40° in 5° increments.

Once the Mueller matrices are obtained, the retardance can be determined using matrix entries m_{33}, m_{34}, m_{43}, m_{44} and Eq. 5.35 which gives 4 separate values. Ideally, these values should all be the same, but due to experimental errors, there are slight deviations between them, as expected. In order to get a final value for the retardance, we find the average of δ_1, δ_2, δ_3 and δ_4 and compute the standard deviation to obtain an associated error. The results of the experimentally measured δ in relation to the QWP tilt angle are shown in Figure 5.15 as orange data points.

In Figure 5.15, we also plot a fit to the data and the theoretical fit to the retardance against tilt angle for comparison. To determine the theoretically expected retardance and also the correct fitting function, we follow a similar procedure as outlined in [350], but modified for a multi-order waveplate rather than a zero-order waveplate, as used in the mentioned paper. The theoretical retardance can therefore be calculated as,

$$\delta_T(\theta,\alpha) = \frac{2\pi T}{\lambda}\left(\sqrt{n_e^2 - \frac{n_e^2\cos^2(\theta) + n_o^2\sin^2(\theta)}{n_o^2}\sin^2(\alpha)} - \sqrt{n_o^2 - \sin^2(\alpha)}\right), \tag{5.36}$$

where θ is the angle of the waveplates fast axis, α is the angle of incidence, T is the thickness of the waveplate, n_o and n_e are the ordinary and extraordinary refractive indices and λ is the wavelength, which, in our case, $\lambda = 632.8$ nm. The refractive indices are wavelength dependent, and for this wavelength, the relevant refractive indices of crystalline quartz are $n_o = 1.543$ and $n_e = 1.552$ [351]. The thickness of the QWP can be found from the manufacturers website [98].

For a waveplate with its fast axis at 0°, Eq. 5.36 reduces to,

$$\delta_T(\theta=0,\alpha) = \frac{2\pi T}{\lambda}\left(\sqrt{n_e^2\left(1 - \frac{\sin^2(\alpha)}{n_o^2}\right)} - \sqrt{n_o^2 - \sin^2(\alpha)}\right). \tag{5.37}$$

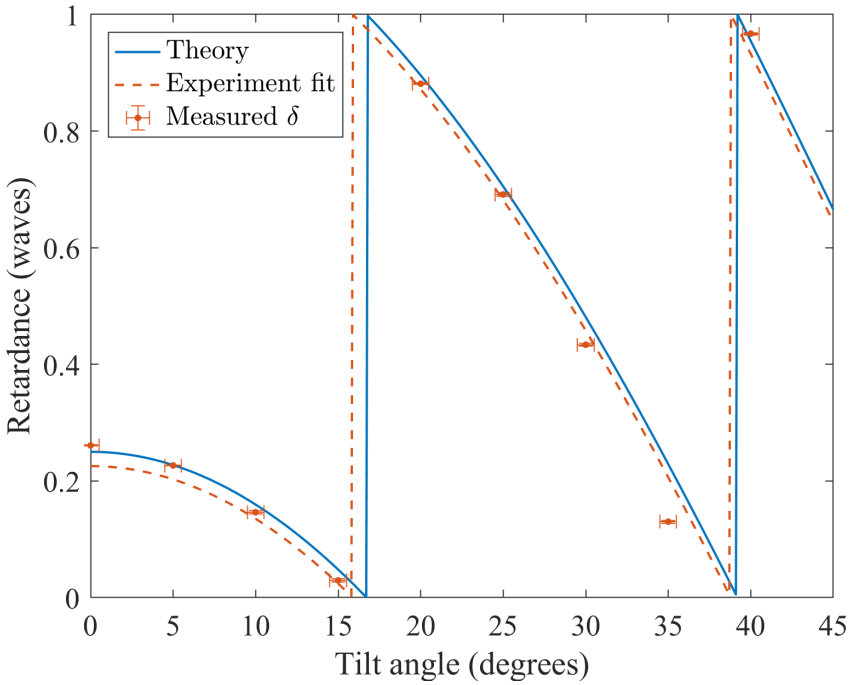

Figure 5.15: Retardance against angle of incidence for a QWP with its fast axis at 0°. Measured retardance from Mueller matrix measurements are shown as orange data points with the corresponding fit given as a dashed orange line. Solid blue line shows the theoretical values calculated using Eqs. 5.37.

To obtain δ_T in units of waves, we can simply apply the modulo operation, to get the result in the range $[0, 2\pi]$ and divide by 2π. As an equation, this unit conversion can be written as,

$$\delta'_T(\theta = 0, \alpha) = \frac{1}{2\pi}\left(\delta_T - 2\pi \left\lfloor \frac{\delta_T}{2\pi} \right\rfloor\right), \tag{5.38}$$

where δ'_T is in units of waves, as plotted in Figure 5.15.

The theoretical retardance vs. tilt angle relation obtained using these equations is shown as the blue line in Figure 5.15. We note however, that the values for n_e and n_o available from Ref. [351] are only known to 4 significant figures. Therefore, a fit was also performed to the experimentally measured retardance using Eqs. 5.37 and 5.38, and is shown as the dashed orange line in Figure 5.15. Allowing the refractive indices to be determined as $n_0 = 1.54302 \pm 0.00032$ and $n_e = 1.55199 \pm 0.00033$ and the thickness of the material to be $T = 1.0023 \pm 0.0001$ mm, all of which are similar to the expected values quoted above.

5.5 Chapter 5 conclusion

To conclude, this chapter began by discussing the concept of measurement in quan-

tum mechanics and some of the different measurement processes that exist, before focusing on generalised measurements in the form of minimum informationally complete positive operator value measures (MIC-POVMs). A way in which these ideas from quantum mechanics could be applied to polarisation was then outlined. Towards the end of Chapter 5 part 1 (in § 5.2.4), I provided a summary of the work performed previously within the group to develop an experimental system for realising spatially resolved POVM measurements, allowing the characterisation of vector beams in a single-shot. This experimental setup implemented a Mach-Zehnder interferometric system in order to construct the variable partially polarising beam splitter.

In Chapter 5 part 2 (§ 5.3), I then began to discuss my own contribution to the work. This first involved building on and developing the ideas from the previous experimental system to try and improve one of its practical challenges - its stability. The solution ultimately proposed, was to redesign the setup to be based on a Sagnac interferometer rather than a Mach-Zehnder, as Sagnac configurations are naturally more stable due to the common geometric beam path. The polarisation tomography results produced from this setup were of equal quality to those presented in Ref [269] using the previous setup, but we could now achieve an improved interferometric stability, with the new system remaining suitably aligned over a period of hours in a quiet lab, rather than minutes.

The improved experimental stability allowed this single-shot technique for spatially varying polarisation characterisation to be considered for more practical applications. In Chapter 5 part 3 (§ 5.4), one such application was proposed and performed: single-shot Mueller matrix polarimetry. Mueller matrix polarimetry is an important technique for determining the optical activity of media. By implementing generalised measurements and using a full Poincaré beam as a probe beam, the Mueller matrix can be determined in a single-shot, allowing the possibility for dynamic measurements.

The method was tested for stationary HWPs and QWPs rotated to different angles, and a tilted QWP, obtaining excellent agreement with theoretical predictions with comparable errors to conventional rotating wave plate measurements. Therefore, this method, could provide a convenient alternative approach for the real-time monitoring of rapid optical activity changes. For example, those caused by biological phenomena, physical or chemical reaction processes, and complex fluid studies, but equally for the long-time non-invasive investigation of slow biochemical processes relevant e.g. for monitoring in agriculture and food industries. The implementation of the method is wavelength independent, as with only a simple change of the wavelength-dependent optical elements used in the system, and a suitable camera chosen, it can be applied for studies at any wavelength. Additionally, its temporal resolution is only limited by the video refresh rate of the camera, promising resolutions in the range of nanoseconds with commercial scientific cameras.

Chapter 6

BB84 protocol using rotationally symmetric states

6.1 Chapter 6 introduction

In this chapter, I will outline a short project that was undertaken in order to develop a BB84 protocol using rotationally symmetric states, with the aim of removing the need for shared coordinate reference frames between the sender and receiver. For this, we developed a new measurement system for projecting onto the rotationally symmetric bases. This system incorporates an optical component known as a Fresnel cone [34], which provides advantages such as being wavelength-independent, unlike other polarisation optics.

Here, I will begin with an introduction to the Fresnel cone and how it can be used to shape light, and give a general overview of quantum key distribution and the BB84 protocol. Afterwards, I will introduce the chosen rotationally symmetric basis, and provide details of the devised measurement system for implementation of the BB84 protocol, before presenting some preliminary experimental results.

The experimental work presented in this chapter is not complete, and as such, is not yet published. Additionally, the experiment was performed using classical light, as opposed to single photons required for quantum experiments. Nonetheless, the early experimental data shows a working experimental system providing results in line with theory and stands as a proof-of-principle experiment, allowing for further work to be undertaken. A manuscript outlining this work is currently in preparation and more experimental measurements will be performed using an optimised system, as will be briefly described in § 6.6.1.

6.2 The Fresnel cone

The Fresnel cone, is a solid glass cone with an apex angle of 90° [34, 345], the geometry of which is shown in Figure 6.1. A beam incident on the cone will be

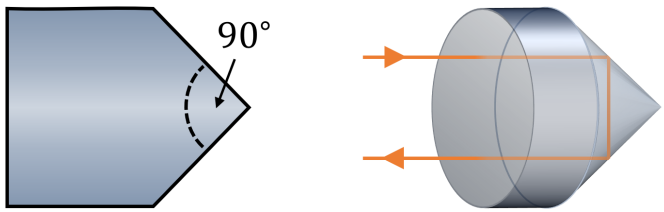

Figure 6.1: Geometry of the Fresnel cone. The left image shows a side view of the cone, with an apex angle of 90° and the right demonstrates the total internal reflection from the back surface of the cone for an off-centre incident beam.

completely reflected from the back surface, as the angle of incidence is greater than that required for total internal reflection. Just like with a mirror (c.f. § 2.2.2), upon reflection from a surface, a phase shift occurs between the orthogonal s and p polarisation components, where the p component lies parallel to the plane of incidence, and s perpendicular to it. Due to the cones geometry, the angle of the plane of incidence varies azimuthally around the tip of the cone, therefore, the decomposition into the s and p polarisation components also varies azimuthally, resulting in azimuthally varying changes to the polarisation. It has previously been shown that back reflection from a Fresnel cone also results in a spin redirection phase, occurring due to conversion from spin to orbital angular momentum [34]. As the Fresnel cone only relies on geometry and total internal reflection, the way in which it can alter polarisation is not wavelength dependent, making it suitable for applications using broadband light.

A light ray entering the cone will experience two total internal reflections. As the incidence angle is above the critical angle, only the phase is affected (i.e. there is no reduction in intensity), allowing the Jones matrix of the two reflections to be written as,

$$\mathbf{J}_{\text{wedge}} = \begin{pmatrix} r_p^2 & 0 \\ 0 & r_s^2 \end{pmatrix} = r_p^2 \begin{pmatrix} 1 & 0 \\ 0 & \mathrm{e}^{2i\delta} \end{pmatrix}, \tag{6.1}$$

where r_p and r_s are the Fresnel reflection coefficients and δ describes the differential phase shift between the s and p polarisation and is given by,

$$\delta = \arg(r_s) - \arg(r_p) = \arg\left(\frac{n^2 - i\sqrt{1-2n^2}}{1-n^2}\right), \tag{6.2}$$

where n relates to the refractive indices of air and the glass cone via $n = n_{\text{air}}/n_{\text{cone}}$ [34].

In the following experiments, a 633 nm laser was used. At this wavelength, $n_{\text{cone}} = 1.56$, giving $\delta = 0.26\pi$ [339]. For two reflections, this is close to $2\delta = \pi/2$, the phase shift induced by a quarter wave plate, meaning that the cone has an effect

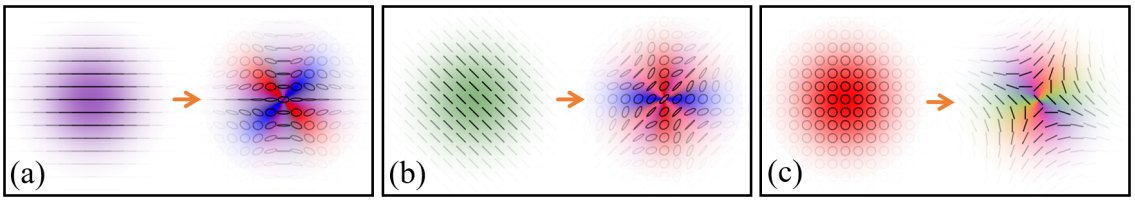

Figure 6.2: Simulated polarisation profiles before (left) and after (right) reflection from the Fresnel cone for three different homogeneously polarised input beams. (a) Horizontal, (b) anti-diagonal and (c) right-handed circular polarised input beams.

on the polarisation similar to that of a quarter-wave plate ($\mathbf{J}_{\text{wedge}} \approx \mathbf{J}_{\text{QWP}}$) but in the azimuthal direction.

The Jones matrix describing the entire effect of the cone, $\mathbf{J}_{\text{cone}}$, is given by [34],

$$\mathbf{J}_{\text{cone}} = \mathbf{R}(-\theta)\mathbf{J}_{\text{wedge}}\mathbf{R}(-\theta). \tag{6.3}$$

Here, a polarisation state written in terms of an x-y coordinate system is rotated to the local $s-p$ polarisation coordinate system of the cone using a standard 2D rotation matrix denoted by $\mathbf{R}(\theta)$. The two reflections are applied (using $\mathbf{J}_{\text{wedge}}$) and then a final rotation is performed in order to get back to the original x-y coordinate system. As the back reflection has changed the beams propagation direction, the sense of rotation has changed, requiring the final rotation to be applied in the same direction as the first.

In Figure 6.2, I give simulated examples of homogeneously polarised beams after reflection from the cone, where it is evident that the cone does indeed act like a QWP but with an azimuthally varying fast axis. Additionally, from Figure 6.2(c), it can be seen that the circularly polarised beam has resulted in one containing all the possible orientations of linear polarisation, spanning the equator of the Poincaré sphere. Using a series of half-wave plates after this beam we can convert it to the familiar radially and azimuthally polarised beams.

Work fully describing all of the different vector beams that can be generated using a Fresnel cone, looking at their focusing properties, and using a Fresnel cone as a broadband polarimeter can be seen in Refs. [34], [20] and [345].

6.3 Quantum key distribution

Quantum key distribution (QKD) is an implementation of quantum cryptography, promising secure communications, where data is encrypted using a secret key generated between two parties [352, 353]. By using quantum entanglement, the presence of a third party trying to obtain the key can be detected, making entanglement desirable for information processing and communication. However, entanglement is known for being unstable - when quantum systems interact with an environment,

entanglement decays through decoherence [354]. Due to this, it is appealing to use photonic quantum states which exploit the weak interacting properties of photons. Within optics, it has been traditional to use polarisation as the degree of freedom to implement QKD protocols, as polarisation is well understood, can be easily controlled and measured using standard optical elements, and is robust to atmospheric turbulence, [354, 355].

The first protocol for quantum cryptography was proposed by Bennett and Brassard in 1984 (BB84) [356], and almost all subsequently proposed QKD protocols can be viewed as adaptations of the original BB84 method [357]. In this section, I will briefly summarise the BB84 key distribution protocol, in terms of photon polarisation, before moving on to § 6.4 and § 6.5 where I outline one way in which this protocol can be implemented using rotationally symmetric states and a Fresnel cone as a measurement device, which together, have the benefit of making the protocol rotational reference frame invariant.

6.3.1 General overview of the BB84 protocol

For a BB84 protocol, two bases must be chosen with the same dimension, d. If the first basis is chosen to be $|\Psi_i\rangle\,, i = 1, ..., d$, then the second must be chosen to satisfy,

$$|\,\langle\Psi_i|\Phi_j\rangle\,|^2 = \frac{1}{d}, \tag{6.4}$$

such that we now have a set of mutually unbiased bases (MUB). MUBs are commonly used within quantum state tomography as they are beneficial for designing efficient QKD protocols [358], as projective measurements provide no knowledge of the state in any other basis. This means that if a state belonging to one basis is prepared, and a measurement is performed in the other basis, then all outcomes will occur with equal probability, losing all stored information.

Traditionally, the *rectilinear* and *diagonal* polarisation bases are used. The former is formed of horizontal and vertical ($|\hat{h}\rangle$, $|\hat{v}\rangle$) polarisation states, with unit vectors $(1, 0)$ and $(0, 1)$, whereas, the diagonal basis consists of diagonal and antidiagonal ($|\hat{d}\rangle$, $|\hat{a}\rangle$) polarisation states, with $(1/\sqrt{2}, 1/\sqrt{2})$ $(1/\sqrt{2}, -1/\sqrt{2})$ as the corresponding unit vectors. It is apparent that these form an MUB as we cannot simultaneously measure polarisation in the rectilinear and diagonal bases.

The BB84 protocol is usually described with the aid of a named sender and receiver, conventionally named Alice and Bob. The sender, Alice, prepares photons polarised in one of the four directions, which she sends to Bob, the receiver. Bob will then choose to make a measurement either in the $|\hat{h}\rangle/|\hat{v}\rangle$ or $|\hat{d}\rangle/|\hat{a}\rangle$ basis, recording the basis chosen and the corresponding result. Whenever Bob measures in the same basis that Alice used to prepare the state, they get perfectly correlated results. When different bases are used, they get uncorrelated results, leaving Bob with a string of bits with a 25% error rate [352]. However, it is straightforward for Alice and

Bob to account for these errors. By using classical communication, they announce which basis they used for each photon, disregarding any bits when the bases were different, as they know that their results will be perfectly correlated when the basis is the same. At the end of this procedure, only around 50% of the bit string is kept.

Here, the BB84 protocol was described for 2 particular polarisation bases, but of course any MUB can be used. Another obvious choice is to use the circular polarisation basis along with one of the two bases mentioned above. However, other MUBs have been used, such as those consisting of OAM states [358–361], or vector beams, exploiting the entanglement between spatial modes and polarisation [362, 363]. When fibres are used for transmission, it is inconvenient to use polarisation states, as fibres are not always polarisation maintaining. Instead, phase encoding may be used, where the MUB contain phase differences that are realised through use of an asymmetric Mach-Zehnder interferometer [364].

6.4 Rotationally symmetric basis

Many QKD protocols have the need for a shared reference frame between the sender and receiver. For polarisation encoding, we require alignment of polarisation states, or interferometric stability for phase encoding [365]. However, there are some scenarios in which establishing a shared reference frame for QKD becomes impractical. An example of which includes earth-to-satellite QKD, in which only one axis of the reference frame (aligned along the propagation direction) is well defined, with a rotation between the others [365]. Another being handheld QKD devices, where again, the relative orientation between the emitter and receiver can be variable [366]. Previously, this problem has been addressed by encoding information in angular momentum states which are invariant under rotation [367], or by using entanglement [368].

It is evident that by performing a QKD protocol employing MUBs with rotationally symmetric states, we can discard the need for a shared coordinate reference frame, with only the direction of the axis along the propagation direction needing to be known. If polarisation encoding is to be used, then using circular polarisation becomes an obvious choice, as it is rotation independent, however, beams with spatially varying polarisation have also been used [369, 370]. Here, I will also use vector beams with rotational symmetry to implement the BB84 protocol, where the difference from previous work lies within the measurement system. The previous work relied on optical elements such as q-plates [369, 370] which are wavelength dependent, whereas, for the system being presented here, a wavelength independent Fresnel cone is implemented.

It is possible to generate rotationally symmetric polarisation profiles using superpositions of orthogonally polarised LG modes. Here, we chose beams of the

form,

$$\frac{1}{\sqrt{2}}\Big(|\mathrm{LG}_0^1\rangle\,|\hat{r}\rangle + \mathrm{e}^{i\phi}\,|\mathrm{LG}_0^{-1}\rangle\,|\hat{l}\rangle \Big), \tag{6.5}$$

for $\phi = 0, \pi, \pm\frac{\pi}{2}$. This allows us to construct two mutually unbiased bases with dimension $d = 2$. The first of which corresponds to radially and azimuthally polarised beams,

$$\begin{aligned} |\Psi_0\rangle &= \frac{1}{\sqrt{2}}\Big(|\mathrm{LG}_0^1\rangle\,|\hat{r}\rangle + |\mathrm{LG}_0^{-1}\rangle\,|\hat{l}\rangle \Big), \\ |\Psi_1\rangle &= \frac{1}{\sqrt{2}}\Big(|\mathrm{LG}_0^1\rangle\,|\hat{r}\rangle - |\mathrm{LG}_0^{-1}\rangle\,|\hat{l}\rangle \Big), \end{aligned} \tag{6.6}$$

and the second corresponds to clockwise rotational and anticlockwise rotational polarised beams,

$$\begin{aligned} |\Phi_0\rangle &= \frac{1}{\sqrt{2}}\Big(|\mathrm{LG}_0^1\rangle\,|\hat{r}\rangle + i\,|\mathrm{LG}_0^{-1}\rangle\,|\hat{l}\rangle \Big), \\ |\Phi_1\rangle &= \frac{1}{\sqrt{2}}\Big(|\mathrm{LG}_0^1\rangle\,|\hat{r}\rangle - i\,|\mathrm{LG}_0^{-1}\rangle\,|\hat{l}\rangle \Big), \end{aligned} \tag{6.7}$$

examples of which are shown in Figure 6.3. To verify that $|\Psi_i\rangle$ and $|\Phi_i\rangle$ form a set of MUBs, we can explicitly calculate the mode overlap. In doing so the relation $|\,\langle\Psi_i|\Phi_j\rangle\,|^2 = 1/2$, as given in Eq. 6.4, was confirmed.

Experimentally, these beams are generated using the DMD setup, as described previously in § 2.6 and shown in Figure 2.12. In terms of performing a BB84 protocol, the sender would randomly generate one of these 4 rotationally symmetric modes which are then sent to, and measured by, the receiver.

6.5 Measurement system

The BB84 protocol requires a measurement system in which the basis to measure in can be chosen at random. For the rotationally symmetric states described above, this reduces to splitting a beam into either its radial and azimuthal components or, its clockwise/anticlockwise rotational components. A schematic of the setup used for this is shown in Figure 6.4.

Letting the Jones vector of the input mode to be denoted by $\mathbf{J}_{\mathrm{in}}$, the action of the measurement system up to and including the quarter wave plate can be described by,

$$\mathbf{J}_{\mathrm{out}} = \mathbf{J}_{\mathrm{QWP}}\left(\frac{\pi}{4}\right)\mathbf{J}_{\mathrm{cone}}\mathbf{J}_{\mathrm{HWP}}(\varphi)\mathbf{J}_{\mathrm{HWP}}(0)\mathbf{J}_{\mathrm{in}}, \tag{6.8}$$

where, $\mathbf{J}_{\mathrm{HWP}}$ and $\mathbf{J}_{\mathrm{QWP}}$ represent the Jones matrices for a half waveplate and quarter waveplate with their fast axis rotated to the angle indicated in brackets, with respect to the horizontal, and $\mathbf{J}_{\mathrm{cone}}$ is the Jones matrix for the Fresnel cone. In the

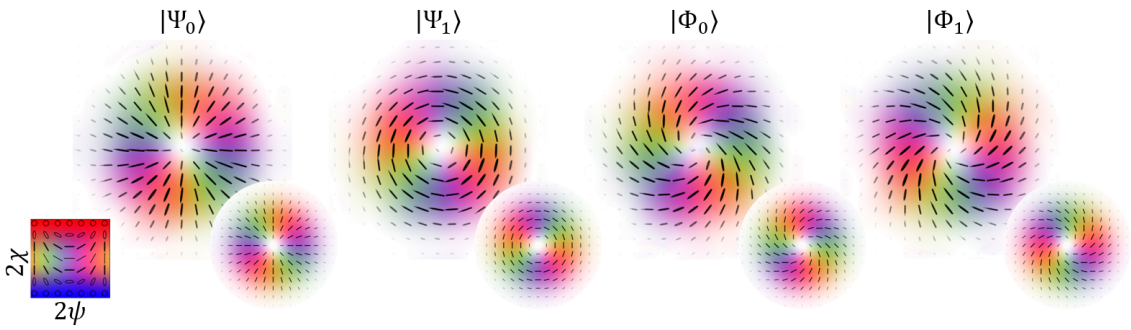

Figure 6.3: Two-dimensional MUBs consisting of rotationally symmetric polarisation states. $|\Psi_i\rangle$ are radial and azimuthally polarised modes, described by Eq. 6.6. $|\Phi_i\rangle$ are clockwise and anticlockwise rotational modes as described by Eq. 6.7. Smaller inserts show the equivalent simulated polarisation plots. On the left, the colour map used to depict polarisation is shown, where ψ and χ represent the orientation and ellipticity if the polarisation ellipses, respectively. Intensity is shown as opacity.

measurement system, the second half waveplate, as indicated by the blue box in Figure 6.4, is used to select the measurement basis. To perform measurements in $|\Psi\rangle$, the radial/azimuthal basis, φ is set to $\pi/8$ and $\varphi = \pi/4$ for the $|\Phi\rangle$ basis.

A telescope (lenses f_1 and f_2) is used to expand the input beams to fill as much of the cone as possible, avoiding the noisy cone centre. The beams are then demagnified again such that they fit on the camera sensor and the back surface of the cone is imaged.

It is possible to write the Jones vectors of the basis modes as,

$$\begin{gathered} \mathbf{J}_{\Psi_0} = \begin{pmatrix} \cos\alpha \\ \sin\alpha \end{pmatrix}, \ \mathbf{J}_{\Psi_1} = \begin{pmatrix} i\sin\alpha \\ -i\cos\alpha \end{pmatrix}, \\ \mathbf{J}_{\Phi_0} = \frac{1}{\sqrt{2}} \begin{pmatrix} \cos\alpha - \sin\alpha \\ \cos\alpha + \sin\alpha \end{pmatrix}, \ \mathbf{J}_{\Phi_1} = \frac{1}{\sqrt{2}} \begin{pmatrix} \sin\alpha + \cos\alpha \\ \sin\alpha - \cos\alpha \end{pmatrix}, \end{gathered} \tag{6.9}$$

which describes the polarisation as you travel in an azimuthal direction around the beams centre, characterised by the angle α. By using these as $\mathbf{J}_{\text{in}}$ in Eq. 6.8, it can be shown that $\mathbf{J}_{\text{out}}$ will correspond to either horizontal or vertical polarisation if the correct measurement basis is used. This can be translated to intensity measurements by using a polarisation beam splitter (PBS), as shown in Figure 6.4. However, if the incorrect measurement basis is used, then $\mathbf{J}_{\text{out}}$ will contain equal weightings of horizontal and vertical polarisation components over the entire beam profile, but with different phases between them.

Figures 6.5 and 6.6 show simulated polarisation profiles of the beams after each optical component. Figure 6.5 corresponds to measurements made in the $|\Psi\rangle$ basis, when the second HWP is set to 22.5°. From this it can be seen that intensity is

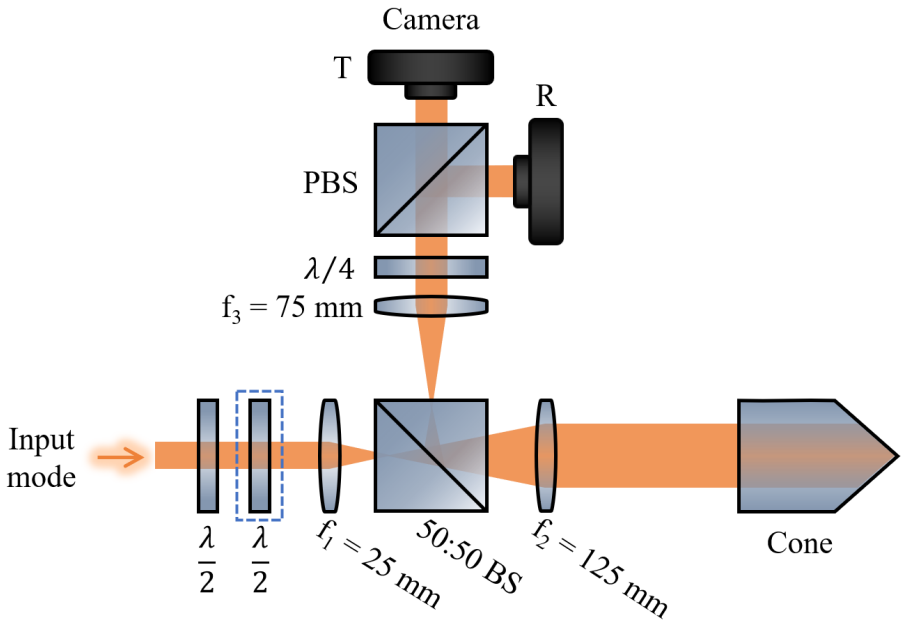

Figure 6.4: Measurement system for BB84 protocol using rotationally symmetric states. Input modes are generated to the left, using the digital micromirror device setup discussed previously. $\lambda/2$: half waveplate, $\lambda/4$: quarter waveplate, BS: 50:50 beam splitter, PBS: polarising beam splitter. T and R label the transmitted and reflected outputs after the PBS, corresponding to horizontal and vertical polarisation components, respectively. The fast axis of the first half waveplate and the quarter waveplate are set at 0° and 45° to the horizontal, respectfully. The second half waveplate, indicated with the blue box, is used for choosing the measurement basis by rotating to either 22.5° or 45°.

expected in only one arm after the PBS for the radial and azimuthal beams, and the intensity is split equally between the transmitted and reflected outputs when the clockwise and anticlockwise rotational beams are used as inputs. Equivalent plots are shown in Figure 6.6 for the $|\Phi\rangle$ measurement basis, when the second HWP is set to 45°

One benefit of using a measurement system implementing a Fresnel cone, is that it is not wavelength dependent, as mentioned above. If broadband light is to be used, then the entire system in Figure 6.4 can be made wavelength independent by replacing the HWP and QWP with Fresnel rhombs [1, 371]. These are glass prisms which impart phase shifts using total internal reflection, rather than relying on the birefringent materials used in waveplates.

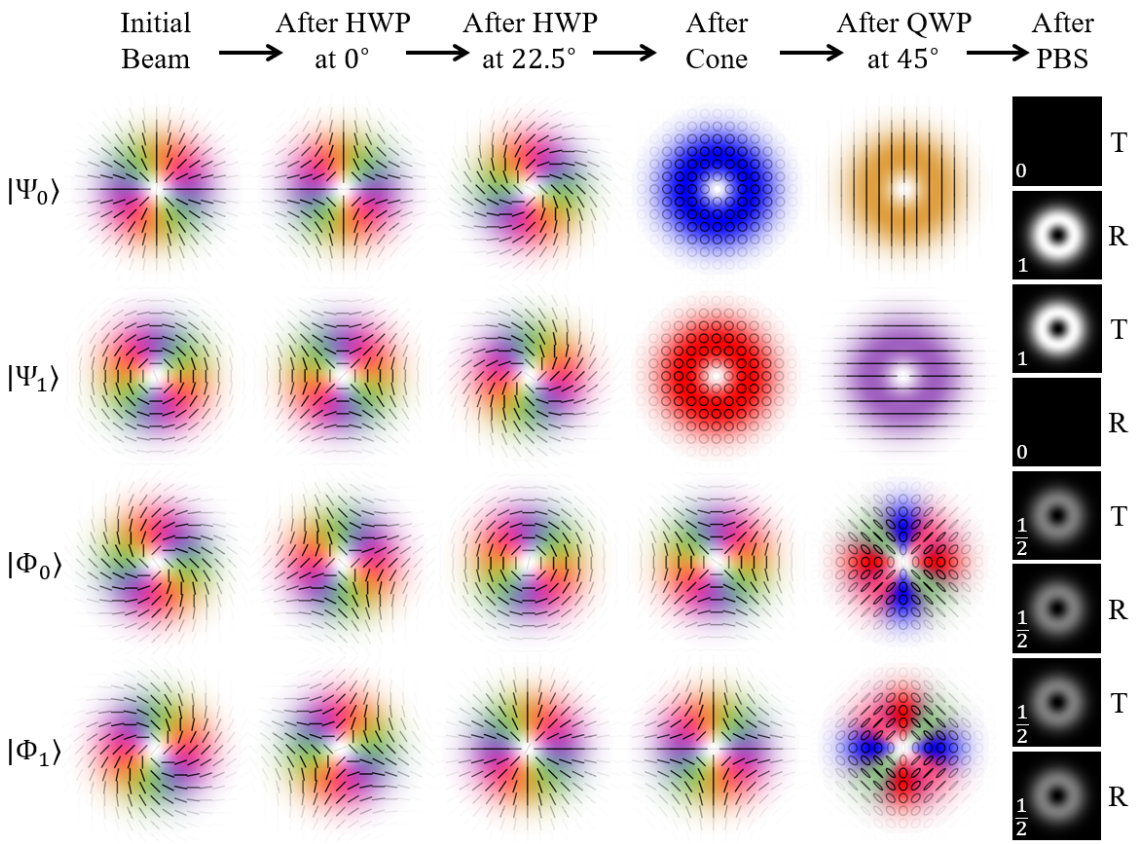

Figure 6.5: Simulated polarisation profiles of the input beams given in Figure 6.3 after each optical element of the set up shown in Figure 6.4, for measuring in the $|\Psi\rangle$ by setting $\varphi = 22.5°$. The last column shows the expected intensity profiles and fraction of total intensity after transmission (T) and reflection (R) from the polarising beam splitter.

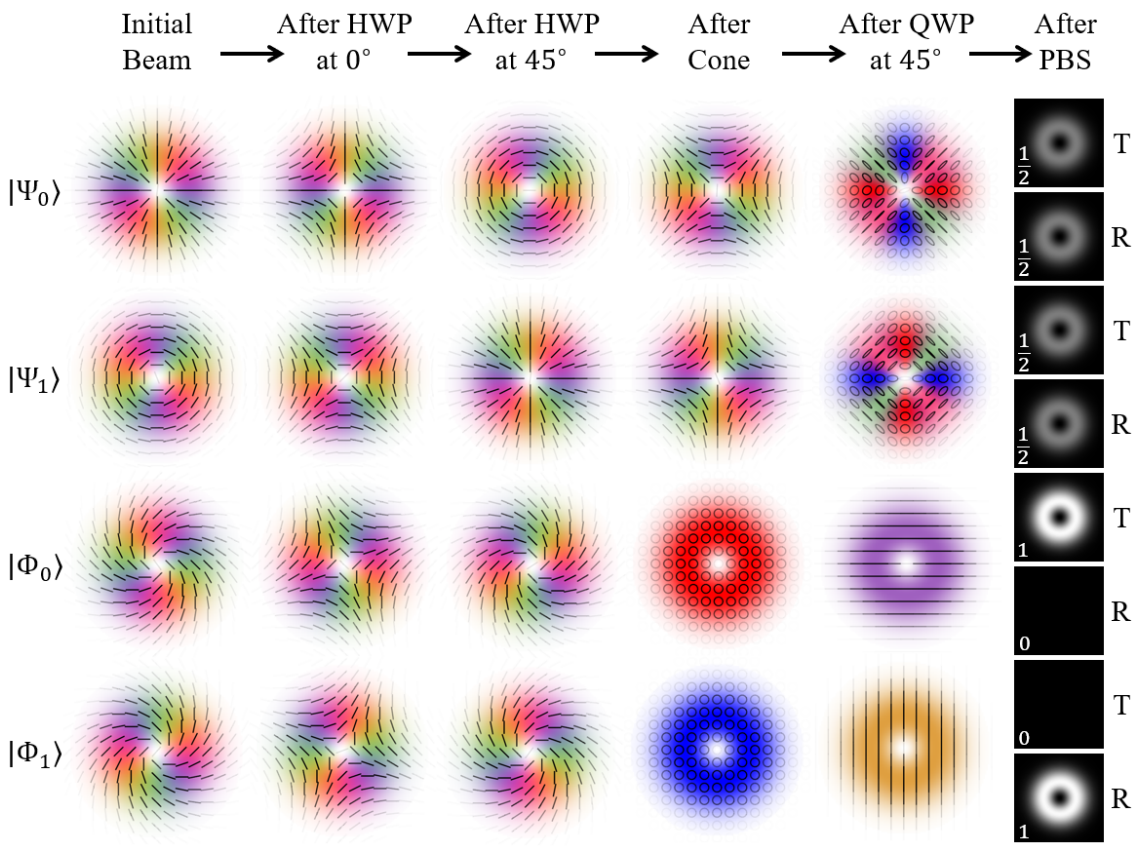

Figure 6.6: Same as Figure 6.5 but for measurements performed in the $|\Phi\rangle$ basis by setting $\varphi = 45°$.

6.6 Early BB84 measurement results

Preliminary results obtained from implementing the BB84 protocol with rotationally symmetric polarised beams will now be discussed. The rotationally symmetric vector beams were generated using the DMD setup shown in Figure 2.12 (with an additional QWP after the DMD to allow generation of the beams using the right- and left-handed circular polarisation basis) and directed towards the measurement system described above and shown in Figure 6.4. The setup in Figure 6.4 was used, but with the slight modification of a linear polariser in place of the PBS. Therefore, for each input beam, two measurements had to be taken, one for the polariser rotated to allow horizontal polarisation to pass, and another for vertical. However, if information is to be sent using single photons, then a PBS would be required.

For both bases, a horizontal (transmitted) and vertical (reflected) measurement was recorded using a CMOS camera for each of the four input modes, corresponding to a total of sixteen measurements. For each pair of measurements, the fraction of the total intensity in the horizontal and vertical polarisation images was found. The results of this can be seen in Table 6.1, and a visual representation of the results is given in Figure 6.7.

Table 6.1: Experimental data for BB84 protocol using rotationally symmetric vector beams. For each measurement basis, $|\Psi\rangle$ and $|\Phi\rangle$, selected by HWP angles of 22.5° and 45°, respectively, the fraction of intensity found in the transmitted (T) and reflected (R) outputs is given for each of the input modes described by equations 6.6 and 6.7.

Measurement basis		$\|\Psi_0\rangle$	$\|\Psi_1\rangle$	$\|\Phi_0\rangle$	$\|\Phi_0\rangle$
$\|\Psi\rangle$	T	0.131	0.824	0.464	0.486
	R	0.869	0.176	0.536	0.514
$\|\Phi\rangle$	T	0.526	0.460	0.854	0.120
	R	0.474	0.540	0.146	0.880

Ideally, when measuring in the correct basis, all of the intensity will be in either the T or R output, and when measuring in the incorrect basis, the intensity should be split equally between the two outputs. In order to quantify the quality of the experimental results we can employ a measure known as the quantum bit error rate (QBER) [372, 373]. For a BB84 protocol carried out using single photons, this is the fraction of bits (photons) that disagree when comparing the state of the photon generated to the state detected. Therefore, the QBER can be calculated using,

$$\text{QBER} = \frac{\text{number of error bits}}{\text{total number of bits received}}. \tag{6.10}$$

This ratio should be as small as possible, but must be less than the maximum

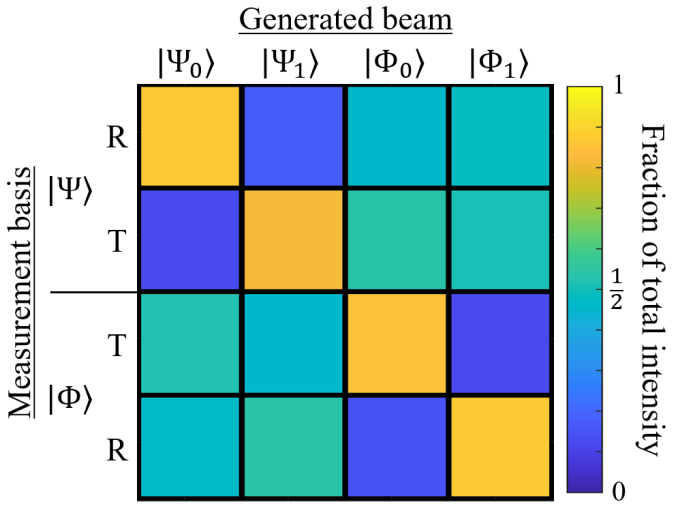

Figure 6.7: Visual representation of the BB84 intensity results given in Table 6.1.

tolerable error rate for the specific protocol being carried out, in order to have secure, reliable communication.

In our case, classical light beams were used and so, the probabilities that would be obtained over multiple sequential single photon measurements are contained within the intensity measurements. As such, the QBER can be calculated directly from the values in Table 6.1. From this we obtain a QBER of 14.3%, which is greater than the maximum of 11% that a BB84 protocol, as it is carreied out here, can tolerate[1] [373, 374].

6.6.1 Discussion of results and proposed experimental improvements

From Table 6.1, and Figure 6.7 it can be seen that the proposed measurement system has been demonstrated to give results close to expected, however they are not perfect, as confirmed by the 14.3% QBER obtained. Looking at the measured intensity profiles directly (Figure 6.8), it is evident that there exists an uneven intensity distribution over some of the measured output profiles, where as, from simulation (Figure 6.5 and 6.6), we know that we should expect to have rotationally symmetric intensity distributions (or zero intensity) in all cases. This was thought to be due to small misalignments of optical components, non-ideal optical components or errors within the beam generation. To confirm this suspicion and investigate it further, "bad" simulations of the entire experimental system were performed. This included simulating imperfect input beams, imperfect optical components, misaligned optical components (either aligned off centre or at non-normal incidence) and waveplates

[1] Note that it is possible to increase the tolerable QBER using various methods, such as advantage distillation protocols [374].

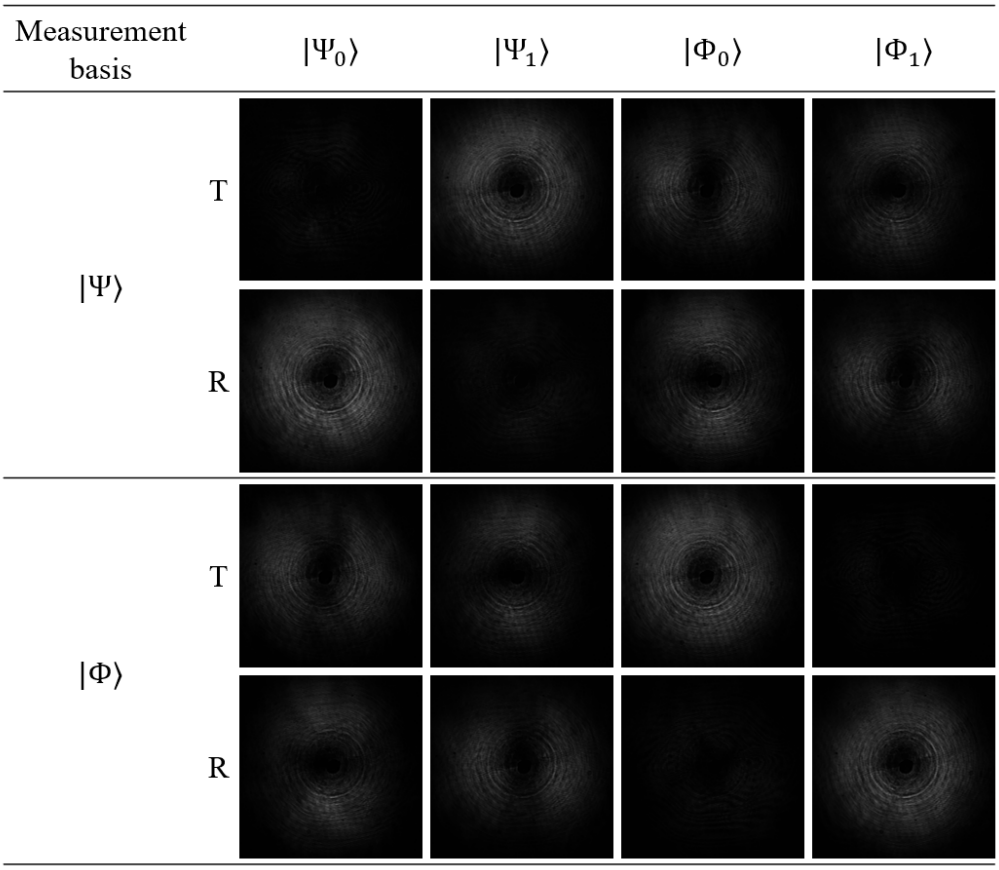

Figure 6.8: Raw experimental intensity images for the BB84 protocol using rotationally symmetric states. The generated beam is indicated at the top and the measurement basis used indicated on the left, where T and R correspond to the transmitted (horizontally polarised) or reflected (vertically polarised) experimental outputs.

at incorrect fast axis angles.

We can generate vector beams with high fidelity using the DMD system, and by comparison of the measured input beams to theoretical plots in Figure 6.3, it can be seen that they are appear very similar. From the simulations, it was found that simulating imperfect input vector modes would not result in the particular uneven intensity distributions as seen in Figure 6.8, confirming that the experimental errors obtained were not a result of the beam generation. Similarly, modelling misaligned lenses, waveplates, imperfect waveplates or a misaligned Fresnel cone, would give errors in the results but not with the the same "lobe"-type intensity distributions seen in the experimental data. From this thorough simulation-based investigation, it was concluded that the errors present in the experimental data most likely arose from a non-ideal 50:50 beam splitter.

50:50 beam splitters are well known for introducing unwanted phase shifts upon reflection [375], resulting in unwanted polarisation changes. In fact, in a similar optical setup implementing a Fresnel cone [345], it was found that one of the main sources of polarisation shifts originated from the 50:50 BS. To counteract this, the Mueller matrices of the beam splitter in transmission and reflection were included in the equation representing the system. This is something that could also be considered here. Alternatively, the Mueller matrix of the BS could be measured, and the effects of this precompensated, using the methods outlined in Ref. [376], by incorporating an additional HWP and QWP in the system just before the BS. By doing this, we can effectively make the Mueller matrix of the combined HWP, QWP and 50:50 BS equal to that of an ideal 50:50 BS. This is the method that will be used for future measurements, with the aim of reducing the QBER to below the 11% threshold.

One other aspect to note about the measurement system being used here is that it has an efficiency of only 25%, arising due to the use of a 50:50 beam splitter and that light travels through this element twice. This results in low output intensities that are sensitive to noise. Redesigning the system to accounting for this, by perhaps removing the BS and instead incorporating a pick-up mirror to retrieve the reflected beam from the cone, could improve results, and also allow the system to be more easily used for single photon QKD protocols.

6.7 Chapter 6 conclusion

To conclude, in this chapter, I have presented a proof-of-concept experiment for the implementation of a BB84 protocol using rotationally symmetric states and a Fresnel-cone based measurement system.

I began by introducing the Fresnel cone, its Jones matrix description and provided examples of the way in which it can alter polarisation. I then provided an overview of QKD focusing on the BB84 protocol, and introduced the rotationally symmetric basis that will be used. These basis states were in the form of vector beams, with spatially varying polarisation, where it is the polarisation profiles themselves that have rotational symmetry. Here, the familiar radial and azimuthally polarised beams were used as well as those with a "swirly" clockwise and anticlockwise rotating polarisation distribution.

In § 6.5, I outlined the measurement system for implementing the BB84 protocol, where we could perform projections into either the radial/azimuthal or clockwise/anticlockwise rotational bases. This measurement system incorporated a Fresnel cone, which, due to its geometry, is ideal for performing projections into bases where its states have rotational symmetry. Additionally, the rotational symmetric basis and measurement system presented in this chapter provides a way of implementing a rotational reference frame invariant BB84 protocol, useful for situations

where it is difficult or impractical to establish a shared rotational reference frame between the sender and receiver, e.g., for earth-to-satellite QKD. The polarisation modifications by the Fresnel cone result only from phase shifts induced by total internal reflection at the cones back surface, and does not rely on birefringence, unlike other polarisation optics. Therefore, it is largely wavelength independent, meaning that by changing the waveplates in the the setup in Figure 6.4 to Fresnel rhombs, we would have a broadband system.

The results presented in this chapter are in the form of preliminary experimental data, and contain slight deviations from theoretical predictions. Nonetheless, the results follow simulations closely enough to demonstrate a working principle, warranting further experimental effort. Simulations were carried out to identify possible sources of experimental error, concluding that they most likely result from unwanted phase shifts upon reflection from the 50:50 beam splitter. A plan has been put in place to experimentally precompensate for these phase shifts (as detailed above), hopefully allowing improved data to be acquired with a lower QBER, and a manuscript is currently in preparation.

Chapter 7

Short projects

7.1 Chapter 7 Introduction

In this chapter, I will briefly introduce two shorter projects that I contributed to. Both of these projects were undertaken in collaboration with research groups from other universities, where I played a role in some of the experimental data collection and analysis. Although the experiments discussed here were undertaken as an aside to my main PhD work, they nevertheless incorporate some of the main themes discussed throughout: Namely, holography and beam shaping, and the propagation, analysis and classification of vector beams.

7.2 Complex Zernike modes

For 2 months the University of Glasgow Optics Group had a visiting PhD student, Kerr Maxwell, from the Theoretical Physics Research Group at the University of Birmingham. In a collaboration with this student, we looked at the generation, propagation and characterisation of complex Zernike modes, where I was responsible for working on the experimental side of the project (building the experimental setup, hologram design, beam generation, and data acquisition). I also performed the simulations required for the figures in this thesis. K. Maxwell was responsible for the more theoretical aspects of this work, along with his PhD supervisor, Mark R. Dennis. A manuscript detailing this work is currently in preparation, and the following sections will summarise some of the results.

7.2.1 Zernike polynomials and complex Zernike modes

Over the last two decades, the development of light shaping tools such as spatial light modulators, digital micromirror devices and q-plates, have allowed complex families of spatial modes to be experimentally generated and explored. Some of

the most well established mode-families are the Hermite-, Laguerre- [53] and Ince-Gaussian [54] modes, all of which are solutions to the paraxial wave equation in Cartesian, cylindrical and elliptical coordinates, respectively. However, although HG and LG modes are often the most commonly used mode sets, other examples include Bessel [55], Mathieu [57], Airy [56] and Pearcey beams [58].

Here, yet another family of beams, the complex Zernike modes, will be discussed. These modes are defined on a circular domain, or aperture, and are constructed by combining the well-known Zernike polynomials $\left(R_p^\ell\right)$ [377] with an azimuthal phase factor,

$$\mathcal{Z}_p^\ell(r,\phi) = \mathrm{e}^{i\ell\phi} R_p^\ell(r) \quad \text{for} \quad |\ell|, p \in \mathbb{N} \quad \text{and} \quad 0 \leq r \leq w_0. \tag{7.1}$$

Here, r denotes the radial distance from the optical axis, which is constricted to a disk with maximum radius w_0, the chosen beam waist, and the $e^{i\ell\phi}$ factor means that each mode can carry orbital angular momentum (OAM). The Zernike polynomials, R_p^ℓ, can be evaluated using,

$$R_p^\ell(r) = \sum_{k=0}^{p} \frac{(-1)^k (2p+\ell-k)!}{k!\,(\ell+p-k)!\,(p-k)!} r^{2p+\ell-2k}, \tag{7.2}$$

where we chose to index using a radial polynomial number p and an OAM number ℓ. As Zernike polynomials are defined on a unit disk, they are often used for describing aberrations in apertured systems [378–380]. For this they are conventionally labelled using an (n,m) indexing scheme (R_n^m) [377]. However, here the choice of (ℓ,p) brings the modes more in line with the way in which the familiar LG modes are indexed, with the mode order being given by $N = 2p+|\ell|$, and we can easily convert between the indexing schemes via $(\ell,p) = (m, \frac{n-m}{2})$.

One property of the complex Zernike modes, that differs from other beams carrying OAM, such as Bessel beams or LG modes, is that any $\mathcal{Z}_p$ can be embedded with an arbitrary value of orbital angular momentum while maintaining it's chosen apertured radius.

7.2.2 Experimental generation, results and propagation measurements

For the experimental generation of Zernike modes, we employ a liquid-crystal-based phase-only spatial light modulator (SLM) along with well established digital holography techniques (as seen in Refs. [119, 381–385] and as discussed previously in § 2.5.1), which allows us to modulate both the intensity and phase of an incident beam. SLM's are unable to modulate all of he incident light, typically having a conversion efficiency between 79% and 97% [386]. Therefore, modulating the phase and amplitude directly will result in contamination of the shaped beam with unmodulated light. To overcome this, it is possible to superimpose the desired hologram with a blazed diffraction grating. This has the effect of separating the converted

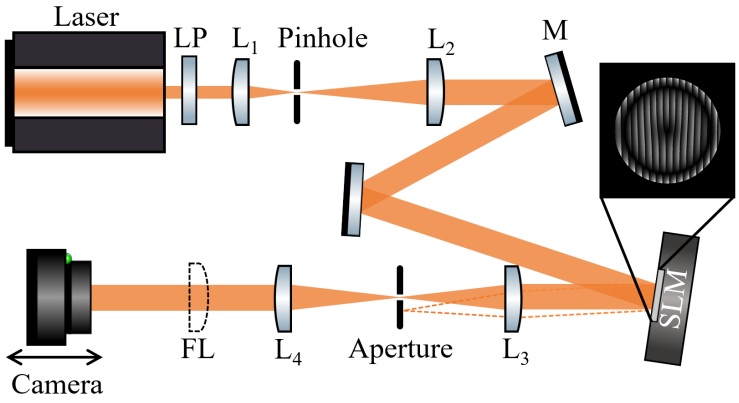

Figure 7.1: Experimental setup for generating complex Zernike modes using an SLM. LP: linear polariser, L_i: Lens, M: mirror, FL: Fourier lens. An example hologram for a $\mathcal{Z}_1^1$ mode is shown as an inset (grating not to scale). The hologram has greyscale values of 0-255, corresponding to 8-bits.

from the unconverted light, with the desired shaped beam appearing in the first diffraction order.

A schematic of the experimental setup can be seen in Figure 7.1. We use an external cavity diode laser with a 795 nm wavelength, which is cleaned, expanded and collimated (using lenses L_1 and L_2 and a 40 µm pinhole) to overfill the active area of the SLM (Hamamatsu X13138-02, 1270 × 1024 pixels, effective active area of 15.9 × 12.8 mm). It is only possible for the phase of incident light to be modulated if the orientation of its polarisation is aligned with the liquid crystals of the SLM. As such, a linear polariser (LP) is used after the laser to ensure horizontally polarised light.

On the SLM, a hologram to generate a desired Zernike mode is displayed, using techniques described in [120,387] and § 2.5.1, to effectively modulate both the phase and intensity of the incident Gaussian beam. An example of which is shown in the inset of Figure 7.1. After the SLM, we have a telescope (L_3 and L_4) to demagnify the beam to fit on the camera sensor, in the Fourier plane of which, a variable aperture is used to select the first diffraction order and block all other unwanted orders. The desired beam can then be viewed and recorded by a CMOS camera (jAi GO-5000M-USB) in the image plane of the SLM. To view the Fourier transform of the experimentally generated Zernike modes we include an additional Fourier lens. To observe the full propagation, the camera is mounted on a translation stage controlled by a stepper motor, allowing precise displacement along the optical axis.

The left of Figure 7.2 shows experimentally measured Zernike beams for $p \in [0, 3]$ and $\ell \in [0, 4]$ and the right shows an experimentally measured and simulated Z_4^4, for comparison. Here, only beams with positive ℓ are shown, but the intensity distributions for negative ℓ are identical. The only difference in the beams with

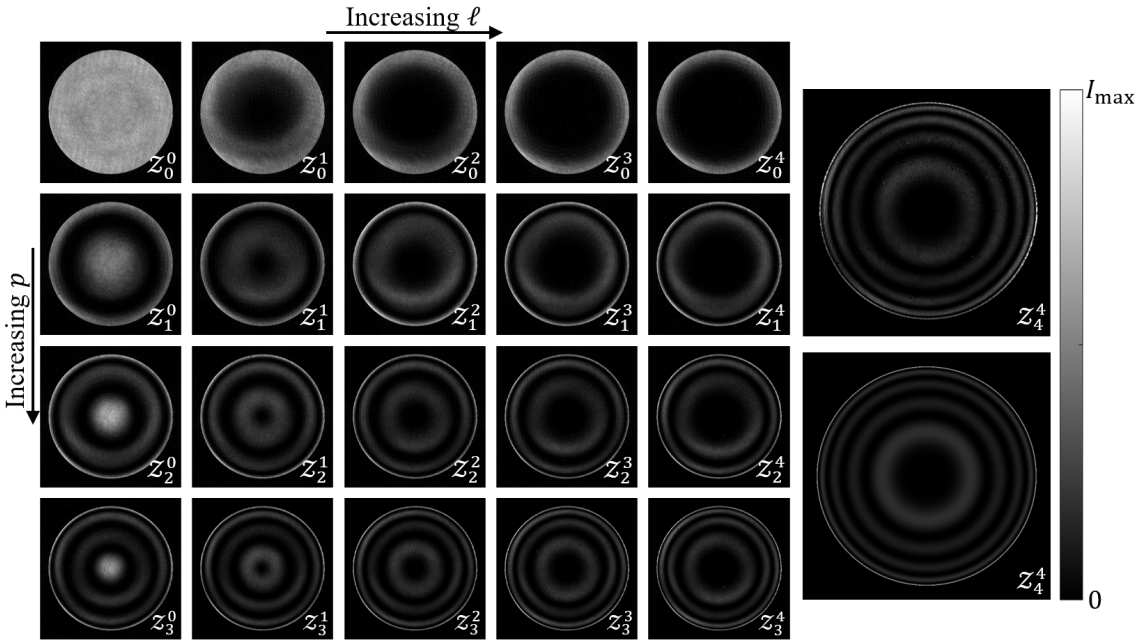

Figure 7.2: Experimentally measured Zernike modes, $\mathcal{Z}_p^\ell$. On the right is an experimentally measured $\mathcal{Z}_4^4$ mode (top) compared to simulation (bottom).

either $\pm\ell$ is in the handedness of the helical phase fronts. From Figure 7.2, we can see that the Zernike modes consist of $p+1$ radial oscillations, including a sharp peak at the beam periphery as well as a slightly smaller central peak if $\ell = 0$. As mentioned previously, increasing ℓ does not increase the size of the mode, but instead shifts the peaks closer towards the beam edge.

Figure 7.3 shows the behaviour of a Z_3^4 mode upon propagation. For this, multiple transverse planes were imaged (at 1 mm intervals), and slices through the centre of these images stitched together to display the longitudinal intensity profiles. The free space, paraxial propagation over a distance of 360 mm is given in Figure 7.3(a), displayed as a half and half comparison with theory (top), as the modes are radially symmetric. Figures (b-d) show the propagation under weak focusing using a 100 mm lens. Experimental results are given in (b), and intensity profiles of the original beam (at 0 mm) and the focused beam (at 100 mm) are given in (c). Simulation of the Z_3^4 mode propagating to the focus and an additional focal length past the focus is given in (d), where a clear bottle beam [388–390] is created around the focus.

Unlike other structured light beams (e.g. the HG and LG modes), Zernike modes change form upon propagation, as apparent from Figure 7.3. Another difference that should be noted, is that the Zernike beams are are only well defined by closed mathematical expressions in the aperture plane and the Fourier plane. However, their form in the far field can be approximated using the Zernike-Nijboer theory [377,391] and the *extended* Zernike-Nijboer theory, developed by Augustus J. E. M.

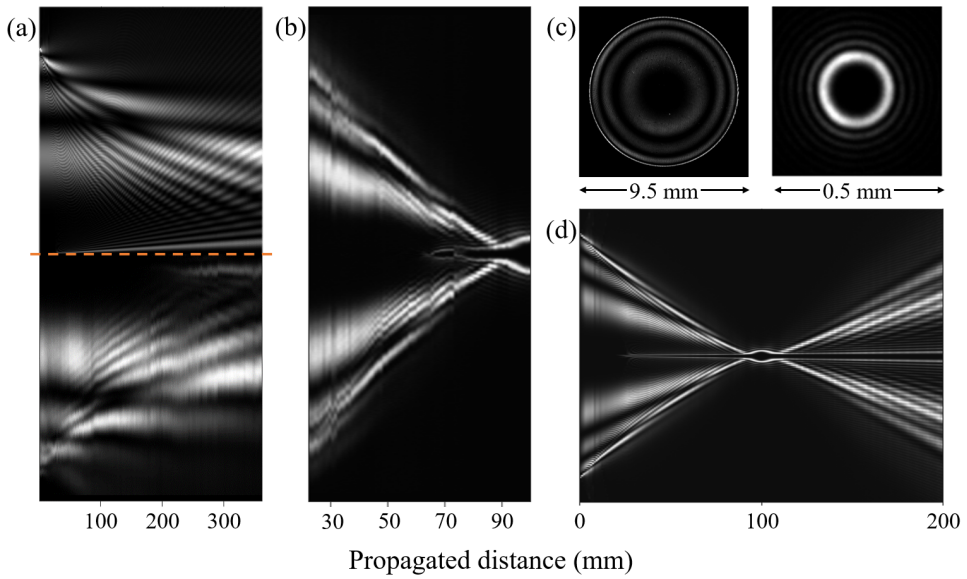

Figure 7.3: Longitudinal cross-sections of a propagating Z_3^4 mode. (a) Half and half comparison between theory (top) and experiment (bottom) of paraxial, free space propagation, over a distance of 360 mm. (b) Experimental results of propagation after a 100 mm lens, with transverse profiles of the original beam and focused beams given in the left and right of (c), respectively. (d) Simulated propagation over 2 focal lengths, with the focus occurring at a distance of 100 mm.

Janssen, can be used for approximating their propagation more generally [392, 393]. The details of these these approximations will be covered in the manuscript currently in preparation.

7.2.3 Measuring orbital angular momentum

Being able to extract the orbital angular momentum (OAM) of vortex beams is of great importance in many application involving OAM carrying beams. For example, OAM modes can be used as a basis for mode-division multiplexing in both free space and fibre communications. Many different techniques exist for measuring OAM, such as interfering the mode with a Gaussian beam [394,395], self-interference [396], using annular gratings [397], or via mode separation [398–400]. Here, to determine the magnitude and sign of the orbital angular momentum number ℓ of the generated complex Zernike modes, we employ the the tilted lens method [401]. This method provides a simple but robust way to measure the average topological charge of a beam from a single camera image. In the focal plane behind the tilted lens, the number of lobes is given by $|\ell| + 1$, and thus the number of dark stripes directly corresponds to $|\ell|$. Additionally, the sign of the OAM number can be determined from the direction of the tilt of the intensity pattern.

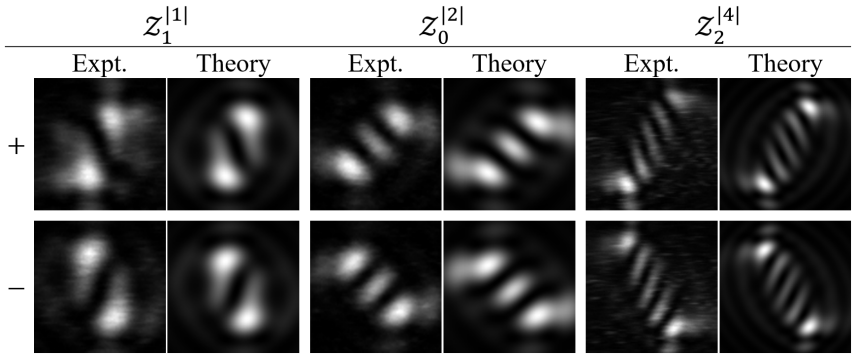

Figure 7.4: Experimentally measured and theoretically predicted intensity distributions in the focal plane of a tilted lens for complex Zernike modes $\mathcal{Z}_1^{\pm 1}$, $\mathcal{Z}_0^{\pm 2}$ and $\mathcal{Z}_1^{\pm 4}$. The top row shows results for positive ℓ, and negative ℓ are given in the bottom row.

Experimental measurements were taken using a 100 mm lens, the results of which show excellent agreement to theory as shown in Figure 7.4.

7.3 Measuring the invariance of vector beams in chiral media

In this section, I will give a brief overview of a project I contributed to in collaboration with the Structured Light group at the University of the Witwatersrand. This work looked at the invariance of vectorial structured light to unitary perturbations and can be seen in Ref. [402].

A propagating light beam can experience distortions in both amplitude and phase. These can occur from misalignments or imperfections in optical components or from propagation through perturbing media, such as turbulent air or optical fibres. Any distortions in amplitude and phase can result in changes to polarisation patterns, however, the work outlined in [402] aims to show that although the polarisation structure changes, its inhomogeneous nature remains unaltered.

We begin by writing a vectorial structured light beam using a quantum notation,

$$|\Psi\rangle = |u_1\rangle_A |v_1\rangle_B + |u_2\rangle_A |v_2\rangle_B \,, \tag{7.3}$$

where A and B denote the spatial and polarisation degrees of freedom (DoF), respectively. In this form, the non-separable form of the two DoF is highlighted - mimiking local quantum entanglement. Aditionally, from Eq. 7.3 it can be seen that the light field resembles a pair of qubits. For qubit pairs, the entanglement can be determined through a simple measure, namely, the concurrence [403]. This measure of entanglement in two dimensions has been shown to be a good measure of the degree of non-separability of vector beams [70, 404, 405]. Hence, concurrence

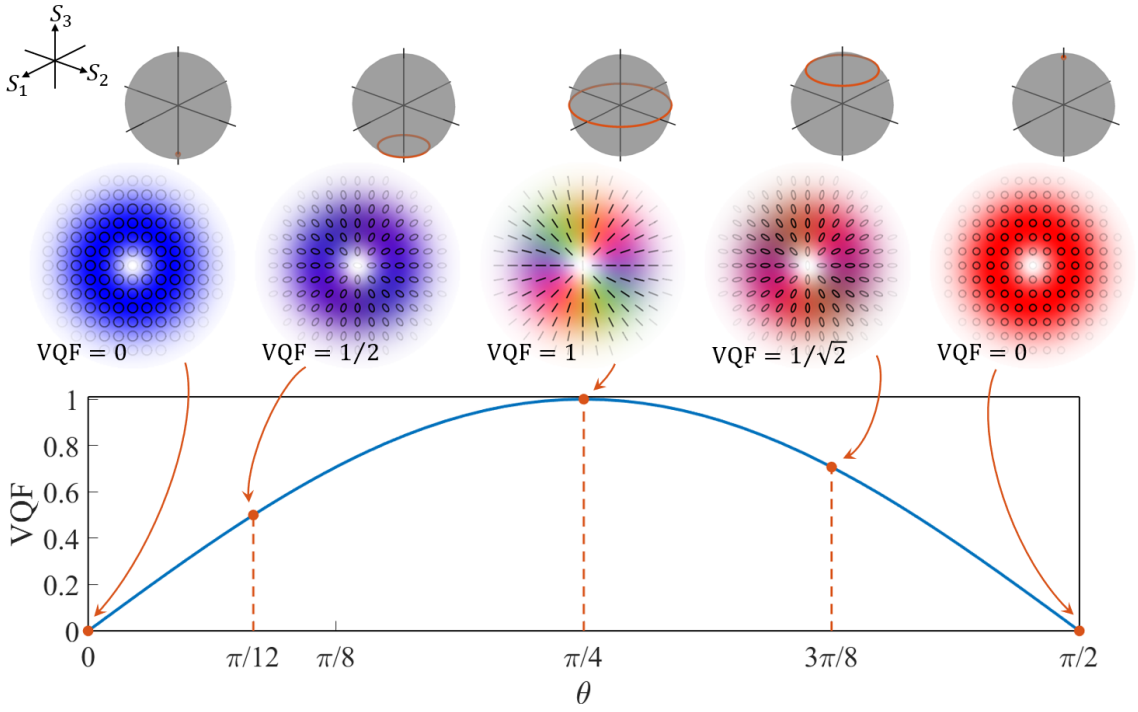

Figure 7.5: Examples of theoretical vector beams and associated VQF. The middle row shows polarisation profiles of beams of the form of Eq. 7.5 with $\ell = 1$ and different θ values as indicated. Below is a plot depicting the relationship between θ in Eq. 7.5 and VQF. The top row displays the coverage on the Poincaré sphere, where it can clearly be seen that VQF = 1 when the beam contains all polarisations along a great circle on the sphere.

is often referred to as non-separability or vector quality factor (VQF), as it will be in the rest of this section to keep in line with Ref. [402].

We can define the vector quality factor (VQF), using global Stokes parameters $\bar{S}_i$, as,

$$\mathrm{VQF} = \sqrt{1 - \left(\frac{\bar{S}_1^2}{\bar{S}_0^2} + \frac{\bar{S}_2^2}{\bar{S}_0^2} + \frac{\bar{S}_3^2}{\bar{S}_0^2}\right)}. \tag{7.4}$$

The VQF can give values ranging from 0 to 1, corresponding to completely homogeneous polarisation (VQF = 0), or to ideally inhomogeneous polarisation (VQF = 1), containing all polarisations along a great circle on the Poincaré sphere. Figure 7.5 gives examples of vector beams with different VQF values and shows how the VQF changes in relation to the weighting between the two polarisation DoF. To determine the VQF of a measured beam profile, only the global Stokes parameters are required, so we integrate over the entire beam profile, i.e. $\bar{S}_i = \int S_i(\mathbf{r}) d\mathbf{r}$.

For my contribution to the work, I performed measurements of vector beams of

the form,

$$|\Psi_{\text{in}}\rangle = \sin(\theta)\text{LG}_0^{+\ell}\,|\hat{\text{r}}\rangle + \cos(\theta)\text{LG}_0^{-\ell}\,|\hat{\text{l}}\rangle\,, \tag{7.5}$$

for $\theta = \pi/12$ and $\pi/4$, corresponding to beams with VQF = 0.5 and 1, respectfully. Examples of the polarisation plots for beams with $\ell = \pm 2, \pm 4$ are shown in in the first two columns of Figure 7.6. I then allowed the beams to propagate through a 5 cm glass cell containing various liquid medium. One of which was D-Limonene, which is known for its chiral properties, causing a rotation of the polarisation, dependent on the length of the medium propagated through. The resulting polarisation profiles of this can be seen in the third and fourth columns of Figure 7.6, showing that we do indeed observe a rotation of the polarisation structures.

After propagation through various liquids, the VQF was measured for beams with $\ell = \pm 1, \pm 2$ and ± 4, the results of which are plotted in Figure 7.6. For this, we used a variation of Eq. 7.4, relying on the fact that theoretically $S_0 = I_h + I_v = I_d + I_a = I_r + I_l$,

$$\text{VQF} = \sqrt{1 - \left(\frac{\bar{S}_1^2}{(\overline{I_h + I_v})^2} + \frac{\bar{S}_2^2}{(\overline{I_d + I_a})^2} + \frac{\bar{S}_3^2}{(\overline{I_r + I_l})^2}\right)}. \tag{7.6}$$

This allows us to account for any variations in the experimental Stokes measurements due to optical elements absorbing different ways for different polarisations, as discussed in chapter 2.

Regardless of the medium, the non-separability of the beam remains invariant, which is particularly evident for the beams with VQF = 1. Any deviation from theory in the results can primarily be explained due to the presence of background noise. In the low intensity beam areas, there is a lower signal-to-noise ratio (SNR), and because of the normalisation in both Eq. 7.4 and 7.6, these areas can cause large fluctuations in the measured Stokes parameters. The VQF gives a measure of the non-separability of the polarisation and spatial DoF, which, interestingly, means that any spatial fluctuation due to partial polarisation or noise, results in the overestimation of VQF. This is evident in the experimental results for the VQF = 0.5 beams and was also an effect seen and discussed previously in [70, 103].

The other components of the work also demonstrate the robustness of the "vectorness" of vectorial light to complex media by simulating atmospheric turbulence on a DMD, and propagation through a tilted lens, an optical fibre and turbulent air created using a temperature controlled hot plate. All the details of this can be found in [402].

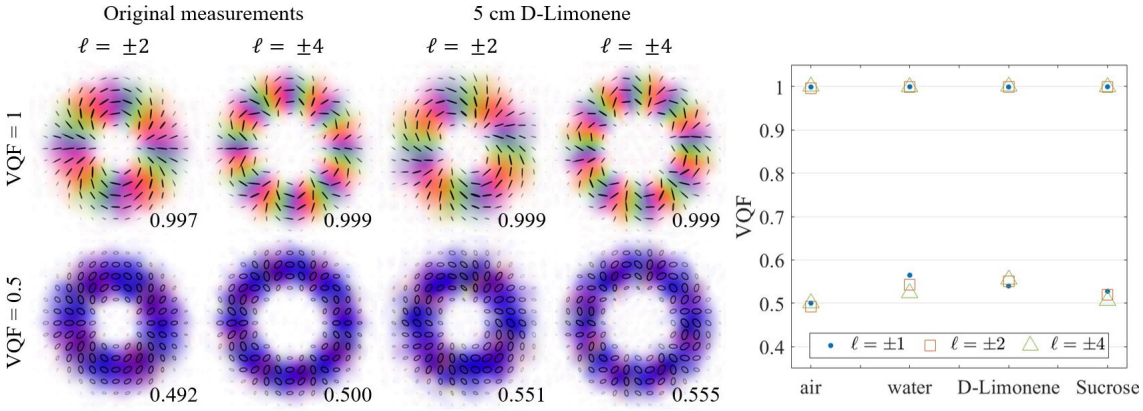

Figure 7.6: Experimentally measured polarisation profiles of beams corresponding to Eq. 7.5, with VQF = 1 (top row) and VQF = 0.5 (bottom row), before and after propagating through a 5 cm glass cell containing D-Limonene. The calculated VQF values are indicated for each beam. The plot shows calculated VQF for beams with $\ell = \pm 1, \pm 2$ and ± 4 after propagation through various liquids.

Chapter 8

Conclusions

The work presented in this thesis centred around the generation, characterisation and properties of vectorial light fields, in some cases highlighting the properties that are not obvious at first glance. In the following sections, I will first summarise the main outcomes of each of the individual experiments performed throughout the course of my PhD and then briefly suggest some of the future work that could be carried out as an extension to this work.

8.1 Thesis summary

Chapter 1 focused on the background theory that formed the foundation of the work in this thesis. In this chapter, I introduced the wave nature of light, describing how a light field can be described in terms of its amplitude, phase and polarisation. The concept of polarisation was discussed in detail, providing explanations of the different ways it can be represented, both mathematically and visually. I provided examples of higher-order Gaussian modes and described how we can theoretically construct vector beams with spatially varying polarisation by using superpositions of orthogonally polarised spatial modes.

Chapter 2 focused more on the relevant experimental details. This included how simple optical elements work (e.g. waveplates) and their uses, as well as an exploration of the ways in which a light beam can be shaped using digital devices. Specifically, the mechanisms for the use liquid crystal spatial light modulators for arbitrary phase and amplitude modulation was discussed, and an experimental setup incorporating a digital micromirror device for the generation of arbitrary vector beams was presented.

Geometric phases are an important concept in physics. In optics, they manifest in additional phase shifts acquired by a light beam relating to the geometry of the system in which it propagates. In chapter 3, I presented an experiment that investigated the non-planar propagation of both scalar and vector beams. The rotations seen in both the polarisation and intensity were linked to geometric phases,

namely, spin- and orbital-redirection phases, respectively, with the magnitude of the rotation dependent on the non-planarity of the system. From the non-planar propagation of vector beams it was shown that the beams acquire an additional phase dependent on the total angular momentum number, j, of the beam, allowing us to introduce the concept of the angular momentum redirection phase. Additionally, beams with $j = 0$, such as the radial and azimuthally polarised modes, acquire no geometric phase, and are unaffected by non-planar propagation, allowing them to be considered as eigenmodes of the system.

Chapter 4 began with an introduction to a topological structure that has become of interest in the field of optics in recent years, the skyrmion. Skyrmionic structures can be found in paraxial light beams with a continuously varying polarisation distribution and can be characterised by the skyrmion number. In chapter 4, I discussed ways in which the simplest optical skyrmions can be constructed as well as ways to generate optical multi-skyrmions. However, the main focus of this chapter was to present a derivation of a new topological approach of calculating skyrmion numbers. It was shown that our topological approach is more robust and predictable when evaluating skyrmion numbers from noisy data compared to the traditional surface integral approach. Additionally, the topological method provides an intuitive geometric insight into optical skyrmions, allowing individual skyrmionic structures to be identified. The field of optical skyrmions is still in the early stages of development, however, we believe that our new method to identify skyrmion numbers could benefit its growth, particularly due to the methods performance in the presence of noise and the intuitive understanding it brings. Additionally, it is believed that the tunable multi-skyrmions presented in § 4.8 are an interesting addition to the growing research field, and present one example of the ways in which optics can be used to investigate topologies not permitted in other fields.

In chapter 5, I moved away from looking at some of the properties and topologies of vector beams (as in chapters 3 and 4) and focused on their tomography and using them to measure optical activity. I introduced an experimental system capable of determining spatially resolved polarisation profiles in a single-shot. For this, generalised measurements were performed using a Sagnac interferometer-based setup, building on previous experimental work. It was shown that we could achieve interferometric stability over a number of hours. A method for performing single-shot Mueller matrix measurements was then proposed, using generalised measurements and a Poincaré beam as a probe. Muller matrix polarimetry is an important technique for determining the action of optical elements or optically active media on a light beam by monitoring polarisation changes. Here, a proof-of-principal experiment was carried out to validate the method by obtaining Mueller matrices of tilted and rotated waveplates. The single-shot nature of this method means that it is suitable for real-time monitoring of rapid optical activity changes due to biological phenomena, physical or chemical reaction processes, with a temporal resolution limited only by the frame rate of the camera.

In chapter 6, I again focused on the measurement of vector beams but this time it was for the implementation of a BB84 protocol in a proof-of-principle experiment. This protocol used rotationally symmetric states and a Fresnel cone based measurement system. The benefits of this implementation is that it is entirely rotational reference frame invariant and the measurement system can be easily made wavelength independent, as the Fresnel cone relies only on total internal reflection.

Finally, in chapter 7, I outlined two shorter projects that I was involved in as part of my PhD work. The first involved the generation, propagation and characterisation of a new orthonormal mode family - the Zernike beams - based on the complex Zernike polynomials. We were able to generate these modes with high fidelity, using a spatial light modulator, and accurately determine their orbital angular momentum using the tilted lens method. The second project looked at the invariance of vector beams under unitary transformations and perturbations. For this, I investigated the propagation of vector beams with different vector quality factors (VQF) through various liquid media, including a chiral liquid. From this it was shown that although the polarisation distributions were altered, the VQF remained unchanged.

8.2 Closing remarks and future work

Despite the progress and discoveries made in the field of structured light in recent decades, there is still much more left to explore. In terms of the projects presented in this thesis, there are a few key areas in which I think further investigations and work could be carried out.

The first is related to the work on optical skyrmions. At the end of chapter 4, I introduced a new way of generating tunable optical multi-skyrmions using split-vortex beams. All of the examples shown for these specific beams were simulation, therefore, it would be good to generate these experimentally and investigate further any possible applications or benefits of creating multi-skyrmions in this way. Additionally, I think there is more scope to explore the propagation of optical skyrmions, both in free space, in different media, and under strong focusing conditions to study the conservation (or not) of the skyrmion number. In this thesis, only the propagation of $n = 1$ beams were shown under weak focusing, therefore investigating the propagation of beams with higher n and of multi-skyrmions could be interesting. The fields of optics and structured light provide an ideal platform for studying topologies not permitted in other research areas, hence I see the research into optical skyrmions, as well as other topological beams, continuing to grow.

The second relates to the BB84 protocol using rotationally symmetric states. As outlined in chapter 6, the main experimental errors arose from unwanted phase shifts upon reflection from the 50:50 beam splitter. It is believed that these phase shifts, resulting in undesired polarisation changes can be experimentally removed for by the addition of an extra quarter- and half-wave plate. By placing the waveplates before

the measurement system, it should be possible to precompensate for the phase shifts. It order to obtain the correct waveplate angles, a Mueller matrix measurement will be performed of the 50:50 beam splitter.

In the field of structured light more generally, the recent emergence of programmable light shaping devices such as spatial light modulators and digital micromirror devices has allowed for many developments and interesting studies. This includes fundamental physics research in areas such as cold atom trapping and manipulation [406, 407], the storage of vector beams in atomic vapours [408], or using structured light as analogues to the quantum regime [409]. More practical applications lie within imaging and microscopy, where structured light can be used to overcome the diffraction limit [71, 410] or image through scattering media [411, 412], as well as within metrology [292] and microstructure fabrication [22, 23].

By fully understanding the additional degrees of freedom offered by vector light beams, I believe that it is possible to to unlock new possibilities and applications, whether in the form of improved imaging techniques, enhanced data transmission rates, or precise control over light propagation for free-space communication. Structured light and vector light beams will hopefully continue to offer exciting opportunities for advancement in photonics and related fields.

Bibliography

[1] E. Hecht, *Optics*. Pearson Education, Incorporated, 5 ed., 2017.

[2] D. Gabor, "A new microscopic principle.," *Nature*, vol. 161, p. 777–778, 1948. https://doi.org/10.1038/161777a0.

[3] T. H. Maiman, "Stimulated optical radiation in ruby," *Nature*, vol. 187, no. 4736, p. 493–494, 1960. http://dx.doi.org/10.1038/187493a0.

[4] K. J. Nutt, N. Hempler, G. T. Maker, G. P. A. Malcolm, M. J. Padgett, and G. M. Gibson, "Developing a portable gas imaging camera using highly tunable active-illumination and computer vision," *Optics Express*, vol. 28, no. 13, p. 18566, 2020. http://dx.doi.org/10.1364/OE.389634.

[5] V. Weldon, J. O'Gorman, P. Phelan, J. Hegarty, and T. Tanbun-Ek, "H2S and CO2 gas sensing using DFB laser diodes emitting at 1.57 μm," *Sensors and Actuators B: Chemical*, vol. 29, no. 1–3, p. 101–107, 1995. http://dx.doi.org/10.1016/0925-4005(95)01669-4.

[6] M.-C. Amann, T. M. Bosch, M. Lescure, R. A. Myllylae, and M. Rioux, "Laser ranging: a critical review of unusual techniques for distance measurement," *Optical engineering*, vol. 40, pp. 10–19, 2001. http://dx.doi.org/10.1117/1.1330700.

[7] T. Raj, F. H. Hashim, A. B. Huddin, M. F. Ibrahim, and A. Hussain, "A survey on lidar scanning mechanisms," *Electronics*, vol. 9, no. 5, p. 741, 2020. http://dx.doi.org/10.3390/electronics9050741.

[8] W. Demtröder, *Laser Spectroscopy 2: Experimental Techniques*. Springer Berlin Heidelberg, 2015. http://dx.doi.org/10.1007/978-3-662-44641-6.

[9] K.-J. Halbhuber and K. König, "Modern laser scanning microscopy in biology, biotechnology and medicine," *Annals of Anatomy - Anatomischer Anzeiger*, vol. 185, no. 1, p. 1–20, 2003. http://dx.doi.org/10.1016/S0940-9602(03)80002-X.

[10] K. Carlsson, P. E. Danielsson, A. Liljeborg, L. Majlöf, R. Lenz, and N. Åslund, "Three-dimensional microscopy using a confocal laser scanning microscope," *Optics Letters*, vol. 10, no. 2, p. 53, 1985. http://dx.doi.org/10.1364/OL.10.000053.

[11] C. Herbert, P. Anandarajah, P. Perry, D. Jones, A. Kaszubowska-Anandarajah, L. Barry, B. Kelly, J. O'Carroll, J. O'Gorman, M. Rensing, and R. Phelan, "Discrete mode lasers for communication applications," *IET Optoelectronics*, vol. 3, no. 1, p. 1–17, 2009. http://dx.doi.org/10.1049/iet-opt:20080028.

[12] E. Agrell, M. Karlsson, A. R. Chraplyvy, D. J. Richardson, P. M. Krummrich, P. Winzer, K. Roberts, J. K. Fischer, S. J. Savory, B. J. Eggleton, M. Secondini, F. R. Kschischang, A. Lord, J. Prat, I. Tomkos, J. E. Bowers, S. Srinivasan, M. Brandt-Pearce, and N. Gisin, "Roadmap of optical communications," *Journal of Optics*, vol. 18, no. 6, p. 063002, 2016. http://dx.doi.org/10.1088/2040-8978/18/6/063002.

[13] A. Forbes, "Structured light: Tailored for purpose," *Optics and Photonics News*, vol. 31, no. 6, p. 24, 2020. http://dx.doi.org/10.1364/OPN.31.6.000024.

[14] H. Rubinsztein-Dunlop, A. Forbes, M. V. Berry, M. R. Dennis, D. L. Andrews, M. Mansuripur, C. Denz, C. Alpmann, P. Banzer, T. Bauer, E. Karimi, L. Marrucci, M. Padgett, M. Ritsch-Marte, N. M. Litchinitser, N. P. Bigelow, C. Rosales-Guzmán, A. Belmonte, J. P. Torres, T. W. Neely, M. Baker, R. Gordon, A. B. Stilgoe, J. Romero, A. G. White, R. Fickler, A. E. Willner, G. Xie, B. McMorran, and A. M. Weiner, "Roadmap on structured light," *Journal of Optics*, vol. 19, no. 1, p. 013001, 2016. http://dx.doi.org/10.1088/2040-8978/19/1/013001.

[15] G. Lazarev, A. Hermerschmidt, S. Krüger, and S. Osten, "Lcos spatial light modulators: Trends and applications," 2012. http://dx.doi.org/10.1002/9783527648443.ch1.

[16] Y. Yang, A. Forbes, and L. Cao, "A review of liquid crystal spatial light modulators: devices and applications," *Opto-Electronic Science*, vol. 2, no. 8, p. 230026–230026, 2023. http://dx.doi.org/10.29026/oes.2023.230026.

[17] Y.-X. Ren, M. Li, K. Huang, J.-G. Wu, H.-F. Gao, Z.-Q. Wang, and Y.-M. Li, "Experimental generation of laguerre-gaussian beam using digital micromirror device," *Applied Optics*, vol. 49, no. 10, p. 1838, 2010. http://dx.doi.org/10.1364/AO.49.001838.

[18] Y. Ren, R. Lu, and L. Gong, "Tailoring light with a digital micromirror device," *Annalen der Physik*, vol. 527, no. 7–8, p. 447–470, 2015. http://dx.doi.org/10.1002/andp.201500111.

[19] Z. Nie, G. Shi, D. Li, X. Zhang, Y. Wang, and Y. Song, "Tight focusing of a radially polarized laguerre–bessel–gaussian beam and its application to manipulation of two types of particles," *Physics Letters A*, vol. 379, no. 9, p. 857–863, 2015. http://dx.doi.org/10.1016/j.physleta.2014.11.029.

[20] R. D. Hawley, R. Offer, N. Radwell, and S. Franke-Arnold, "Tight focal spots using azimuthally polarised light from a fresnel cone," in *Biomedical Spectroscopy, Microscopy, and Imaging* (J. Popp and C. Gergely, eds.), SPIE, 2020. http://dx.doi.org/10.1117/12.2559535.

[21] M. Woerdemann, C. Alpmann, M. Esseling, and C. Denz, "Advanced optical trapping by complex beam shaping," *Laser & Photonics Reviews*, vol. 7, no. 6, p. 839–854, 2013. http://dx.doi.org/10.1002/lpor.201200058.

[22] D. Flamm, D. G. Grossmann, M. Sailer, M. Kaiser, F. Zimmermann, K. Chen, M. Jenne, J. Kleiner, J. Hellstern, C. Tillkorn, D. H. Sutter, and M. Kumkar, "Structured light for ultrafast laser micro- and nanoprocessing," *Optical Engineering*, vol. 60, no. 02, 2021. http://dx.doi.org/10.1117/1.OE.60.2.025105.

[23] J. Strobelt, D. Stolz, M. Leven, M. V. Soelen, L. Kurlandski, H. Abourahma, and D. J. McGee, "Optical microstructure fabrication using structured polarized illumination," *Optics Express*, vol. 30, no. 5, p. 7308, 2022. http://dx.doi.org/10.1364/OE.451414.

[24] J. Wang, J.-Y. Yang, I. M. Fazal, N. Ahmed, Y. Yan, H. Huang, Y. Ren, Y. Yue, S. Dolinar, M. Tur, and A. E. Willner, "Terabit free-space data transmission employing orbital angular momentum multiplexing," *Nature Photonics*, vol. 6, no. 7, p. 488–496, 2012. http://dx.doi.org/10.1038/nphoton.2012.138.

[25] J. Liu, S.-M. Li, L. Zhu, A.-D. Wang, S. Chen, C. Klitis, C. Du, Q. Mo, M. Sorel, S.-Y. Yu, X.-L. Cai, and J. Wang, "Direct fiber vector eigenmode multiplexing transmission seeded by integrated optical vortex emitters," *Light: Science & Applications*, vol. 7, no. 3, p. 17148–17148, 2017. http://dx.doi.org/10.1038/lsa.2017.148.

[26] M. Al-Amri, D. Andrews, and M. Babiker, *Structured Light for Optical Communication*. Nanophotonics, Elsevier Science, 2021. Available at: https://books.google.co.uk/books?id=PiMZEAAAQBAJ.

[27] J. Wang, "Advances in communications using optical vortices," *Photonics Research*, vol. 4, no. 5, p. B14, 2016. http://dx.doi.org/10.1364/PRJ.4.000B14.

[28] C. P. Jisha, S. Nolte, and A. Alberucci, "Geometric Phase in Optics: From Wavefront Manipulation to Waveguiding," *Laser and Photonics Reviews*, vol. 15, no. 10, pp. 1–21, 2021. https://doi.org/10.1002/lpor.202100003.

[29] T. Kupko, M. von Helversen, L. Rickert, J.-H. Schulze, A. Strittmatter, M. Gschrey, S. Rodt, S. Reitzenstein, and T. Heindel, "Tools for the performance optimization of single-photon quantum key distribution," *npj Quantum Information*, vol. 6, no. 1, 2020. http://dx.doi.org/10.1038/s41534-020-0262-8.

[30] L. Zhang, C. Silberhorn, and I. A. Walmsley, "Secure quantum key distribution using continuous variables of single photons," *Physical Review Letters*, vol. 100, no. 11, 2008. http://dx.doi.org/10.1103/PhysRevLett.100.110504.

[31] T. E. Chapuran, P. Toliver, N. A. Peters, J. Jackel, M. S. Goodman, R. J. Runser, S. R. McNown, N. Dallmann, R. J. Hughes, K. P. McCabe, J. E. Nordholt, C. G. Peterson, K. T. Tyagi, L. Mercer, and H. Dardy, "Optical networking for quantum key distribution and quantum communications," *New Journal of Physics*, vol. 11, no. 10, p. 105001, 2009. http://dx.doi.org/10.1088/1367-2630/11/10/105001.

[32] T. K. Paraïso, R. I. Woodward, D. G. Marangon, V. Lovic, Z. Yuan, and A. J. Shields, "Advanced laser technology for quantum communications (tutorial review)," *Advanced Quantum Technologies*, vol. 4, no. 10, 2021. http://dx.doi.org/10.1002/qute.202100062.

[33] P. A. Hiskett, D. Rosenberg, C. G. Peterson, R. J. Hughes, S. Nam, A. E. Lita, A. J. Miller, and J. E. Nordholt, "Long-distance quantum key distribution in optical fibre," *New Journal of Physics*, vol. 8, no. 9, p. 193–193, 2006. http://dx.doi.org/10.1088/1367-2630/8/9/193.

[34] N. Radwell, R. D. Hawley, J. B. Götte, and S. Franke-Arnold, "Achromatic vector vortex beams from a glass cone," *Nature Communications*, vol. 7, no. 1, p. 10564, 2016. https://doi.org/10.1038/ncomms10564.

[35] D. J. Griffiths and D. F. Schroeter, *Introduction to Quantum Mechanics*. Cambridge University Press, 2018. http://dx.doi.org/10.1017/9781316995433.

[36] J. C. Maxwell, "A dynamical theory of the electromagnetic field," *Philosophical Transactions of the Royal Society of London*, vol. 155, p. 459–512, 1865. http://dx.doi.org/10.1098/rstl.1865.0008.

[37] R. P. Feynman, "Mathematical formulation of the quantum theory of electromagnetic interaction," *Physical Review*, vol. 80, no. 3, p. 440–457, 1950. http://dx.doi.org/10.1103/PhysRev.80.440.

[38] G. B. Arfken, H. J. Weber, and F. E. Harris, *Mathematical Methods for Physicists: A comprehensive guide*. Elsevier, 7 ed., 2012. http://dx.doi.org/10.1016/C2009-0-30629-7.

[39] J. D. Jackson, *Classical Electrodynamics*. John Wiley and Sons Inc, 3 ed., 2012.

[40] J. Peatross and M. J. Ware, *Physics of Light and Optics*. Brigham Young University, 2015. Available from: https://optics.byu.edu/docs/opticsbook.pdf.

[41] D. S. Simon, *A Guided Tour of Light Beams*. IOP Publishing, 2020. http://dx.doi.org/10.1088/978-0-7503-3467-9.

[42] B. E. A. Saleh and M. C. Teich, *Fundamentals of Photonics*. Wiley, 1991. http://dx.doi.org/10.1002/0471213748.

[43] H. Crew, C. Huygens, T. Young, A. J. Fresnel, and F. Arago, *The Wave Theory of Light: Memoirs by Huygens, Young and Fresnel*. New York, Cincinnati American Book Company, 1900.

[44] E. Collett, *Field Guide to Polarization*. SPIE, 2005. http://dx.doi.org/10.1117/3.626141.

[45] M. Born and E. Wolf, *Principles of Optics: 60th Anniversary Edition*. Cambridge University Press, 2019. http://dx.doi.org/10.1017/9781108769914.

[46] R. C. Jones, "A new calculus for the treatment of optical systemsi description and discussion of the calculus," *Journal of the Optical Society of America*, vol. 31, no. 7, p. 488, 1941. http://dx.doi.org/10.1364/JOSA.31.000488.

[47] G. G. Stokes, "On the composition and resolution of streams of polarized light from different sources," *Trans. Cambridge Philos. Soc.*, vol. 9, pp. 399–416, 1852. https://doi.org/10.1017/CBO9780511702266.010.

[48] C. Rosales-Guzmán, B. Ndagano, and A. Forbes, "A review of complex vector light fields and their applications," *Journal of Optics*, vol. 20, no. 12, p. 123001, 2018. http://dx.doi.org/10.1088/2040-8986/aaeb7d.

[49] H. Poincaré, *Théorie mathématique de la lumiére II*, ch. Chapitre XII: Polarisation rotatoire. Paris, 1892.

[50] H. Mueller, "Memorandum on the polarization optics of the photoelastic shutter," Report No. 2 of the OSRD project OEMsr-576, Nov. 15, 1943.

[51] W. S. Bickel and W. M. Bailey, "Stokes vectors, mueller matrices, and polarized scattered light," *American Journal of Physics*, vol. 53, no. 5, p. 468–478, 1985. http://dx.doi.org/10.1119/1.14202.

[52] N. N. Rogovtsov and F. N. Borovik, *Light Scattering Reviews 4*. Springer Praxis Publishing, 2009. https://doi.org/10.1007/978-3-540-74276-0_7.

[53] A. E. Siegman, *Lasers*. University Science Books, 1986.

[54] M. A. Bandres and J. C. Gutiérrez-Vega, "Ince–Gaussian beams," *Optics Letters*, vol. 29, no. 2, p. 144, 2004. https://doi.org/10.1364/ol.29.000144.

[55] J. Durnin, J. J. Miceli, and J. H. Eberly, "Diffraction-free beams," *Phys. Rev. Lett.*, vol. 58, pp. 1499–1501, 1987. https://doi.org/10.1103/PhysRevLett.58.1499.

[56] N. K. Efremidis, Z. Chen, M. Segev, and D. N. Christodoulides, "Airy beams and accelerating waves: an overview of recent advances," *Optica*, vol. 6, no. 5, pp. 686–701, 2019. https://doi.org/10.1364/OPTICA.6.000686.

[57] J. C. Gutiérrez-Vega, M. D. Iturbe-Castillo, and S. Chávez-Cerda, "Alternative formulation for invariant optical fields: Mathieu beams," *Opt. Lett.*, vol. 25, no. 20, pp. 1493–1495, 2000. https://doi.org/10.1364/OL.25.001493.

[58] J. D. Ring, J. Lindberg, A. Mourka, M. Mazilu, K. Dholakia, and M. R. Dennis, "Auto-focusing and self-healing of pearcey beams," *Opt. Express*, vol. 20, no. 17, pp. 18955–18966, 2012. https://doi.org/10.1364/OE.20.018955.

[59] L. Allen, M. W. Beijersbergen, R. J. C. Spreeuw, and J. P. Woerdman, "Orbital angular momentum of light and the transformation of laguerre-gaussian laser modes," *Physical Review A*, vol. 45, no. 11, p. 8185–8189, 1992. http://dx.doi.org/10.1103/PhysRevA.45.8185.

[60] R. L. Phillips and L. C. Andrews, "Spot size and divergence for laguerre gaussian beams of any order," *Applied Optics*, vol. 22, no. 5, p. 643, 1983. http://dx.doi.org/10.1364/AO.22.000643.

[61] J. E. Curtis and D. G. Grier, "Structure of optical vortices," *Physical Review Letters*, vol. 90, no. 13, 2003. http://dx.doi.org/10.1103/PhysRevLett.90.133901.

[62] J. Zhang, S.-J. Huang, F.-Q. Zhu, W. Shao, and M.-S. Chen, "Dimensional properties of laguerre–gaussian vortex beams," *Applied Optics*, vol. 56, no. 12, p. 3556, 2017. http://dx.doi.org/10.1364/AO.56.003556.

[63] R. M. Corless, G. H. Gonnet, D. E. G. Hare, D. J. Jeffrey, and D. E. Knuth, "On the lambertw function," *Advances in Computational Mathematics*, vol. 5, no. 1, p. 329–359, 1996. http://dx.doi.org/10.1007/BF02124750.

[64] M. Beijersbergen, L. Allen, H. van der Veen, and J. Woerdman, "Astigmatic laser mode converters and transfer of orbital angular momentum," *Optics Communications*, vol. 96, no. 1–3, p. 123–132, 1993. http://dx.doi.org/10.1016/0030-4018(93)90535-D.

[65] J. Goodman, *Introduction to Fourier Optics*. Electrical Engineering Series, McGraw-Hill, 1996. Available from: https://books.google.co.uk/books?id=QllRAAAAMAAJ.

[66] B. Richards, E. Wolf, and D. Gabor, "Electromagnetic diffraction in optical systems, ii. structure of the image field in an aplanatic system," *Proceedings of the Royal Society of London. Series A. Mathematical and Physical Sciences*, vol. 253, no. 1274, pp. 358–379, 1959. http://dx.doi.org/10.1098/rspa.1959.0200.

[67] L. Novotny and B. Hecht, *Principles of Nano-Optics*. Cambridge University Press, 2012. http://dx.doi.org/10.1017/CBO9780511794193.

[68] R. Learn and E. Feigenbaum, "Adaptive step-size algorithm for fourier beam-propagation method with absorbing boundary layer of auto-determined width," *Applied Optics*, vol. 55, no. 16, p. 4402, 2016. http://dx.doi.org/10.1364/AO.55.004402.

[69] O. V. Angelsky, A. Y. Bekshaev, S. G. Hanson, C. Y. Zenkova, I. I. Mokhun, and J. Zheng, "Structured light: Ideas and concepts," *Frontiers in Physics*, vol. 8, 2020. http://dx.doi.org/10.3389/fphy.2020.00114.

[70] A. Selyem, C. Rosales-Guzmán, S. Croke, A. Forbes, and S. Franke-Arnold, "Basis-independent tomography and nonseparability witnesses of pure complex vectorial light fields by Stokes projections," *Physical Review A*, vol. 100, no. 6, pp. 1–8, 2019. https://doi.org/10.1103/PhysRevA.100.063842.

[71] Q. Zhan, "Cylindrical vector beams: from mathematical concepts to applications," *Advances in Optics and Photonics*, vol. 1, no. 1, p. 1, 2009. http://dx.doi.org/10.1364/AOP.1.000001.

[72] E. J. Galvez, *Vector beams in free space*, p. 51–70. Cambridge University Press, 2012. http://dx.doi.org/10.1017/CBO9780511795213.004.

[73] S. E. Skelton, M. Sergides, R. Saija, M. A. Iatì, O. M. Maragó, and P. H. Jones, "Trapping volume control in optical tweezers using cylindrical vector beams," *Optics Letters*, vol. 38, no. 1, p. 28, 2013. http://dx.doi.org/10.1364/OL.38.000028.

[74] M. Venkatesh, R. A. Ganeev, V. V. Kim, G. S. Boltaev, I. B. Sapaev, J. Liang, J. Yu, and W. Li, "Application of vector beams for enhanced high-order harmonics generation in laser-induced plasmas," *Optics Express*, vol. 30, no. 10, p. 17080, 2022. http://dx.doi.org/10.1364/OE.454379.

[75] V. Aita and A. V. Zayats, "Enhancement of optical spin-orbit coupling in anisotropic enz metamaterials," *IEEE Photonics Journal*, vol. 15, no. 1, p. 1–8, 2023. http://dx.doi.org/10.1109/JPHOT.2022.3232460.

[76] B. Ndagano, R. Brüning, M. McLaren, M. Duparré, and A. Forbes, "Fiber propagation of vector modes," *Optics Express*, vol. 23, no. 13, p. 17330, 2015. http://dx.doi.org/10.1364/OE.23.017330.

[77] M.-J. Li and D. A. Nolan, "Optical transmission fiber design evolution," *Journal of Lightwave Technology*, vol. 26, no. 9, p. 1079–1092, 2008. http://dx.doi.org/10.1109/JLT.2008.922150.

[78] S. E. Skelton, *Applications of cylindrical vector beams for optical micromanipulation*. PhD thesis, Department of Physics and Astronomy, University College London, 2013.

[79] D. S. Simon, *Topology in Optics (Second Edition): Tying light in knots*. IOP Publishing, May 2021.

[80] T. Frankel, *The Geometry of Physics: An Introduction*. Cambridge University Press, 2011. http://dx.doi.org/10.1017/CBO9781139061377.

[81] T. Fösel, V. Peano, and F. Marquardt, "L lines, c points and chern numbers: understanding band structure topology using polarization fields," *New Journal of Physics*, vol. 19, no. 11, p. 115013, 2017. http://dx.doi.org/10.1088/1367-2630/aa8a9f.

[82] M. R. Dennis, K. O'Holleran, and M. J. Padgett, *Chapter 5 Singular Optics: Optical Vortices and Polarization Singularities*, p. 293–363. Elsevier, 2009. http://dx.doi.org/10.1016/S0079-6638(08)00205-9.

[83] S. Kumar Pal, Ruchi, and P. Senthilkumaran, "C-point and v-point singularity lattice formation and index sign conversion methods," *Optics Communications*, vol. 393, p. 156–168, 2017. http://dx.doi.org/10.1016/j.optcom.2017.02.048.

[84] S. Bansal, S. K. Pal, and P. Senthilkumaran, *A Method to Distinguish C-Point from V-Point*, p. 561–563. Springer Singapore, 2021. http://dx.doi.org/10.1007/978-981-15-9259-1_129.

[85] V. Kumar and N. K. Viswanathan, "Topological structures in vector-vortex beam fields," *Journal of the Optical Society of America B*, vol. 31, no. 6, p. A40, 2014. http://dx.doi.org/10.1364/josab.31.000a40.

[86] M. V. Berry and J. H. Hannay, "Umbilic points on gaussian random surfaces," *Journal of Physics A: Mathematical and General*, vol. 10, no. 11, p. 1809–1821, 1977. http://dx.doi.org/10.1088/0305-4470/10/11/009.

[87] J. F. Nye, "Lines of circular polarization in electromagnetic wave fields," *Proceedings of the Royal Society of London. A. Mathematical and Physical Sciences*, vol. 389, no. 1797, p. 279–290, 1983. http://dx.doi.org/10.1098/rspa.1983.0109.

[88] G. Arora, Ruchi, S. K. Pal, and P. Senthilkumaran, "Full poincaré beam delineation based on the stokes vortex ring," *Journal of Optics*, vol. 23, no. 10, p. 105201, 2021. http://dx.doi.org/10.1088/2040-8986/ac0317.

[89] A. M. Beckley, T. G. Brown, and M. A. Alonso, "Full poincaré beams ii: partial polarization," *Optics Express*, vol. 20, no. 9, p. 9357, 2012. http://dx.doi.org/10.1364/OE.20.009357.

[90] B. Radhakrishna, G. Kadiri, and G. Raghavan, "Polarimetric method of generating full poincaré beams within a finite extent," *Journal of the Optical Society of America A*, vol. 39, no. 4, p. 662, 2022. http://dx.doi.org/10.1364/josaa.452086.

[91] A. N. Black and R. W. Boyd, "Generation of volumetrically full poincaré beams," *Journal of the Optical Society of America A*, vol. 39, no. 12, p. C161, 2022. http://dx.doi.org/10.1364/JOSAA.473363.

[92] S. Franke-Arnold, "30 years of orbital angular momentum of light," *Nature Reviews Physics*, vol. 4, no. 6, p. 361–361, 2022. http://dx.doi.org/10.1038/s42254-022-00467-x.

[93] J. H. Poynting, "The wave motion of a revolving shaft, and a suggestion as to the angular momentum in a beam of circularly polarised light," *Proceedings of the Royal Society of London. Series A, Containing Papers of a Mathematical and Physical Character*, vol. 82, no. 557, pp. 560–567, 1909. https://doi.org/10.1098/rspa.1909.0060.

[94] M. J. Padgett, "Orbital angular momentum 25 years on [invited]," *Optics Express*, vol. 25, no. 10, p. 11265, 2017. http://dx.doi.org/10.1364/OE.25.011265.

[95] K. Volke-Sepulveda, V. Garcés-Chávez, S. Chávez-Cerda, J. Arlt, and K. Dholakia, "Orbital angular momentum of a high-order bessel light beam," *Journal of Optics B: Quantum and Semiclassical Optics*, vol. 4, no. 2, p. S82–S89, 2002. http://dx.doi.org/10.1088/1464-4266/4/2/373.

[96] "Thorabs: Polymer circular polarizers." https://www.thorlabs.com/newgrouppage9.cfm?objectgroup_id=10498. Accessed: 2024-04-23.

[97] "Thorabs: Polarizers." https://www.thorlabs.com/navigation.cfm?guide_id=24. Accessed: 2024-04-23.

[98] "Thorabs: Mounted multi-order wave plates." https://www.thorlabs.com/newgrouppage9.cfm?objectgroup_id=713&pn=WPMQ05M-633. Accessed: 2023-10-03.

[99] "Thorabs: Fused silica broadband dielectric mirrors." https://www.thorlabs.com/newgrouppage9.cfm?objectgroup_id=139. Accessed: 2024-04-26.

[100] J. H. Apfel, "Phase retardance of periodic multilayer mirrors," *Applied Optics*, vol. 21, no. 4, p. 733, 1982. http://dx.doi.org/10.1364/AO.21.000733.

[101] D. T. Smithey, M. Beck, M. G. Raymer, and A. Faridani, "Measurement of the wigner distribution and the density matrix of a light mode using optical homodyne tomography: Application to squeezed states and the vacuum," *Phys. Rev. Lett.*, vol. 70, pp. 1244–1247, 1993. https://link.aps.org/doi/10.1103/PhysRevLett.70.1244.

[102] E. Toninelli, B. Ndagano, A. Vallés, B. Sephton, I. Nape, A. Ambrosio, F. Capasso, M. J. Padgett, and A. Forbes, "Concepts in quantum state tomography and classical implementation with intense light: a tutorial," *Advances in Optics and Photonics*, vol. 11, no. 1, p. 67, 2019. http://dx.doi.org/10.1364/aop.11.000067.

[103] A. Selyem, *Three-dimensional Light Sculptures and their Interaction with Atomic Media: An experimentalist's guide*. PhD thesis, School of Physics and Astronomy, College of Science and Engineering, University of Glasgow, 2019.

[104] "Thorabs: Film polarizers." https://www.thorlabs.com/navigation.cfm?guide_id=2459. Accessed: 2024-03-25.

[105] L. Marrucci, C. Manzo, and D. Paparo, "Optical spin-to-orbital angular momentum conversion in inhomogeneous anisotropic media," *Physical Review Letters*, vol. 96, no. 16, 2006. http://dx.doi.org/10.1103/PhysRevLett.96.163905.

[106] L. Marrucci, "The q-plate and its future," *Journal of Nanophotonics*, vol. 7, no. 1, p. 078598, 2013. https://doi.org/10.1117/1.JNP.7.078598.

[107] A. Rubano, F. Cardano, B. Piccirillo, and L. Marrucci, "Q-plate technology: a progress review [invited]," *Journal of the Optical Society of America B*, vol. 36, no. 5, p. D70, 2019. http://dx.doi.org/10.1364/JOSAB.36.000D70.

[108] S. Khonina, V. Kotlyar, M. Shinkaryev, V. Soifer, and G. Uspleniev, "The phase rotor filter," *Journal of Modern Optics*, vol. 39, no. 5, p. 1147–1154, 1992. http://dx.doi.org/10.1080/09500349214551151.

[109] S. S. R. Oemrawsingh, J. A. W. van Houwelingen, E. R. Eliel, J. P. Woerdman, E. J. K. Verstegen, J. G. Kloosterboer, and G. W. 't Hooft, "Production and characterization of spiral phase plates for optical wavelengths," *Applied Optics*, vol. 43, no. 3, p. 688, 2004. http://dx.doi.org/10.1364/AO.43.000688.

[110] M. Massari, G. Ruffato, M. Gintoli, F. Ricci, and F. Romanato, "Fabrication and characterization of high-quality spiral phase plates for optical applications," *Applied Optics*, vol. 54, no. 13, p. 4077, 2015. http://dx.doi.org/10.1364/AO.54.004077.

[111] J. Scheuer, "Metasurfaces-based holography and beam shaping: engineering the phase profile of light," *Nanophotonics*, vol. 6, no. 1, p. 137–152, 2016. http://dx.doi.org/10.1515/nanoph-2016-0109.

[112] T. Dresel, M. Beyerlein, and J. Schwider, "Design and fabrication of computer-generated beam-shaping holograms," *Applied Optics*, vol. 35, no. 23, p. 4615, 1996. http://dx.doi.org/10.1364/AO.35.004615.

[113] F. Reinitzer, "Beiträge zur kenntniss des cholesterins," *Monatshefte für Chemie - Chemical Monthly*, vol. 9, no. 1, p. 421–441, 1888. http://dx.doi.org/10.1007/BF01516710.

[114] M. J. Stephen and J. P. Straley, "Physics of liquid crystals," *Reviews of Modern Physics*, vol. 46, no. 4, p. 617–704, 1974. http://dx.doi.org/10.1103/RevModPhys.46.617.

[115] R. Li and L. Cao, "Progress in phase calibration for liquid crystal spatial light modulators," *Applied Sciences*, vol. 9, no. 10, p. 2012, 2019. http://dx.doi.org/10.3390/app9102012.

[116] Z. Zhao, Z. Xiao, Y. Zhuang, H. Zhang, and H. Zhao, "An interferometric method for local phase modulation calibration of lc-slm using self-generated phase grating," *Review of Scientific Instruments*, vol. 89, no. 8, 2018. http://dx.doi.org/10.1063/1.5031938.

[117] Y. Dai, J. Antonello, and M. J. Booth, "Calibration of a phase-only spatial light modulator for both phase and retardance modulation," *Optics Express*, vol. 27, no. 13, p. 17912, 2019. http://dx.doi.org/10.1364/oe.27.017912.

[118] E. G. Loewen, M. Nevière, and D. Maystre, "Grating efficiency theory as it applies to blazed and holographic gratings," *Applied Optics*, vol. 16, no. 10, p. 2711, 1977. http://dx.doi.org/10.1364/AO.16.002711.

[119] J. A. Davis, D. M. Cottrell, J. Campos, M. J. Yzuel, and I. Moreno, "Encoding amplitude information onto phase-only filters," *Appl. Opt.*, vol. 38, no. 23, pp. 5004–5013, 1999. https://doi.org/10.1364/AO.38.005004.

[120] T. W. Clark, R. F. Offer, S. Franke-Arnold, A. S. Arnold, and N. Radwell, "Comparison of beam generation techniques using a phase only spatial light modulator," *Optics Express*, vol. 24, no. 6, p. 6249, 2016. https://doi.org/10.1364/oe.24.006249.

[121] "Texas instruments dlp3000 dmd." https://www.ti.com/product/DLPC300?keyMatch=DLP3000%20chip. Accessed: 2024-05-03.

[122] V. Lerner, D. Shwa, Y. Drori, and N. Katz, "Shaping laguerre–gaussian laser modes with binary gratings using a digital micromirror device," *Optics Letters*, vol. 37, no. 23, p. 4826, 2012. http://dx.doi.org/10.1364/OL.37.004826.

[123] M. Mirhosseini, O. S. Magaña-Loaiza, C. Chen, B. Rodenburg, M. Malik, and R. W. Boyd, "Rapid generation of light beams carrying orbital angular momentum," *Optics Express*, vol. 21, no. 25, p. 30196, 2013. http://dx.doi.org/10.1364/OE.21.030196.

[124] B. R. Brown and A. W. Lohmann, "Complex spatial filtering with binary masks," *Applied Optics*, vol. 5, no. 6, p. 967, 1966. http://dx.doi.org/10.1364/AO.5.000967.

[125] K. J. Mitchell, S. Turtaev, M. J. Padgett, T. Čižmár, and D. B. Phillips, "High-speed spatial control of the intensity, phase and polarisation of vector beams using a digital micro-mirror device," *Optics Express*, vol. 24, no. 25, p. 29269, 2016. http://dx.doi.org/10.1364/oe.24.029269.

[126] M. A. A. Neil, F. Massoumian, R. Juškaitis, and T. Wilson, "Method for the generation of arbitrary complex vector wave fronts," *Optics Letters*, vol. 27, no. 21, p. 1929, 2002. http://dx.doi.org/10.1364/OL.27.001929.

[127] X.-L. Wang, J. Ding, W.-J. Ni, C.-S. Guo, and H.-T. Wang, "Generation of arbitrary vector beams with a spatial light modulator and a common path interferometric arrangement," *Optics Letters*, vol. 32, no. 24, p. 3549, 2007. http://dx.doi.org/10.1364/OL.32.003549.

[128] H. Chen, J. Hao, B.-F. Zhang, J. Xu, J. Ding, and H.-T. Wang, "Generation of vector beam with space-variant distribution of both polarization and phase," *Optics Letters*, vol. 36, no. 16, p. 3179, 2011. http://dx.doi.org/10.1364/OL.36.003179.

[129] S. Liu, P. Li, T. Peng, and J. Zhao, "Generation of arbitrary spatially variant polarization beams with a trapezoid sagnac interferometer," *Optics Express*, vol. 20, no. 19, p. 21715, 2012. http://dx.doi.org/10.1364/OE.20.021715.

[130] D. Maluenda, I. Juvells, R. Martínez-Herrero, and A. Carnicer, "Reconfigurable beams with arbitrary polarization and shape distributions at a given plane," *Optics Express*, vol. 21, no. 5, p. 5432, 2013. http://dx.doi.org/10.1364/OE.21.005432.

[131] S. Chen, X. Zhou, Y. Liu, X. Ling, H. Luo, and S. Wen, "Generation of arbitrary cylindrical vector beams on the higher order poincaré sphere," *Optics Letters*, vol. 39, no. 18, p. 5274, 2014. http://dx.doi.org/10.1364/OL.39.005274.

[132] I. Moreno, J. A. Davis, T. M. Hernandez, D. M. Cottrell, and D. Sand, "Complete polarization control of light from a liquid crystal spatial light modulator,"

Optics Express, vol. 20, no. 1, p. 364, 2011. http://dx.doi.org/10.1364/OE.20.000364.

[133] C. Alpmann, C. Schlickriede, E. Otte, and C. Denz, "Dynamic modulation of poincaré beams," *Scientific Reports*, vol. 7, no. 1, 2017. http://dx.doi.org/10.1038/s41598-017-07437-9.

[134] C. Rosales-Guzmán, X.-B. Hu, A. Selyem, P. Moreno-Acosta, S. Franke-Arnold, R. Ramos-Garcia, and A. Forbes, "Polarisation-insensitive generation of complex vector modes from a digital micromirror device," *Scientific Reports*, vol. 10, no. 1, 2020. http://dx.doi.org/10.1038/s41598-020-66799-9.

[135] A. McWilliam, C. M. Cisowski, R. Bennett, and S. Franke-Arnold, "Angular momentum redirection phase of vector beams in a non-planar geometry," *Nanophotonics*, vol. 11, no. 4, pp. 727–736, 2022. https://doi.org/10.1515/nanoph-2021-0528.

[136] H. Jiao, R. Wilkinson, R. Y. Chiao, and H. Nathel, "Two topological phases in optics by means of a nonplanar Mach-Zehnder interferometer," *Physical Review A*, vol. 39, no. 7, 1989. https://doi.org/10.1103/PhysRevA.39.3475.

[137] V. Vladimirskiy, "The rotation of a polarization plane for curved light ray," *Dokl. Akad. Nauk. SSSR*, vol. 31, 1941.

[138] F. D. M. Haldane, "Path dependence of the geometric rotation of polarization in optical fibers," *Optics Letters*, vol. 11, no. 11, p. 730, 1986. https://doi.org/10.1364/ol.11.000730.

[139] E. J. Galvez and C. D. Holmes, "Geometric phase of optical rotators," *J. Opt. Soc. Am. A*, vol. 16, no. 8, pp. 1981–1985, 1999. https://doi.org/10.1364/JOSAA.16.001981.

[140] K. Y. Bliokh, "Geometrical optics of beams with vortices: Berry phase and orbital angular momentum hall effect," *Phys. Rev. Lett.*, vol. 97, p. 043901, 2006. https://doi.org/10.1103/PhysRevLett.97.043901.

[141] M. Segev, R. Solomon, and A. Yariv, "Manifestation of berry's phase in image-bearing optical beams," *Phys. Rev. Lett.*, vol. 69, pp. 590–592, 1992. https://doi.org/10.1103/PhysRevLett.69.590.

[142] I. V. Kataevskaya and N. D. Kundikova, "Influence of the helical shape of a fibre waveguide on the propagation of light," *Quantum Electronics*, vol. 25, no. 9, pp. 927–928, 1995. https://doi.org/10.1070/qe1995v025n09abeh000504.

[143] M. V. Berry, "Quantal phase factors accompanying adiabatic changes," *Proc. R. Soc. Lond. A*, vol. 392, pp. 45–57, 1984. https://doi.org/10.1142/9789813221215_0006.

[144] S. Pancharatnam, "Generalized theory of interference, and its applications - Part I. Coherent pencils," *Proceedings of the Indian Academy of Sciences - Section A*, vol. 44, no. 5, pp. 247–262, 1956. https://doi.org/10.1007/BF03046050.

[145] H. C. Longuet-Higgins, U. Öpik, M. H. L. Pryce, and R. A. Sack, "Studies of the jahn-teller effect .ii. the dynamical problem," *Proceedings of the Royal Society of London. Series A. Mathematical and Physical Sciences*, vol. 244, no. 1236, pp. 1–16, 1958. https://doi.org/10.1098/rspa.1958.0022.

[146] W. Gao, B. Yang, M. Lawrence, F. Fang, B. Béri, and S. Zhang, "Photonic Weyl degeneracies in magnetized plasma," *Nature Communications*, vol. 7, no. 12435, 2016. https://doi.org/10.1038/ncomms12435.

[147] J. B. Parker, J. B. Marston, S. M. Tobias, and Z. Zhu, "Topological gaseous plasmon polariton in realistic plasma," *Phys. Rev. Lett.*, vol. 124, p. 195001, 2020. https://doi.org/10.1103/PhysRevLett.124.195001.

[148] H. Sonoda, "Berry's phase in chiral gauge theories," *Nuclear Physics B*, vol. 266, no. 2, pp. 410–422, 1986. https://doi.org/10.1016/0550-3213(86)90097-0.

[149] B. Simon, "Holonomy, the quantum adiabatic theorem, and berry's phase," *Phys. Rev. Lett.*, vol. 51, pp. 2167–2170, 1983. https://doi.org/10.1103/PhysRevLett.51.2167.

[150] Q. Niu, D. J. Thouless, and Y.-S. Wu, "Quantized hall conductance as a topological invariant," *Phys. Rev. B*, vol. 31, pp. 3372–3377, 1985. https://doi.org/10.1103/PhysRevB.31.3372.

[151] F. D. M. Haldane and S. Raghu, "Possible realization of directional optical waveguides in photonic crystals with broken time-reversal symmetry," *Phys. Rev. Lett.*, vol. 100, p. 013904, 2008. https://doi.org/10.1103/PhysRevLett.100.013904.

[152] S. Raghu and F. D. M. Haldane, "Analogs of quantum-hall-effect edge states in photonic crystals," *Phys. Rev. A*, vol. 78, p. 033834, 2008. https://doi.org/10.1103/PhysRevA.78.033834.

[153] M. A. Alonso, "Geometric phases in optics," in *Latin America Optics and Photonics Conference*, p. W2B.1, Optica Publishing Group, 2018. https://doi.org/10.1364/LAOP.2018.W2B.1.

[154] E. Cohen, H. Larocque, F. Bouchard, F. Nejadsattari, Y. Gefen, and E. Karimi, "Geometric phase from Aharonov–Bohm to Pancharatnam–Berry and beyond," *Nature Reviews Physics*, vol. 1, pp. 437–449, 2019. https://doi.org/10.1038/s42254-019-0071-1.

[155] C. Cisowski, J. B. Götte, and S. Franke-Arnold, "Colloquium: Geometric phases of light: Insights from fiber bundle theory," *Reviews of Modern Physics*, vol. 94, no. 3, p. 31001, 2022. https://doi.org/10.1103/RevModPhys.94.031001.

[156] D. Subbarao, "Topological phase in Gaussian beam optics," *Optics Letters*, vol. 20, no. 21, pp. 2162—-2164, 1995. https://doi.org/10.1364/ol.20.002162.

[157] M. V. Berry, "The adiabatic phase and Pancharatnum's phase for polarized light," *Journal of Modern Optics*, vol. 34, no. 11, pp. 1401–1407, 1987. https://doi.org/10.1080/09500348714551321.

[158] R. Y. Chiao and Y.-S. Wu, "Manifestations of berry's topological phase for the photon," *Phys. Rev. Lett.*, vol. 57, pp. 933–936, 1986. https://doi.org/10.1103/PhysRevLett.57.933.

[159] M. V. Berry, "Interpreting the anholonomy of coiled light," *Nature*, vol. 326, pp. 277–278, 1987. https://doi.org/10.1038/326277a0.

[160] R. Y. Chiao and T. F. Jordan, "Lorentz-group Berry phases in squeezed light," *Physics Letters A*, vol. 132, no. 2, pp. 77–81, 1988. https://doi.org/10.1016/0375-9601(88)90255-1.

[161] R. Chiao, "Lorentz-group berry phases in squeezed light," *Nuclear Physics B - Proceedings Supplements*, vol. 6, pp. 327–333, 1989. https://doi.org/10.1016/0920-5632(89)90466-0.

[162] F. Wilczek and A. Shapere, *Geometric Phases in Physics*. WORLD SCIENTIFIC, 1989. https://doi.org/10.1142/0613.

[163] A. Bohm, A. Mostafazadeh, H. Koizumi, Q. Niu, and J. Zwanziger, *The Geometric Phase in Quantum Systems: Foundations, Mathematical Concepts, and Applications in Molecular and Condensed Matter Physics*. Springer Berlin Heidelberg, 2003. http://dx.doi.org/10.1007/978-3-662-10333-3.

[164] C. Song, S.-B. Zheng, P. Zhang, K. Xu, L. Zhang, Q. Guo, W. Liu, D. Xu, H. Deng, K. Huang, D. Zheng, X. Zhu, and H. Wang, "Continuous-variable geometric phase and its manipulation for quantum computation in a superconducting circuit," *Nature Communications*, vol. 8, no. 1, 2017. http://dx.doi.org/10.1038/s41467-017-01156-5.

[165] Z. Chen, "Observable-geometric phases and quantum computation," *International Journal of Theoretical Physics*, vol. 59, no. 4, p. 1255–1276, 2020. http://dx.doi.org/10.1007/s10773-020-04404-5.

[166] E. Galvez, "Applications of Geometric Phase in Optics," *Recent Research Developments in Optics*, vol. 2, pp. 165–82, 2002. https://api.semanticscholar.org/CorpusID:15269085.

[167] R. Bhandari, "Polarization of light and topological phases," *Physics Report*, vol. 281, no. 1, pp. 1–64, 1997. https://doi.org/10.1016/S0370-1573(96)00029-4.

[168] C. Liu, Y. Bai, Q. Zhao, Y. Yang, H. Chen, J. Zhou, and L. Qiao, "ully Controllable Pancharatnam-Berry Metasurface Array with High Conversion Efficiency and Broad Bandwidth," *Scientific Reports*, vol. 6, no. 34819, 2016. https://doi.org/10.1038/srep34819.

[169] M. Jiang, H. Yu, X. Feng, Y. Guo, I. Chaganava, T. Turiv, O. Lavrentovich, and Q.-H. Wei, "Liquid crystal pancharatnam-berry micro-optical elements for laser beam shaping," *Advanced Optical Materials*, vol. 6, p. 1800961, 2018. https://doi.org/10.1002/adom.201800961.

[170] J. Kim, Y. Li, M. N. Miskiewicz, C. Oh, M. W. Kudenov, and M. J. Escuti, "Fabrication of ideal geometric-phase holograms with arbitrary wavefronts," *Optica*, vol. 2, no. 11, pp. 958–964, 2015. https://doi.org/10.1364/OPTICA.2.000958.

[171] B. Piccirillo, V. Kumar, L. Marrucci, and E. Santamato, "Pancharatnam-Berry phase optical elements for generation and control of complex light: generalized superelliptical q-plates," in *Complex Light and Optical Forces IX* (E. J. Galvez, J. Glückstad, and D. L. Andrews, eds.), vol. 9379, p. 937907, International Society for Optics and Photonics, SPIE, 2015. https://doi.org/10.1117/12.2078372.

[172] R. Crane, "Interference phase measurement," *Appl. Opt.*, vol. 8, no. 3, pp. 538–542, 1969.

[173] J. P. Huignard and J. P. Herriau, "Frequency shifters for photorefractive crystals," *Appl. Opt.*, vol. 24, no. 24, pp. 4285–4286, 1985. https://doi.org/10.1364/AO.24.004285.

[174] M. Martinelli and P. Vavassori, "A geometric (pancharatnam) phase approach to the polarization and phase control in the coherent optics circuits," *Optics Communications*, vol. 80, no. 2, pp. 166–176, 1990. https://doi.org/10.1016/0030-4018(90)90380-C.

[175] M. V. Berry and S. Klein, "Geometric phases from stacks of crystal plates," *Journal of Modern Optics*, vol. 43, no. 1, pp. 165–180, 1996. https://doi.org/10.1080/09500349608232731.

[176] S. Ramaseshan and R. Nityananda, "The interference of polarized light as an early example of berry's phase," *Current Science*, vol. 55, no. 24, pp. 1225–1226, 1986. http://www.jstor.org/stable/24090242.

[177] R. Bhandari and J. Samuel, "Observation of topological phase by use of a laser interferometer," *Phys. Rev. Lett.*, vol. 60, pp. 1211–1213, 1988. https://doi.org/10.1103/PhysRevLett.60.1211.

[178] T. H. Chyba, L. J. Wang, L. Mandel, and R. Simon, "Measurement of the pancharatnam phase for a light beam," *Opt. Lett.*, vol. 13, no. 7, pp. 562–564, 1988. https://doi.org/10.1364/OL.13.000562.

[179] A. Hannonen, H. Partanen, A. Leinonen, J. Heikkinen, T. K. Hakala, A. T. Friberg, and T. Setälä, "Measurement of the pancharatnam–berry phase in two-beam interference," *Optica*, vol. 7, no. 10, pp. 1435–1439, 2020. https://doi.org/10.1364/OPTICA.401993.

[180] T. Malhotra, R. Gutiérrez-Cuevas, J. Hassett, M. R. Dennis, A. N. Vamivakas, and M. A. Alonso, "Measuring geometric phase without interferometry," *Phys. Rev. Lett.*, vol. 120, p. 233602, 2018. https://doi.org/10.1103/PhysRevLett.120.233602.

[181] S. Feng and H. G. Winful, "Physical origin of the Gouy phase shift," *Optics Letters*, vol. 26, no. 8, p. 485, 2001. https://doi.org/10.1364/ol.26.000485.

[182] L. G. Gouy, "Sur une propriété nouvelle des ondes lumineuses," *Comptes rendus de l'Académie des Sciences Paris*, vol. 110, 1890.

[183] R. Simon and N. Mukunda, "Bargmann invariant and the geometry of the Güoy Effect," *Physical Review Letters*, vol. 70, no. 7, pp. 880–883, 1993. https://doi.org/10.1103/PhysRevLett.70.880.

[184] R. Y. Zhong, Z. H. Zhu, H. J. Wu, C. Rosales-Guzmán, S. W. Song, and B. S. Shi, "Gouy-phase-mediated propagation variations and revivals of transverse structure in vectorially structured light," *Physical Review A*, vol. 103, no. 5, pp. 1–9, 2021. https://doi.org/10.1103/PhysRevA.103.053520.

[185] S. Rytov, "On transition from wave to geometrical optics," in *Dokl. Akad. Nauk SSSR*, vol. 18, pp. 263–266, 1938.

[186] J. N. Ross, "The rotation of the polarization in low birefringence monomode optical fibres due to geometric effects," *Optical and Quantum Electronics*, vol. 16, no. 5, pp. 455–461, 1984. https://doi.org/10.1007/bf00619638.

[187] M. Kitano, T. Yabuzaki, and T. Ogawa, "Comment on Observation of Berrys topological phase by use of an optical fiber," *Physical Review Letters*, vol. 58, no. 5, p. 523, 1987. https://doi.org/10.1103/PhysRevLett.58.523.

[188] R. Y. Chiao, A. Antaramian, K. M. Ganga, H. Jiao, S. R. Wilkinson, and H. Nathel, "Observation of a topological phase by means of a nonplanar Mach-Zehnder interferometer," *Physical Review Letters*, vol. 60, no. 13, pp. 1214–1217, 1988. https://doi.org/10.1103/PhysRevLett.60.1214.

[189] M. V. Berry, "Quantum adiabatic anholonomy." Lectures given at Ferrara School on Anomalies, Defects, Phases..., June 1989.

[190] S. C. Tiwari, "Topological defects, geometric phases, and the angular momentum of light," *Optik*, vol. 120, no. 9, pp. 414–417, 2009. https://doi.org/10.1016/j.ijleo.2007.10.008.

[191] A. T. O'Neil and J. Courtial, "Mode transformations in terms of the constituent Hermite-Gaussian or Laguerre-Gaussian modes and the variable-phase mode converter," *Optics Communications*, vol. 181, no. 1, pp. 35–45, 2000. https://doi.org/10.1016/S0030-4018(00)00736-7.

[192] G. Yun, K. Crabtree, and R. A. Chipman, "Three-dimensional polarization ray-tracing calculus I: definition and diattenuation," *Applied Optics*, vol. 50, no. 18, pp. 2855–2865, 2011. https://doi.org/10.1364/AO.50.002855.

[193] Z. Ma and S. Ramachandran, "Propagation stability in optical fibers: role of path memory and angular momentum," *Nanophotonics*, vol. 10, no. 1, pp. 209–224, 2021. https://doi.org/10.1515/nanoph-2020-0404.

[194] K. S. Youngworth and T. G. Brown, "Focusing of high numerical aperture cylindrical-vector beams," *Opt. Express*, vol. 7, no. 2, pp. 77–87, 2000. https://doi.org/10.1364/OE.7.000077.

[195] L. W. Clark, N. Schine, C. Baum, N. Jia, and J. Simon, "Observation of Laughlin states made of light," *Nature*, vol. 582, no. 7810, p. 41–45, 2020. http://dx.doi.org/10.1038/s41586-020-2318-5.

[196] S. J. M. Habraken and G. Nienhuis, "Modes of a twisted optical cavity," *Phys. Rev. A*, vol. 75, p. 033819, 2007. https://doi.org/10.1103/PhysRevA.75.033819.

[197] A. Forbes, "Structured light from lasers," *Laser & Photonics Reviews*, vol. 13, no. 11, p. 1900140, 2019. https://doi.org/10.1002/lpor.201900140.

[198] V. D'Ambrosio, N. Spagnolo, L. Del Re, S. Slussarenko, Y. Li, L. Kwek, L. Marrucci, S. Walborn, L. Aolita, and F. Sciarrino, "Photonic polarization gears for ultra-sensitive angular measurements," *Nature communications*, vol. 4, p. 2432, 2013. https://doi.org/10.1038/ncomms3432.

[199] Y. Shen, X. Wang, Z. Xie, C. Min, X. Fu, Q. Liu, M. Gong, and X. Yuan, "Optical vortices 30 years on: Oam manipulation from topological charge to multiple singularities," *Light: Science & Applications*, vol. 8, no. 1, 2019. http://dx.doi.org/10.1038/s41377-019-0194-2.

[200] F. Wang, X. Yin, Z. Zhang, Z. Chen, H. Wang, P. Li, Y. Hu, X. Zhou, and C. Peng, "Fundamentals and applications of topological polarization singularities," *Frontiers in Physics*, vol. 10, 2022. http://dx.doi.org/10.3389/fphy.2022.862962.

[201] S. Gao, F. C. Speirits, F. Castellucci, S. Franke-Arnold, S. M. Barnett, and J. B. Götte, "Paraxial skyrmionic beams," *Physical Review A*, vol. 102, no. 5, 2020. https://doi.org/10.1103/PhysRevA.102.053513.

[202] W. F. Basener, *Topology and Its Applications*. Wiley, 2006. http://dx.doi.org/10.1002/9780470067949.

[203] S. Inouye, S. Gupta, T. Rosenband, A. P. Chikkatur, A. Görlitz, T. L. Gustavson, A. E. Leanhardt, D. E. Pritchard, and W. Ketterle, "Observation of vortex phase singularities in bose-einstein condensates," *Physical Review Letters*, vol. 87, no. 8, 2001. http://dx.doi.org/10.1103/PhysRevLett.87.080402.

[204] D. Gannon, "On the topology of spacelike hypersurfaces, singularities, and black holes," *General Relativity and Gravitation*, vol. 7, no. 2, p. 219–232, 1976. http://dx.doi.org/10.1007/BF00763437.

[205] A. I. Awad and K. Baba, *Fingerprint Singularity Detection: A Comparative Study*, p. 122–132. Springer Berlin Heidelberg, 2011. http://dx.doi.org/10.1007/978-3-642-22170-5_11.

[206] Y. C. Kim and M. Matsui, "Analytical and empirical models of tornado vortices: A comparative study," *Journal of Wind Engineering and Industrial Aerodynamics*, vol. 171, p. 230–247, 2017. http://dx.doi.org/10.1016/j.jweia.2017.10.009.

[207] M. F. Hasler, *Singular Solutions to Equations of Fluid Mechanics and Dynamics Near a Hurricane's Eye*, p. 373–380. Springer International Publishing, 2021. http://dx.doi.org/10.1007/978-3-030-87502-2_38.

[208] V. G. Danilov, G. A. Omel'yanov, and D. Rozenknop, "Calculations of the hurricane eye motion based on singularity propagation theory," *Electronic Journal of Differential Equations*, vol. 2002, 2002. https://api.semanticscholar.org/CorpusID:54862644.

[209] A. McWilliam, C. M. Cisowski, Z. Ye, F. C. Speirits, J. B. Götte, S. M. Barnett, and S. Franke-Arnold, "Topological approach of characterizing optical skyrmions and multi-skyrmions," *Laser & Photonics Reviews*, vol. 17, no. 9, p. 2300155, 2023. https://doi.org/10.1002/lpor.202300155.

[210] S. M. Barnett, C. M. Cisowski, A. McWilliam, F. C. Speirits, Z. Ye, J. B. Götte, and S. Franke-Arnold, "Optical skyrmions," in *Active Photonic Platforms (APP) 2023* (G. S. Subramania and S. Foteinopoulou, eds.), vol. 12647, p. 126470A, International Society for Optics and Photonics, SPIE, 2023. https://doi.org/10.1117/12.2676688.

[211] A. McWilliam, C. M. Cisowski, Z. Ye, F. C. Speirits, J. B. Goette, S. M. Barnett, and S. Franke-Arnold, "A topological approach for characterising optical skyrmions," in *Complex Light and Optical Forces XVIII* (D. L. Andrews, E. J. Galvez, and H. Rubinsztein-Dunlop, eds.), SPIE, 2024. http://dx.doi.org/10.1117/12.3002420.

[212] Z. Ye, S. M. Barnett, S. Franke-Arnold, J. B. Götte, A. McWilliam, F. C. Speirits, and C. M. Cisowski, "Theory of paraxial optical skyrmions," *Proceedings of the Royal Society A*, vol. 480, no. 2297, 2024. http://dx.doi.org/10.1098/rspa.2024.0109.

[213] T. H. R. Skyrme and B. F. J. Schonland, "A non-linear field theory," *Proceedings of the Royal Society of London. Series A. Mathematical and Physical Sciences*, vol. 260, no. 1300, pp. 127–138, 1961. https://doi.org/10.1098/rspa.1961.0018.

[214] M. Nakahara, *Geometry, Topology and Physics*. CRC Press, 2018. http://dx.doi.org/10.1201/9781315275826.

[215] W. Lee, A. H. Gheorghe, K. Tiurev, T. Ollikainen, M. Möttönen, and D. S. Hall, "Synthetic electromagnetic knot in a three-dimensional skyrmion," *Science Advances*, vol. 4, no. 3, 2018. http://dx.doi.org/10.1126/sciadv.aao3820.

[216] P. Sutcliffe, "Skyrmion knots in frustrated magnets," *Physical Review Letters*, vol. 118, no. 24, 2017. http://dx.doi.org/10.1103/PhysRevLett.118.247203.

[217] D. Cortés-Ortuño, W. Wang, M. Beg, R. A. Pepper, M.-A. Bisotti, R. Carey, M. Vousden, T. Kluyver, O. Hovorka, and H. Fangohr, "Thermal stability and topological protection of skyrmions in nanotracks," *Scientific Reports*, vol. 7, no. 1, 2017. http://dx.doi.org/10.1038/s41598-017-03391-8.

[218] D. Bazeia, J. Ramos, and E. Rodrigues, "Topological strength of magnetic skyrmions," *Journal of Magnetism and Magnetic Materials*, vol. 423, p. 411–420, 2017. http://dx.doi.org/10.1016/j.jmmm.2016.10.021.

[219] S. Gao, *Skyrmionic beams and quantum matched filtering*. PhD thesis, School of Physics and Astronomy, College of Science and Engineering, University of Glasgow, 2022. https://theses.gla.ac.uk/83183/.

[220] R. F. Moss, "J. r. weeks, the shape of space: how to visualize surfaces and three-dimensional manifolds," *Proceedings of the Edinburgh Mathematical Society*, vol. 30, pp. 327 – 327, 1987. http://dx.doi.org/10.1017/s001309150002842x.

[221] N. S. Manton, *Skyrmions – A Theory of Nuclei*. WORLD SCIENTIFIC (EUROPE), 2022. http://dx.doi.org/10.1142/q0368.

[222] T. Skyrme, "A unified field theory of mesons and baryons," *Nuclear Physics*, vol. 31, p. 556–569, 1962. http://dx.doi.org/10.1016/0029-5582(62)90775-7.

[223] C. Naya and P. Sutcliffe, "Skyrmions and clustering in light nuclei," *Physical Review Letters*, vol. 121, no. 23, 2018. http://dx.doi.org/10.1103/PhysRevLett.121.232002.

[224] D. Vollhardt and P. Wolfle, *The Superfluid Phases of Helium 3*. Dover Books on Physics, Dover Publications, 2013. https://books.google.co.uk/books?id=4grCAgAAQBAJ.

[225] M. Rho and I. Zahed, *The Multifaceted Skyrmion*. WORLD SCIENTIFIC, 2015. https://doi.org/10.1142/9710.

[226] P. Sutcliffe, "Skyrmions, instantons and holography," *Journal of High Energy Physics*, vol. 2010, no. 8, 2010. https://doi.org/10.1007/jhep08(2010)019.

[227] U. Al Khawaja and H. Stoof, "Skyrmions in a ferromagnetic Bose–Einstein condensate," *Nature*, vol. 411, p. 918–920, 2001. https://doi.org/10.1038/35082010.

[228] C. D. Parmee, M. R. Dennis, and J. Ruostekoski, "Optical excitations of skyrmions, knotted solitons, and defects in atoms," *Communications Physics*, vol. 5, no. 1, 2022. https://doi.org/10.1038/s42005-022-00829-y.

[229] A. N. Bogdanov and C. Panagopoulos, "Physical foundations and basic properties of magnetic skyrmions," *Nature Reviews Physics*, vol. 2, no. 9, pp. 492–498, 2020. https://doi.org/10.1038/s42254-020-0203-7.

[230] Y. Tokura and N. Kanazawa, "Skyrmions in a ferromagnetic Bose–Einstein condensate," *Chemical Reviews*, vol. 5, no. 121, pp. 2857–2897, 2021. https://doi.org/10.1021/acs.chemrev.0c00297.

[231] C. Back, V. Cros, H. Ebert, K. Everschor-Sitte, A. Fert, M. Garst, T. Ma, S. Mankovsky, T. L. Monchesky, M. Mostovoy, N. Nagaosa, S. S. P. Parkin, C. Pfleiderer, N. Reyren, A. Rosch, Y. Taguchi, Y. Tokura, K. von Bergmann, and J. Zang, "The 2020 skyrmionics roadmap," *Journal of Physics D: Applied Physics*, vol. 53, no. 36, p. 363001, 2020. https://doi.org/10.1088/1361-6463/ab8418.

[232] S. Tsesses, E. Ostrovsky, K. Cohen, B. Gjonaj, N. H. Lindner, and G. Bartal, "Optical skyrmion lattice in evanescent electromagnetic fields," *Science*, vol. 361, no. 6406, pp. 993–996, 2018. https://doi.org/10.1126/science.aau0227.

[233] D. Sugic, R. Droop, E. Otte, D. Ehrmanntraut, F. Nori, J. Ruostekoski, C. Denz, and M. R. Dennis, "Particle-like topologies in light," *Nature Communications*, vol. 12, no. 1, 2021. https://doi.org/10.1038/s41467-021-26171-5.

[234] R. Gutiérrez-Cuevas and E. Pisanty, "Optical polarization skyrmionic fields in free space," *Journal of Optics*, vol. 23, no. 2, p. 024004, 2021. https://doi.org/10.1088/2040-8986/abe8b2.

[235] S. Seki, M. Garst, J. Waizner, R. Takagi, N. D. Khanh, Y. Okamura, K. Kondou, F. Kagawa, Y. Otani, and Y. Tokura, "Propagation dynamics of spin excitations along skyrmion strings," *Nature Communications*, vol. 11, no. 1, 2020. http://dx.doi.org/10.1038/s41467-019-14095-0.

[236] M. T. Birch, D. Cortés-Ortuño, L. A. Turnbull, M. N. Wilson, F. Groß, N. Träger, A. Laurenson, N. Bukin, S. H. Moody, M. Weigand, G. Schütz, H. Popescu, R. Fan, P. Steadman, J. A. T. Verezhak, G. Balakrishnan,

J. C. Loudon, A. C. Twitchett-Harrison, O. Hovorka, H. Fangohr, F. Y. Ogrin, J. Gräfe, and P. D. Hatton, "Real-space imaging of confined magnetic skyrmion tubes," *Nature Communications*, vol. 11, no. 1, 2020. http://dx.doi.org/10.1038/s41467-020-15474-8.

[237] S. Seki and M. Mochizuki, "Summary and perspective," in *Skyrmions in Magnetic Materials*, p. 67–69, Springer International Publishing, 2015. http://dx.doi.org/10.1007/978-3-319-24651-2_5.

[238] S. Mühlbauer, B. Binz, F. Jonietz, C. Pfleiderer, A. Rosch, A. Neubauer, R. Georgii, and P. Böni, "Skyrmion lattice in a chiral magnet," *Science*, vol. 323, no. 5916, p. 915–919, 2009. http://dx.doi.org/10.1126/science.1166767.

[239] A. Fert, V. Cros, and J. Sampaio, "Skyrmions on the track," *Nature Nanotechnology*, vol. 8, no. 3, p. 152–156, 2013. http://dx.doi.org/10.1038/nnano.2013.29.

[240] D. Foster, C. Kind, P. J. Ackerman, J.-S. B. Tai, M. R. Dennis, and I. I. Smalyukh, "Two-dimensional skyrmion bags in liquid crystals and ferromagnets," *Nature Physics*, vol. 15, no. 7, p. 655–659, 2019. http://dx.doi.org/10.1038/s41567-019-0476-x.

[241] C. H. Marrows and K. Zeissler, "Perspective on skyrmion spintronics," *Applied Physics Letters*, vol. 119, no. 25, 2021. http://dx.doi.org/10.1063/5.0072735.

[242] Y. Ishikawa, K. Tajima, D. Bloch, and M. Roth, "Helical spin structure in manganese silicide mnsi," *Solid State Communications*, vol. 19, no. 6, p. 525–528, 1976. http://dx.doi.org/10.1016/0038-1098(76)90057-0.

[243] J. Beille, J. Voiron, and M. Roth, "Long period helimagnetism in the cubic B20 $Fe_xCo_{1-x}Si$ and $Co_xMn_{1-x}Si$ alloys," *Solid State Communications*, vol. 47, no. 5, p. 399–402, 1983. http://dx.doi.org/10.1016/0038-1098(83)90928-6.

[244] B. Lebech, J. Bernhard, and T. Freltoft, "Magnetic structures of cubic FeGe studied by small-angle neutron scattering," *Journal of Physics: Condensed Matter*, vol. 1, no. 35, p. 6105–6122, 1989. http://dx.doi.org/10.1088/0953-8984/1/35/010.

[245] B. Lebech, P. Harris, J. Skov Pedersen, K. Mortensen, C. Gregory, N. Bernhoeft, M. Jermy, and S. Brown, "Magnetic phase diagram of MnSi," *Journal of Magnetism and Magnetic Materials*, vol. 140–144, p. 119–120, 1995. http://dx.doi.org/10.1016/0304-8853(94)01115-X.

[246] S. Sachdev, *Quantum Phase Transitions*. Cambridge University Press, 2011. http://dx.doi.org/10.1017/CBO9780511973765.

[247] S. Li, X. Wang, and T. Rasing, "Magnetic skyrmions: Basic properties and potential applications," *Interdisciplinary Materials*, vol. 2, no. 2, p. 260–289, 2023. http://dx.doi.org/10.1002/idm2.12072.

[248] K. Everschor-Sitte, J. Masell, R. M. Reeve, and M. Kläui, "Perspective: Magnetic skyrmions—overview of recent progress in an active research field," *Journal of Applied Physics*, vol. 124, no. 24, 2018. http://dx.doi.org/10.1063/1.5048972.

[249] B. Göbel, I. Mertig, and O. A. Tretiakov, "Beyond skyrmions: Review and perspectives of alternative magnetic quasiparticles," *Physics Reports*, vol. 895, p. 1–28, 2021. http://dx.doi.org/10.1016/j.physrep.2020.10.001.

[250] A. M. Beckley, T. G. Brown, and M. A. Alonso, "Full poincaré beams," *Optics Express*, vol. 18, no. 10, p. 10777, 2010. http://dx.doi.org/10.1364/OE.18.010777.

[251] C. Cisowski, C. Ross, and S. Franke-Arnold, "Building paraxial optical skyrmions using rational maps," *Advanced Photonics Research*, vol. 4, no. 4, 2023. http://dx.doi.org/10.1002/adpr.202200350.

[252] S. M. Barnett, F. C. Speirits, and J. B. Götte, "On lines of constant polarisation in structured light beams," *Epl*, vol. 143, no. 3, 2023. https://doi.org/10.1209/0295-5075/ace8b7.

[253] E. Schmidt, "Zur theorie der linearen und nichtlinearen integralgleichungen," *Mathematische Annalen*, vol. 63, no. 4, p. 433–476, 1907. http://dx.doi.org/10.1007/BF01449770.

[254] S. M. Barnett, *Quantum Information*. Oxford University Press, Inc., 2009.

[255] D. Vollhardt and P. Woelfle, *The Superfluid Phases Of Helium 3*. CRC Press, 1 ed., 1990. http://dx.doi.org/10.1201/b12808.

[256] G. E. Volovik, *The Universe in a Helium Droplet*. Oxford University PressOxford, 2009. http://dx.doi.org/10.1093/acprof:oso/9780199564842.001.0001.

[257] M. M. Salomaa and G. E. Volovik, "Quantized vortices in superfluid ^{3}He," *Reviews of Modern Physics*, vol. 59, no. 3, p. 533–613, 1987. http://dx.doi.org/10.1103/RevModPhys.59.533.

[258] G. Palumbo and M. Cirio, "Skyrmion superfluidity in two-dimensional interacting fermionic systems," *Scientific Reports*, vol. 5, no. 1, 2015. http://dx.doi.org/10.1038/srep10824.

[259] S. Donati, L. Dominici, G. Dagvadorj, D. Ballarini, M. De Giorgi, A. Bramati, G. Gigli, Y. G. Rubo, M. H. Szymańska, and D. Sanvitto, "Twist of generalized skyrmions and spin vortices in a polariton superfluid," *Proceedings of the National Academy of Sciences*, vol. 113, no. 52, p. 14926–14931, 2016. http://dx.doi.org/10.1073/pnas.1610123114.

[260] N. D. Mermin and T.-L. Ho, "Circulation and angular momentum in the $\boldsymbol{A}$ phase of superfluid helium-3," *Physical Review Letters*, vol. 36, no. 11, p. 594–597, 1976. http://dx.doi.org/10.1103/PhysRevLett.36.594.

[261] Y. Shen, "Topological bimeronic beams," *Optics Letters*, vol. 46, no. 15, p. 3737, 2021. http://dx.doi.org/10.1364/ol.431122.

[262] Y. Shen, E. C. Martínez, and C. Rosales-Guzmán, "Generation of Optical Skyrmions with Tunable Topological Textures," *ACS Photonics*, 2022. http://dx.doi.org/10.1021/acsphotonics.1c01703.

[263] H. Teng, J. Zhong, J. Chen, X. Lei, and Q. Zhan, "Physical conversion and superposition of optical skyrmion topologies," *Photon. Res.*, vol. 11, no. 12, pp. 2042–2053, 2023. http://dx.doi.org/10.1364/PRJ.499485.

[264] K. Singh, P. Ornelas, A. Dudley, and A. Forbes, "Synthetic spin dynamics with bessel-gaussian optical skyrmions," *Opt. Express*, vol. 31, no. 10, pp. 15289–15300, 2023. http://dx.doi.org/10.1364/OE.483936.

[265] A. Y. Bekshaev, M. S. Soskin, and M. V. Vasnetsov, "An optical vortex as a rotating body: Mechanical features of a singular light beam," *Journal of Optics A: Pure and Applied Optics*, vol. 6, no. 5, 2004. http://dx.doi.org/10.1088/1464-4258/6/5/004.

[266] G. Arora, S. Joshi, H. Singh, V. Haridas, and P. Senthilkumaran, "Perturbation of V-point polarization singular vector beams," *Optics and Laser Technology*, vol. 158, no. PA, p. 108842, 2023. https://doi.org/10.1016/j.optlastec.2022.108842.

[267] J. Řeháček, B. G. Englert, and D. Kaszlikowski, "Minimal qubit tomography," *Physical Review A - Atomic, Molecular, and Optical Physics*, vol. 70, no. 5 A, pp. 1–13, 2004. https://doi.org/10.1103/PhysRevA.70.052321.

[268] A. Ling, K. P. Soh, A. Lamas-Linares, and C. Kurtsiefer, "Experimental polarization state tomography using optimal polarimeters," *Physical Review A*,

vol. 74, no. 2, pp. 022309–1–7, 2006. https://doi.org/10.1103/PhysRevA.74.022309.

[269] M. A. Al Khafaji, C. M. Cisowski, H. Jimbrown, S. Croke, S. Pádua, and S. Franke-Arnold, "Single-shot characterization of vector beams by generalized measurements," *Optics Express*, vol. 30, no. 13, p. 22396, 2022. https://doi.org/10.1364/oe.458352.

[270] A. McWilliam, M. Al Khafaji, S. Svensson, S. Pádua, and S. Franke-Arnold, "Dynamic mueller matrix polarimetry using generalized measurements," *Optics Express*, vol. 32, no. 12, pp. 21909–21924, 2024. http://dx.doi.org/10.1364/OE.521069.

[271] D. F. James, P. G. Kwiat, W. J. Munro, and A. G. White, "Measurement of qubits," *Physical Review A - Atomic, Molecular, and Optical Physics*, vol. 64, no. 5, p. 15, 2001. https://doi.org/10.1103/PhysRevA.64.052312.

[272] P. Walther, K. J. Resch, T. Rudolph, E. Schenck, H. Weinfurter, V. Vedral, M. Aspelmeyer, and A. Zeilinger, "Experimental one-way quantum computing," *Nature*, vol. 434, no. 7030, p. 169–176, 2005. http://dx.doi.org/10.1038/nature03347.

[273] Z. Hu and S. Kais, "Characterization of quantum states based on creation complexity," *Advanced Quantum Technologies*, vol. 3, no. 9, 2020. http://dx.doi.org/10.1002/qute.202000043.

[274] M. Dušek, N. Lütkenhaus, and M. Hendrych, *Quantum cryptography*, p. 381–454. Elsevier, 2006. http://dx.doi.org/10.1016/s0079-6638(06)49005-3.

[275] G. Cariolaro, *Quantum Communications*. Springer International Publishing, 2015. http://dx.doi.org/10.1007/978-3-319-15600-2.

[276] J. Altepeter, E. Jeffrey, and P. Kwiat, "Photonic state tomography," in *Advances In Atomic, Molecular, and Optical Physics* (P. Berman and C. Lin, eds.), vol. 52, pp. 105–159, Academic Press, 2005. https://doi.org/10.1016/S1049-250X(05)52003-2.

[277] V. I. Yashin, E. O. Kiktenko, A. S. Mastiukova, and A. K. Fedorov, "Minimal informationally complete measurements for probability representation of quantum dynamics," *New Journal of Physics*, vol. 22, no. 10, p. 103026, 2020. http://doi.org/10.1088/1367-2630/abb963.

[278] T. Durt, B.-G. Englert, I. Bengtsson, and K. Życzkowski, "On mutuallt unbiased bases," *International Journal of Quantum Information*, vol. 08, no. 04, p. 535–640, 2010. http://dx.doi.org/10.1142/S0219749910006502.

[279] M. A. Nielsen and I. L. Chuang, *Quantum Computation and Quantum Information: 10th Anniversary Edition*. Cambridge University Press, 2010. http://dx.doi.org/10.1017/CBO9780511976667.

[280] R. B. M. Clarke, V. M. Kendon, A. Chefles, S. M. Barnett, E. Riis, and M. Sasaki, "Experimental realization of optimal detection strategies for overcomplete states," *Phys. Rev. A*, vol. 64, p. 012303, 2001. https://doi.org/10.1103/PhysRevA.64.012303.

[281] P. Busch, "Informationally complete sets of physical quantities," *International Journal of Theoretical Physics*, vol. 30, no. 9, p. 1217–1227, 1991. http://doi.org/10.1007/BF00671008.

[282] P. Busch, G. Cassinelli, and P. J. Lahti, "Probability structures for quantum state spaces," *Reviews in Mathematical Physics*, vol. 07, no. 07, p. 1105–1121, 1995. http://doi.org/10.1142/S0129055X95000402.

[283] J. M. Renes, R. Blume-Kohout, A. J. Scott, and C. M. Caves, "Symmetric informationally complete quantum measurements," *Journal of Mathematical Physics*, vol. 45, no. 6, pp. 2171–2180, 2004. https://doi.org/10.1063/1.1737053.

[284] C. Paiva-Sánchez, E. Burgos-Inostroza, O. Jiménez, and A. Delgado, "Quantum tomography via equidistant states," *Phys. Rev. A*, vol. 82, p. 032115, 2010. https://doi.org/10.1103/PhysRevA.82.032115.

[285] P. G. Kwiat, K. Mattle, H. Weinfurter, A. Zeilinger, A. V. Sergienko, and Y. Shih, "New high-intensity source of polarization-entangled photon pairs," *Phys. Rev. Lett.*, vol. 75, pp. 4337–4341, 1995. https://doi.org/10.1103/PhysRevLett.75.4337.

[286] J. Zeuner, A. N. Sharma, M. Tillmann, R. Heilmann, M. Gräfe, A. Moqanaki, A. Szameit, and P. Walther, "Integrated-optics heralded controlled-not gate for polarization-encoded qubits," *npj Quantum Information*, vol. 4, no. 1, 2018. http://dx.doi.org/10.1038/s41534-018-0068-0.

[287] F. Flamini, N. Spagnolo, and F. Sciarrino, "Photonic quantum information processing: a review," *Reports on Progress in Physics*, vol. 82, no. 1, p. 016001, 2018. http://dx.doi.org/10.1088/1361-6633/aad5b2.

[288] A. Luis, "Chapter five - polarization in quantum optics," in *Progress in Optics* (T. D. Visser, ed.), vol. 61, pp. 283–331, Elsevier, 2016. https://doi.org/10.1016/bs.po.2015.10.003.

[289] D. Stifter, P. Burgholzer, O. Höglinger, E. Götzinger, and C. Hitzenberger, "Polarisation-sensitive optical coherence tomography for material characterisation and strain-field mapping," *Appl. Phys. A*, vol. 76, no. 6, pp. 947–951, 2003. https://doi.org/10.1007/s00339-002-2065-5.

[290] E. Hearn, "Chapter 6 - experimental stress analysis," in *Mechanics of Materials 2 (Third Edition)* (E. Hearn, ed.), pp. 166–192, Oxford: Butterworth-Heinemann, third edition ed., 1997. https://doi.org/10.1016/B978-075063266-9/50007-X.

[291] Z. Li, C. Cui, X. Zhou, S. Bian, O. Arteaga, and X. Xu, "Characterization of amorphous carbon films from 5 nm to 200 nm on single-side polished a-plane sapphire substrates by spectroscopic ellipsometry," *Frontiers in Physics*, vol. 10, 2022. https://doi.org/10.3389/fphy.2022.968101.

[292] H. Fujiwara, *Spectroscopic ellipsometry: principles and applications*. John Wiley & Sons, 2007. https://doi.org/10.1002/9780470060193.

[293] P. M. Johnson, D. A. Olson, S. Pankratz, T. Nguyen, J. Goodby, M. Hird, and C. C. Huang, "Structure of the liquid-crystal ferrielectric phases as determined by ellipsometry," *Phys. Rev. Lett.*, vol. 84, pp. 4870–4873, 2000. https://doi.org/10.1103/PhysRevLett.84.4870.

[294] A. V. Syroeshkin, T. V. Pleteneva, E. V. Uspenskaya, O. V. Levitskaya, M. A. Tribot-laspiere, I. A. Zlatsky, N. A. Khodorovich, M. V. Nikifirova, and S. A. Zaytseva, "Polarimetric research of pharmaceutical substances in aqueous solutions with different water isotopologues ratio," *International Journal of Applied Pharmaceutics*, vol. 10, no. 5, p. 243, 2018. https://doi.org/10.22159/ijap.2018v10i5.28151.

[295] S. Alali and A. Vitkin, "Polarized light imaging in biomedicine: emerging mueller matrix methodologies for bulk tissue assessment," *Journal of Biomedical Optics*, vol. 20, no. 6, p. 061104, 2015. https://doi.org/10.1117/1.jbo.20.6.061104.

[296] D. Gottlieb and O. Arteaga, "Mueller matrix imaging with a polarization camera: application to microscopy," *Opt. Express*, vol. 29, no. 21, pp. 34723–34734, 2021. https://doi.org/10.1364/OE.439529.

[297] A. Peres, "Neumark's theorem and quantum inseparability," *Foundations of Physics*, vol. 20, no. 12, p. 1441–1453, 1990. https://doi.org/10.1007/BF01883517.

[298] A. Ling, K. P. Soh, A. Lamas-Linares, and C. Kurtsiefer, "An optimal photon counting polarimeter," *Journal of Modern Optics*, vol. 53, no. 10, p. 1523–1528, 2006. http://dx.doi.org/10.1080/09500340600674242.

[299] M. A. Al Khafaji, C. M. Cisowski, H. Jimbrown, S. Croke, S. Pádua, and S. Franke-Arnold, "Single-shot characterization of vector beams by generalized measurements: supplement," *Optics Express*, vol. 30, no. 13, p. 22396, 2022. https://doi.org/10.6084/m9.figshare.19771954.

[300] N. Kiesel, C. Schmid, U. Weber, R. Ursin, and H. Weinfurter, "Linear optics controlled-phase gate made simple," *Phys. Rev. Lett.*, vol. 95, p. 210505, 2005. https://doi.org/10.1103/PhysRevLett.95.210505.

[301] R. Okamoto, H. F. Hofmann, S. Takeuchi, and K. Sasaki, "Demonstration of an optical quantum controlled-not gate without path interference," *Phys. Rev. Lett.*, vol. 95, p. 210506, 2005. https://doi.org/10.1103/PhysRevLett.95.210506.

[302] N. K. Langford, T. J. Weinhold, R. Prevedel, K. J. Resch, A. Gilchrist, J. L. O'Brien, G. J. Pryde, and A. G. White, "Demonstration of a simple entangling optical gate and its use in bell-state analysis," *Phys. Rev. Lett.*, vol. 95, p. 210504, 2005. https://doi.org/10.1103/PhysRevLett.95.210504.

[303] T. Kopyciuk, M. Lewandowski, and P. Kurzyński, "Pre- and post-selection paradoxes in quantum walks," *New Journal of Physics*, vol. 21, no. 10, p. 103054, 2019. https://doi.org/10.1088/1367-2630/ab4cf8.

[304] L. Xiao, W.-T. Xue, F. Song, Y.-M. Hu, W. Yi, Z. Wang, and P. Xue, "Observation of non-Hermitian edge burst in quantum dynamics," *arXiv:2303.12831v1 [cond-mat.mes-hall]*, no. March, 2023. https://arxiv.org/abs/2303.12831.

[305] Z. E. D. Medendorp, F. A. Torres-Ruiz, L. K. Shalm, G. N. M. Tabia, C. A. Fuchs, and A. M. Steinberg, "Experimental characterization of qutrits using symmetric informationally complete positive operator-valued measurements," *Phys. Rev. A*, vol. 83, p. 051801, 2011. https://doi.org/10.1103/PhysRevA.83.051801.

[306] F. Kaiser, T. Coudreau, P. Milman, D. B. Ostrowsky, and S. Tanzilli, "Entanglement-enabled delayed-choice experiment," *Science*, vol. 338, no. 6107, pp. 637–640, 2012. https://doi.org/10.1126/science.1226755.

[307] M. Jara, J. P. Marrou, M. Uria, C. M. L. Torre, and F. D. Zela, "Experimental display of generalized wave-particle duality," *Opt. Express*, vol. 30, no. 19, pp. 34740–34749, 2022. https://doi.org/10.1364/OE.466010.

[308] J. Flórez, N. J. Carlson, C. H. Nacke, L. Giner, and J. S. Lundeen, "A variable partially polarizing beam splitter," *Review of Scientific Instruments*, vol. 89, no. 2, p. 023108, 2018. https://doi.org/10.1063/1.5004805.

[309] P. Hariharan, *Basics of Interferometry*. Elsevier, 2007. http://dx.doi.org/10.1016/B978-0-12-373589-8.X5000-7.

[310] M. Totzeck, *Interferometry*, p. 1255–1283. Springer Berlin Heidelberg, 2012. http://dx.doi.org/10.1007/978-3-642-19409-2_16.

[311] D. Malacara, *Twyman–Green Interferometer*, ch. 2, pp. 46–96. John Wiley & Sons, Ltd, 2007. https://doi.org/10.1002/9780470135976.ch2.

[312] G. Pavlath, "Fiber-optic gyroscopes," in *Proceedings of LEOS'94*, vol. 2, pp. 237–238 vol.2, 1994. https://doi.org/10.1109/LEOS.1994.586467.

[313] A. Freise and K. Strain, "Interferometer techniques for gravitational-wave detection," *Living Reviews in Relativity*, vol. 13, no. 1, 2010. http://dx.doi.org/10.12942/lrr-2010-1.

[314] H. Kandpal, R. Mehrotra, and S. Raman, "Determination of surface flatness by spectral interferometric method," *Optics and Lasers in Engineering*, vol. 43, no. 12, p. 1315–1321, 2005. http://dx.doi.org/10.1016/j.optlaseng.2005.02.002.

[315] C. Xu, L. Chen, and J. Yin, "Method for absolute flatness measurement of optical surfaces," *Applied Optics*, vol. 48, no. 13, p. 2536, 2009. http://dx.doi.org/10.1364/AO.48.002536.

[316] J. Hough, "Polarimetry: a powerful diagnostic tool in astronomy," *Astronomy & Geophysics*, vol. 47, no. 3, pp. 3.31–3.35, 2006. https://doi.org/10.1111/j.1468-4004.2006.47331.x.

[317] B. W. Lites, M. Kubo, H. Socas-Navarro, T. Berger, Z. Frank, R. Shine, T. Tarbell, A. Title, K. Ichimoto, Y. Katsukawa, S. Tsuneta, Y. Suematsu, T. Shimizu, and S. Nagata, "The horizontal magnetic flux of the quiet-sun internetwork as observed with the hinode spectro-polarimeter," *The Astrophysical Journal*, vol. 672, no. 2, p. 1237, 2008. https://dx.doi.org/10.1086/522922.

[318] E. Costa, P. Soffitta, R. Bellazzini, A. Brez, N. Lumb, and G. Spandre, "An efficient photoelectric x-ray polarimeter for the study of black holes and neutron stars," *Nature*, vol. 411, no. 6838, pp. 662–665, 2001. https://doi.org/10.1038/35079508.

[319] D. N. Ignatenko, A. V. Shkirin, Y. P. Lobachevsky, and S. V. Gudkov, "Applications of mueller matrix polarimetry to biological and agricultural diagnostics: A review," *Applied Sciences*, vol. 12, no. 10, 2022. https://www.mdpi.com/2076-3417/12/10/5258.

[320] A. Arango-Restrepo, O. Arteaga, D. Barragán, and J. M. Rubi, "Chiral symmetry breaking induced by energy dissipation," *Phys. Chem. Chem. Phys.*, vol. 25, pp. 9238–9248, 2023. http://dx.doi.org/10.1039/D2CP05939H.

[321] C. He, H. He, J. Chang, B. Chen, H. Ma, and M. J. Booth, "Polarisation optics for biomedical and clinical applications: a review," *Light: Science & Applications*, vol. 10, no. 194, 2021. http://dx.doi.org/10.1038/s41377-021-00639-x.

[322] N. Ghosh and I. A. Vitkin, "Tissue polarimetry: concepts, challenges, applications, and outlook," *Journal of biomedical optics*, vol. 16, no. 11, pp. 110801–11080129, 2011. http://dx.doi.org/10.1117/1.3652896.

[323] J. C. Ramella-Roman, I. Saytashev, and M. Piccini, "A review of polarization-based imaging technologies for clinical and preclinical applications," *Journal of Optics*, vol. 22, no. 12, p. 123001, 2020. https://dx.doi.org/10.1088/2040-8986/abbf8a.

[324] H. He, R. Liao, N. Zeng, P. Li, Z. Chen, X. Liu, and H. Ma, "Mueller matrix polarimetry—an emerging new tool for characterizing the microstructural feature of complex biological specimen," *Journal of Lightwave Technology*, vol. 37, no. 11, pp. 2534–2548, 2019. https://dx.doi.org/10.1109/JLT.2018.2868845.

[325] I. Ahmad, A. Khaliq, M. Iqbal, and S. Khan, "Mueller matrix polarimetry for characterization of skin tissue samples: A review," *Photodiagnosis and Photodynamic Therapy*, vol. 30, p. 101708, 2020. https://doi.org/10.1016/j.pdpdt.2020.101708.

[326] M. H. Smith, P. D. Burke, A. Lompado, E. A. Tanner, and L. W. Hillman, "Mueller matrix imaging polarimetry in dermatology," in *Biomedical Diagnostic, Guidance, and Surgical-Assist Systems II* (T. Vo-Dinh, W. S. G. M.D., and D. A. B. M.D., eds.), vol. 3911, pp. 210 – 216, International Society for Optics and Photonics, SPIE, 2000. https://doi.org/10.1117/12.384904.

[327] I. Pardo, S. Bian, J. Gomis-Brescó, E. Pascual, A. Canillas, S. Bosch, and O. Arteaga, "Wide-field mueller matrix polarimetry for spectral characterization of basic biological tissues: Muscle, fat, connective tissue, and skin," *Journal of Biophotonics*, p. e202300252, 2023. https://doi.org/10.1002/jbio.202300252.

[328] V. V. Tuchin, "Polarized light interaction with tissues," *Journal of Biomedical Optics*, vol. 21, no. 7, p. 071114, 2016. https://doi.org/10.1117/1.jbo.21.7.071114.

[329] A. Z. Goldberg, "Quantum theory of polarimetry: From quantum operations to mueller matrices," *Phys. Rev. Res.*, vol. 2, p. 023038, 2020. https://doi.org/10.1103/PhysRevResearch.2.023038.

[330] D. Klyshko, "Multiphoton interference and polarization effects," *Physics Letters A*, vol. 163, no. 5, pp. 349–355, 1992. https://doi.org/10.1016/0375-9601(92)90837-C.

[331] A. Z. Goldberg, "Chapter three - quantum polarimetry," in *Progress in Optics* (T. D. Visser, ed.), vol. 67, pp. 185–274, Elsevier, 2022. https://doi.org/10.1016/bs.po.2022.01.001.

[332] D. Bouwmeester, J.-W. Pan, K. Mattle, M. Eibl, H. Weinfurter, and A. Zeilinger, "Experimental quantum teleportation," *Nature*, vol. 390, pp. 575–579, 1997. https://doi.org/10.1038/37539.

[333] I. Dahl, "How to measure the mueller matrix of liquid-crystal cells," *Measurement Science and Technology*, vol. 12, no. 11, p. 1938, 2001. https://dx.doi.org/10.1088/0957-0233/12/11/325.

[334] M. K. Lars M.S. Aas, Pål G. Ellingsen and M. Lindgren, "Dynamic response of a fast near infra-red mueller matrix ellipsometer," *Journal of Modern Optics*, vol. 57, no. 17, pp. 1603–1610, 2010. https://doi.org/10.1080/09500340.2010.515750.

[335] Y. Li, W. Jia, R. Chen, H. Wang, M. Wang, and J. Yang, "Novel measurement of Mueller matrix for cells," in *2008 International Conference on Optical Instruments and Technology: Optoelectronic Measurement Technology and Applications* (S. Ye, G. Zhang, and J. Ni, eds.), vol. 7160, p. 716007, International Society for Optics and Photonics, SPIE, 2009. https://doi.org/10.1117/12.805691.

[336] B. I. Gramatikov, "Using a dynamic Mueller matrix in modeling of retinal birefringence scanning systems," *Results in Optics*, vol. 12, p. 100437, 2023. https://doi.org/10.1016/j.rio.2023.100437.

[337] K. M. Twietmeyer, R. A. Chipman, A. E. Elsner, Y. Zhao, and D. VanNasdale, "Mueller matrix retinal imager with optimized polarization conditions," *Opt. Express*, vol. 16, no. 26, pp. 21339–21354, 2008. https://doi.org/10.1364/OE.16.021339.

[338] H. Philpott, E. Garcia-Caurel, O. Guaitella, and A. Sobota, "Optimizing Mueller polarimetry in noisy systems throughover-determination," *Appl. Opt.*, vol. 60, no. 31, pp. 9594–9606, 2021. https://doi.org/10.1364/AO.435085.

[339] R. D. Hawley, *Applications and practical considerations of polarisation structuring by a Fresnel cone*. PhD thesis, School of Physics and Astronomy, College of Science and Engineering, University of Glasgow, 2022. https://theses.gla.ac.uk/id/eprint/82650.

[340] R. Petkovšek, J. Petelin, J. Možina, and F. Bammer, "Fast ellipsometric measurements based on a single crystal photo-elastic modulator," *Opt. Express*, vol. 18, no. 20, pp. 21410–21418, 2010. https://doi.org/10.1364/OE.18.021410.

[341] S. Zhang, H. Jiang, H. Gu, X. Chen, and S. Liu, "High-speed mueller matrix ellipsometer with microsecond temporal resolution," *Opt. Express*, vol. 28, no. 8, pp. 10873–10887, 2020. https://doi.org/10.1364/OE.389825.

[342] M. Dubreuil, S. Rivet, B. L. Jeune, and J. Cariou, "Snapshot mueller matrix polarimeter by wavelength polarization coding," *Opt. Express*, vol. 15, no. 21, pp. 13660–13668, 2007. https://doi.org/10.1364/OE.15.013660.

[343] Y. Feng, J. Huang, J. Zhou, S. Gao, W. Liu, X. Jiang, S. Huang, and Z. Li, "Ultrafast mueller matrix polarimetry with 10 nanosecond temporal resolution based on optical time-stretch," *Optics Letters*, vol. 47, no. 6, p. 1403, 2022. http://dx.doi.org/10.1364/OL.451766.

[344] F. Töppel, A. Aiello, C. Marquardt, E. Giacobino, and G. Leuchs, "Classical entanglement in polarization metrology," *New Journal of Physics*, vol. 16, no. 7, p. 073019, 2014. https://dx.doi.org/10.1088/1367-2630/16/7/073019.

[345] R. D. Hawley, J. Cork, N. Radwell, and S. Franke-Arnold, "Passive broadband full Stokes polarimeter using a Fresnel cone," *Scientific Reports*, vol. 9, no. 1, pp. 1–8, 2019. https://doi.org/10.1038/s41598-019-39118-0.

[346] J. Zhang, F. Fan, W. Fu, J. Zeng, and J. Wang, "Broadband real-time full-stokes polarimetry by multi-tasking geometric phase element array," *Journal of Optics*, vol. 24, p. 045801, mar 2022. https://dx.doi.org/10.1088/2040-8986/ac51b3.

[347] J. C. Suárez-Bermejo, J. C. González de Sande, M. Santarsiero, and G. Piquero, "Mueller matrix polarimetry using full Poincaré beams," *Optics and Lasers in Engineering*, vol. 122, no. May, pp. 134–141, 2019. https://dx.doi.org/10.1016/j.optlaseng.2019.05.030.

[348] J. C. Suárez-Bermejo, J. C. González de Sande, G. Piquero, A. V. Failla, and M. Santarsiero, "Full Poincaré Mueller Polarimetry Using a CCD Camera," *Photonics*, vol. 9, no. 10, pp. 1–12, 2022. https://dx.doi.org/10.3390/photonics9100702.

[349] A. Ben-Israel and T. N. E. Greville, *Generalized Inverses. Theory and Applications*. Springer, 2 ed., 2003. https://dx.doi.org/10.1007/b97366.

[350] H. Gu, X. Chen, C. Zhang, H. Jiang, and S. Liu, "Study of the retardance of a birefringent waveplate at tilt incidence by Mueller matrix ellipsometer," *Journal of Optics (United Kingdom)*, vol. 20, no. 1, 2018. = https://dx.doi.org/10.1088/2040-8986/aa9b05.

[351] "The Crystan Handbook of Infra-Red and Ultra-Violet Optical Materials." https://issuu.com/crystran/docs/handbook_2016_web, 2020. Accessed: 2023-10-03.

[352] T. Koshiba, "Quantum cryptography," *Handbook of Natural Computing*, vol. 3-4, no. January, pp. 1521–1543, 2012. https://doi.org/10.1007/978-3-540-92910-9_45.

[353] V. Scarani, H. Bechmann-Pasquinucci, N. J. Cerf, M. Dušek, N. Lütkenhaus, and M. Peev, "The security of practical quantum key distribution," *Reviews of Modern Physics*, vol. 81, no. 3, pp. 1301–1350, 2009. https://doi.org/10.1103/RevModPhys.81.1301.

[354] A. Forbes and I. Nape, "Quantum mechanics with patterns of light: Progress in high dimensional and multidimensional entanglement with structured light," *AVS Quantum Science*, vol. 1, no. 1, p. 011701, 2019. https://doi.org/10.1116/1.5112027.

[355] B. Ndagano, I. Nape, B. Perez-Garcia, S. Scholes, R. I. Hernandez-Aranda, F. S. Roux, T. Konrad, and A. Forbes, "Quantum-key distribution with vector modes," *Complex Light and Optical Forces XI*, vol. 10120, no. February 2017, p. 101200X, 2017. https://doi.org/10.1117/12.2251465.

[356] C. H. Bennett and G. Brassard, "Quantum cryptography: Public key distribution and coin tossing," *IEEE International Conference on Computers, Systems and Signal Processing*, 1984. https://doi.org/10.1016/j.tcs.2011.08.039.

[357] T. Attema, J. W. Bosman, and N. M. Neumann, "Optimizing the decoy-state BB84 QKD protocol parameters," *Quantum Information Processing*, vol. 20, no. 4, pp. 1–26, 2021. https://doi.org/10.1007/s11128-021-03078-0.

[358] M. Mafu, A. Dudley, S. Goyal, D. Giovannini, M. McLaren, M. J. Padgett, T. Konrad, F. Petruccione, N. Lütkenhaus, and A. Forbes, "Higher-dimensional orbital-angular-momentum-based quantum key distribution with mutually unbiased bases," *Physical Review A - Atomic, Molecular, and Optical Physics*, vol. 88, no. 3, 2013. https://doi.org/10.1103/PhysRevA.88.032305.

[359] F. Bouchard, K. Heshami, D. England, R. Fickler, R. W. Boyd, B. G. Englert, L. L. Sánchez-Soto, and E. Karimi, "Experimental investigation of high-dimensional quantum key distribution protocols with twisted photons," *Quantum*, vol. 2, 2018. https://doi.org/10.22331/q-2018-12-04-111.

[360] S. Gröblacher, T. Jennewein, A. Vaziri, G. Weihs, and A. Zeilinger, "Experimental quantum cryptography with qutrits," *New Journal of Physics*, vol. 8, 2006. https://doi.org/10.1088/1367-2630/8/5/075.

[361] M. Mirhosseini, O. S. Magaña-Loaiza, M. N. O'Sullivan, B. Rodenburg, M. Malik, M. P. Lavery, M. J. Padgett, D. J. Gauthier, and R. W. Boyd, "High-dimensional quantum cryptography with twisted light," *New Journal of Physics*, vol. 17, pp. 1–12, 2015. https://doi.org/10.1088/1367-2630/17/3/033033.

[362] I. Nape, B. Ndagano, B. Perez-Garcia, S. Scholes, R. I. Hernandez-Aranda, T. Konrad, and A. Forbes, "High-bit-rate quantum key distribution with entangled internal degrees of freedom of photons," *arXiv:1612.09261v1 [quant-ph]*, no. December, 2016. http://arxiv.org/abs/1612.09261.

[363] S. F. Mousavi, G. Vallone, P. Villoresi, and R. Nouroozi, "Generation of mutually unbiased bases for 4D-QKD with structured photons via LNOI photonic wire," *Journal of Optics (United Kingdom)*, vol. 20, no. 9, 2018. https://doi.org/10.1088/2040-8986/aad793.

[364] K. Inoue, "Quantum key distribution technologies," *IEEE Journal on Selected Topics in Quantum Electronics*, vol. 12, no. 4, pp. 888–896, 2006. https://doi.org/10.1109/JSTQE.2006.876606.

[365] A. Laing, V. Scarani, J. G. Rarity, and J. L. O'Brien, "Reference-frame-independent quantum key distribution," *Physical Review A - Atomic, Molecular, and Optical Physics*, vol. 82, no. 1, pp. 1–5, 2010. https://doi.org/10.1103/PhysRevA.82.012304.

[366] J. Wabnig, D. Bitauld, H. W. Li, A. Laing, J. L. O'brien, and A. O. Niskanen, "Demonstration of free-space reference frame independent quantum key distribution," *New Journal of Physics*, vol. 15, 2013. https://doi.org/10.1088/1367-2630/15/7/073001.

[367] V. D'Ambrosio, E. Nagali, S. P. Walborn, L. Aolita, S. Slussarenko, L. Marrucci, and F. Sciarrino, "Complete experimental toolbox for alignment-free quantum communication," *Nature Communications*, vol. 3, 2012. https://doi.org/10.1038/ncomms1951.

[368] J. C. Boileau, R. Laflamme, M. Laforest, and C. R. Myers, "Robust quantum communication using a polarization-entangled photon pair," *Physical Review Letters*, vol. 93, no. 22, pp. 1–4, 2004. https://doi.org/10.1103/PhysRevLett.93.220501.

[369] G. Vallone, V. D'Ambrosio, A. Sponselli, S. Slussarenko, L. Marrucci, F. Sciarrino, and P. Villoresi, "Free-space quantum key distribution by rotation-invariant twisted photons," *Physical Review Letters*, vol. 113, no. 6, pp. 1–5, 2014. https://doi.org/10.1103/PhysRevLett.113.060503.

[370] D. Chen, S. H. Zhao, L. Shi, and Y. Liu, "Measurement-device-independent quantum key distribution with pairs of vector vortex beams," *Physical Review A*, vol. 93, no. 3, pp. 1–5, 2016. https://doi.org/10.1103/PhysRevA.93.032320.

[371] "Thorabs: Fresnel rhomb retarders." https://www.thorlabs.com/newgrouppage9.cfm?objectgroup_id=154. Accessed: 2024-05-11.

[372] A. A. Abdullah and Y. H. Jassem, "Enhancement of quantum key distribution protocol bb84," *Journal of Computational and Theoretical Nanoscience*, vol. 16, no. 3, p. 1138–1154, 2019. http://dx.doi.org/10.1166/jctn.2019.8009.

[373] D. Gottesman and H.-K. Lo, "Proof of security of quantum key distribution with two-way classical communications," *IEEE Transactions on Information Theory*, vol. 49, no. 2, p. 457–475, 2003. http://dx.doi.org/10.1109/TIT.2002.807289.

[374] G. Murta, F. Rozpędek, J. Ribeiro, D. Elkouss, and S. Wehner, "Key rates for quantum key distribution protocols with asymmetric noise," *Physical Review A*, vol. 101, no. 6, 2020. http://dx.doi.org/10.1103/PhysRevA.101.062321.

[375] R. A. Chipman, W.-S. T. Lam, and G. Young, *Polarized Light and Optical Systems*. CRC Press, 2018. http://dx.doi.org/10.1201/9781351129121.

[376] C.-K. Chou, W.-L. Chen, P. T. Fwu, S.-J. Lin, H.-S. Lee, and C.-Y. Dong, "Polarization ellipticity compensation in polarization second-harmonic generation microscopy without specimen rotation," *Journal of Biomedical Optics*, vol. 13, no. 1, p. 014005, 2008. http://dx.doi.org/10.1117/1.2824379.

[377] M. Born and E. Wolf, *Principles of Optics*. Cambridge University Press, 7 ed., 1999. https://doi.org/10.1017/CBO9781139644181.

[378] V. N. Mahajan, "Zernike polynomials and optical aberrations," *Appl. Opt.*, vol. 34, no. 34, pp. 8060–8062, 1995. https://doi.org/10.1364/AO.34.008060.

[379] B. Tatian, "Aberration balancing in rotationally symmetric lenses∗," *J. Opt. Soc. Am.*, vol. 64, no. 8, pp. 1083–1091, 1974. https://doi.org/10.1364/JOSA.64.001083.

[380] V. N. Mahajan, "Zernike annular polynomials for imaging systems with annular pupils," *J. Opt. Soc. Am.*, vol. 71, no. 1, pp. 75–85, 1981. https://doi.org/10.1364/JOSA.71.000075.

[381] O. Mendoza-Yero, G. Mínguez-Vega, and J. Lancis, "Encoding complex fields by using a phase-only optical element," *Opt. Lett.*, vol. 39, no. 7, pp. 1740–1743, 2014. https://doi.org/10.1364/OL.39.001740.

[382] A. S. Ostrovsky, C. Rickenstorff-Parrao, and V. Arrizón, "Generation of the "perfect" optical vortex using a liquid-crystal spatial light modulator," *Opt. Lett.*, vol. 38, no. 4, pp. 534–536, 2013. https://doi.org/10.1364/OL.38.000534.

[383] C. K. Hsueh and A. A. Sawchuk, "Computer-generated double-phase holograms," *Appl. Opt.*, vol. 17, no. 24, pp. 3874–3883, 1978. https://doi.org/10.1364/AO.17.003874.

[384] V. Arrizón, U. Ruiz, R. Carrada, and L. A. González, "Pixelated phase computer holograms for the accurate encoding of scalar complex fields," *J. Opt. Soc. Am. A*, vol. 24, no. 11, pp. 3500–3507, 2007. https://doi.org/10.1364/JOSAA.24.003500.

[385] E. Bolduc, N. Bent, E. Santamato, E. Karimi, and R. W. Boyd, "Exact solution to simultaneous intensity and phase encryption with a single phase-only hologram," *Opt. Lett.*, vol. 38, no. 18, pp. 3546–3549, 2013. https://doi.org/10.1364/OL.38.003546.

[386] Hamamatsu. https://www.hamamatsu.com/eu/en/product/optical-components/lcos-slm/for-research-and-development.html. Accessed: 2023-04-19.

[387] N. Radwell, R. F. Offer, A. Selyem, and S. Franke-Arnold, "Optimisation of arbitrary light beam generation with spatial light modulators," *Journal of Optics (United Kingdom)*, vol. 19, no. 9, 2017. https://doi.org/0.1088/2040-8986/aa7f50.

[388] J. Arlt and M. J. Padgett, "Generation of a beam with a dark focus surrounded by regions of higher intensity: the optical bottle beam," *Opt. Lett.*, vol. 25, no. 4, pp. 191–193, 2000. https://doi.org/10.1364/OL.25.000191.

[389] C. Alpmann, M. Esseling, P. Rose, and C. Denz, "Holographic optical bottle beams," *Applied Physics Letters*, vol. 100, no. 11, 2012. https://doi.org/10.1063/1.3691957.

[390] Y. Xiao, Z. Yu, R. A. Wambold, H. Mei, G. Hickman, R. H. Goldsmith, M. Saffman, and M. A. Kats, "Efficient generation of optical bottle beams," *Nanophotonics*, vol. 10, no. 11, pp. 2893–2901, 2021. https://doi.org/10.1515/nanoph-2021-0243.

[391] J. Braat and P. Török, *Imaging Optics*. Cambridge University Press, 2019. http://dx.doi.org/10.1017/9781108552264.

[392] A. J. E. M. Janssen, "Extended nijboer–zernike approach for the computation of optical point-spread functions," *Journal of the Optical Society of America A*, vol. 19, no. 5, p. 849, 2002. http://dx.doi.org/10.1364/JOSAA.19.000849.

[393] S. v. Haver and A. J. E. M. Janssen, "Advanced analytic treatment and efficient computation of the diffraction integrals in the extended nijboer-zernike theory," *Journal of the European Optical Society: Rapid Publications*, vol. 8, 2013. http://dx.doi.org/10.2971/jeos.2013.13044.

[394] M. S. Soskin, V. N. Gorshkov, M. V. Vasnetsov, J. T. Malos, and N. R. Heckenberg, "Topological charge and angular momentum of light beams carrying optical vortices," *Phys. Rev. A*, vol. 56, pp. 4064–4075, 1997. https://doi.org/10.1103/PhysRevA.56.4064.

[395] I. Basistiy, V. Bazhenov, M. Soskin, and M. Vasnetsov, "Optics of light beams with screw dislocations," *Optics Communications*, vol. 103, no. 5, pp. 422–428, 1993. https://doi.org/10.1016/0030-4018(93)90168-5.

[396] J. Leach, E. Yao, and M. J. Padgett, "Observation of the vortex structure of a non-integer vortex beam," *New Journal of Physics*, vol. 6, no. 1, p. 71, 2004. https://doi.org/10.1088/1367-2630/6/1/071.

[397] S. Zheng and J. Wang, "Measuring Orbital Angular Momentum (OAM) States of Vortex Beams with Annular Gratings," *Sci. Rep.*, vol. 7, no. 40781, pp. 1–9, 2017. https://doi.org/10.1038/srep40781.

[398] G. C. G. Berkhout, M. P. J. Lavery, J. Courtial, M. W. Beijersbergen, and M. J. Padgett, "Efficient sorting of orbital angular momentum states of light," *Phys. Rev. Lett.*, vol. 105, p. 153601, 2010. https://doi.org/10.1103/PhysRevLett.105.153601.

[399] J. Leach, M. J. Padgett, S. M. Barnett, S. Franke-Arnold, and J. Courtial, "Measuring the orbital angular momentum of a single photon," *Phys. Rev. Lett.*, vol. 88, p. 257901, 2002. https://doi.org/10.1103/PhysRevLett.88.257901.

[400] A. Mair, A. Vaziri, G. Weihs, and A. Zeilinger, "Entanglement of the orbital angular momentum states of photons," *Nature*, vol. 412, pp. 313–316, 2001. https://doi.org/10.1038/35085529.

[401] P. Vaity, J. Banerji, and R. P. Singh, "Measuring the topological charge of an optical vortex by using a tilted convex lens," *Physics Letters, Section A: General, Atomic and Solid State Physics*, vol. 377, no. 15, pp. 1154–1156, 2013. http://doi.org/10.1016/j.physleta.2013.02.030.

[402] I. Nape, K. Singh, A. Klug, W. Buono, C. Rosales-Guzman, A. McWilliam, S. Franke-Arnold, A. Kritzinger, P. Forbes, A. Dudley, and A. Forbes, "Revealing the invariance of vectorial structured light in perturbing media," *Nature Photonics*, vol. 16, pp. 538–546, 2022. https://doi.org/10.1038/s41566-022-01023-w.

[403] W. K. Wootters, "Entanglement of formation and concurrence," *Quantum Informaion and Computation*, vol. 1, no. 1, pp. 27–44, 2001. https://doi.org/10.26421/QIC1.1-3.

[404] A. F. Abouraddy, A. V. Sergienko, B. E. Saleh, and M. C. Teich, "Quantum entanglement and the two-photon stokes parameters," *Optics Communications*, vol. 201, no. 1, pp. 93–98, 2002. https://doi.org/10.1016/S0030-4018(01)01645-5.

[405] M. Żukowski, W. Laskowski, and M. Wieśniak, "Normalized stokes operators for polarization correlations of entangled optical fields," *Phys. Rev. A*, vol. 95, p. 042113, 2017. https://doi.org/10.1103/PhysRevA.95.042113.

[406] E. Otte and C. Denz, "Optical trapping gets structure: Structured light for advanced optical manipulation," *Applied Physics Reviews*, vol. 7, no. 4, 2020. http://dx.doi.org/10.1063/5.0013276.

[407] N. Radwell, G. Walker, and S. Franke-Arnold, "Cold-atom densities of more than 10^{12} cm^{-3} in a holographically shaped dark spontaneous-force optical trap," *Physical Review A*, vol. 88, no. 4, 2013. http://dx.doi.org/10.1103/PhysRevA.88.043409.

[408] Y.-H. Ye, M.-X. Dong, Y.-C. Yu, D.-S. Ding, and B.-S. Shi, "Experimental realization of optical storage of vector beams of light in warm atomic vapor,"

Optics Letters, vol. 44, no. 7, p. 1528, 2019. http://dx.doi.org/10.1364/OL.44.001528.

[409] T. Konrad and A. Forbes, "Quantum mechanics and classical light," *Contemporary Physics*, vol. 60, no. 1, p. 1–22, 2019. http://dx.doi.org/10.1080/00107514.2019.1580433.

[410] S. So, M. Kim, D. Lee, D. M. Nguyen, and J. Rho, "Overcoming diffraction limit: From microscopy to nanoscopy," *Applied Spectroscopy Reviews*, vol. 53, no. 2–4, p. 290–312, 2017. http://dx.doi.org/10.1080/05704928.2017.1323309.

[411] E. Kristensson, E. Berrocal, and M. Aldén, "Quantitative 3d imaging of scattering media using structured illumination and computed tomography," *Optics Express*, vol. 20, no. 13, p. 14437, 2012. http://dx.doi.org/10.1364/OE.20.014437.

[412] J. Nylk, K. McCluskey, M. A. Preciado, M. Mazilu, Z. Yang, F. J. Gunn-Moore, S. Aggarwal, J. A. Tello, D. E. K. Ferrier, and K. Dholakia, "Light-sheet microscopy with attenuation-compensated propagation-invariant beams," *Science Advances*, vol. 4, no. 4, 2018. http://dx.doi.org/10.1126/sciadv.aar4817.